STUDY ON INFLUENCE OF DIFFERENT FORMS OF DAMPING AND OPERATING TEMPERATURE ON WHIRLING SPEEDS OF ROTORS

Submitted in partial fulfillment of the requirements for the award of the degree of

DOCTOR OF PHILOSOPHY

in

MECHANICAL ENGINEERING

by

RAVINDRA GARDAS

Roll No. 700912

under the Guidance of

PROF. P. BANGARU BABU

Department of Mechanical Engineering
National Institute of Technology, Warangal

&

RVBS MURTY

Senior Manager, Rotating Machines
General Electric (GE),
Hyderabad Technology Centre, Hyderabad

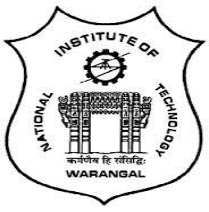

Department of Mechanical Engineering
NATIONAL INSTITUTE OF TECHNOLOGY
WARANGAL - 506004

2017

Thesis Approval Sheet

Study on Influence of Different forms of Damping and Operating Temperature on Whirling Speeds of Rotors

by

RAVINDRA GARDAS

is approved for the degree of

Doctor of philosophy

_____

Prof. _____

(Examiner)

_____

_____

_____

Prof P. BANGARU BABU

(Supervisor)

Department of Mechanical Engineering

National Institute of Technology

Warangal-506004

_____

RVBS MURTY

(Co-supervisor)

Senior Manager, Rotating Machines

General Electric (GE),

Hyderabad Technology Centre, Hyderabad

_____

Prof P. Bangaru Babu

Head & Chairman DSC

Department of Mechanical Engineering

National Institute of Technology

Warangal-506004

Department of Mechanical Engineering
NATIONAL INSTITUTE OF TECHNOLOGY
WARANGAL - 506004

This is to certify that the dissertation work entitled "**STUDY ON INFLUENCE OF DIFFERENT FORMS OF DAMPING AND OPERATING TEMPERATURE ON WHIRLING SPEEDS OF ROTORS**" which is being submitted by Mr. **Ravindra Gardas (Roll No.700912)**, his bonafide work is submitted to National Institute of Technology, Warangal, in partial fulfilment of requirement for the award of degree of **Doctor of Philosophy in Mechanical Engineering**.

To the best of our knowledge, the work incorporated in this thesis has not been submitted elsewhere for the award of any degree.

Prof P. Bangaru Babu
Internal - Supervisor
Department of Mechanical Engineering
National Institute of Technology
Warangal-506004

RVBS Murty
External - Supervisor
Senior Manager, Rotating Machines
General Electric (GE)
Hyderabad Technology Centre
Hyderabad -500081

Prof P. Bangaru Babu
Head & Chairman DSC
Department of Mechanical Engineering
National Institute of Technology
Warangal-506004

Dedicated
to
My Family

DECLARATION

This is to certify that the work presented in the thesis entitled **"STUDY ON INFLUENCE OF DIFFERENT FORMS OF DAMPING AND OPERATING TEMPERATURE ON WHIRLING SPEEDS OF ROTORS"** is a bonafide work done by me under the supervision of Dr P. Bangaru Babu, Professor Mechanical Department and was not submitted elsewhere for the award of any degree. I declare that this written submission represents my ideas in my own words and where others ideas or words have been included. I have adequately cited and referenced the original sources. I also declare that I have adhered to all principles of academic honesty and integrity and have not misrepresented or fabricated or falsified any idea/data/fact/source in my submission. I understand that any violation of the above will be a cause for disciplinary action by the institute and can also evoke penal action from the sources which have not been properly cited or from whom proper permission has not been taken when needed.

Ravindra Gardas
Roll No. - 700912
Date: - - 2017

ACKNOWLEDGEMENTS

I take this opportunity to express my sincere gratitude to my guide, Prof. P. Bangaru Babu and RVBS Murty for their invaluable guidance, suggestions and support during my work.

I am grateful to my Doctoral Scrutiny Committee (DSC) members, Prof. R. Narasimha Rao, Department of Mechanical Engineering and Prof. V. T. Somasekhar, Department of Electrical and Electronics Engineering for their support and suggestions at every level from starting to completion of work.

I am thankful DSC, Head of Mechanical Engineering Department and Director & Dean Academics, National Institute of Technology, Warangal for their support and encouragement.

I am very much obliged to my mother; spouse and children for their continuous support and encouragement in materializing my dream.

Date: - - 2017 **Ravindra Gardas**

ABSTRACT

Accurate prediction of rotor whirl speeds and critical speeds are fundamentally important in the design of rotating machinery. There has been an impressive progress in the study of rotor dynamics in the last decade. The use of finite elements for the simulation of rotor system makes it possible to handle complex problems. Literature shows that the influence of different forms of damping e.g. internal viscous damping, internal hysteretic damping and external viscous damping studied independently and predicted the rotor whirl speed. The change in the material properties with respect to temperature is studied extensively for different materials. The critical material properties are Young's modulus and Poisson's ratio which decides the whirl speeds and critical speeds. The effect of operating temperature on rotor whirl speeds is not available in the literature. In practical rotors, different forms of damping and operating temperature acting either independently or simultaneously with different combinations. There is a gap in the literature about consideration of different forms of damping acting together along with operating temperature. The present research aimed to fill this literature gap and predict the whirl speeds and critical speeds considering different forms of damping and operating temperature acting together along with different applications.

Finite element based dynamic model is developed in Mathcad environment for the prediction of whirling speeds and critical speeds of rotor. The rotor is discretized into finite elements and dynamic equations of motion are developed using Lagrangian method. Different forms of damping viz., internal viscous damping, internal hysteretic damping and external viscous damping are modelled along with operating temperature. These parameters are incorporated into the equations of motion. Expressed the equations of motion in fixed frame or inertial reference frame and rotating or whirl frame of reference. State space method is used to solve the equations of motion and extracting the eigenvalues. Dynamic model is validated with the whirl speed results published in literature for the case studies of individual parameters acting alone viz., undamped rotor, internal viscous damping and internal hysteretic damping.

The validated dynamic model is further used in simulation studies of different combinations of internal viscous damping, internal hysteretic damping, external viscous damping and operating temperature acting on the rotor either independently or simultaneously. The prediction of whirl speeds and critical speeds are done with all sixteen combinations of critical parameters. The practical rotors in all over the industrial applications

are categorized and grouped into sixteen possible combinations. Evolved systematic methodology to understand the effect of the critical parameters on the whirl speed with influence of different forms of damping and operating temperature. It is a systematic way of understanding the behavior of the critical parameters at high rotor spin speed along with different forms of damping and operating temperature. This technique helps to understand the importance of critical parameters, its effect on the output parameters like rotor backward whirl, forward whirl and critical speed.

A clear understanding of the influence of different forms of damping and operating temperature on rotor whirls speed and critical speed, helps in optimize the rotor in the design stage and making the robust design for different application, monitoring the rotor vibration and its behavior in the field which can avoid uncontrolled and undesired vibrations results into catastrophic failures.

Keywords: -

Forward whirl speed, backward whirl speed, critical speed, internal viscous damping, internal hysteretic damping, external viscous damping and operating temperature

TABLE OF CONTENTS

LIST OF FIGURES

LIST OF TABLES

NOMENCLATURE

English Letters

A - Cross sectional area

C_{xx} - Direct damping coefficient in X direction

C_{yy} - Direct damping coefficient in Y direction

C_{xy} - Cross coupled damping coefficient

C_{yx} - Cross coupled damping coefficient

Ce - External viscous damping

d - Inner diameter of the shaft

D - Outer diameter of the shaft

E - Young's modulus

E_0 - Complex modulus

E_1 - Storage modulus

E_2 - Loss modulus

E_t - Young's modulus with temperature effect

EI - Bending modulus

G - Shear modulus

I - Moment of Inertia

I_d^e - Diametral moment of inertia per unit length

I_p^e - Polar moment of inertia per unit length

K_{xx} - Direct stiffness coefficient in X direction

K_{yy} - Direct stiffness coefficient in Y direction

K_{xy} - Cross stiffness damping coefficient

K_{yx} - Cross stiffness damping coefficient

L - Length of the shaft

m^e - Mass per unit length

M_y - Bending moment in X-Z plane

M_x - Bending moment in Y-Z plane

q - Heat generation per unit time

Q_x - Shear force in X-Z plane

Q_y - Shear force in Y-Z plane

T - Kinetic energy

V - Potential energy

Matrices and Vectors

$[C_b]$ - Bearing damping matrix

$[G^e]$ - Gyroscopic matrix

$[G_t^e]$ - Gyroscopic matrix with temperature effect

$[K_B^e]$ - Stiffness matrix

$[K_{Bt}^e]$ - Stiffness matrix with temperature effect

$[K_b]$ - Bearing stiffness matirx

$[M_T^e]$ - Translatory mass matrix

$[M_{Tt}^e]$ - Translatory mass matrix with temperature effect

$[M_R^e]$ - Rotational mass matrix

$[M^{e}_{Rt}]$ - Rotational mass matrix with temperature effect

$[N_T(s)]$ - Translatory shape functions

$[N_R(s)]$ - Rotational shape functions

$[T_n]$ - Transformation matrix

$\bar{q}_n^{f}(t)$ - Nodal displacement vector

Greek Letters

β_y - Shear deformation in X-Z plane

β_x - Shear deformation in Y-Z plane

γ - Spin whirl ratio

ε - Strain

η_H - Internal hysteretic loss factor

η_v - Internal viscous damping

θ - Angular rotation in Y-Z plane

κ - Shear correction factor

κ_t - Shear correction factor with temperature effect

κGA - Effective shear modulus

μ_i - Viscosity

ν - Poisson's ratio

ϕ - Angular rotation in X-Z plane

φ - Phase angle

ρ - Density of the material

σ_S - Stiffness Stress

σ_D - Damping stress

ΔWR - Change in whirl speed ratio (%)

Φ - Shape factor

Φ_t - Shape factor with temperature effect

$\mathfrak{I}$ - Fixed or Inertial frame of reference

$\mathfrak{R}$ - Rotation or Whirl frame of reference

Ω - Spin speed

ABBREVIATIONS

BW - Backward whirl

DOE - Design of experiments

FW - Forward whirl

IHD - Internal hysteretic Damping

IVD - Internal viscous Damping

N - Number of revolution per sec

RD - Dissipation function

SWE - Synchronous whirl excitation

SM - Separation margin

TEMP - Operating temperature

CHAPTER 1

INTRODUCTION

1.1 OVERVIEW

High-Speed turbomachinery is used in a wide variety of applications, ranging from power generation turbines, generators, motors to industrial machine tools. Uncontrolled and undesired vibrations in the rotating machines can lead to catastrophic failures which result into an extra cost due to downtime repair and involves human and property loss. Because of continuing demand for increased power and performance, many modern machines in petrochemical and natural gas services are now being designed to operate at high speed and at high operating temperature. Rotors of these machines are highly unstable at high speed and high operating temperature.

The modelling and analysis of rotor-bearing system are not exactly same as the dynamics of spring, mass and dashpot system. The reference state for spring mass dashpot system is a stationary while for rotor bearing system it is rotational. The motion of the rotational axis of a rotating body in classical mechanics is called as precession motion whereas in rotor dynamic terminology term it is called as whirl motion. The whirl is a two-dimensional orbital motion made by the geometric center of the rotor. The angular velocity of the rotor in a bent state is referred as whirl speed. When the direction of whirl orbit is same as the direction of rotor spin speed, the whirl is called as a forward whirl. When the direction of whirl orbit is opposite to the direction of spin speed, the whirl is called as a backward whirl. The whirl speeds are also classified as synchronous whirl and asynchronous whirl. When the

whirling speed equals to the rotor spin speed, the whirl is called synchronous whirl and if it is different than the rotor spin speed then, the whirl is called asynchronous whirl.

The whirl speed and its nature depend upon rotor properties and spin speed. In the case of ideal undamped rotors, forward whirl speed increases and backward whirl speed decreases with increase in rotor spin speed. When the excitation due to the rotor unbalance coincides with the natural frequency of the rotor, the amplitude of the rotor vibration increases and resulted in ultimate failure.

The rotors are classified as rigid rotors and flexible rotors based on the operating speed. Rigid rotors are those rotors whose 'operating speed is below 70 % of its first critical speed'. These rotors are never subjected the resonance conditions. Flexible rotors those rotors whose 'operating speed is higher than the first natural frequency'. The difference between rigid rotors and flexible rotors are shown in Figure 1-1.

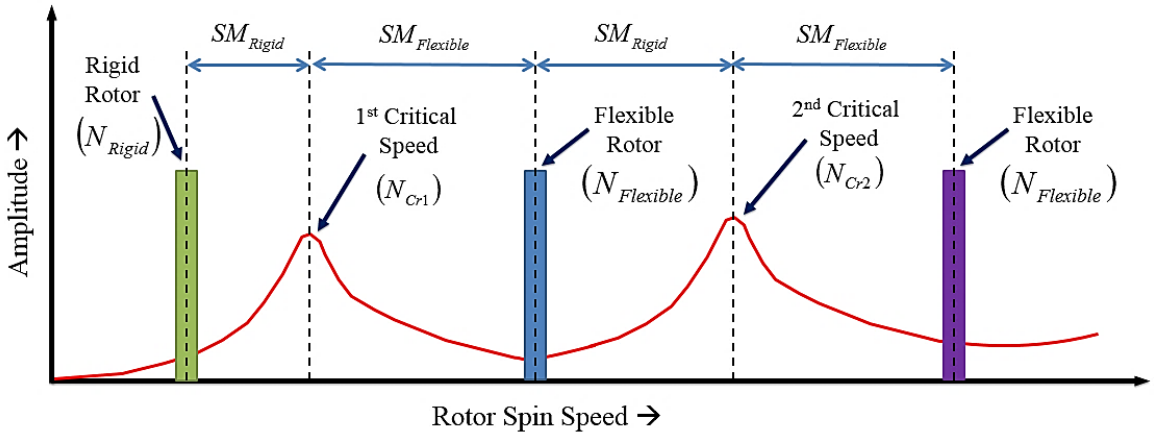

Figure 1-1 Rigid Rotor and Flexible Rotor design

Separation Margin (SM) is a parameter used while designing the rotor of rigid and flexible construction. This parameter is used to understand the gap between critical speed and operating speed of the rotor.

Separation margin is calculated for rigid rotors as below,

$$SM_{Rigid} = \frac{N_{Cr1} - N_{Rigid}}{N_{Cr1}} \tag{1-1}$$

Separation margin is calculated for flexible rotors as below,

$$SM_{Rigid} = \frac{N_{Cr2} - N_{Flexible}}{N_{Cr2}} \quad (1\text{-}2)$$

$$SM_{Flexible} = \frac{N_{Flexible} - N_{Cr1}}{N_{Cr1}} \quad (1\text{-}3)$$

It is very difficult or sometimes impossible to design the rigid rotor for high-speed application. Flexible rotors are the only solution for the high-speed application. The rotors are mathematically modelled as continues system which has an infinite number of critical speeds. These rotors are modelled as discretized finite elements which have a finite number of critical speeds based on the number of degrees of freedom. Rotors are not allowed to operate near critical speeds. While designing the flexible rotor, the designer should take care of critical speeds with the separation margin for the given rotor operating spin speed. The critical speeds prediction is very important for flexible rotors, an error in prediction may results into the resonance within the vicinity of critical speeds.

In rotating machines, the damping is conventionally classified into external damping and internal damping. The traditional definition of damping in rotor dynamics literature is ‘to stabilize the rotor by an irreversible conversion of energy that causes vibration into heat’. The external damping meets the traditional definition. But internal damping plays a role which opposes the effect of external damping and transfers the rotational energy into rotors which create vibration. Dissipation of energy in the material under cyclic bending is referred as internal damping. This is an important parameter in rotating machines and vibrating structures. It is further classified depending upon the material behavior as internal hysteretic damping and internal viscous damping.

In practical rotors, different forms of damping and operating conditions influence the critical speeds. The major factors that influence the whirl speeds are in the form of damping through different sources, viz. internal viscous damping, internal hysteretic damping, external viscous damping, the temperature rise due to hysteric loss and operating temperature based on the application. A clear understanding of the influence of damping and operating temperature on the whirls speeds and critical speeds are essential in the design, operations, and maintenance of the rotors.

1.2 MOTIVATION AND OBJECTIVES

The current research is motivated by the need for prediction of rotor whirl speeds and critical speeds under the influence of different forms of damping like internal viscous damping, internal hysteretic damping, external viscous damping and operating temperature effect either independently or simultaneously acting together. This will enable the designer to model and analyze the real-world rotor. This analysis is useful for the optimum design of rotor and to make accurate diagnoses of rotating machine.

The detailed objective of the present research work is achieved in the following stages.

- The first step to achieve this objective is to model the rotor with finite element method. Formulate the equations of motion in a fixed frame or inertial frame of reference and rotating frame or whirl frame of reference. Model different forms of damping e.g. internal viscous damping, internal hysteretic damping and external viscous damping. It also includes the modelling the effect of operating temperature. Update the equations of motion by incorporating the influence of all forms of damping and operating temperature.
- The second step is to develop the simulation scheme for prediction of whirl speeds. Arrive the optimum number of elements for convergence. Validate the model with the published data. Define the non-dimensional term as 'change in whirl speed ratio' to understand the rotor behavior with different combinations.
- The third step is to carry out the simulation studies to understand the influence of different forms of damping and operating temperature on the whirl speeds and critical speeds. Predict the whirl speed and critical speed with different critical parameters viz. internal viscous damping, internal hysteretic damping, external viscous damping and operating temperature acting either independently or simultaneously for all combinations. Compare and differentiate the rotor behavior with the non-dimensional term 'change in whirl speed ratio', to understand the effect of critical parameters acting either independently or simultaneously on rotor whirl speeds.
- The fourth step is to evolve the systematic methodology to understand the effect of critical parameters on the whirl speeds by using six sigma methodologies. This is a systematic way of understanding the behavior of the critical parameters at high rotor spin speed along with different forms of damping and operating temperature. This enables the designer to understand the importance of critical parameters, its effect on the output parameters like

rotor backward whirl, forward whirl and critical speed. It also gives the information about the response (output) of the analysis with respect to the different input parameters.

Thus, the scope of this research is to:

- Develop the finite element based mathematical model in Mathcad which can consider different forms of damping; internal viscous damping, internal hysteretic damping, external viscous damping and operating temperature.
- Use state space method to solve the equation of motion and predict the forward whirl speed and backward whirl speed. Calculate the critical speed with rotor synchronous whirl excitation from the Campbell Diagram.
- Carry out the simulation with all possible combinations, tabulate and compare the results. Discuss the conclusions and application of each load case.
- Use six sigma methodologies which are the systematic way of understanding the rotor behavior with different input parameters; internal viscous damping, internal hysteretic damping, external viscous damping and operating temperature for different output parameters as forward whirl speed and backward whirl speed.

1.3 ORGANISATION OF THESIS

The thesis is organized as follows.

Chapter 1 - Introduction

It covers the terminologies related to rotor dynamics. It explains the fundamentals about backward whirl speeds and forward whirl speeds along with factors affecting on it. It also covers the motivation behind the research and consideration of different forms of damping viz., internal viscous damping, internal hysteretic damping, external viscous damping and operating temperature on the shaft or rotor whirl speeds. This chapter brings out objective and scope of the present work.

Chapter 2 - Literature Survey

It discusses the fundamental research work done on the rotor dynamics. It also discusses the contribution of different authors, engineers and scientists in advanced rotor

dynamics which include finite element modelling technique. Different researchers studied and documented the change in material properties of steel due to temperature variations through experimentation. Contributions and studies are done in the rotor bearing system with one form of damping either internal viscous damping or internal hysteretic damping at one time only.

Chapter 3 - Modelling of Rotors

It gives a brief review on modelling of the rotor with finite element method. It includes different types of beam theories; Euler – Bernoulli Beam theory and Timoshenko Beam theory. It also gives the information on using these beam theories in formulating the rotor bearing system. The equations of motion are derived from Lagrange's formulation. The equations of motion are represented in a fixed frame or inertial frame of reference and rotating frame or whirl frame of reference.

Chapter 4 – Modelling and Influence of Different forms of Damping and Operating Temperature

It focuses on mathematical modelling of different forms of damping viz., internal viscous damping, internal hysteretic damping and external viscous damping. It explains about the incorporation of the above damping models into the basic equations of motion. This chapter is also focused on modelling of operating temperature. This is due to heat generation in the shaft because of rotation and based on the application temperature. The equations of motion are extended to take care of operating temperature variations in inertial and whirl frame of reference. Arrived the final equations of motion which take care of different forms of damping like internal viscous damping, internal hysteretic damping, external viscous damping and operating temperature.

Chapter 5 – Computational Scheme and Model validation

It includes a computational scheme for solving the equation of motion. State space formulation is explained for calculating the eigenvalues or whirl frequencies. This also includes flow chart about the simulation procedure along with different inputs parameters like geometry data, material data, critical parameters data and shaft spin speed. This chapter also deals with the validation of finite element code for different case studies; undamped, internal viscous damping and internal hysteretic damping with published data to get more

confidence. It also deals with finite element model convergence to arrive the optimum number of elements required for the prediction of whirl speeds of a rotor-bearing system. Whirl speeds are compared regarding the number of elements for a given numerical example in the case study.

Chapter 6 – Study on Individual Influence of Parameters on Whirling Speed of Rotors

It also explains about the non-dimensional parameter "change in whirl speed ratio". This parameter is useful in deciding the effect of different forms of damping in the whirl speeds. It also deals with the prediction of whirl speeds and critical speeds of the rotor-bearing system with individual parameters; undamped, internal viscous damping, internal hysteretic damping, external viscous damping and operating temperature and their conclusions.

Chapter 7 – Study on Combined Influence of Parameters on Whirling Speed of Rotors

It explains about the different critical parameters and their combinations. All the critical four parameters with 'consider' and 'not consider' options, there are sixteen possible combinations are listed for the simulation. It deals with the prediction of whirl speeds and critical speeds of the rotor-bearing system with combined parameters and their conclusions. This includes the different combinations of internal viscous damping, internal hysteretic damping, external viscous damping and operating temperature.

Chapter 8 – Sensitivity Analysis

It deals with the design of experiments based on six sigma methodology. Different types of plots are used to understand the behavior of all the critical parameters and their effect. The effect of each critical parameter, their interactions, response surface and response contour plots are explained. Pareto charts are used to find out the most important parameter for the whirling speed.

Chapter 9 – Summary and Conclusions

It summarizes the research work done on the behavior of the rotor-bearing system. It concludes the effect of the different form of damping and operating temperature with independent and combined on rotor whirl speeds and critical speeds. It also talks about the practical application or situation for all the combinations of different forms of damping and

operating temperature. The prediction of whirl speed and critical speed with combinations of different forms of damping and operating temperature fills the gap which was identified in the literature review. It also highlights about the scope for an extension of a future work.

CHAPTER 2

LITERATURE SURVEY

Rotating machinery such as compressors, turbines, pumps, jet engines, turbochargers, etc. are subject to vibrations and in these machines, the rotor is the principal elements. The research on rotor dynamics spans at least fourteen decades of history.

Accurate prediction of whirl speeds and critical speeds are very important in the design stage of the rotors. This helps to optimize the rotor and make a safe design. Hence the improvement in accurate prediction of whirls speeds and critical speeds for complex rotors has been attracting researchers for the past several years. There are different methods and techniques of predicting the whirl speeds and critical speeds. Few of them are, classical methods based on the formulae, transfer matrix method, finite element method etc. The most accurate method of modelling the rotor is using finite elements. In this method, the shaft or rotor is discretized into finite elements, the blades; fans and lamination stacks are modelled as point masses with equivalent stiffness or equivalent disks. Different forms of damping like internal damping and external damping can be added at different locations based on the rotor geometry or construction. The change in material properties due to a different application with surrounding temperature is also critical parameters in the rotor design. Research and development happened in the field of rotor dynamics over the period are summarized in Figure 2-1.

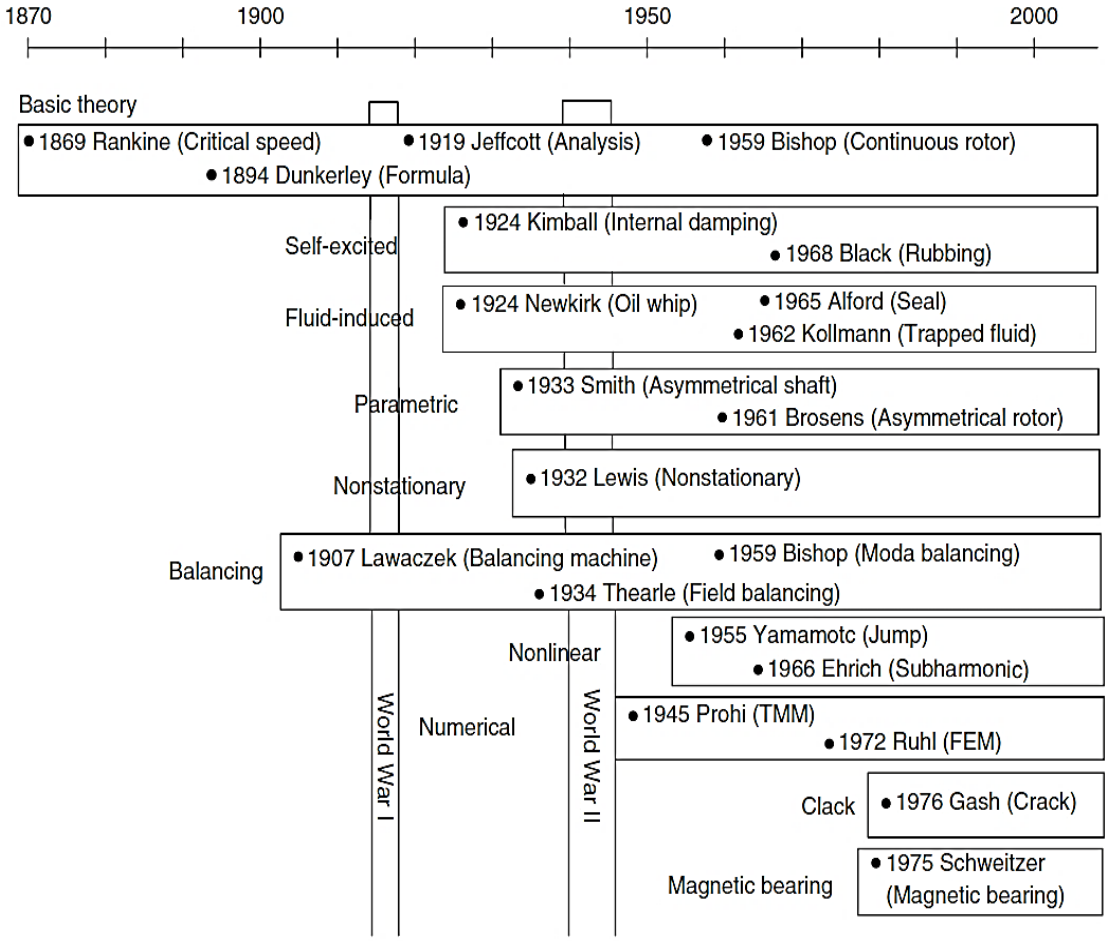

Figure 2-1 Brief history of Rotor Dynamics [1]

In this chapter, the published literature in rotor dynamics along with a different form of damping viz. internal damping and external damping and the research work carried out by various investigators on material properties of steel is presented.

2.1 HISTORICAL REVIEW ON ROTOR DYNAMICS

The design of rotor applied to rotating machinery initially started with the construction of stiff rotors or rigid rotors. Rankine published an article on April 9th, 1869, 'On the Centrifugal Force of Rotating shafts'. He performed the first analysis of a spinning shaft. Rankine chose two degrees of freedom model consisting of a rigid mass whirling in an orbit with elastic spring acting in the radial direction as shown in Figure 2-2.

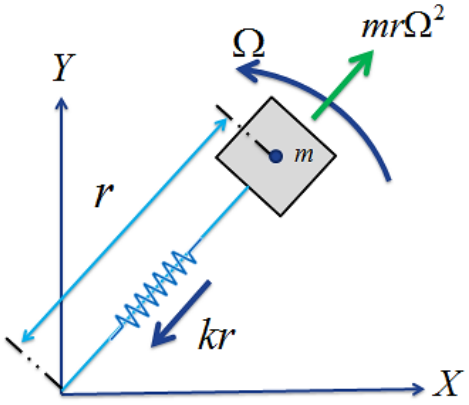

Figure 2-2 Rankine's Rotor Model

Rankine defined first time the word as 'whirling speed of rotor'. This is the speed at which the radial deflection of the shaft increases drastically. Whirling refers to the orbital motion of the rotor. These rotors operate below its first critical speed. The attempts have been made to establish accurate methods for the estimation of critical whirling speeds of complex systems. Fundamental research work on the theory of shaft whirling is studied and published by Downham [2].

In 1883, Swedish engineer de Laval developed high-speed impulse steam turbine. He successfully operated the turbine at 42000 rpm without any failures. First time, he observed the self-centering phenomenon of the flexible rotor after critical speeds. He proved that the flexible rotors can operate safely above their critical speeds with proper balancing techniques. The turbine built by Parsons in 1884 also operated at 18000 rpm safely without any failures. Dunkerley created the calculation methodology for the prediction of the fundamental critical speed of complicated structures in 1895. In 1916, Kerr published a paper on his experimental results of second critical speed. In fact, this result itself showed that the rotor had crossed the first critical speed without any issue. The first rotor model was proposed and analyzed by August Föppl in 1895. It consists of a single disk centrally located on a circular shaft, without an external damping.

Jeffcott proposed the rotor model with an external damping as an extension of Föppl' s contribution. He published his paper in 1919 where he clearly mentioned about the fundamental theory of rotordynamics. Thus, a single disk rotor with an external damping is called Jeffcott rotor. Over the period, the different variations in the Jeffcott rotor have been

studied. The different variations may be internal damping in the shaft, cross coupling terms in the sleeve bearings as external stiffness and damping, multidisc rotors with complicated structures, damping consideration in the shrink fits, couplings and joints etc. Jeffcott rotor model is oversimplified in comparison to the real-world rotors. It is easy to understand the dynamic behavior like whirl speeds, critical speeds, gyroscopic effect, effect of different forms of damping like internal damping and external damping of Jeffcott rotor. Later the study can be extended to the real-world rotors. The rotors could be operated safely beyond their first critical speeds with proper rotor balancing techniques. This trend in rotordynamics is changed only after Jeffcott's analysis. It was determined that rotors can work correctly even above the first critical speed with proper balancing.

In 1924, Stodola developed and presented the graphical procedure to calculate the critical speeds. This was the beginning of supercritical turbomachinery.

2.2 LITERATURE REVIEW ON ROTOR DYNAMICS

The rigid rotor models were replaced by more flexible rotor models, however; several failures were encountered at the supercritical speed. These failures were first observed in 1924 by Dr. A. L. Kimball and Dr. B. L. Newkirk. They were the first researchers to identify internal hysteretic damping in rotating machines. The studies were carried out on different rotor dynamic tests with different materials. It is observed that as the shaft was rotated, a small deflection of the weight to one side occurred in no matter whatever rotation speed was used. They revealed that internal friction was a major cause of rotor dynamic instability. Kimball described the experimental measurements of internal friction in different rotor material. He explained that internal hysteresis in a material during spin will cause the shaft to deflect sideways in the direction of the forward whirl. Based on his experiments, he concluded that shrink fits rather than the material internal hysteresis are a much more important mechanism of the forward whirl instability. Oil whirl and oil whip phenomenon is observed with the rotor having sleeve bearings. The internal friction is also one of the main causes of oil whipping were concluded by Newkirk and Taylor [3, 4].

In 1933, Smith contributed in the form of simple formulae that predicted the threshold spin speed for supercritical rotors. He evaluated the effects of internal viscous damping on a rotating system. He proved that the addition of internal viscous damping in a rotating system without external damping, the system would become unstable at the first critical speed. This

speed was called the instability threshold. He also showed that the internal viscous damping has the stabilizing effects if the rotor is at sub-critical speed and destabilizing effects above the critical speed.

In 1976, H. Black came up with different types of internal friction models to understand and analyze the stability of rotors. His studies were limited to flexible rotors. He proposed different internal friction models like viscous, coulomb and hysteretic friction models.

Ehrich [5] proposed the mathematical model of internal friction which states that the internal friction stresses act in a direction perpendicular to the shaft deflection plane and their magnitude is proportional to the rate of change of strain of the shaft fibers. He concluded that the ratio of the threshold speed of instability to the first critical speed depends upon the amount of internal damping and external damping of the rotor. He analyzed and verified the Smith's claim and showed that the introduction of internal viscous damping causes the rotor unstable. He also showed that with the addition of external damping, the stability can be improved. He introduced a direct and simple method by beginning with the constitutive relation of the stress and strain with linearized beam theory.

Gunter [6, 7] explained some of the experimental results of Newkirk. He developed and proposed a model with an internal damping of the rotor. He studied the effect of bearing stiffness and damping and foundation support flexibility. He showed that external damping stabilizes the rotor by increasing its threshold speed of instability. He also showed that the unstable rotors can be stabilized with the addition of external damping. External damping can be provided in the rotor bearing system by bearings. His research was also on the fluid film or sleeve journal bearings. The destabilization in the fluid film bearings are due to the cross-coupling stiffness and damping because of which oil whirl or oil whip can occur.

Lund [8] analyzed various models of internal friction due to axial splines and shrink fit joints in a rotor. He conducted different experiments on theoretical research on internal friction. He considered the work done by Kimball and incorporated internal hysteretic damping into the rotor dynamic equations of motion. He formulated the equation for constitutive relationship between the bending strain and bending stress for the rotor model. He proposed the internal friction as a system of internal moments rather than forces. He modified the conventional finite element model beam equations and converted them into a form suitable for the Myklestad - Prohl numerical method. This method involved representing the rotor by a series of lumped masses located at stations connected by uniform shaft sections. In

a separate study mentioned by Lund, he added external damping through the bearings to the rotating system and found that the forward mode stability could be achieved for all speeds.

Ishida and Yamamoto [1] studied the effect of internal friction in the rotor. They modelled the internal friction as a system of internal moments. These internal moments do not produce any instability below the first critical speeds. Their formulations are almost same as Lund's formulations.

Nelson and McVaugh [9] used the finite element technique to model the rotor bearing system. They considered the four degrees of freedom model i.e. two translational and two rotational degrees of freedom at each node. They used third order shape functions to describe the bending of the elements. Inertia is assumed to be rigid discs with lumped mass properties and the bearings are assumed to be linear and discrete. Their model includes rotary inertia, gyroscopic moments and shear deformation. They demonstrated the finite element methodology with a numerical example of rotor.

Nelson [10] formulated the rotor finite element model with Timoshenko beam theory. He established the shape functions and included transverse shear effects in his finite element model. The comparison is made of the finite element analysis with classical closed form Timoshenko beam theory analysis for nonrotating and rotating shafts.

Zorzi and Nelson [11, 12] also used the finite element method to simulate the rotor dynamic analysis. They included internal hysteretic damping model and external viscous damping model in the finite element model. The equations of motion are formulated using the variational approach. They concluded that, by the inclusion of axial torque gives rise to incremental torsional stiffness.

Walton, Artilles, Lund and Zorzi [14] developed different analytical methods of rotor bearing system. They investigated through the experimentation in assessing the effect of internal friction on rotor systems dynamic performance. The effect of speed, bearing stiffness, joint stiffness, external damping, torque and coefficient of friction was evaluated.

Artilles [15] studied and analyzed the effects of internal friction on rotor stability. His study was specific to axial spline couplings. He modeled internal friction as a system of cross-coupled moments which are developed at the spline interface due to relative sliding between the spline teeth. He simulated the rotor with cross coupling terms, rotor unbalance and initial conditions on the stability of the rotor.

Greenhill and Cornejo [16] analyzed the Jeffcott rotor – bearing model with stiffness asymmetry in the coefficients at the support. A critical speed was observed by the unbalance

excitation of a backward precessional mode. Based on the findings, it can be recommended that to avoid exciting backward modes, asymmetry in the direct stiffness terms should be avoided.

Singh and Gupta [17] presented the formulation based on a layer wise beam theory for unbalance response and stability analysis of multi mass, multi bearing composite rotor mounted on fluid film bearings. The layer wise theory is compared with conventionally used equivalent modulus beam theory.

Zabala [18] presented the state space formulation for the analysis of structural dynamics. This formulation was more general and does not present any restrictions on the characteristics of the damping. The eigen problem solution for non-symmetric matrix is studied. This method is implemented in the analysis of active structural control.

Wang [19] investigated the dynamic effect of skewed disk on the flexible shaft. He compared the experimental test results and computer simulation to verify the theory of skewed disk forced response predictions. The agreement between experiment and simulation was very good for most skewed disk response characteristics.

Forrai [20, 21] studied the stability analysis of self-excited bending vibrations of the rotor bearing system. This system was modelled with internal damping using the finite element method. The effect of rotatory inertia and gyroscopic moment are also included in the mathematical model. Based on his study, he concluded that the rotor stability is improved by increasing the damping provided by the bearings.

Patil [22] presented the modal analysis for a general non-conservative system. He presented the state space method to decouple the higher order differential equations into lower order differential equation.

Adhikari [23] performed systematic study on analysis and identification of multiple parameter damped mechanical systems. The attention was focused on viscously and non-viscously damped multiple degree of freedom linear vibrating systems. The concept of proportional damping is critically examined and a generalized form of proportional damping is proposed. It is shown that the proportional damping can exist even when the damping mechanism is non-viscous.

Srinivasan [24] conducted a series of experiments on single disk rotor. He studied the rotor vibrations with different interference fits. He predicted threshold speed of instability for the single disk rotor. These threshold speed of instability were not always repeatable.

Chauvin [25] investigated the effect of lubricant temperature on the presence of whirl instability in journal bearings. The first set of conditions that are studied is an extremely low eccentricity rotor and the occurrence of oil whirl at the start-up of the experiment. Lubricant temperature, bearing temperature, frequency and amplitude of vibration, and rotational speed are monitored and analyzed in relation to presence of whirl instability.

Sinou and Thouverez [26] presented an experimental study of the effects of the bearing temperature on rotor unbalance responses and on the first forward and backward critical speeds. They were demonstrated that rolling-element bearing temperature has no-negligible effects of the amplitude and values of the forward and backward first critical speeds of the flexible rotor. In addition to the investigation of the influences of the bearing temperature on the dynamics of the flexible rotor at the first critical speeds, a brief investigation into the complete dynamic within the speed range of interest was also conducted.

The effects of internal damping and Coulomb friction are investigated via time integration of a run-up. Furthermore, the active modification of mechanical properties to alter the natural frequencies during run-ups were computed with code developed by Fischer and Strackelijan [27].

Jafri [29] presented the experimental and theoretical study of instability in the rotor. This instability was caused by interference and shrink fit. The unstable vibrations occur at the first natural frequency of the rotor bearing system. The instability resulted into complete wreckage of the test rig in one of the setups. Based on the experimental results, he concluded that these vibrations are potentially dangerous to the safe operation of rotating machines. He also mentioned the simulations of various rotor configurations with shrink fit interfaces.

Simon [30] studied the lightweight rotor supported with magnetic bearings. His work addresses the application of adaptive disturbance rejection control method to deal with the rotor dynamic instability caused by internal damping and synchronous vibrations caused by mass imbalance in rotor systems operating at supercritical speeds.

Malta [31] presented the work related to anisotropic rotor supported by rigid bearings and anisotropic flexible bearings. The rotor is modelled by discrete element because of different orientations of the cross section along the shaft. A stability investigation is conducted of an anisotropic rotor through analysis of eigenvalues for a speed dependent rotor system. Experimental investigation of an anisotropic rotor with two disks and different shaft orientations is conducted at constant angular speed and constant angular acceleration. These

experimental results are benchmarked with the numerical simulations of the developed discretized model.

Chattoraj, Sengupta and Majumder [32] have considered an overhanging high inertia horizontal rotor on a flexible isotropic shaft with asymmetric end bearings. They studied the rotor behavior under asymmetric bearings. The effect of the bearing asymmetry is not found to be great, excepting a marginal change in the shape of the stability chart.

Boru [33] presented the unstable behavior of the rotors with non-circular shafts. Few practical examples of the non-circular cross section shafts are 2 pole generators where grooves are provided for the rotor coils. The shaft is asymmetry and there is always a certain risk of a presence of an unstable operation speed range.

Roy and Dutt [34] studied the dynamics of viscoelastic rotor – shaft system where the internal material damping in the rotor shaft introduces a rotary force well known to cause instability. The material constitutive relationship is used to represent he viscoelastic rotor.

Rastogi, Mukherjee and Dasgupta [35] presented the dynamic behavior of the hollow rotor shaft with internal damping driven by a dissipative coupling. The coupling considered in their study is absolutely flexible in transverse and bending and rigid in torsional.

Vervisch, Stockman and Loccufier [36] demonstrated numerically the rotor instability at a certain speed due to rotor internal damping. This stability threshold speed is unique and it is impossible to rotate the rotor above the threshold.

Wagner and Helfrich [37] studied the joint structures like couplings of rotating and non-rotating parts of rotor bearing system. The effect of rotor unbalance on the joint structures are well studied.

Miranda and Faria [39] developed finite element developed to perform the eigenvalue analysis of damped gyroscopic systems, represented by flexible rotors supported on fluid film journal bearings. The influence of the effective damping on the eigenvalue real part sign is analyzed for some examples of rotor-bearing systems, showing how the stability conditions can be predicted by the eigenvalue analysis. This information can provide useful guidelines and technical data about the selection of the more appropriate set of bearing parameters for rotating machines operating at stringent conditions.

Alabart [40] studied the rotor dynamic instability when rotor operates in a supercritical regime. He considered the Jeffcott rotor model with linear viscous internal damping. He analyzed independently the friction mechanism in the interference fit and then transformed into as equivalent viscous damping coefficient. He proposed two models for the interference

fit, for macro- and micro-slip friction. Both are appropriate descriptions and can be converted into an equivalent viscous coefficient.

Tyagi and Chouskey [43] studied the behavior of the asymmetric rotor. They carried out the analysis in the rotating co-ordinate system so that the equations of motion do not include time dependent terms. The asymmetric nature of the rotor gets unstable between some speed ranges.

The most extensive portion of the literature on rotor dynamics is concerned with determining critical speeds, whirl speeds, instability thresholds and unbalance response. Different forms of damping in the rotor viz., internal viscous damping, internal hysteretic damping and external damping was considered independently. There is gap in the literature about considering the different forms of damping acting in combined form.

2.3 HISTORICAL REVIEW ON OPERATING TEMPERATURE

The effect of temperature on the mechanical properties of different materials is well experimented and studied in the literature. The temperature is a crucial parameter in the rotor dynamics behavior. The temperature rise in the rotor is due to continuous bending of the rotor and surrounding temperature based on the application demand.

Ancas and Gorbanescu [28] studied and created the theoretical models for the effect of temperature on the steel properties. When the steel elements and structures are subjected to high temperatures, they progressively lose their stiffness and load carrying capacity because of Young's Modulus and the Poisson's ratio changes.

Gu and Chu [41] presented an analytical analysis of a continuous rotor shaft subjected to universal temperature gradients. The analytical model is derived to investigate the generic thermal vibrations of rotor structures. The analytical solutions are obtained in a rotating frame and include parameters related with both the thermal environment and the rotor dynamic structures. This provides an insight into the mechanisms for the rotor thermal vibration.

Zhuo, Yang and Yu [42] studied the rod fasteners of rotor bearing system at high steady state temperature. For all steady-state thermal related analysis, two kinds of elastic modulus were calculated, i.e., constant and temperature dependent elastic modulus, corresponding to the effect of thermal stress and material degradation, respectively. Both two

steady-state cases were compared with the room temperature results to evaluate the role of these two thermal factors.

Jia and Wang [44] studied the effect of temperature on the influence of mechanical properties of the rotor. They concluded that as the temperature increases, the maximum equivalent stress and equivalent strain of the rotor are increases linearly.

Summary of research carried on rotor dynamics for last fourteen decades is summarized and shown in Figure 2-3.

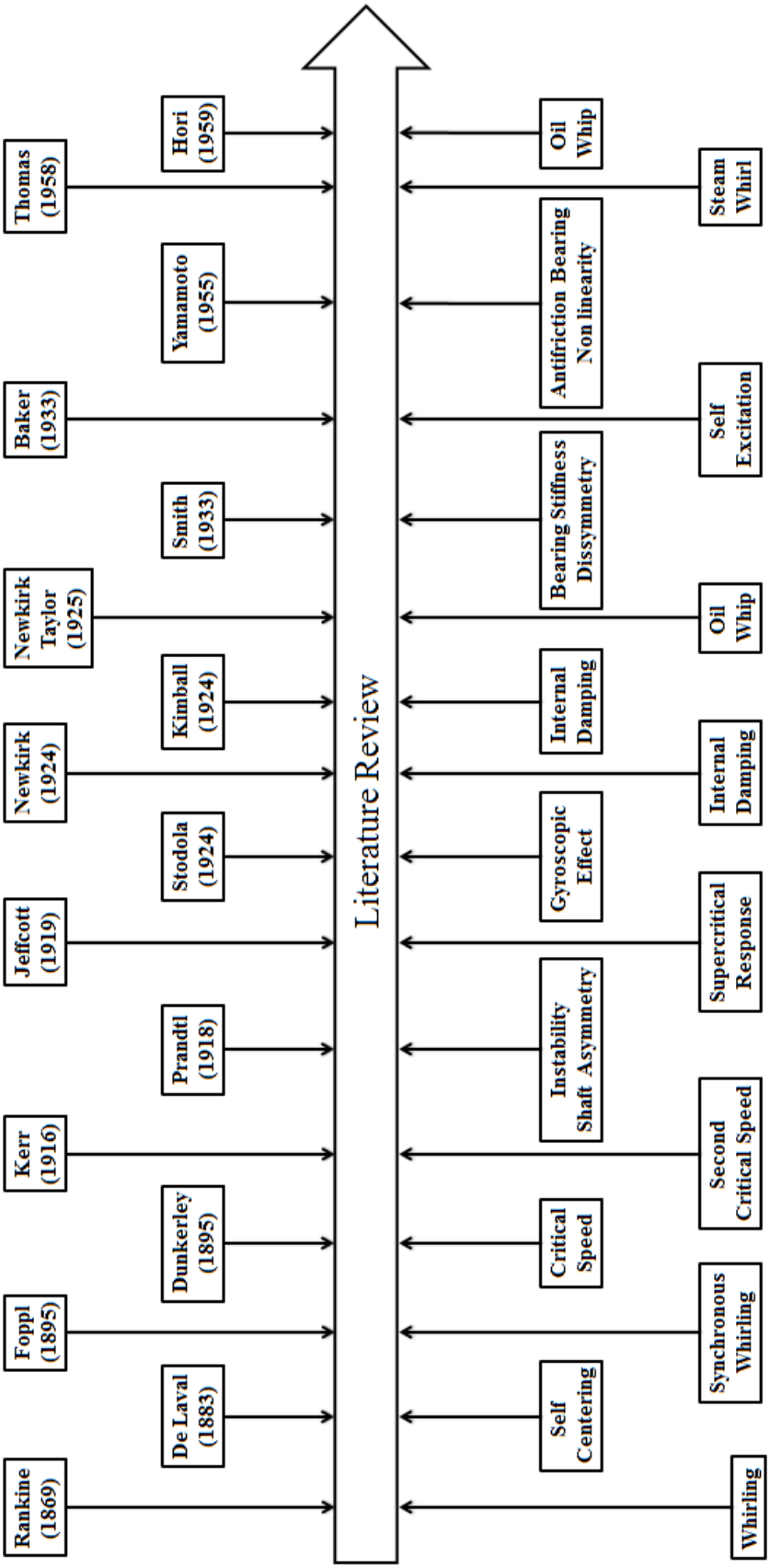

Figure 2-3 Study and Development in Rotor Dynamics

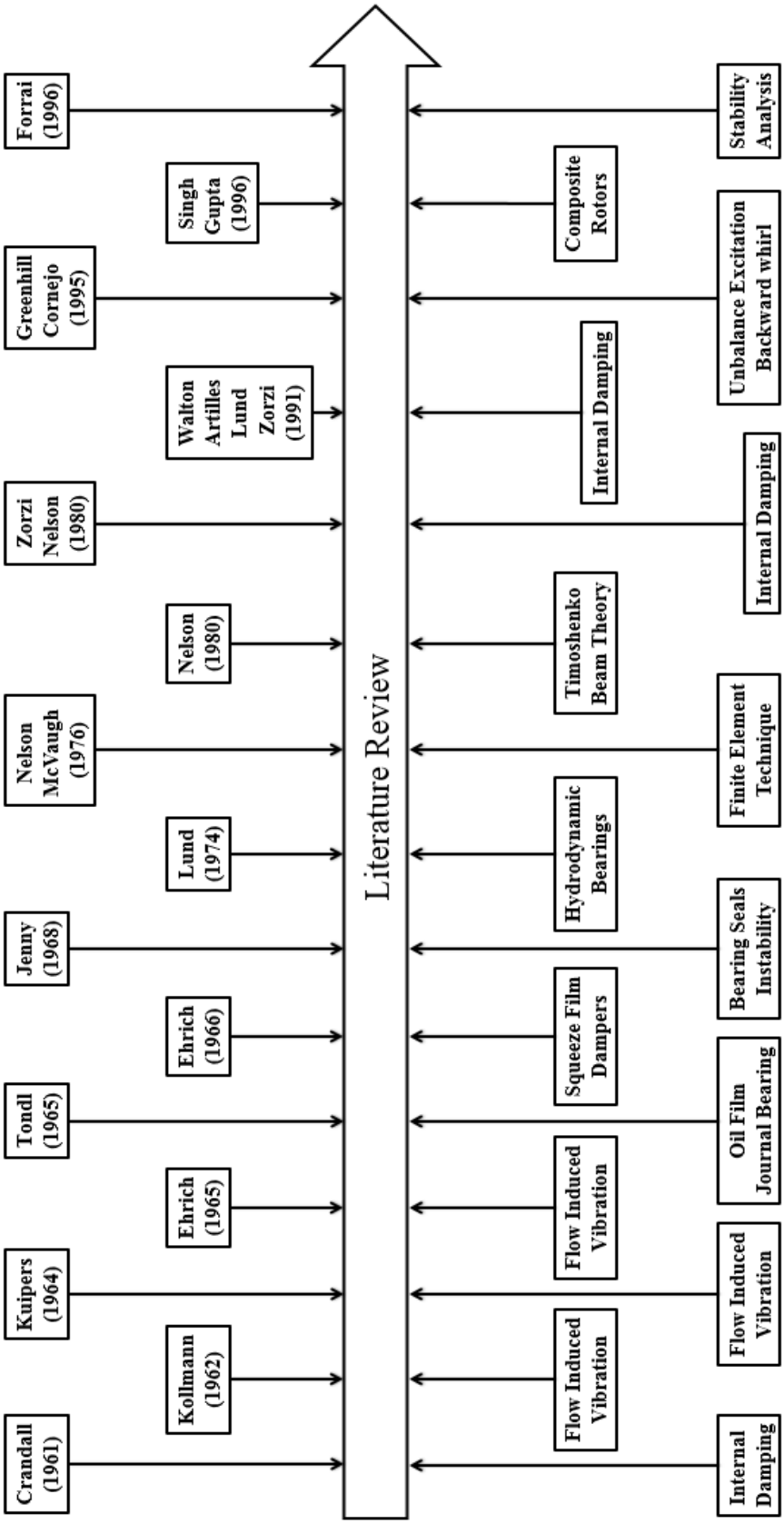

Figure 2-3 Study and Development in Rotor Dynamics contd.

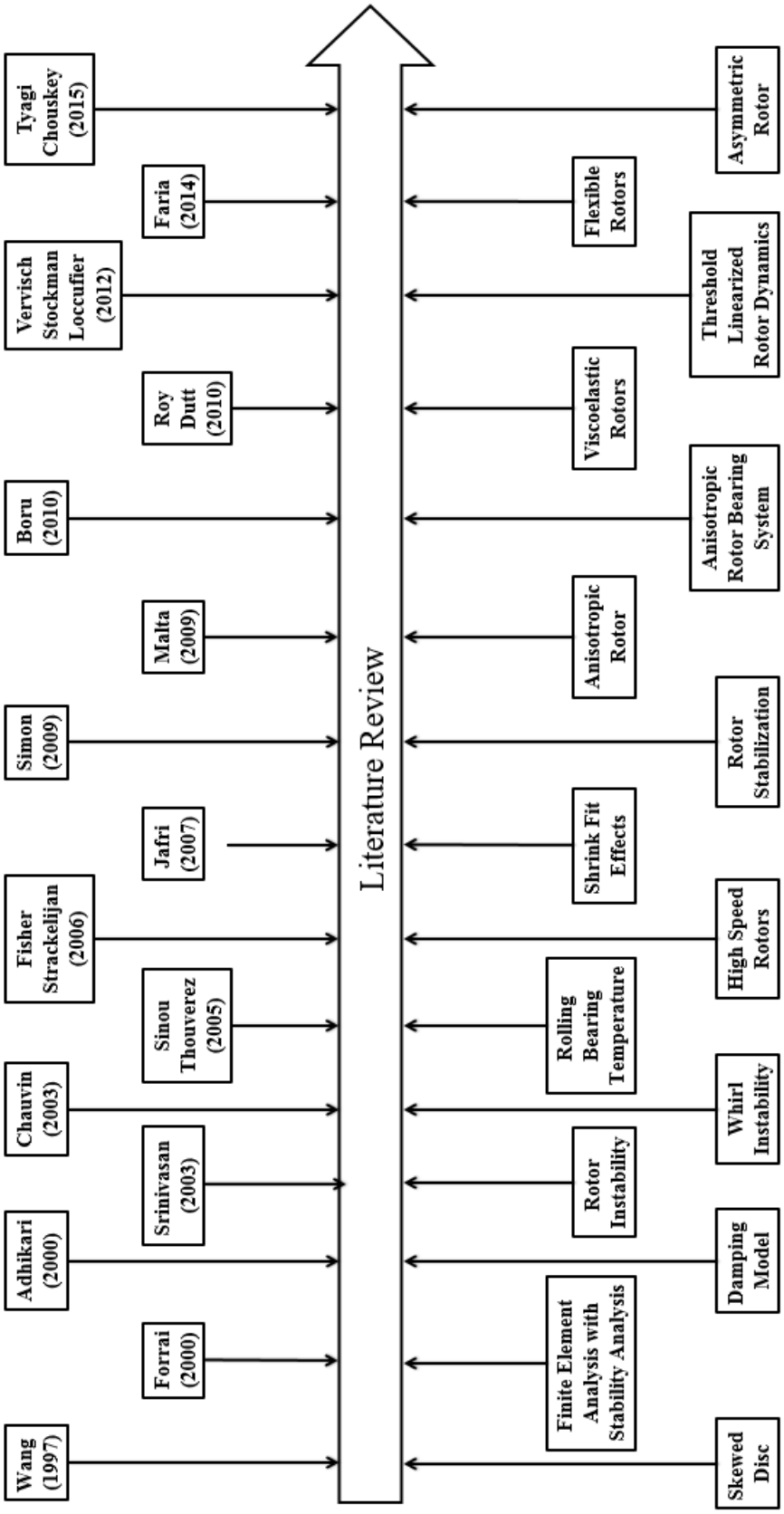

Figure 2-3 Study and Development in Rotor Dynamics contd.

2.4 SUMMARY

Last more than fourteen decades, different scientist and engineers are contributed in the field of rotor dynamics. Different methods or techniques are developed for the prediction of whirl speeds and critical speeds. e.g. classical method based on the formulae, transfer matrix method and finite element method.

Literature study shows that the influence of different forms of damping e.g. internal viscous damping, internal hysteretic damping and external viscous damping studied independently and predicted the rotor whirl speed.

Literature shows that the change in the material properties with respect to temperature is studied extensively for different materials. The critical material properties are Young's modulus and Poisson's ratio which decides the whirl speeds and critical speeds. The effect of operating temperature on rotor whirl speeds is not studied in literature.

In practical rotors, different forms of damping and operating temperature acting either independently or simultaneously with different combinations. There is a gap in the literature about consideration of different forms of damping acting together along with operating temperature. The present research aimed to fill this literature gap and predict the whirl speeds and critical speeds considering different forms of damping and operating temperature acting together along with different applications.

CHAPTER 3

MODELLING OF ROTORS

The dynamic characteristics of rotor system are studied and analyzed by using finite element method. This is the most accurate method of modelling the rotor. In this method, the shaft is discretized into finite elements. For modelling of the rotor, three different beam theories are used; viz. Euler-Bernoulli beam, Rayleigh beam and Timoshenko beam theory.

- In Euler-Bernoulli beam theory, rotation of cross section of the beam is neglected compared to the translation. In addition, the angular distortion due to shear is considered as negligible compared to the bending deformation.
- In Rayleigh beam, the inertia due to the axial displacement of the beam is included. This effect is called rotary inertia.
- In Timoshenko beam theory, the effect of shear deformation, in addition to the effect of rotary inertia is considered.

Experience show that the natural frequencies of a free vibrating beam determined by the Euler-Bernoulli beam theory are higher than the values determined from experiments. The Rayleigh beam theory therefore tries to reduce the discrepancy by considering the rotational inertia besides the translational inertia. Considering the rotary inertia along with shear deformation i.e. increasing the flexibility of the beam element was taken into account in Timoshenko beam theory which is an extension of Euler-Bernoulli beam and Rayleigh beam for more accuracy.

In Euler – Bernoulli beam theory, shear deformations are neglected, and plane sections remain plane and normal to the longitudinal axis. In the Timoshenko beam theory, plane sections remain plane but are no longer normal to the longitudinal axis. The difference between the normal to the longitudinal axis and the plane section rotation is the shear deformation. The difference between these two beams is shown in Figure 3-1.

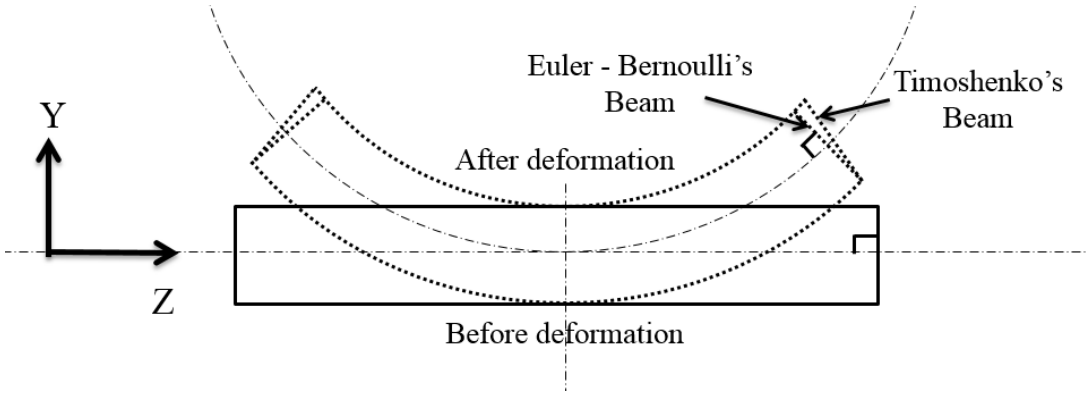

Figure 3-1 Different types of Beams

The Timoshenko beam theory is higher order than the Euler-Bernoulli theory, it is known to be superior in predicting the lateral vibration response of the beam.

3.1 EULER - BERNOULLI BEAM MODEL

This theory is sometimes called the classical theory and this was formulated in the 18th century. It assumes that the major effects of bending in beams are due to pure bending. Cross section of the beam before and after bending remains in the plane and the plane remains normal to the bending axis or neutral axis as shown in Figure 3-2.

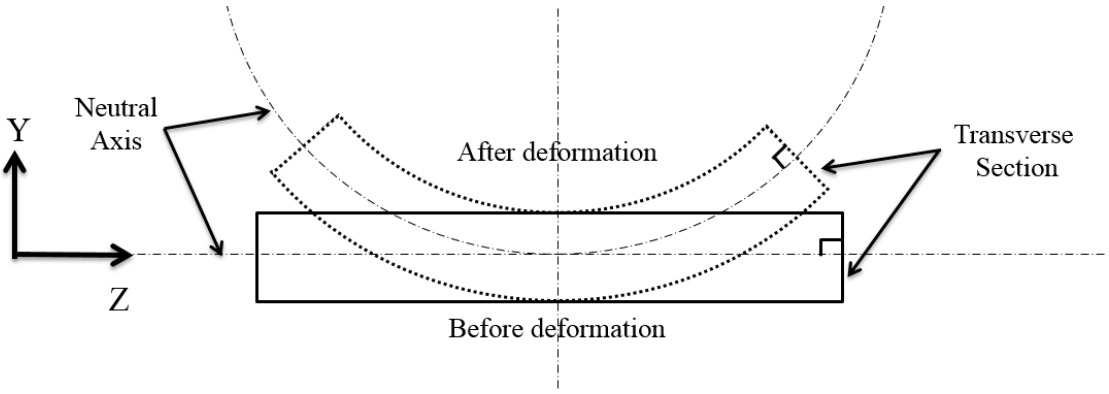

Figure 3-2 Euler - Bernoulli Beam

To determine the shape functions of this beam theory, consider the element in Figure 3-3. The beam without shear deformation, the relation between translation and rotations are in X-Z plane [45] as,

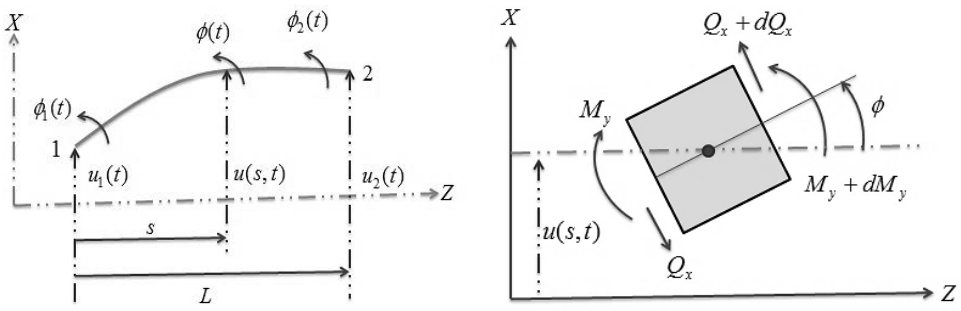

Figure 3-3 Displacement and slope relationship in X-Z plane

The total angular rotation ϕ is equal to the slope $\frac{\partial u}{\partial s}$ of the elastic axis.

$$\phi = \frac{\partial u}{\partial s} \tag{3-1}$$

Bending Moment M_y in X-Z plane is calculated as,

$$M_y = EI\frac{\partial^2 u}{\partial s^2} = EI\frac{\partial \phi}{\partial s} \tag{3-2}$$

Shear Force Q_x in X-Z plane is calculated as,

$$Q_x = \frac{\partial M_y}{\partial s} \tag{3-3}$$

The field variable within the elements in terms of discrete variables and shape functions is expressed as,

$$u(s,t) = N_1(s)u_1(t) + N_2(s)\theta_1(t) + N_3(s)u_2(t) + N_4(s)\theta_2(t) \tag{3-4}$$

The discrete variables are,

$$u(0,t) = u_1(t) \qquad \phi(0,t) = \phi_1(t) = \frac{\partial u}{\partial s}$$

$$u(L,t) = u_2(t) \qquad \phi(L,t) = \phi_2(t) = \frac{\partial u}{\partial s}$$

Since there are total four discrete variables, a cubic polynomial function with four parameters are used to describe the displacements,

$$u(s,t) = c_1 s^3 + c_2 s^2 + c_3 s + c_4 \tag{3-5}$$

To determine the shape functions, consider the element in Figure 3-4. The beam without shear deformation, the relation between translation and rotations are in Y-Z plane [45] as,

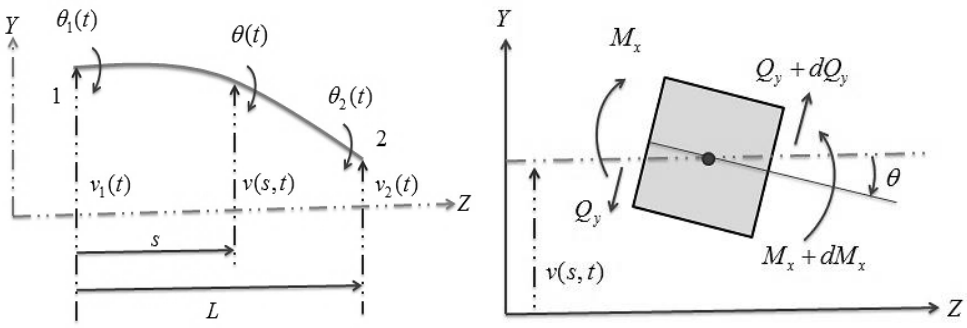

Figure 3-4 Displacement and slope relationship in Y-Z plane

The total angular rotation θ is equal to the slope $\frac{\partial v}{\partial s}$ of the elastic axis.

$$\theta = -\frac{\partial v}{\partial s} \tag{3-6}$$

The negative sign is added in the slope of v deformation for proper ϕ direction as shown in Figure 3-4.

Bending Moment M_x in Y-Z plane is calculated as,

$$M_x = EI\frac{\partial^2 v}{\partial s^2} = EI\frac{\partial \theta}{\partial s} \tag{3-7}$$

Shear Force Q_y in Y-Z plane is calculated as,

$$Q_y = \frac{\partial M_x}{\partial s} \tag{3-8}$$

The field variable within elements in terms of discrete variables and shape functions is expressed as,

$$v(s,t) = N_1(s)v_1(t) + N_2(s)\theta_1(t) + N_3(s)v_2(t) + N_4(s)\theta_2(t) \tag{3-9}$$

The discrete variables are,

$$v(0,t)=v_1(t) \qquad \theta(0,t)=\theta_1(t)=\frac{\partial v}{\partial s}$$

$$v(L,t)=v_2(t) \qquad \theta(L,t)=\theta_2(t)=\frac{\partial v}{\partial s}$$

There are total four discrete variables, a cubic polynomial function with four parameters are used to describe the displacements,

$$v(s,t)=c_1s^3+c_2s^2+c_3s+c_4 \tag{3-10}$$

The cubic displacement shape function satisfies the continuity condition of both the linear and angular displacement at the nodes. The shape function matrix will be,

$$N=\begin{bmatrix} N_T(s) \\ N_R(s) \end{bmatrix}=\begin{bmatrix} N_1 & 0 & 0 & N_2 & N_3 & 0 & 0 & N_4 \\ 0 & N_1 & -N_2 & 0 & 0 & N_3 & -N_4 & 0 \\ 0 & -N_1' & N_2' & 0 & 0 & -N_3' & N_4' & 0 \\ N_1' & 0 & 0 & N_2' & N_3' & 0 & 0 & N_4' \end{bmatrix} \tag{3-11}$$

Shape functions are expressed as below,

$$N_1=1-3\xi^2+2\xi^3, \qquad N_2=L(\xi-2\xi^2+\xi^3),$$

$$N_3=3\xi^2-2\xi^3, \qquad N_4=L(-\xi^2+\xi^3)$$

$$N_1'=\frac{1}{L}(-6\xi+6\xi^2), \qquad N_2'=1-4\xi+3\xi^2,$$

$$N_3'=\frac{1}{L}(6\xi-6\xi^2), \qquad N_4'=-2\xi+3\xi^2$$

where, $\xi=\frac{s}{L}$; Non-dimensional parameter

3.2 TIMOSHENKO BEAM MODEL

This theory accounts for the shear strain energy in the beam bending due to shear force. It considers rotary inertia and shear deformation. These are predominant in the transverse vibration of the beams.

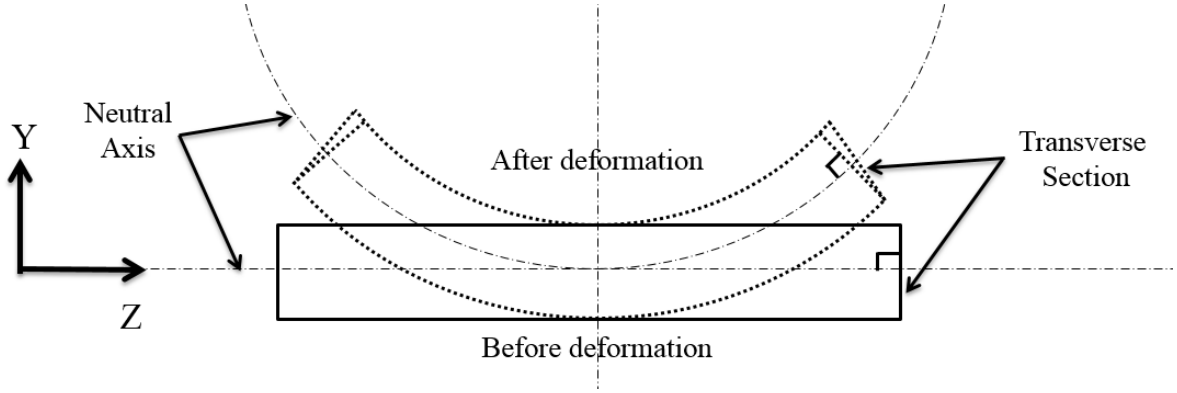

Figure 3-5 Timoshenko Beam

To determine the shape functions of this beam theory, consider the element in Figure 3-6. The beam with shear deformation, the relation between translation and rotations are in X-Z plane [45] as,

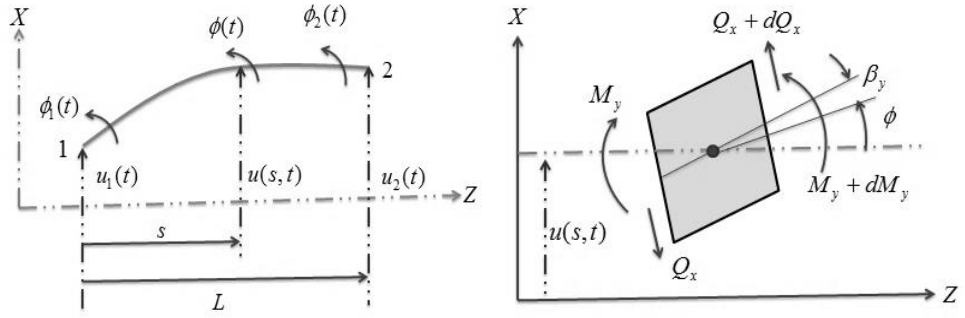

Figure 3-6 Shear deformation in X-Z plane

The rotation of the element is described by rotation angles. The slope of the total deflection curve is the sum of the angular rotation ϕ of the elastic beam and shear deformation β_y .

$$\frac{\partial u(s,t)}{\partial s} = \frac{\partial u_b}{\partial s} + \frac{\partial u_s}{\partial s} = \phi + \beta_y \tag{3-12}$$

The relation of Bending Moment M_y in X-Z plane is expressed as,

$$M_y = EI\frac{\partial^2 u_b}{\partial s^2} = EI\frac{\partial \phi}{\partial s} \tag{3-13}$$

The relation between shearing force and shear deformation in X-Z plane is given as,

$$Q_x = kAG\frac{\partial u_s}{\partial s} = kAG\left[\frac{\partial u}{\partial s} - \phi\right] \tag{3-14}$$

To determine the shape functions, consider the element in Figure 3-7. The beam with shear deformation, the relation between translation and rotations are in Y-Z plane [45] as,

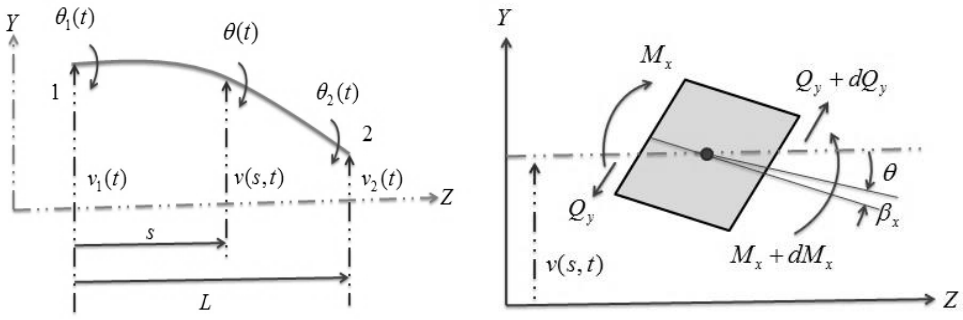

Figure 3-7 Shear deformation in Y-Z plane

The rotation of the element is described by rotation angles. The slope of the total deflection curve is the sum of the angular rotation θ of the elastic beam and shear deformation β_x.

$$\frac{\partial v(s,t)}{\partial s} = \frac{\partial v_b}{\partial s} + \frac{\partial v_s}{\partial s} = -\theta - \beta_x \tag{3-15}$$

The relation of Bending Moment M_x in Y-Z plane given as,

$$M_x = -EI\frac{\partial^2 v_b}{\partial s^2} = EI\frac{\partial \theta}{\partial s} \tag{3-16}$$

The relation between shearing force and shear deformation in Y-Z plane is given as,

$$Q_y = kAG\frac{\partial v_s}{\partial s} = kAG\left[\frac{\partial v}{\partial s} + \theta\right] \tag{3-17}$$

The shape function matrix is,

$$N = \begin{bmatrix} N_T(s) \\ N_R(s) \end{bmatrix} = \begin{bmatrix} N_1 & 0 & 0 & N_2 & N_3 & 0 & 0 & N_4 \\ 0 & N_1 & -N_2 & 0 & 0 & N_3 & -N_4 & 0 \\ 0 & -N_{r1} & N_{r2} & 0 & 0 & -N_{r3} & N_{r4} & 0 \\ N_{r1} & 0 & 0 & N_{r2} & N_{r3} & 0 & 0 & N_{r4} \end{bmatrix} \tag{3-18}$$

The transverse shear effect parameter [45] is defined as,

$$\Phi = \frac{12EI}{kAGL^2} \tag{3-19}$$

Where I is area moment of inertia, k is the shape factor.

The shape factor for hollow circular cross-sectional beam [45] is given as,

$$k = \frac{6(1+\nu)\left(1+\left(\frac{d}{D}\right)^2\right)^2}{(7+6\nu)\left(1+\left(\frac{d}{D}\right)^2\right)^2 + (20+12\nu)\left(\frac{d}{D}\right)^2} \tag{3-20}$$

Where, ν, d and D are the Poisson's ratio, inner diameter and the outer diameter of the rotor respectively.

Shape functions are expressed as below,

$$N_1 = \frac{1}{1+\Phi}(\alpha_1 + \Phi\beta_1), \qquad N_2 = \frac{1}{1+\Phi}(\alpha_2 + \Phi\beta_2),$$

$$N_3 = \frac{1}{1+\Phi}(\alpha_3 + \Phi\beta_3), \qquad N_4 = \frac{1}{1+\Phi}(\alpha_4 + \Phi\beta_4)$$

$$\alpha_1 = 1-3\xi^2+2\xi^3, \qquad \alpha_2 = L(\xi - 2\xi^2 + \xi^3),$$

$$\alpha_3 = 3\xi^2 - 2\xi^3, \qquad \alpha_4 = L(-\xi^2 + \xi^3)$$

$$\beta_1 = 1-\xi, \qquad \beta_2 = \frac{L}{2}(\xi - \xi^2),$$

$$\beta_3 = \xi, \qquad \beta_4 = \frac{L}{2}(-\xi + \xi^2)$$

$$N_{r1} = \frac{1}{1+\Phi}(\alpha_{r1} + \Phi\beta_{r1}), \qquad N_{r2} = \frac{1}{1+\Phi}(\alpha_{r2} + \Phi\beta_{r2}),$$

$$N_{r3} = \frac{1}{1+\Phi}(\alpha_{r3} + \Phi\beta_{r3}), \qquad N_{r4} = \frac{1}{1+\Phi}(\alpha_{r4} + \Phi\beta_{r4})$$

$$\alpha_{r1} = \frac{1}{L}(-6\xi + 6\xi^2), \qquad \alpha_{r2} = 1-4\xi+3\xi^2,$$

$$\alpha_{r3} = \frac{1}{L}(6\xi - 6\xi^2), \qquad \alpha_{r4} = -2\xi + 3\xi^2$$

$$\beta_{r1} = 0, \qquad \beta_{r2} = 1-\xi,$$

$$\beta_{r3} = 0, \qquad \beta_{r4} = \xi$$

Timoshenko beam theory is used in the rotor finite element model as it is superior in predicting the transverse vibration response of the beam.

3.3 ROTOR FINITE ELEMENT MODEL

The finite element method has been described in several books and manuscripts. This process includes dividing the given domain into a set of simple subdomains or finite elements with proper shape functions that allow the approximation of the solution.

A finite element as shown in Figure 3-8 has eight degrees of freedom. It has two translational degrees of freedom (u_1, v_1) at node 1 and (u_2, v_2) at node 2, two rotational degrees of freedom (θ_1, ϕ_1) at node 1 and (θ_2, ϕ_2) at node 2. The internal displacements of an element can be interpolated by shape functions in terms of nodal displacements [45].

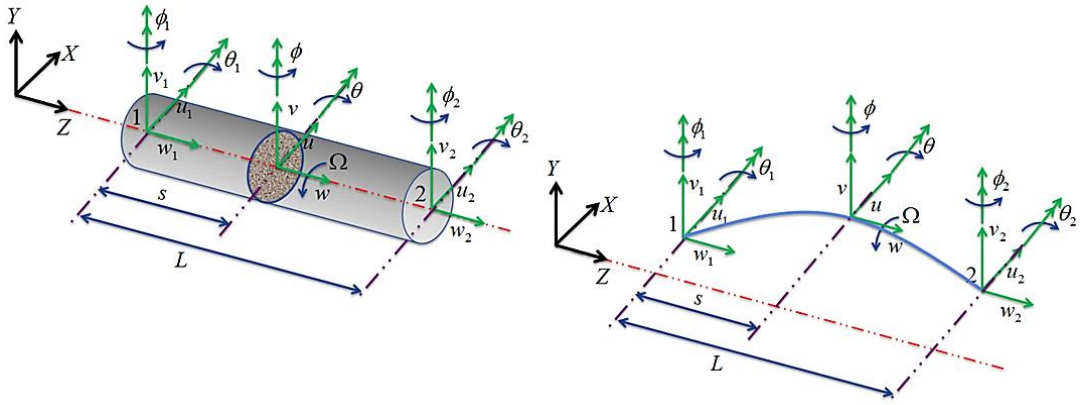

Figure 3-8 Coordinate for finite shaft element

In the finite element method, the continuous displacement field can be approximated in terms of the discretized generalized displacements of the element nodes. The displacement could be approximated as,

$$\begin{Bmatrix} u(s,t) \\ v(s,t) \\ \theta(s,t) \\ \phi(s,t) \end{Bmatrix} = \begin{bmatrix} N_T(s) \\ N_R(s) \end{bmatrix} \bar{q}_n^f(t) \tag{3-21}$$

$$N = \begin{bmatrix} N_T(s) \\ N_R(s) \end{bmatrix} = \begin{bmatrix} N_1 & 0 & 0 & N_2 & N_3 & 0 & 0 & N_4 \\ 0 & N_1 & -N_2 & 0 & 0 & N_3 & -N_4 & 0 \\ 0 & -N_1' & N_2' & 0 & 0 & -N_3' & N_4' & 0 \\ N_1' & 0 & 0 & N_2' & N_3' & 0 & 0 & N_4' \end{bmatrix} \tag{3-22}$$

$$\bar{q}_n^f(t) = \begin{bmatrix} u_1 & v_1 & \theta_1 & \phi_1 & u_2 & v_2 & \theta_2 & \phi_2 \end{bmatrix}^T \tag{3-23}$$

Where the distance s is measured from the left of the point of interest.

The nodal displacement vector $\bar{q}_n^f(t)$ is the end displacement with two translations and two rotations.

3.3.1 KINETIC ENERGY

The kinetic energy of an infinitesimal rotor element has the same form as the kinetic energy of a rigid disk.

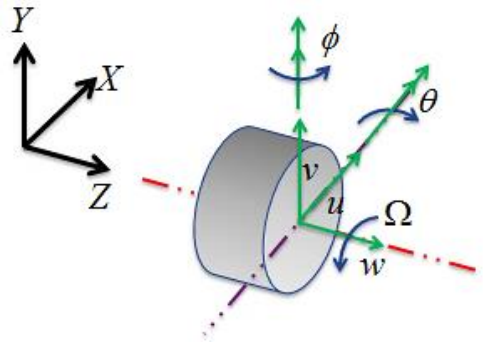

Figure 3-9 Coordinate for finite shaft element

The total kinetic energy of the shaft element is obtained by integrating the differential energy for an infinitesimal rotor element over the length of the element,

$$T = \frac{1}{2}\int_0^L \left\{ m^e(\dot{u}^2 + \dot{v}^2) + I_d^e(\dot{\theta}^2 + \dot{\phi}^2) + \Omega I_p^e(\dot{\theta}\phi - \theta\dot{\phi}) \right\} ds + \frac{1}{2}\Omega^2 \int_0^L I_p^e ds \tag{3-24}$$

Since angular momentum in X-Z and Y-Z plane are opposite in direction and have the same magnitude.

$$\therefore \theta\dot{\phi} = -\dot{\theta}\phi \tag{3-25}$$

$$\therefore T = \frac{1}{2}\int_0^L \left\{ m^e(\dot{u}^2 + \dot{v}^2) + I_d^e(\dot{\theta}^2 + \dot{\phi}^2) - 2\Omega I_p^e \dot{\theta}\phi \right\} ds + \frac{1}{2}\Omega^2 \int_0^L I_p^e ds \tag{3-26}$$

Where, m^e, I_d^e, I_p^e are the mass, diametral and polar moment of inertia per unit length. For circular cross section, $I_p^e = 2I_d^e$. After substituting the shape functions into the element kinetic energy T, the expression for kinetic energy can be written by evaluating above integrals as,

$$\therefore T = \frac{1}{2}\dot{q}^T\left(\left[M_T^e\right]+\left[M_R^e\right]\right)\dot{q} - \Omega q^T\left[G^e\right]\dot{q} + \frac{1}{2}I_p^e L\Omega^2 \tag{3-27}$$

$$\therefore T = \frac{1}{2}\dot{q}^T M^e\dot{q} - \Omega q^T g^e\dot{q} + \frac{1}{2}I_p^e L\Omega^2 \tag{3-28}$$

The element translational mass matrix $\left[M_T^e\right]$, rotational inertia matrix $\left[M_R^e\right]$ are symmetric matrices and the element gyroscopic matrix $\left[G^e\right]$ is skew – symmetric matrix.

3.3.2 POTENTIAL ENERGY

The potential energy of the rotating shaft element consists of the elastic bending energy due to the bending moments, shear energy due to the shear forces. The potential energy V of a rotating shaft is,

$$V = \frac{1}{2}\int_0^L EI\left[\left(\frac{\partial\theta}{\partial s}\right)^2+\left(\frac{\partial\phi}{\partial s}\right)^2\right]ds + \frac{1}{2}\int_0^L \kappa GA\left[\left(\frac{\partial u}{\partial s}-\phi\right)^2+\left(\frac{\partial v}{\partial s}+\theta\right)^2\right]ds \tag{3-29}$$

Where EI is the bending modulus, κGA is the effective shear modulus. Substituting the shape functions relationship, potential energy can be written by evaluating above integrals as,

$$\therefore V = \frac{1}{2}q^T\left[K_B^e\right]q \tag{3-30}$$

Where,

$\left[K_B^e\right]$ is the bending stiffness.

3.4 EQUATIONS OF MOTION

The equations of motion of the system can be obtained from the Lagrange's formulations. For the analysis of natural whirl speeds of the rotor bearing system, the force term can be eliminated. Lagrange function, $L = T - V$

Lagrange's equation can be written as,

$$\frac{d}{dt}\left(\frac{\partial L}{\partial\dot{q}_i}\right) - \frac{\partial L}{\partial q_i} + \frac{\partial RD}{\partial\dot{q}_i} = 0 \tag{3-31}$$

In forming Langrage's equations of motion for a vibrating system, it is necessary to take derivatives of the potential energy V, the kinetic energy T and the dissipation function RD. The potential energy V mainly comes from the beam bending and shear effect. The kinetic energy T is determined by both the lateral and rotary inertia. The energy dissipation in the system as dissipation function RD comes from the external damping and internal damping.

3.4.1 FRAME OF REFERENCE

There are two basic ways to formulate the equations of motion. One way is to write them with respect to a fixed reference frame or inertial reference frame while other is to write with respect to rotating reference frame or whirl reference frame.

3.4.2 EQUATIONS OF MOTION IN INERTIAL REFERENCE FRAME

Whirl speeds can be determined from the solution of eigenvalue problem resulting from the free vibration equation. Substituting the equations (3-28) and (3-30) in Lagrange's equations of motion (3-31), the equations of motion in fixed frame of reference becomes,

$$\left[\left[M_T^e\right]+\left[M_R^e\right]\right]\left\{\ddot{\bar{q}}_n^f\right\}-\Omega\left[G^e\right]\left\{\dot{\bar{q}}_n^f\right\}+\left[K_B^e\right]\left\{\bar{q}_n^f\right\}=\left\{\bar{F}_n^f\right\} \qquad (3\text{-}32)$$

where,

$\left[M_T^e\right]=\left[M_T\right]_0+\Phi\left[M_T\right]_1+\Phi^2\left[M_T\right]_2$;

$\left[M_R^e\right]=\left[M_R\right]_0+\Phi\left[M_R\right]_1+\Phi^2\left[M_R\right]_2$;

$\left[K_B^e\right]=\left[K_B\right]_0+\Phi\left[K_B\right]_1$;

$\left[G^e\right]=\left[G\right]_0+\Phi\left[G\right]_1+\Phi^2\left[G\right]_2$;

The details about the above all matrices are presented in the appendix.

3.4.3 EQUATIONS OF MOTION IN WHIRL REFERENCE FRAME

The fixed frame of reference is expressed as XYZ and rotational frame of reference is represented as xyz, $x'y'z'$ and $x''y''z''$ [9] as shown below Figure 3-10.

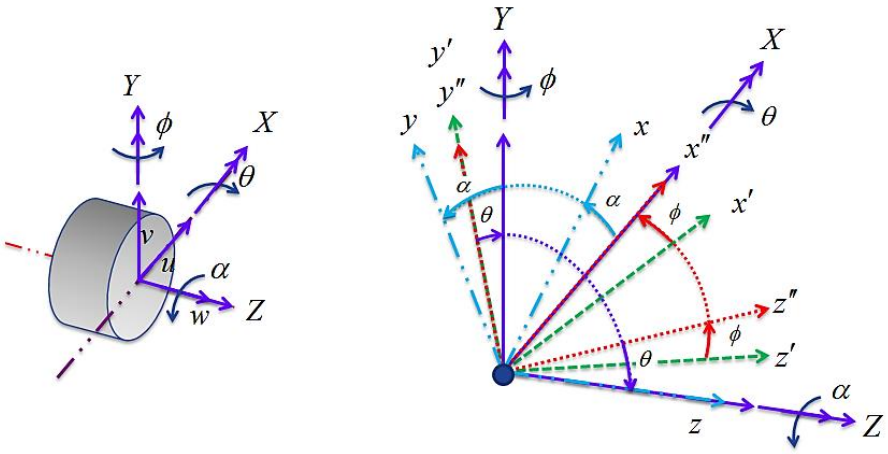

Figure 3-10 Fixed and Rotating Coordinate System

Three independent successive rotations are shown in the below Figure 3-11.

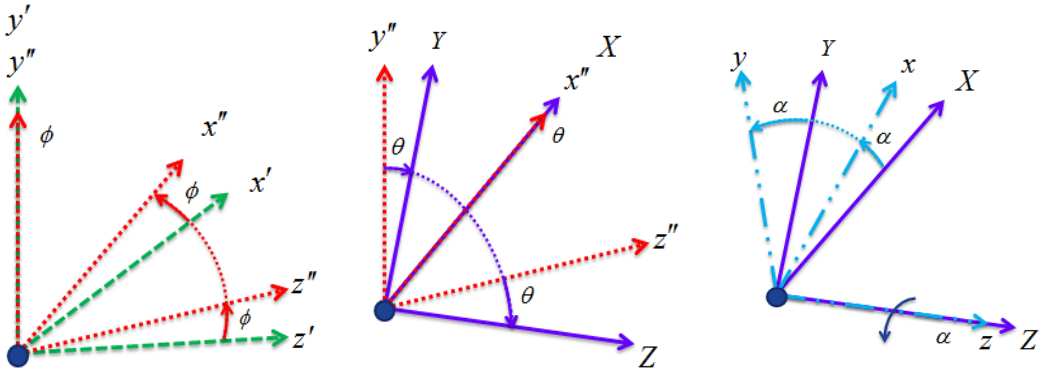

Figure 3-11 Successive Rotations of Coordinate System

The rotations are defining as below,

- Rotation ϕ about y' defines $x'y'z'$
- Rotation θ about x'' defines $x''y''z''$
- Rotation α about z defines xyz

For small deformation, the rotations ϕ and θ are approximately collinear with x'' and y' axes respectively. The displacements (u,v,θ,ϕ) in a fixed frame of reference XYZ are transformed to corresponding displacements $(u^r,v^r,\theta^r,\phi^r)$ relative to the rotating frame of reference xyz by an orthogonal transformation. The $XYZ:\Im$ triad is a fixed coordinate system and $xyz:\Re$ is

rotating coordinate system. $\Re$ is defined relative to $\Im$ by a single rotation $(\alpha = \omega t)$ about Z with ω denoting the whirling speed [9].

The position of any point on the fixed coordinate system can be expressed in terms of rotating coordinate system as below,

$$\{\bar{q}_n^f\} = [T_n]\{\bar{q}_n^r\} \tag{3-33}$$

Whereas,

$$\{\bar{q}_n^f\} = \begin{Bmatrix} u \\ v \\ \theta \\ \phi \end{Bmatrix};\ \{\bar{q}_n^r\} = \begin{Bmatrix} u^r \\ v^r \\ \theta^r \\ \phi^r \end{Bmatrix};\ [T_n] = \begin{bmatrix} \cos(\omega t) & -\sin(\omega t) & 0 & 0 \\ \sin(\omega t) & \cos(\omega t) & 0 & 0 \\ 0 & 0 & \cos(\omega t) & -\sin(\omega t) \\ 0 & 0 & \sin(\omega t) & \cos(\omega t) \end{bmatrix} \tag{3-34}$$

$$\therefore [\dot{T}_n] = \omega \begin{bmatrix} -\sin(\omega t) & -\cos(\omega t) & 0 & 0 \\ \cos(\omega t) & -\sin(\omega t) & 0 & 0 \\ 0 & 0 & -\sin(\omega t) & -\cos(\omega t) \\ 0 & 0 & \cos(\omega t) & -\sin(\omega t) \end{bmatrix} = \omega[S_n] \tag{3-35}$$

$$\therefore [\ddot{T}_n] = -\omega^2 \begin{bmatrix} \cos(\omega t) & -\sin(\omega t) & 0 & 0 \\ \sin(\omega t) & \cos(\omega t) & 0 & 0 \\ 0 & 0 & \cos(\omega t) & -\sin(\omega t) \\ 0 & 0 & \sin(\omega t) & \cos(\omega t) \end{bmatrix} = -\omega^2[T_n] \tag{3-36}$$

Taking time derivative of the above equation (3-33),

$$\{\dot{\bar{q}}_n^f\} = [\dot{T}_n]\{\bar{q}_n^r\} + [T_n]\{\dot{\bar{q}}_n^r\};$$

$$\therefore \{\dot{\bar{q}}_n^f\} = [T_n]\{\dot{\bar{q}}_n^r\} + \omega[S_n]\{\bar{q}_n^r\} \tag{3-37}$$

$$\{\ddot{\bar{q}}_n^f\} = [\ddot{T}_n]\{\bar{q}_n^r\} + 2[\dot{T}_n]\{\dot{\bar{q}}_n^r\} + [T_n]\{\ddot{\bar{q}}_n^r\}$$

$$\{\ddot{\bar{q}}_n^f\} = [T_n]\{\ddot{\bar{q}}_n^r\} + 2\omega[S_n]\{\dot{\bar{q}}_n^r\} - \omega^2[T_n]\{\bar{q}_n^r\} \tag{3-38}$$

Substituting the above equations (3-37) and (3-38) into the equation (3-32), the equation of motion will become as,

$$[[M_T^e]+[M_R^e]][T_n]\{\ddot{\bar{q}}_n^r\}+2\omega[S_n]\{\dot{\bar{q}}_n^r\}-\omega^2[T_n]\{\bar{q}_n^r\}]-\Omega[G^e][[T_n]\{\dot{\bar{q}}_n^r\}+\omega[S_n]\{\bar{q}_n^r\}]+[K_B^e][[T_n]\{\bar{q}_n^r\}]=\{\bar{F}_n^f\}$$

$$\therefore [[M_T^e]+[M_R^e]][T_n]\{\ddot{\bar{q}}_n^r\}+[2\omega[[M_T^e]+[M_R^e]][S_n]-\Omega[G^e][T_n]]\{\dot{\bar{q}}_n^r\}$$

$$+[[K_B^e][T_n]-\Omega[G^e]\omega[S_n]-\omega^2[[M_T^e]+[M_R^e]][T_n]]\{\bar{q}_n^r\}=\{\bar{F}_n^f\}$$

whereas, γ is spin whirl ratio,

$\gamma=\frac{\Omega}{\omega}$ - non-dimensional parameter

$$\therefore [[M_T^e]+[M_R^e]][T_n]\{\ddot{\bar{q}}_n^r\}+\omega[2[[M_T^e]+[M_R^e]][S_n]-\gamma[G^e][T_n]]\{\dot{\bar{q}}_n^r\}$$

$$+[[K_B^e][T_n]-\omega^2[\gamma[G^e][S_n]+[[M_T^e]+[M_R^e]][T_n]]]\{\bar{q}_n^r\}=\{\bar{F}_n^f\}$$

Multiplying $[T_n]^T$ to the above equation and simplifying, the equations of motion in whirl or rotating frame of reference becomes,

$$[[M_T^e]+[M_R^e]]\{\ddot{\bar{q}}_n^r\}+\omega[2[[\hat{M}_T^e]+[\hat{M}_R^e]]-\gamma[G^e]]\{\dot{\bar{q}}_n^r\}+[[K_B^e]-\omega^2[\gamma[\hat{G}^e]+[[M_T^e]+[M_R^e]]]]\{\bar{q}_n^r\}=\{\bar{F}_n^f\} \quad (3\text{-}39)$$

Where,

$[\hat{M}_T^e]=[T_n]^T[M_T^e][S_n];$

$[\hat{M}_R^e]=[T_n]^T[M_R^e][S_n];$

$[\hat{G}^e]=[T_n]^T[G^e][S_n]$

$$\therefore [[M_T^e]+[M_R^e]]\{\ddot{\bar{q}}_n^r\}+\omega[2[\hat{M}_T^e]+(1-\gamma)[G^e]]\{\dot{\bar{q}}_n^r\}+[[K_B^e]-\omega^2[[M_T^e]+(1-2\gamma)[M_R^e]]]\{\bar{q}_n^r\}=\{\bar{F}_n^f\} \quad (3\text{-}40)$$

where,

$$\left[\hat{M}_R^e\right] = \frac{1}{2}\left[G^e\right];$$

$$\left[\hat{G}^e\right] = -2\left[M_R^e\right]$$

The details about the above all matrices are presented in the appendix.

In this chapter, different beam theories and equations of motion by Lagrange's formulation are discussed. The equations of motion for the undamped rotor is developed in the inertial or fixed frame of reference and whirl or rotating frame of reference.

CHAPTER 4

MODELLING AND INFLUENCE OF DIFFERENT FORMS OF DAMPING AND OPERATING TEMPERATURE

In general, physical systems are associated with one or the other type of damping. In certain cases, the amount of damping may be small and in other cases large. In damped free vibrations, the amplitude of vibration decays gradually before it comes to the equilibrium position. The rate and nature at which the amplitude decays, depends upon the type and amount of damping in the system. This chapter covers the modelling of different forms of damping and operating temperature and updating the equations of motion by incorporating the above damping and temperature effect.

4.1 MODELLING OF INTERNAL VISCOUS DAMPING

Few practical applications or situations where the modelling of internal viscous damping can be considered as,

- In gas turbine and steam turbine, the coolant is sent through the tiny axial holes which are provided in the shaft and blades to maintain the uniform temperature of the rotor blades. This helps to maintain the optimum design clearance between stator vanes and rotor vanes.

- In high power density motors and generators, the hydrogen gas is sent through the holes or slots provided in the rotor bars. This helps to maintain the rotor temperature within the design limits.

- To reduce the eddy current losses in the electromagnetic machines, the organic and/or inorganic coating is applied on the thin laminations of the rotors.
- To raise the damping coefficient, the coating is applied on the different rotating components with an energy absorbing material.
- The different sub-assemblies or components like fans, rotor stacks and couplings are mounted on the shaft with interference or shrink fit for power transmission.

Viscoelastic behavior can be described by mechanical models constructed using elastic springs and viscous dashpots. Elastic spring follows Hook's Law and viscous dashpot follows Newton's law of viscosity. The simplest and best mathematical model for describing internal viscous damping is the 'Kelvin – Voigt' model. It assumes the linear viscous model and damping mechanism as dashpot with a viscosity of μ_i as shown in Figure 4-1.

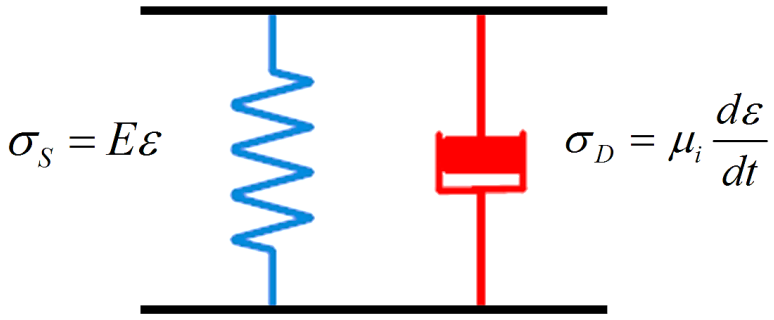

Figure 4-1 Kelvin - Voigt Model for viscoelastic material

Where, σ_S is the stiffness stress, E is the elastic Modulus of the material, ε is the strain that occurs under the given stress, σ_D is the damping stress, μ_i is the viscosity of the material, and $\frac{d\varepsilon}{dt}$ is the time derivative of strain.

The two components of the model are arranged in a parallel as shown in Figure 4-1, the strains in each component are identical.

$$\varepsilon_{Total} = \varepsilon_D = \varepsilon_S \tag{4-1}$$

Similarly, the total stress will be the sum of the stress in each component,

$$\sigma_{Total} = \sigma_S + \sigma_D \tag{4-2}$$

Substituting the equations from the Figure 4-1 in the above equation (4-2)

$$\therefore \sigma_{Total} = E\varepsilon + \mu_i \frac{d}{dt}\varepsilon$$

$$\therefore \sigma = E\varepsilon + \mu_i \frac{d}{dt}\varepsilon \qquad (4\text{-}3)$$

When a sinusoidal exciting force is applied to a viscoelastic material, the strain is having the same angular frequency but retarded or lags the stress. The phase angle between them is denoted by φ. This angle is also called as loss angle. When dealing with forced sinusoidal motions, it is convenient to represent the stress and strain by rotating vectors in the complex plane. These vectors are called as phasors as shown in the following Figure 4-2.

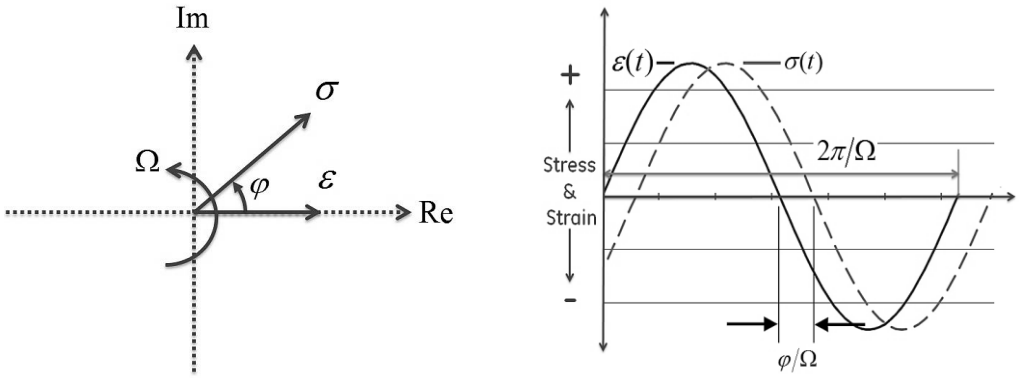

Figure 4-2 Stress and Strain Phasor Diagram

It can be useful to visualize the stress and strain as the projection on the real axis of vectors rotating in the complex plane at a frequency Ω. If we capture their position just as the strain vectors passes the real axis, the stress vector will be ahead of it by the phase angle φ° as shown in Figure 4-2. Based on the phase angle, the few cases for different materials are,

- Ideal elastic material, the stress and strain are in phase i.e. $\varphi = 0^\circ$
- Ideal viscous material, the stress and strain are 90°out of phase i.e. $\varphi = 90^\circ$
- Viscoelastic material, the strain lags stress with an angle φ°

The viscoelastic material under a sinusoidal motion of frequency Ω, the stress σ and strain ε can be expressed as below,

Strain, $\varepsilon = \varepsilon_0 \sin(\Omega t)$ and Stress, $\sigma = \sigma_0 \sin((\Omega t) + \varphi)$

$$\therefore \sigma = \sigma_0 \cos\varphi \sin(\Omega t) + \sigma_0 \sin\varphi \cos(\Omega t) \quad (4\text{-}4)$$

In the above equation, the stress has two components,

The first component $\sigma_0 \cos\varphi$ is in phase with strain whereas the second component $\sigma_0 \sin\varphi$ is out of phase with strain.

Relation between complex modulus E_0, storage modulus E_1 and loss modulus E_2 is shown in the following Figure 4-3.

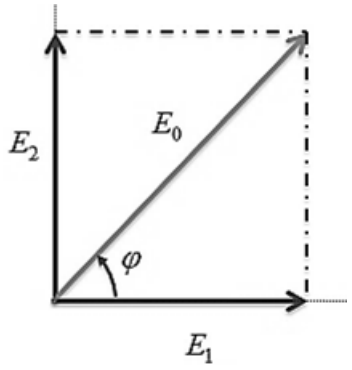

Figure 4-3 Relation between Complex, Storage and Loss Modulus

The storage modulus is expressed in terms of complex modulus as,

$$E_1 = E_0 \cos\varphi = \frac{\sigma_0}{\varepsilon_0} \cos\varphi \quad (4\text{-}5)$$

The loss modulus is expressed in terms of complex modulus as,

$$E_2 = E_0 \sin\varphi = \frac{\sigma_0}{\varepsilon_0} \sin\varphi \quad (4\text{-}6)$$

The loss factor η is defined as the ratio of loss modulus to storage modulus and expressed as,

$$\eta = \frac{E_2}{E_1} = \tan\varphi \quad (4\text{-}7)$$

$$\therefore E_2 = E_1 \tan\varphi \quad (4\text{-}8)$$

The young's modulus is defined as ratio of stress σ to strain ε, it is given as,

$$E_0 = \frac{\sigma}{\varepsilon} = \frac{\sigma_0 e^{i(\Omega t + \varphi)}}{\varepsilon_0 e^{i\Omega t}} \quad (4\text{-}9)$$

where,

$\varepsilon = \varepsilon_0 e^{i\Omega t}$ and

$\sigma = \sigma_0 e^{i(\Omega t+\varphi)}$

$$\therefore E_0 = \frac{\sigma_0}{\varepsilon_0} e^{i\varphi} \tag{4-10}$$

$$\therefore E_0 = \frac{\sigma_0}{\varepsilon_0} (\cos\varphi + i\sin\varphi) \tag{4-11}$$

$$\therefore E_0 = E_1 + iE_2 \tag{4-12}$$

Substituting the E_0 from equation (4-12) into the stress strain equation,

$$\sigma = E_0 \varepsilon \tag{4-13}$$

$$\therefore \sigma = (E_1 + iE_2)\varepsilon \tag{4-14}$$

$$\therefore \sigma = E_1\left(1 + i\frac{E_2}{E_1}\right)\varepsilon \tag{4-15}$$

Putting the value of $\frac{E_2}{E_1} = \eta$ from equation (4-7) into the above equation (4-15),

$$\therefore \sigma = E_1(1 + i\eta)\varepsilon \tag{4-16}$$

$$\therefore \sigma = (E_1 + iE_1\eta)\varepsilon \tag{4-17}$$

The above equation (4-17) gives the relation between stress σ to strain ε with a loss factor η and storage modulus E_1.

The stress σ, strain ε and their rates of change with respect to time t is expressed in the equation (4-3) as below,

$$\sigma = E\varepsilon + \mu_i \frac{d}{dt}\varepsilon$$

The above equation is governed by constitutive relation and it is expressed as a linear first – order differential equation,

$$\therefore \sigma(t) = E\varepsilon(t) + \mu_i \frac{d}{dt}\varepsilon(t) \tag{4-18}$$

Substuting the values,

$\sigma = \sigma_0 e^{i\Omega t}$,

$\varepsilon = \varepsilon_0 e^{i\Omega t}$

with σ_0 and ε_0 are complex quantities.

$$\therefore \sigma e^{i\omega t} = E\varepsilon e^{i\Omega t} + \mu_i \frac{d}{dt}\left(\varepsilon e^{i\Omega t}\right) \tag{4-19}$$

After eliminating the common exponential terms in the above equation, the final equation becomes as,

$$\therefore \sigma = \left(E + i\Omega\mu_i\right)\varepsilon \tag{4-20}$$

Comparing the equation (4-17) and equation (4-20) the common terms are,

$$E_1\eta = \Omega\mu_i \tag{4-21}$$

$$\therefore \eta_{eff} = \eta_v\Omega \tag{4-22}$$

Where,

$$\eta_v = \frac{\mu_i}{E_1}$$

The equation (4-3) is expressed with the above terms as,

$$\sigma = E\varepsilon + \mu_i \frac{d}{dt}\left(\varepsilon\right)$$

$$\therefore \sigma = E\varepsilon + \mu_i\dot{\varepsilon}$$

$$\therefore \sigma = E\varepsilon + E\eta_v\dot{\varepsilon} \tag{4-23}$$

The above equation contains the stiffness terms $E\varepsilon$ and damping terms $E\eta_v\dot{\varepsilon}$.

The stiffness term is expressed as,

$$\sigma = E\varepsilon \tag{4-24}$$

The damping terms which is also known as internal viscous damping is expressed as,

$$\sigma = E\eta_v\dot{\varepsilon} \tag{4-25}$$

4.2 MODELLING INTERNAL HYSTERETIC DAMPING

The flexible or rigid rotor in which half of the fibers of rotating shaft are in tension while other half are in compression. The elastic forces change from tension to compression and vice versa due to the rotation of the shaft. Due to this continuous reversible loading, some energy is dissipated and converted into heat. This phenomenon can be modelled as internal hysteretic damping. This is the practical application or situation where the internal hysteretic damping can be considered.

Hysteretic friction model is less widely utilized in modeling damping and friction in mechanical systems, as compared to the viscous friction model. The relation between the different modulus is already shown in Figure 4-3.

$$\sin\varphi = \frac{E_2}{E_0} = \frac{E_2}{\sqrt{(E_1)^2 + (E_2)^2}} \tag{4-26}$$

$$\cos\varphi = \frac{E_1}{E_0} = \frac{E_1}{\sqrt{(E_1)^2 + (E_2)^2}} \tag{4-27}$$

$$E_0 = \sqrt{(E_1)^2 + (E_2)^2} = E_1\sqrt{(1)^2 + \left(E_2 / E_1\right)^2} \tag{4-28}$$

From the equation (4-7),

$$\tan\varphi = \frac{E_2}{E_1} = \eta_H \tag{4-29}$$

Rearranging the terms and replacing the terms of $\left(E_2 / E_1\right)$, in the above equations (4-26) and (4-27) , the final equations become,

$$\therefore \sin\varphi = \frac{E_2}{E_1\sqrt{(1)^2 + \left(E_2 / E_1\right)^2}} = \frac{\left(E_2 / E_1\right)}{\sqrt{1 + \left(E_2 / E_1\right)^2}} = \frac{\eta_H}{\sqrt{1 + \eta_H{}^2}} \tag{4-30}$$

$$\therefore \cos\varphi = \frac{E_1}{E_1\sqrt{(1)^2 + \left(E_2 / E_1\right)^2}} = \frac{\left(E_1 / E_1\right)}{\sqrt{1 + \left(E_2 / E_1\right)^2}} = \frac{1}{\sqrt{1 + \eta_H{}^2}} \tag{4-31}$$

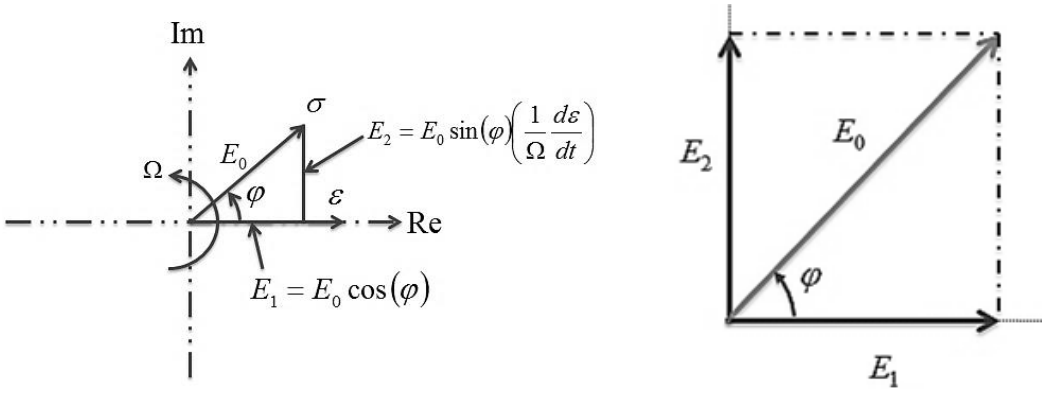

Figure 4-4 Stress and Strain Phasor Diagram

From the constitutive equation for the hysteretic model, stress and strain are calculated. The components along the real axis are found using the familiar in phase stress-strain diagram explained in Figure 4-2.

$$\mathrm{Re}[\sigma] = E_0 \cos(\varphi)\varepsilon \tag{4-32}$$

The components in the imaginary direction of the complex storage modulus is found from the stress – strain law which gives,

$$\mathrm{Im}[\sigma] = E_0 \sin(\varphi)\left(\frac{1}{\Omega}\frac{d\varepsilon}{dt}\right) \tag{4-33}$$

With the above two equations, the final equation for the stress σ becomes,

$$\sigma = \mathrm{Re}[\sigma] + \mathrm{Im}[\sigma] = E_0 \cos(\varphi)\varepsilon + E_0 \sin(\varphi)\left(\frac{1}{\Omega}\frac{d\varepsilon}{dt}\right) \tag{4-34}$$

$$\therefore \sigma = E_0\left[\varepsilon \cos(\varphi) + \sin(\varphi)\left(\frac{1}{\Omega}\frac{d\varepsilon}{dt}\right)\right] \tag{4-35}$$

From equation (4-30) and (4-31),

$\sin\varphi = \dfrac{\eta_H}{\sqrt{1+\eta_H{}^2}}$ and

$\cos\varphi = \dfrac{1}{\sqrt{1+\eta_H{}^2}}$

Replacing the above terms in the equation (4-35), the final equation becomes,

$$\therefore \sigma = E_0\left[\varepsilon\left(\frac{1}{\sqrt{1+\eta_H{}^2}}\right)+\left(\frac{\eta_H}{\sqrt{1+\eta_H{}^2}}\right)\left(\frac{1}{\Omega}\frac{d\varepsilon}{dt}\right)\right] \tag{4-36}$$

Rearranging the terms, the final equation becomes as,

$$\therefore \sigma = E_0\left[\frac{\varepsilon}{\sqrt{1+\eta_H{}^2}}+\frac{1}{\Omega}\frac{\eta_H}{\sqrt{1+\eta_H{}^2}}\dot{\varepsilon}\right] \tag{4-37}$$

The above term is having internal hysteretic damping.

4.3 INFLUENCE OF INTERNAL DAMPING

Internal damping plays an important role in the rotor whirl speeds. Internal damping constitutes linear viscous damping and hysteretic damping. Based on the previous derivations, the equations of motion can be extended to include internal viscous damping and internal hysteretic damping effects.

4.3.1 EQUATIONS OF MOTION IN INERTIAL REFERENCE FRAME

Based on the previous equations derived for internal viscous damping (4-25) and internal hysteretic damping (4-37), the combination of internal damping terms into the constitutive relationship yields as,

$$\sigma = E\eta_v\dot{\varepsilon} + E\left[\frac{\varepsilon}{\sqrt{1+\eta_H{}^2}}+\frac{1}{\Omega}\frac{\eta_H}{\sqrt{1+\eta_H{}^2}}\dot{\varepsilon}\right] \tag{4-38}$$

$$\therefore \sigma_z = E\left\{\frac{\varepsilon_z}{\sqrt{1+\eta_H{}^2}}+\left(\eta_v+\frac{\eta_H}{\Omega\sqrt{1+\eta_H{}^2}}\right)\dot{\varepsilon}_z\right\} \tag{4-39}$$

In the following Figure 4-5, the shaft is whirling about the bearing center line with a speed of ω and spinning about the center of the shaft with speed of Ω.

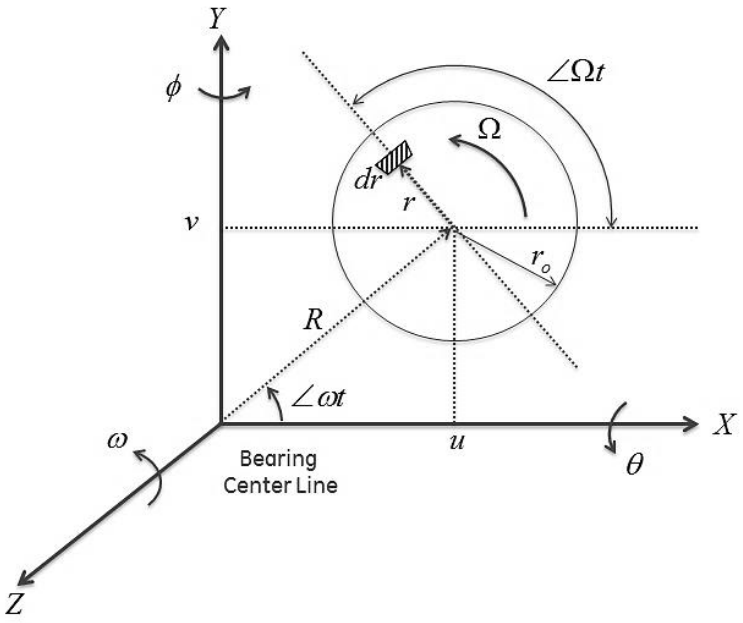

Figure 4-5 Rotor System Configuration

From the Figure 4-5, R is the location of shaft center from the bearing center line, r is the radius of the shaft varies from 0 to r_0 having a differential radial thickness dr and at a distance r.

The strain ε_z and strain rate $\dot{\varepsilon}_z$ are expressed in the Z direction as,

$$\varepsilon_z = -r\cos[(\Omega-\omega)t]\frac{\partial^2 R}{\partial z^2} \tag{4-40}$$

$$\dot{\varepsilon}_z = (\Omega-\omega)r\sin[(\Omega-\omega)t]\frac{\partial^2 R}{\partial z^2} - r\cos[(\Omega-\omega)t]\frac{\partial}{\partial t}\left(\frac{\partial^2 R}{\partial z^2}\right) \tag{4-41}$$

Substituting the above equations (4-40) and (4-41) into the equation (4-39), the final equation becomes as,

$$\therefore \sigma_z = E\left\{\frac{1}{\sqrt{1+\eta_H{}^2}}\left(-r\cos[(\Omega-\omega)t]\frac{\partial^2 R}{\partial z^2}\right)\right\}$$

$$+E\left\{\left(\eta_v+\frac{\eta_H}{\Omega\sqrt{1+\eta_H{}^2}}\right)\left((\Omega-\omega)r\sin[(\Omega-\omega)t]\frac{\partial^2 R}{\partial z^2}-r\cos[(\Omega-\omega)t]\frac{\partial}{\partial t}\left(\frac{\partial^2 R}{\partial z^2}\right)\right)\right\} \quad (4\text{-}42)$$

From the Figure 4-5, the internal bending moments M_x and M_y can be expressed by multiplying the stress with the distance from the neutral axis of the shaft and integrated over the cross-sectional area as,

$$M_x=\int_0^{2\pi}\int_0^{r_o}\left[v+r\sin(\Omega t)\right]\sigma_z\,dr\left(rd(\Omega t)\right) \quad (4\text{-}43)$$

$$M_y=\int_0^{2\pi}\int_0^{r_o}-\left[u+r\cos(\Omega t)\right]\sigma_z\,dr\left(rd(\Omega t)\right) \quad (4\text{-}44)$$

Substituting the modified constitutive relationship equation (4-42) into the internal bending moment equations (4-43) and (4-44), and performing the integration, the moments can be expressed as,

$$M_y=EI\left[\frac{1+\eta_H}{\sqrt{1+\eta_H{}^2}}u''+\eta_v\dot{u}''+\left(\frac{1+\eta_H}{\sqrt{1+\eta_H{}^2}}+\eta_v\Omega\right)v''\right] \quad (4\text{-}45)$$

$$\therefore M_y=EI\left[\frac{1+\eta_H}{\sqrt{1+\eta_H{}^2}}\left(\frac{\partial\theta}{\partial s}\right)+\eta_v\left(\frac{\partial\dot{\theta}}{\partial s}\right)+\left(\frac{1+\eta_H}{\sqrt{1+\eta_H{}^2}}+\eta_v\Omega\right)\left(\frac{\partial\phi}{\partial s}\right)\right] \quad (4\text{-}46)$$

$$\therefore M_y=EI\left[\eta_a\left(\frac{\partial\theta}{\partial s}\right)+\eta_v\left(\frac{\partial\dot{\theta}}{\partial s}\right)+\eta_b\left(\frac{\partial\phi}{\partial s}\right)\right] \quad (4\text{-}47)$$

$$M_x=-EI\left[\left(\frac{1+\eta_H}{\sqrt{1+\eta_H{}^2}}\right)v''+\eta_v\dot{v}''+\left(\frac{1+\eta_H}{\sqrt{1+\eta_H{}^2}}+\eta_v\Omega\right)u''\right] \quad (4\text{-}48)$$

$$\therefore M_x=-EI\left[\left(\frac{1+\eta_H}{\sqrt{1+\eta_H{}^2}}\right)\left(\frac{\partial\phi}{\partial s}\right)+\eta_v\left(\frac{\partial\dot{\phi}}{\partial s}\right)+\left(\frac{1+\eta_H}{\sqrt{1+\eta_H{}^2}}+\eta_v\Omega\right)\left(\frac{\partial\theta}{\partial s}\right)\right] \quad (4\text{-}49)$$

$$\therefore M_x=-EI\left[\eta_a\left(\frac{\partial\phi}{\partial s}\right)+\eta_v\left(\frac{\partial\dot{\phi}}{\partial s}\right)+\eta_b\left(\frac{\partial\theta}{\partial s}\right)\right] \quad (4\text{-}50)$$

Combining the above equations (4-47) and (4-50) and expressed in matrix form as,

$$\begin{Bmatrix} M_y \\ M_x \end{Bmatrix} = EI\begin{bmatrix} \eta_a & \eta_b \\ \eta_b & -\eta_a \end{bmatrix}\begin{Bmatrix} \frac{\partial\theta}{\partial s} \\ \frac{\partial\phi}{\partial s} \end{Bmatrix} + EI\begin{bmatrix} \eta_v & 0 \\ 0 & -\eta_v \end{bmatrix}\begin{Bmatrix} \frac{\partial\dot{\theta}}{\partial s} \\ \frac{\partial\dot{\phi}}{\partial s} \end{Bmatrix} \tag{4-51}$$

$$\therefore \begin{Bmatrix} M_y \\ M_x \end{Bmatrix} = EI\left[\eta_{eq}\right]\begin{Bmatrix} \frac{\partial\theta}{\partial s} \\ \frac{\partial\phi}{\partial s} \end{Bmatrix} + EI\begin{bmatrix} \eta_v & 0 \\ 0 & -\eta_v \end{bmatrix}\begin{Bmatrix} \frac{\partial\dot{\theta}}{\partial s} \\ \frac{\partial\dot{\phi}}{\partial s} \end{Bmatrix} \tag{4-52}$$

Where,

$\eta_a = \dfrac{1+\eta_H}{\sqrt{1+\eta_H{}^2}}$;

$\eta_b = \dfrac{\eta_H}{\sqrt{1+\eta_H{}^2}} + \eta_v\Omega$;

$\left[\eta_{eq}\right] = \begin{bmatrix} \eta_a & \eta_b \\ \eta_b & -\eta_a \end{bmatrix}$

Differential bending energy $d\wp_B^e$ and dissipation function $d\Im_B^e$ [11] are defined as,

$$d\wp_B^e = \frac{1}{2}EI\begin{Bmatrix} \frac{\partial\phi}{\partial s} \\ \frac{\partial\theta}{\partial s} \end{Bmatrix}^T \left[\eta_{eq}\right]\begin{Bmatrix} \frac{\partial\phi}{\partial s} \\ \frac{\partial\theta}{\partial s} \end{Bmatrix} \tag{4-53}$$

$$\therefore d\wp_B^e = \frac{1}{2}EI\left[\eta_{eq}\right]\left[\left(\frac{\partial\theta}{\partial s}\right)^2 + \left(\frac{\partial\phi}{\partial s}\right)^2\right] \tag{4-54}$$

$$d\Im_B^e = \frac{1}{2}EI\begin{Bmatrix} \frac{\partial\dot{\phi}}{\partial s} \\ \frac{\partial\dot{\theta}}{\partial s} \end{Bmatrix}^T \begin{bmatrix} \eta_v & 0 \\ 0 & -\eta_v \end{bmatrix}\begin{Bmatrix} \frac{\partial\dot{\phi}}{\partial s} \\ \frac{\partial\dot{\theta}}{\partial s} \end{Bmatrix} \tag{4-55}$$

$$\therefore d\Im_B^e = \frac{1}{2}\eta_v EI\left[\left(\frac{\partial\dot{\theta}}{\partial s}\right)^2 + \left(\frac{\partial\dot{\phi}}{\partial s}\right)^2\right] \tag{4-56}$$

Now placing the energy contributions from the above equations (4-54) and (4-56) into the appropriate kinetic and potential energy equations.

Now placing the kinetic energy term (4-56) from internal damping in the equation (3-26), the final equation becomes as,

$$T = \frac{1}{2}\int_0^L \left\{ m^e(\dot{u}^2 + \dot{v}^2) + I_d^e(\dot{\theta}^2 + \dot{\phi}^2) - 2\Omega I_p^e \dot{\theta}\phi \right\} ds + \frac{1}{2}\Omega^2 \int_0^L I_p^e ds + \frac{1}{2}\int_0^L \eta_v EI \left[\left(\frac{\partial \dot{\theta}}{\partial s} \right)^2 + \left(\frac{\partial \dot{\phi}}{\partial s} \right)^2 \right] ds \quad (4\text{-}57)$$

Now placing the potential energy term (4-54) from internal damping in the equation (3-29), the final equation becomes as,

$$V = \frac{1}{2}\int_0^L EI \left[\left(\frac{\partial \theta}{\partial s} \right)^2 + \left(\frac{\partial \phi}{\partial s} \right)^2 \right] ds + \frac{1}{2}\int_0^L \kappa GA \left[\left(\frac{\partial u}{\partial s} - \phi \right)^2 + \left(\frac{\partial v}{\partial s} + \theta \right)^2 \right] ds + \frac{1}{2}\int_0^L EI \left[\eta_{eq} \right] \left[\left(\frac{\partial \theta}{\partial s} \right)^2 + \left(\frac{\partial \phi}{\partial s} \right)^2 \right] ds \quad (4\text{-}58)$$

By using the Lagrange's approach, the equation of motion for Timoshenko shaft finite element with internal viscous damping and internal hysteretic damping in fixed coordinate system from the equations (4-57) and (4-58) is given as,

$$\left[\left[M_T^e \right] + \left[M_R^e \right] \right] \left\{ \ddot{\bar{q}}_n^f \right\} + \left[\eta_v \left[K_B^e \right] - \Omega \left[G^e \right] \right] \left\{ \dot{\bar{q}}_n^f \right\} + \left[\eta_a \left[K_B^e \right] + \eta_b \left[K_C^e \right] \right] \left\{ \bar{q}_n^f \right\} = \left\{ \bar{F}_n^f \right\} \quad (4\text{-}59)$$

The details about the above all matrices are presented in the appendix.

4.3.2 EQUATIONS OF MOTION IN WHIRL REFERENCE FRAME

The equations of motion from equation (4-59) is expressed into rotating coordinate system and simplifying as,

$$\left[\left[M_T^e \right] + \left[M_R^e \right] \right] \left\{ \ddot{\bar{q}}_n^r \right\} + \left[\eta_v \left[K_B^e \right] + \omega \left[2\left[\hat{M}_T^e \right] + (1-\gamma) \left[G^e \right] \right] \right] \left\{ \dot{\bar{q}}_n^r \right\}$$
$$+ \left[\eta_a \left[K_B^e \right] + \eta_b \left[K_C^e \right] - \omega \eta_v \left[K_C^e \right] - \omega^2 \left[\left[M_T^e \right] + (1-2\gamma) \left[M_R^e \right] \right] \right] \left\{ \bar{q}_n^r \right\} = \left\{ \bar{F}_n^f \right\} \quad (4\text{-}60)$$

The details about the above all matrices are presented in the appendix.

4.4 MODELLING OF OPERATING TEMPERATURE

Most of the applications as discussed above operate at high temperature. Few practical applications or situations where the operating temperature can be considered as,

- Gas turbines operate at high temperature. The combustion gasses are passed through the different stages of the turbine.
- Steam turbines operate at high temperature. The high-temperature steam is passed through the rotor and stator vanes.
- Motors and Generators operate at high temperature. The copper losses, iron losses and eddy current losses contribute to the rise in temperature of the machine.

Due to high operating temperature, the material properties like Young's modulus and Poisson's ratio changes with respect to temperature. The change in these material properties can be modelled as a function of the stiffness of the material.

Temperature plays an important role in the rotor vibrations. There are a couple of reasons for the rotor to operate at high temperature. One reason is that when the rotor is in operation, the continuous bending of the rotor generates heat due to strain energy transformation. The material loss factor is the main cause for the above heat generation. Another reason is the application demand as discussed above. Therefore, the temperature of the rotor is high due to heat generation in the rotor and surrounding temperature based on the application.

4.4.1 HEAT GENERATION DUE TO SHAFT BENDING

A uniform shaft is supposed to rotate at a constant speed and carry static loads as shown in Figure 4-6. Because of rotation, the shaft material undergoes alternating bending stresses. Due to the internal damping of the material may be assumed as linear viscous or hysteretic; a certain amount of heat is generated within the shaft material. For elastic deformation, part of the strain energy is transformed into heat depending on the material loss factor [38].

The energy of elastic deformation w for unit volume under bending stress σ will be, for a static load mg at the mid-span of the rotor,

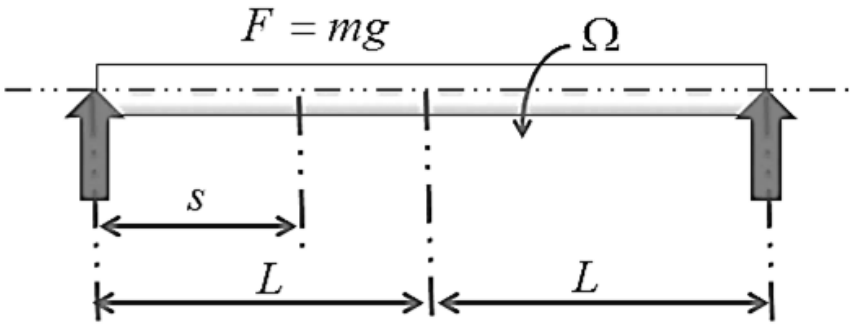

Figure 4-6 Shaft with both ends supported

The energy due to elastic deformation is calculated as,

$$w = \frac{\sigma^2}{2E} \tag{4-61}$$

Where, σ is the bending stress and E is young's modulus.

$$\sigma = \frac{Mr}{I};$$

$$M = \frac{mgz}{2};$$

$$I = \frac{\pi d^4}{64}$$

Putting the above terms in the equation (4-61), the final equation becomes,

$$\therefore w = \frac{2(mgzr)^2}{\pi^2 ER^8} \tag{4-62}$$

Heat generation per unit time q due to material damping / loss factor η is given as,

$$q = \frac{\pi \eta w}{2} \tag{4-63}$$

Heat generation in revolution per sec with N is the number of revolution per sec,

$$\therefore q = \frac{\pi \eta w}{2} N = \frac{\eta N (mgzr)^2}{\pi ER^8} \tag{4-64}$$

The conduction equation for the shaft will be,

$$\frac{\partial^2 T}{\partial r^2}+\frac{1}{r}\frac{\partial T}{\partial r}+\frac{\partial^2 T}{\partial z^2}+\frac{q}{k}=0 \tag{4-65}$$

$$\therefore \frac{\partial^2 T}{\partial r^2}+\frac{1}{r}\frac{\partial T}{\partial r}+\frac{\partial^2 T}{\partial z^2}=-Az^2r^2 \tag{4-66}$$

Where,

$$A=\frac{\eta N(mg)^2}{\pi kER^8}$$

The above equation (4-66) is solved by Fourier transformation,

$$F(r,n)=\int_0^L T(r,z)\cos\frac{\pi nz}{L}\,dz \tag{4-67}$$

The equation (4-66) becomes,

$$\therefore \frac{\partial^2 F}{\partial r^2}+\frac{1}{r}\frac{\partial F}{\partial z}-a^2F=-Ar^2\int_0^L z^2\cos az\,dz \tag{4-68}$$

Where,

$$\int_0^L \frac{\partial^2 T}{\partial r^2}\cos\frac{\pi nz}{L}\,dz=\frac{\partial^2}{\partial r^2}\int_0^L T\cos\frac{\pi nz}{L}\,dz=\frac{\partial^2 F}{\partial r^2};$$

$$\int_0^L \frac{1}{r}\frac{\partial T}{\partial r}\cos\frac{\pi nz}{L}\,dz=\frac{1}{r}\frac{\partial}{\partial r}\int_0^L T\cos\frac{\pi nz}{L}\,dz=\frac{1}{r}\frac{\partial F}{\partial r}$$

$$\int_0^L \frac{\partial^2 T}{\partial z^2}\cos\frac{\pi nz}{L}\,dz=\frac{\partial^2}{\partial z^2}\int_0^L T\cos\frac{\pi nz}{L}\,dz=-\left(\frac{\pi n}{L}\right)^2 F$$

$$\therefore \frac{\partial^2 F}{\partial r^2}+\frac{1}{r}\frac{\partial F}{\partial z}-a^2F=-Ar^2\frac{2L^3\cos\pi n}{(\pi n)^2} \tag{4-69}$$

$$\therefore \frac{\partial^2 F}{\partial r^2}+\frac{1}{r}\frac{\partial F}{\partial z}-a^2F=-Ar^2\frac{2L^3(-1)^n}{(\pi n)^2}$$

$$\therefore \frac{\partial^2 F}{\partial r^2}+\frac{1}{r}\frac{\partial F}{\partial z}-a^2F=\beta_n r^2 \tag{4-70}$$

Where, $\beta_n=-\dfrac{2AL^3(-1)^n}{(\pi n)^2}$

4.4.2 EFFECT OF TEMPERATURE ON MATERIAL PROPERTIES

The effect of temperature on the mechanical properties of steel is well studied in the literature. From a lot of results presented in different works regarding the laws adopted in the analysis of steel elements and structure, thermo-mechanical response at high temperature are studied. This factor is important to the applications like a gas turbine, steam turbine where the rotor operates at high temperature. Based on the literature study, there are two conditions exists for the change in the Young's Modulus and Poisson's Ratio for a given temperature range [28].

4.4.2.1 EFFECT OF TEMPERATURE ON YOUNG'S MODULUS

The change in the young's modulus based on the temperature range is as given below [28],

a) The change in the modulus of elasticity when the operating temperature is in between $20^{o}C$ and $600^{o}C$,

$$\frac{E_t}{E} = 1.0 + \frac{T}{2000\ln\left(\frac{T}{1100}\right)} \tag{4-71}$$

b) The change in the modulus of elasticity when the operating temperature is in between $600^{o}C$ and $1000^{o}C$,

$$\frac{E_t}{E} = \frac{690 - 0.69T}{T - 53.5} \tag{4-72}$$

Where,

E_t is Young's Modulus at temperature T °C;

E is Young's modulus at a temperature $20^{o}C$

4.4.2.2 EFFECT OF TEMPERATURE ON POISSON'S RATIO

Similarly, change in the Poisson's ratio based on the temperature range is as given below [28],

a) The change in the Poisson's ratio when the operating temperature is in between $20^{o}C$ and $450^{o}C$,

$$\nu(T) = 0.283 + 3.78 \times 10^{-5} T \quad (4\text{-}73)$$

b) The change in the Poisson's ratio when the operating temperature is above $450^{o}C$,

$$\nu(T) = 0.259 + 9.2 \times 10^{-5} T \quad (4\text{-}74)$$

Where,

$\nu(T)$ is the Poisson's ratio at temperature T°C.

Summary of the change in Young's Modulus and Poisson's ratio with temperature is plotted and as shown in Figure 4-7.

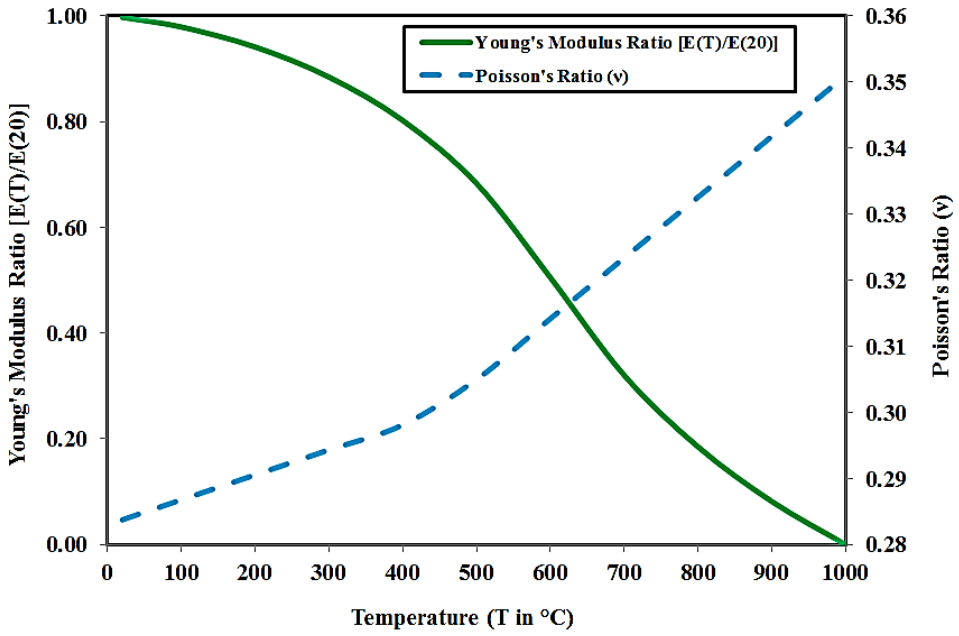

Figure 4-7 Effect of Temperature on Young's Modulus and Poisson's ratio

Due to the change in the material properties, the stiffness of the shaft material changes which affects the whirling speed and critical speed of the rotor.

4.5 INFLUENCE OF OPERATING TEMPERATURE

Temperature plays an important role in the rotor whirl speeds. In most of the applications, the temperature of the rotor is high due to operating condition and continuous rotation of the rotor. The effect of the temperature is predominant on the material properties

like modulus of elasticity and Poisson's ratio which in turn affects the stiffness of the rotor. Based on the previous derivations, the equation of motion can be extended to include temperature effects.

4.5.1 EQUATIONS OF MOTION IN INERTIAL REFERENCE FRAME

The equations of motion are developed to consider the operating temperature effect.

From equations (3-19) and (3-20),

Φ is a function of κ

$\therefore \Phi = f(\kappa)$

κ is a function of ν

$\therefore k = f(\nu)$

$\therefore \Phi = f(\nu)$

Therefore, the below matrices are expressed as a function of ν and E,

$M_T^e = f(\Phi); \therefore M_T^e = f(\nu)$

$M_R^e = f(\Phi); \therefore M_R^e = f(\nu)$

$K_B^e = f(\Phi, E); \therefore K_B^e = f(\nu, E)$

$K_C^e = f(\Phi, E); \therefore K_C^e = f(\nu, E)$

$G^e = f(\Phi); \therefore G^e = f(\nu)$

By considering the operating temperature, translatory mass matrix $[M_T^e]$, rotational mass matrix $[M_R^e]$, gyroscopic matrix $[G^e]$, stiffness matrix $[K_B^e]$ and circulatory stiffness matrix $[K_C^e]$ are transformed into $[M_{Tt}^e]$, $[M_{Rt}^e]$, $[G_t^e]$, $[K_{Bt}^e]$ and $[K_{Ct}^e]$ respectively.

The above equation of motion is extended to include the temperature effects in fixed frame of reference frame as,

$$[[M_{Tt}^e] + [M_{Rt}^e]]\{\ddot{\bar{q}}_n^f\} + [\eta_v[K_{Bt}^e] - \Omega[G_t^e]]\{\dot{\bar{q}}_n^f\} + [\eta_a[K_{Bt}^e] + \eta_b[K_{Ct}^e]]\{\bar{q}_n^f\} = \{\bar{F}_n^f\} \quad (4\text{-}75)$$

Where,

$$\left[M_{Tt}^{e}\right]=\left[M_{Tt}\right]_0+\Phi\left[M_{Tt}\right]_1+\Phi^2\left[M_{Tt}\right]_2;$$

$$\left[M_{Rt}^{e}\right]=\left[M_{Rt}\right]_0+\Phi\left[M_{Rt}\right]_1+\Phi^2\left[M_{Rt}\right]_2;$$

$$[K_{Bt}^{e}]=[K_{Bt}]_0+\Phi[K_{Bt}]_1;$$

$$\left[G_{t}^{e}\right]=\left[G_{t}\right]_0+\Phi\left[G_{t}\right]_1+\Phi^2\left[G_{t}\right]_2;$$

$$\Phi_t=\frac{12E_tI}{\kappa_tAGL^2};$$

$$k_t=\frac{6(1+\nu_t)\left(1+\left(\frac{d}{D}\right)^2\right)^2}{(7+6\nu_t)\left(1+\left(\frac{d}{D}\right)^2\right)^2+(20+12\nu_t)\left(\frac{d}{D}\right)^2}$$

The details about the above all matrices are presented in the appendix.

4.5.2 EQUATIONS OF MOTION IN WHIRL REFERENCE FRAME

Converting the above equation (4-75) into rotating coordinate system and simplifying,

$$\left[\left[M_{Tt}^{e}\right]+\left[M_{Rt}^{e}\right]\right]\left\{\ddot{\bar{q}}_n^r\right\}+\left[\eta_v\left[K_{Bt}^{e}\right]+\omega\left[2\left[\hat{M}_{Tt}^{e}\right]+(1-\gamma)\left[G_t^{e}\right]\right]\right]\left\{\dot{\bar{q}}_n^r\right\}$$
$$+\left[\eta_a\left[K_{Bt}^{e}\right]+\eta_b\left[K_{Ct}^{e}\right]-\omega\eta_v\left[K_{Ct}^{e}\right]-\omega^2\left[\left[M_{Tt}^{e}\right]+(1-2\gamma)\left[M_{Rt}^{e}\right]\right]\right]\left\{\bar{q}_n^r\right\}=\left\{\bar{F}_n^f\right\} \qquad (4\text{-}76)$$

The details about the above all matrices are presented in the appendix.

4.6 MODELLING OF EXTERNAL VISCOUS DAMPING

External damping refers to the damping in the bearings. Different types of bearings are used in different applications based on the loads, operating speed and temperature. These bearings are broadly classified as antifriction bearing and sleeve bearing. The damping present in the antifriction bearings is small and can be neglected for most of the rotor dynamic analysis, e.g. ball and roller bearings. Sleeve/journal bearings are used in large gas and steam

turbines. These are hydrodynamic bearings. These bearings are having the large load carrying capacity and can operate at high speeds. This applications or situation can be considered as external viscous damping.

The damping present in the sleeve bearings is considerable and this is the important parameter in damping of the rotor vibrations. The energy is dissipated due to friction occurring between stationary and rotating elements, and/or fluid dynamic resistance in the rotor environment.

A viscous damper can be constructed using sleeve/journal bearing having A is the surface area of the rotating surface with a fluid of viscosity μ as shown in the following Figure 4-8.

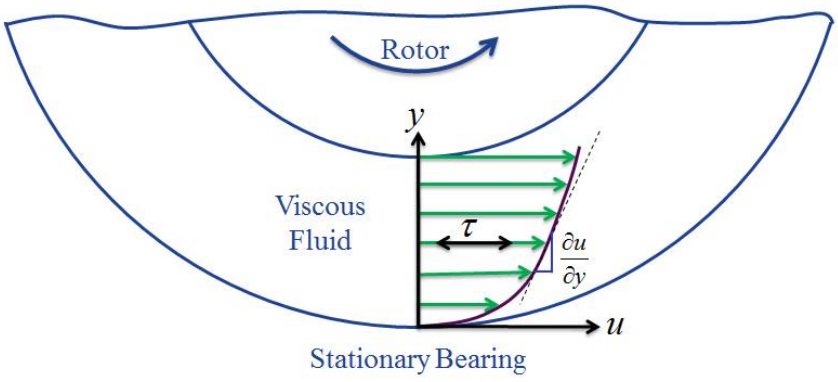

Figure 4-8 External Viscous Damping (Bearing) Model

As per Newton's Laws of viscous flow, the shear stress τ developed in the fluid layer is given as,

$$\tau = \mu \frac{\partial u}{\partial y} \tag{4-77}$$

The shear or resisting force F is expressed as,

$$F = \tau A = \mu A \frac{\partial u}{\partial y} \tag{4-78}$$

For the linear viscous damping model, the above equation can be modified and given as,

$$F = \mu A \frac{u}{y}$$

$$\therefore F = C_e u \quad \because C_e = \frac{\mu A}{y} \tag{4-79}$$

Where, C_e is the external linear viscous damping.

There are different types of fluids broadly classified as Newtonian and Non – Newtonian fluids. Following Figure 4-9 gives an idea about the behavior of the different types of fluids and their behavior.

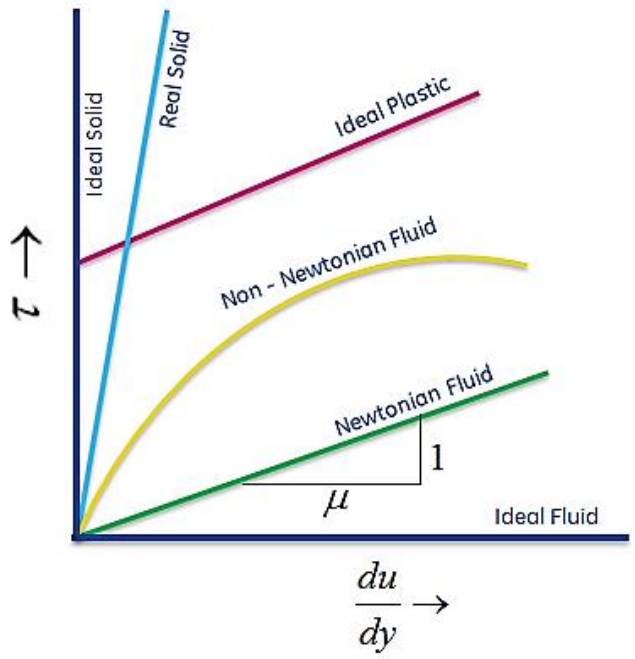

Figure 4-9 Different types of fluids and solids

The equation of motion with external viscous damping is represented as,

$$m\ddot{x} + c_e\dot{x} + kx = 0 \tag{4-80}$$

Where, m, c_e and k represents the mass, viscous damping coefficient and stiffness of the system respectively. The solution of the above equation (4-80) will be,

$$x = C_1 e^{s_1 t} + C_2 e^{s_2 t} \tag{4-81}$$

Where, C_1 and C_2 are the two arbitrary constants to be determined from the initial conditions.

$$s_{1,2} = -\frac{c}{2m} \pm \sqrt{\left(\frac{c}{2m}\right)^2 - \frac{k}{m}} \qquad \because \frac{c}{2m} = \zeta.\omega_n; \qquad \frac{c}{c_0} = \zeta; \qquad \frac{k}{m} = \omega_n^{\,2}$$

$$\therefore s_{1,2} = \left(-\zeta \pm \sqrt{\zeta^2 - 1}\right)\omega_n \tag{4-82}$$

Where, ζ, c_0 and ω_n are the damping ratio, critical damping and natural frequency respectively. There are three different systems and solutions based on the damping ratio ζ.

a. Over damped system,

$$x = C_1 e^{\left(-\zeta+\sqrt{\zeta^2-1}\right)\omega_n t} + C_2 e^{\left(-\zeta-\sqrt{\zeta^2-1}\right)\omega_n t} \tag{4-83}$$

b. Critically damped system,

$$x = (C_1 + C_2 t) e^{-\omega_n t} \tag{4-84}$$

c. Under damped system,

$$x = C_1 e^{\left(-\zeta+i\sqrt{1-\zeta^2}\right)\omega_n t} + C_2 e^{\left(-\zeta-i\sqrt{1-\zeta^2}\right)\omega_n t} \tag{4-85}$$

4.7 INFLUENCE OF EXTERNAL VISCOUS DAMPING

Damping elements are mechanical elements which dissipate energy and usually combined with rotor models. The commonly used dampers are velocity proportional. Hence the equation of motion can be extended to incorporate the external viscous damping. The classical linearized bearing model are assumed to follow the governing equations of the following form,

$$[C_b]\{\dot{\bar{q}}_n^{\,f}\} + [K_b]\{\bar{q}_n^{\,f}\} = \{\bar{F}_b^{\,f}\} \tag{4-86}$$

$$\therefore \begin{bmatrix} C_{xx} & C_{xy} \\ C_{yx} & C_{yy} \end{bmatrix} \{\dot{\bar{q}}_n^{\,f}\} + \begin{bmatrix} K_{xx} & K_{xy} \\ K_{yx} & K_{yy} \end{bmatrix} \{\bar{q}_n^{\,f}\} = \{\bar{F}_b^{\,f}\} \tag{4-87}$$

Where, C_{xx}, C_{yy} are the direct damping coefficients and C_{xy}, C_{yx} are the cross-coupled damping coefficients. K_{xx}, K_{yy} are the direct stiffness coefficients and K_{xy}, K_{yx} are the cross-coupled stiffness coefficients.

Bearings are classified as sleeve / journal bearings and anti-friction / rolling element bearings.

- Sleeve Bearings: The damping coefficients and stiffness coefficients are calculated based on the radial load on the bearing, rotor spin speed, oil temperature and viscosity.
- Anti-friction Bearing: The damping is assumed as negligible. The stiffness coefficients are calculated based on the radial load on the bearings.

4.8 SUMMARY

In this chapter, the formulation is done on different forms of damping and operating temperature. The equations of motion are developed with the incorporation of the above damping and operating temperature in a fixed frame or inertial frame of reference and rotating frame or whirl frame of reference. This equation takes care of different forms of damping viz., internal viscous damping, internal hysteretic damping, external viscous damping and operating temperature either independently or simultaneously acting together. The finalized equations (4-75) and (4-87) are considered for the simulations.

CHAPTER 5

COMPUTATIONAL SCHEME AND MODEL VALIDATION

Based on the dynamic model developed in the previous chapter, a computational scheme is developed and validated. The rotor is discretized into finite elements and equations of motion are obtained at element level and these equations are assembled. Equations of motion are obtained at the assembly level. All the forms of damping viz. internal viscous damping, internal hysteretic damping, external viscous damping and operating temperature are introduced into the equations of motion. A simulation scheme is developed to compute forward whirl, backward whirl and critical speeds. Time domain equations are taken into state space for further simulations.

5.1 STATE SPACE FORMULATION

A state space formulation is used to decouple the high order differential equations into the simpler low order equivalents 18]. The set of first order differential equations are related to inputs and outputs of a system by a variable called the state.

The equations of motion is in simplified form is expressed in fixed frame of reference from the equation (4-75),

$$\left[M_{st}^{f}\right]\left\{\ddot{\bar{q}}_{n}^{f}\right\}+\left[C_{st}^{f}\right]\left\{\dot{\bar{q}}_{n}^{f}\right\}+\left[K_{st}^{f}\right]\left\{\bar{q}_{n}^{f}\right\}=\left\{\bar{F}_{n}^{f}\right\} \qquad (5\text{-}1)$$

For the computation of whirl speeds of the rotor bearing system, the homogeneous equation is obtained with the force term zero.

$$\left[M_{st}^{f}\right]\left\{\ddot{\bar{q}}_{n}^{f}\right\}+\left[C_{st}^{f}\right]\left\{\dot{\bar{q}}_{n}^{f}\right\}+\left[K_{st}^{f}\right]\left\{\bar{q}_{n}^{f}\right\}=\{0\} \qquad (5\text{-}2)$$

where,

$\left[M_{st}^{f}\right]=\left[M_{Tt}^{e}\right]+\left[M_{Rt}^{e}\right]$;

$\left[C_{st}^{f}\right]=\eta_v\left[K_{Bt}^{e}\right]-\Omega\left[G_{t}^{e}\right]$ and

$\left[K_{st}^{f}\right]=\eta_a\left[K_{Bt}^{e}\right]+\eta_b\left[K_{Bt}^{e}\right]$

For the ease of computation of eigenvalues and eigenvectors, the homogeneous part of the system equations of motion can be written in the first order state vector form as,

$$[A]\{\dot{h}\}+[B]\{h\}=\{0\} \qquad (5\text{-}3)$$

Where,

$$[A]=\begin{bmatrix}[0] & \left[M_{st}^{f}\right]\\ \left[M_{st}^{f}\right] & \left[C_{st}^{f}\right]\end{bmatrix};$$

$$[B]=\begin{bmatrix}-\left[M_{st}^{f}\right] & [0]\\ [0] & \left[K_{st}^{f}\right]\end{bmatrix} \text{ and}$$

$$\{h\}=\begin{Bmatrix}\{\dot{q}\}\\ \{q\}\end{Bmatrix}$$

The associated eigenvalue problem is sought from an assumed solution form as,

$\{h\}=\{h_0\}e^{\beta t}$ and

$\{\dot{h}\}=\beta\{h_0\}e^{\beta t}$

Substituting the above solution in the equations of motion,

$$\beta[A]\{h_0\}e^{\beta t}+[B]\{h_0\}e^{\beta t}=\{0\} \qquad (5\text{-}4)$$

The eigenvalue problem becomes,

$$[D]\{h_0\}=\frac{1}{\beta}\{h_0\} \qquad \because [D]=[B]^{-1}[A] \qquad (5\text{-}5)$$

Where,

$\beta=\lambda\pm i\omega$ is the complex eigenvalue.

and ω is the whirl natural frequency.

The eigenvalues from the above equation give the natural whirl frequencies. There are two natural frequencies for each mode, one always positive and the other negative. The positive and negative natural frequencies are known to be associated with forward whirl speed and backward whirl speed respectively.

5.2 COMPUTATIONAL PROCEDURE

The mass, stiffness, damping and gyroscopic matrices are constructed using the models developed in the previous chapter. Elemental equations are assembled using the compatibility and the system matrices are obtained. The eigenvalues problem is solved for every rotational speed using state space solution methodology. From the eigenvalue of the system, the forward and backward whirl speeds are obtained for every spin speed. The whirl frequencies are plotted against the shaft spin speed. The different inputs are mentioned below.

- The geometrical parameters are the physical dimensions of the rotor like inner diameter, outer diameter and length of the shaft. It also includes the material properties like young’s modulus, Poisson's ratio and shear modulus.
- Critical parameters are internal viscous damping, internal hysteretic damping, external viscous damping and operating temperature.
- The additional input is rotor spin speed.

The outline of this methodology is presented in the form of the flow chart in Figure 5-1.

Based on this computational scheme, a program is developed in Mathcad environment. This program is capable of considering different forms of damping and operating temperature either independently or simultaneously acting together.

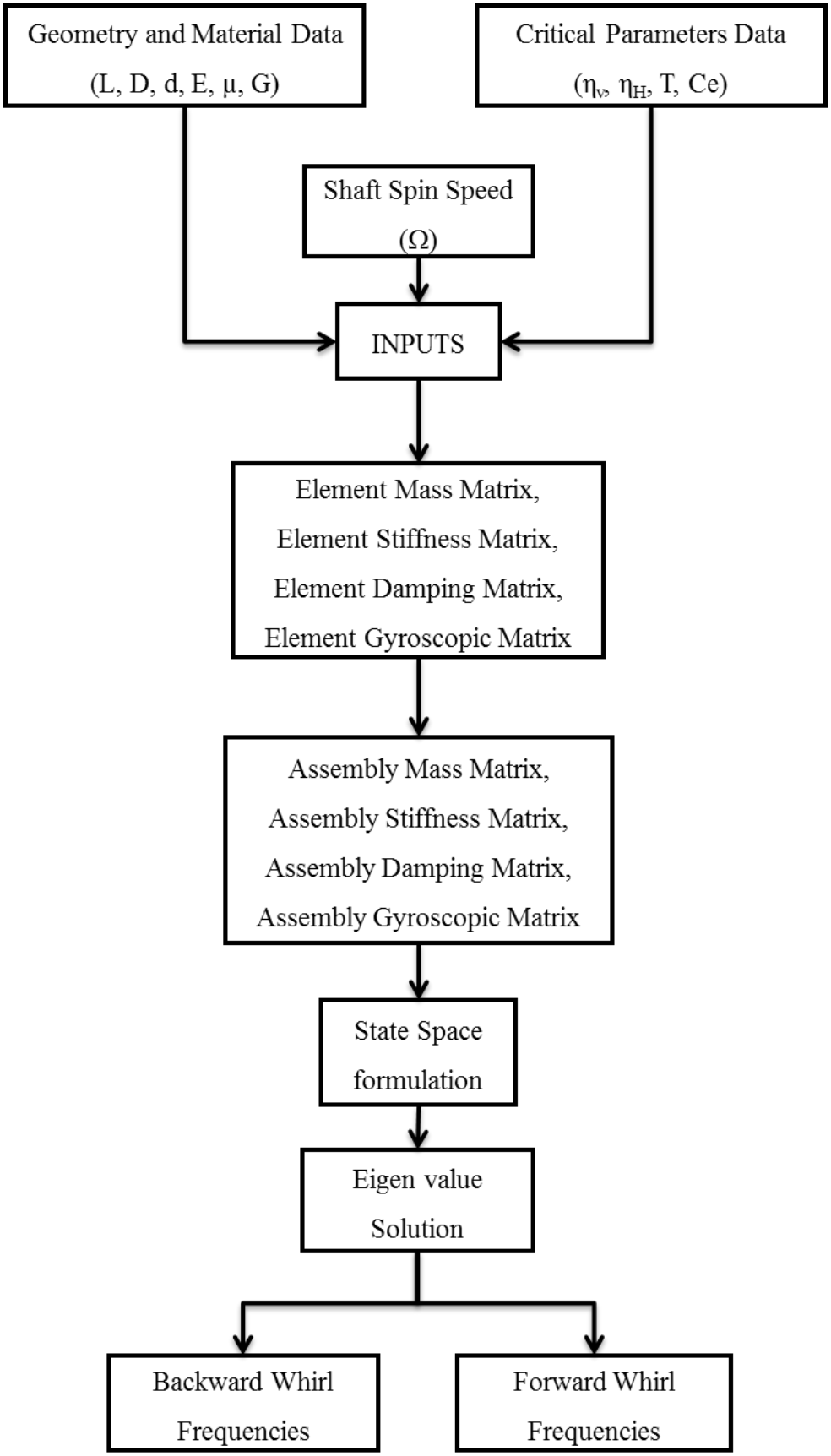

Figure 5-1 Flow Chart for Solution Procedure

5.3 CAMPBELL DIAGRAM

Campbell diagram is plotted with the whirl speeds / frequencies on ordinate and rotor spin speed on abscissa. This is used to find out the critical speeds of rotor. The intersection point of synchronous whirl excitation (SWE) and whirl speeds give the critical speed which is shown in Figure 5-2.

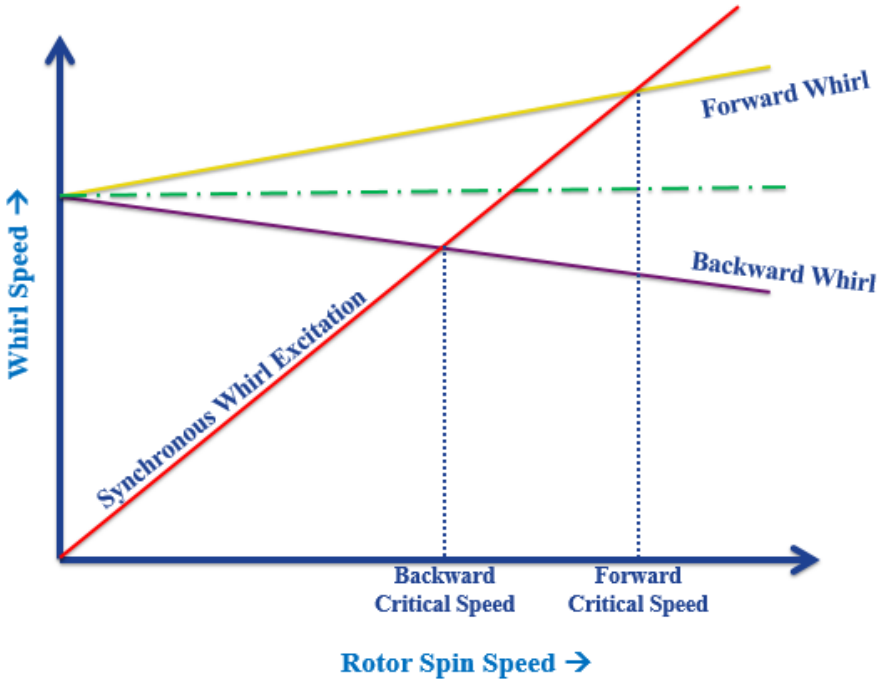

Figure 5-2 Campbell Diagram

5.4 FINITE ELEMENT CODE VALIDATION

The finite element code is validated for first four mode shapes with the computational scheme mentioned in the previous section. The numerical example available in the literature is being considered for the model validation as a case study. The shaft is supported on the sleeve or fluid film journal bearings at both ends. The bearings are modelled as stiffness coefficients and damping coefficients.

5.4.1 CASE STUDY

A simply supported shaft studied by Glasgow, D. A. and Nelson, H. D. [13] with hydrodynamic bearings is considered as a case study. The system consists of a 10.16 cm

diameter and 127 cm long steel shaft supported by identical bearings of stiffness $K_{xx} = K_{yy} =$ 1.7513 x10^7 N/m. The elastic modulus, modulus of rigidity and density of the shaft are 2.068 x10^{11} N/m^2, 0.79x10^{11} N/m^2 and 7833 kg/m^3 respectively. The schematic diagram about the shaft with bearings is shown in Figure 5-3.

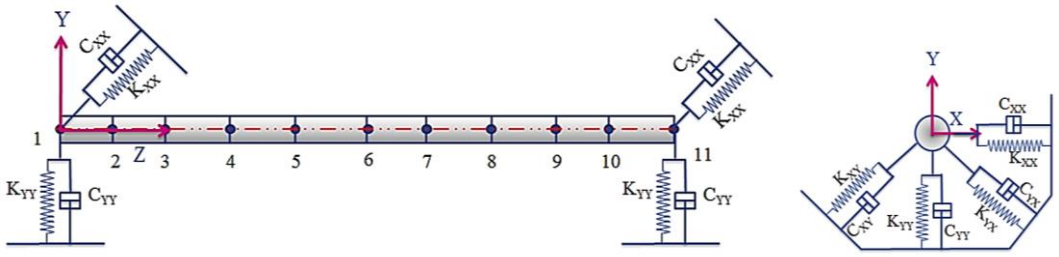

Figure 5-3 Finite Element Model of Shaft with Bearings

The results are available for a few cases in the literature. The model is validated with the available case studies as below.

5.4.2 UNDAMPED OR BASELINE CASE STUDY

This case study includes a shaft with bearing stiffness only. It does not include internal viscous damping (η_v), internal hysteretic damping (η_H), operating temperature (T) and external viscous damping (C_e).

Suppressing the operating temperature and different forms of damping in equations (4-75) and (4-86),

- External viscous damping, $C_{xx} = 0$, $C_{yy} = 0$, $C_{xy} = 0$ and $C_{yx} = 0$
- Internal viscous damping, $\eta_v = 0$
- Internal hysteretic damping, $\eta_H = 0$

$$\therefore \eta_a = \frac{1+\eta_H}{\sqrt{1+\eta_H{}^2}} = 1; \text{ and } \therefore \eta_b = \frac{\eta_H}{\sqrt{1+\eta_H{}^2}} + \eta_v \Omega = 0$$

The equations of motion for undamped or baseline becomes,

$$\left[\left[M_T^e\right] + \left[M_R^e\right]\right]\left\{\ddot{\bar{q}}_n^f\right\} - \Omega\left[G^e\right]\left\{\dot{\bar{q}}_n^f\right\} + \left[K_B^e\right]\left\{\bar{q}_n^f\right\} = \left\{\bar{F}_n^f\right\} \qquad (5\text{-}6)$$

This case study simulates the condition of the ideal undamped rotor. The backward whirl speeds and forward whirl speeds (rad/sec) are calculated for first four modes at constant rotor spin speed of 4000 rpm and compared with the published data. The percentage error between present work and published data is calculated. The results are tabulated and compared with published data in Table 5-1.

Table 5-1 Whirl speeds (rad/sec) at rotor spin speed of 4000 (rpm)

Mode	Published Data [13]	Present Work	% Error
1st BW	520.46	518.97	0.29 %
1st FW	521.02	519.61	0.27 %
2nd BW	1093.20	1091.07	0.19 %
2nd FW	1096.70	1094.27	0.22 %
3rd BW	2237.80	2223.13	0.66 %
3rd FW	2253.10	2236.45	0.74 %
4th BW	5058.10	4931.31	2.51 %
4th FW	5093.40	4961.18	2.60 %

The Very close agreement is observed between the published data and present work.

5.4.3 INTERNAL VISCOUS DAMPING CASE STUDY

This case study includes only internal viscous damping (η_v). It does not include internal hysteretic damping (η_H), operating temperature (T) and external viscous damping (C_e) Suppressing the operating temperature and different forms of damping in equations (4-75) and (4-86),

- External viscous damping, $C_{xx}=0$, $C_{yy}=0$, $C_{xy}=0$ and $C_{yx}=0$
- Internal hysteretic damping, $\eta_H=0$

$$\therefore \eta_a=\frac{1+\eta_H}{\sqrt{1+\eta_H{}^2}}=1; \text{ and } \therefore \eta_b=\frac{\eta_H}{\sqrt{1+\eta_H{}^2}}+\eta_v\Omega=\eta_v\Omega$$

The equations of motion for internal viscous damping becomes,

$$\left[\left[M_T^e\right]+\left[M_R^e\right]\right]\left\{\ddot{\bar{q}}_n^f\right\}+\left[\eta_v\left[K_B^e\right]-\Omega[G]\right]\left\{\dot{\bar{q}}_n^f\right\}+\left[\left[K_B^e\right]+\eta_v\Omega\left[K_C^e\right]\right]\left\{\bar{q}_n^f\right\}=\left\{\bar{F}_n^f\right\} \quad (5\text{-}7)$$

This case study simulates the condition of the internal viscous damped rotor. The backward whirl speeds and forward whirl speeds (rad/sec) are calculated for first four modes at constant rotor spin speed of 4000 rpm and compared with the published data. The percentage error between present work and published data is calculated. The results are tabulated and compared with published data as shown in Table 5-2.

Table 5-2 Whirl speeds (rad/sec) for η_v = 0.0002 s, at rotor spin speed of 4000 (rpm)

Mode	Published Data [13]	Present Work	% Error
1st BW	521.01	519.62	0.27 %
1st FW	522.74	521.31	0.27 %
2nd BW	1096.60	1094.94	0.15 %
2nd FW	1097.40	1094.96	0.22 %
3rd BW	2214.60	2201.35	0.60 %
3rd FW	2230.90	2215.00	0.71 %
4th BW	4454.50	4379.38	1.69 %
4th FW	4492.00	4411.65	1.79 %

The very close agreement is observed between the published data and present work.

5.4.4 INTERNAL HYSTERETIC DAMPING CASE STUDY

This case study includes only internal hysteretic damping (η_H). It does not include internal viscous damping (η_v), operating temperature (T) and external viscous damping (C_e). Suppressing the operating temperature and different forms of damping in equations (4-75) and (4-86),

- External viscous damping, $C_{xx}=0$, $C_{yy}=0$, $C_{xy}=0$ and $C_{yx}=0$
- Internal viscous damping, $\eta_v=0$

$$\therefore \eta_a=\frac{1+\eta_H}{\sqrt{1+\eta_H^{\,2}}}\text{; and } \therefore \eta_b=\frac{\eta_H}{\sqrt{1+\eta_H^{\,2}}}+\eta_v\Omega=\frac{\eta_H}{\sqrt{1+\eta_H^{\,2}}}$$

The equations of motion for internal hysteretic damping becomes,

$$\left[\left[M_T^e\right]+\left[M_R^e\right]\right]\left\{\ddot{\bar{q}}_n^f\right\}-\Omega\left[G^e\right]\left\{\dot{\bar{q}}_n^f\right\}+\left[\frac{1+\eta_H}{\sqrt{1+\eta_H^2}}\left[K_B^e\right]+\frac{\eta_H}{\sqrt{1+\eta_H^2}}\left[K_C^e\right]\right]\left\{\bar{q}_n^f\right\}=\left\{\bar{F}_n^f\right\} \quad (5\text{-}8)$$

This case study simulates the condition of the internal hysteretic damped rotor. The backward whirl speeds and forward whirl speeds (rad/sec) are calculated for first four modes at constant rotor spin speed of 4000 rpm and compared with the published data. The percentage error between present work and published data is calculated. The results are tabulated and compared as shown in Table 5-3.

Table 5-3 Whirl Speeds (rad/sec) for η_H = 0.0002, at rotor spin speed of 4000 (rpm)

Mode	Published Data [13]	Present Work	% Error
1st BW	520.48	518.99	0.29 %
1st FW	521.04	519.63	0.27 %
2nd BW	1093.20	1091.08	0.19 %
2nd FW	1096.70	1094.28	0.22 %
3rd BW	2238.00	2223.27	0.66 %
3rd FW	2253.20	2236.59	0.74 %
4th BW	5058.60	4931.77	2.51 %
4th FW	5093.90	4961.64	2.60 %

The very close agreement is observed between the published data and present work.

5.4.5 CONCLUSION

The dynamic model is validated with the published data for the undamped rotor, internal viscous damping and internal hysteretic damping cases as an independent critical parameter alone. The Very close agreement is observed between the present finite element solution and the results of published data.

5.5 ELEMENT CONVERGENCE

Element convergence is done to decide the optimum number of elements for finite element code which can be used for further simulations. In order to illustrate the accuracy of the finite element program developed, the numerical example mentioned case study 5.4.1 is considered.

Element convergence is done with different element combinations. Results are summarized in Table 5-4.

Table 5-4 Whirl Speeds (rad/sec) with respect to Number of Elements

Number of Elements	1st Mode		2nd Mode		3rd Mode		4th Mode	
	BW	FW	BW	FW	BW	FW	BW	FW
2	520.2	520.8	1100.3	1103.8	2233.8	2248.4	5699.5	5736.2
4	519.1	519.7	1092.0	1095.3	2229.9	2243.9	4987.1	5018.7
6	519.0	519.6	1091.3	1094.5	2225.1	2238.5	4950.5	4980.9
8	519.0	519.6	1091.1	1094.3	2223.7	2237.0	4937.2	4967.1
10	519.0	519.6	1091.1	1094.3	2223.1	2236.4	4931.3	4961.2

Results are also shown in Figure 5-4, Figure 5-5, Figure 5-6 and Figure 5-7 where the abscissa shows the number of elements and ordinate shows the backward whirl speeds and forward whirl speeds in rad/sec.

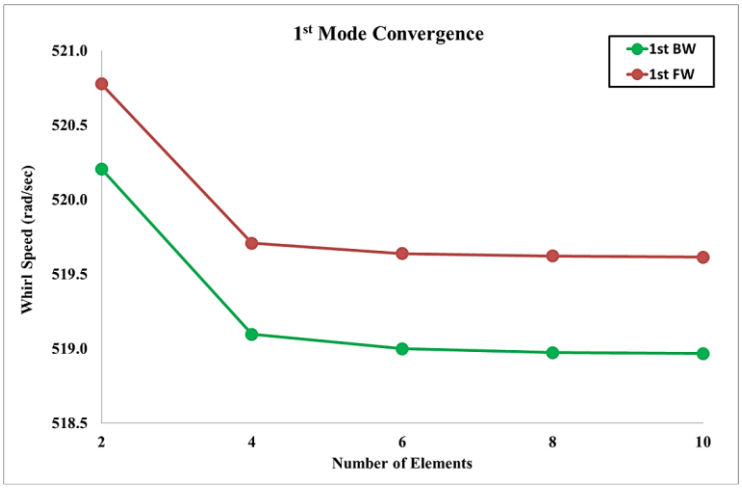

Figure 5-4 BW and FW Speed w. r.t. Number of Elements for 1st Mode

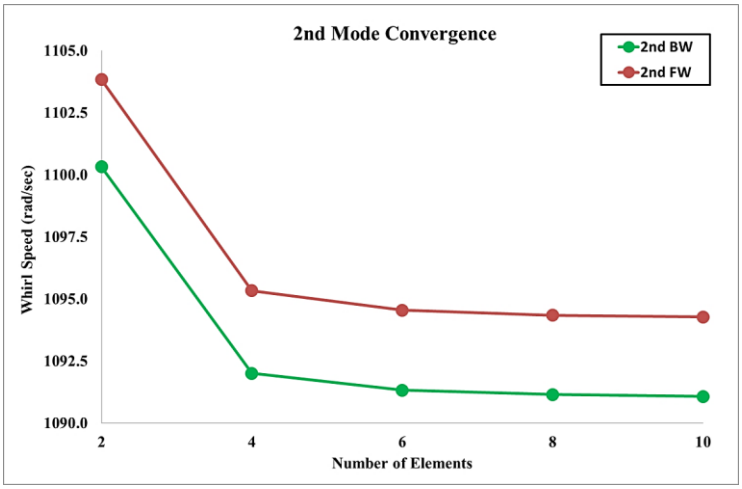

Figure 5-5 BW and FW Speed w. r.t. Number of Elements for 2nd Mode

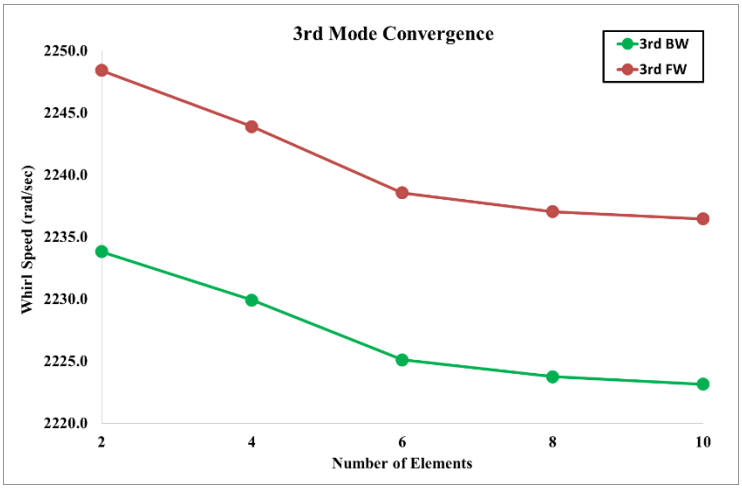

Figure 5-6 BW and FW Speed w. r.t. Number of Elements for 3rd Mode

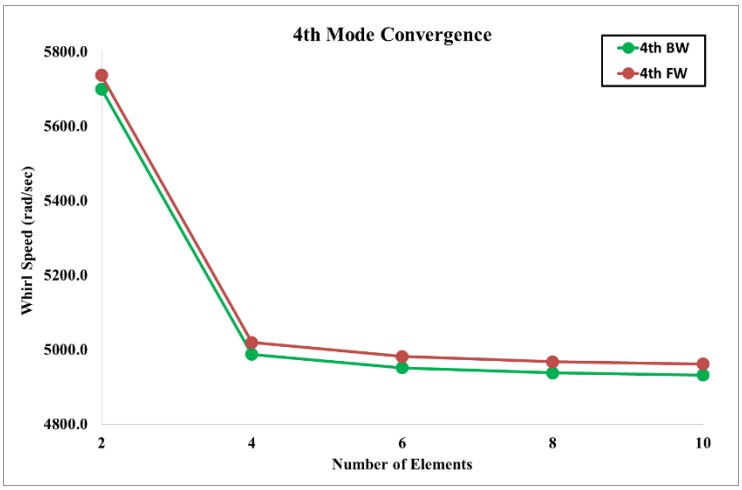

Figure 5-7 BW and FW Speed w. r.t. Number of Elements for 4th Mode

This study is conducted with a different number of elements for making a convergence test and offers the solution accuracy for several elements used in the system simulation. Based on the above study, the optimum number of elements arrived as ten elements. These numbers of elements are used for further simulations.

CHAPTER 6

STUDY ON INDIVIDUAL INFLUENCE OF PARAMETERS ON WHIRLING SPEEDS OF ROTOR

The dynamic model is validated with published data in the previous chapter. In this chapter, the influence of different forms of damping viz., internal viscous damping, internal hysteretic damping, external viscous damping and operating temperature are discussed. The main intension of this chapter is to understand the behavior of the rotor with different forms of damping and operating temperatures acting independently. Computations are done to predict the forward whirl, backward whirl and critical speeds. Influence of each critical parameter on the whirl speeds is studied and concluded.

6.1 CHANGE IN WHIRL SPEED RATIO

The new non-dimensionless term is defined as the 'change in whirl speed ratio ΔWR.' It is the ratio of the difference between forward whirl and backward whirl at the corresponding rotor spin speed to the whirl speed at zero rotor spin speed. It is expressed in percentage as,

$$\Delta WR = \left(\frac{FW_{@rpm} - BW_{@rpm}}{BW_{@zero\_rpm}} \right) * 100 \qquad (6\text{-}1)$$

By using the above term, the influence of different critical parameters like gyroscopic effect, internal viscous damping, internal hysteretic damping, external viscous damping and operating temperature can be compared either independently or simultaneously.

6.2 CRITICAL PARAMETERS

There are different parameters which are inputs for the rotor dynamic analysis. Below are the lists of critical parameters,

- Internal Viscous Damping (η_v)
- Internal Hysteretic Damping (η_H)
- External Viscous Damping (C_e)
- Operating Temperature (T)

Based on the critical parameters, the different case studies are created.

1. Undamped / Baseline Rotor
2. Internal Viscous Damping acting alone
3. Internal Hysteretic Damping acting alone
4. External Viscous Damping acting alone
5. Operating Temperature acting alone

The above case studies are analyzed in detail as below.

6.3 BASELINE OR UNDAMPED ROTOR

This case study includes a shaft with bearing stiffness only. It does not include internal viscous damping (η_v), internal hysteretic damping (η_H), operating temperature (T) and external viscous damping (C_e). Suppressing the operating temperature and different forms of damping in equations (4-75) and (4-86),

- External viscous damping, $C_{xx}=0$, $C_{yy}=0$, $C_{xy}=0$ and $C_{yx}=0$
- Internal viscous damping, $\eta_v=0$
- Internal hysteretic damping, $\eta_H=0$

$$\therefore \eta_a=\frac{1+\eta_H}{\sqrt{1+\eta_H{}^2}}=1; \text{ and } \quad \therefore \eta_b=\frac{\eta_H}{\sqrt{1+\eta_H{}^2}}+\eta_v\Omega=0$$

The equations of motion for undamped or baseline becomes,

$$\left[\left[M_T^e\right]+\left[M_R^e\right]\right]\left\{\ddot{\bar{q}}_n^f\right\}-\Omega\left[G^e\right]\left\{\dot{\bar{q}}_n^f\right\}+\left[K_B^e\right]\left\{\bar{q}_n^f\right\}=\left\{\bar{F}_n^f\right\} \tag{6-2}$$

6.3.1 WHIRL SPEED AND CAMPBELL DIAGRAM FOR ALL MODES

Simulation is performed at different rotor spin speeds and predicted the forward whirl and backward whirl speeds for first four modes. Results are tabulated in Table 6-1 and shown in shown Figure 6-1.

Table 6-1 Whirl Speeds (rad/sec) for different rotor spin speeds

Mode	0 rpm (0 rad/sec)	2000 rpm (209.4 rad/sec)	4000 rpm (418.9 rad/sec)	6000 rpm (628.3 rad/sec)
1st BW	519.29	519.13	518.97	518.80
1st FW	519.29	519.45	519.61	519.77
2nd BW	1092.67	1091.87	1091.07	1090.27
2nd FW	1092.67	1093.47	1094.27	1095.07
3rd BW	2229.78	2226.45	2223.13	2219.82
3rd FW	2229.78	2233.11	2236.45	2239.79
4th BW	4946.23	4938.76	4931.31	4923.86
4th FW	4946.23	4953.70	4961.18	4968.67

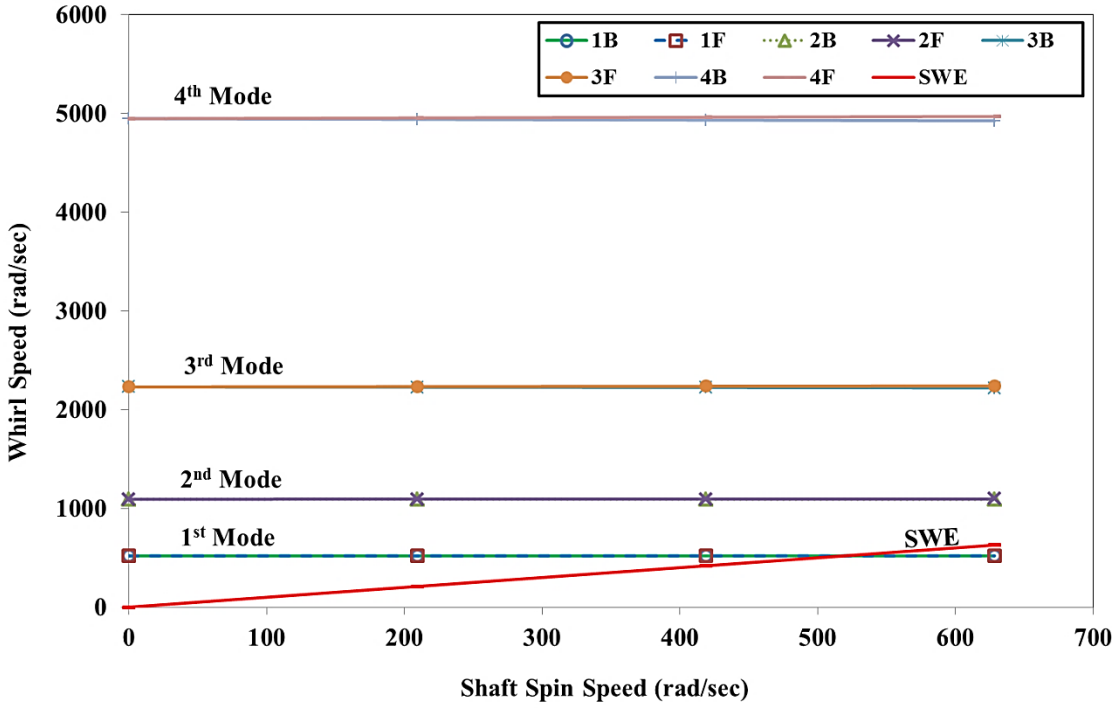

Figure 6-1 Campbell Diagram for Different Modes

Based on the results from the Table 6-1, the backward whirl speed is decreasing and forward whirl speed is increasing with increase in rotor spin speed. The more decrease in magnitude is observed for a backward whirl with higher modes and the more increase in magnitude is observed for a forward whirl with higher modes. For a given rotor synchronous whirl excitation (SWE), the excitation line is intersecting at different locations for different modes. It is shown in Figure 6-1. The intersection point at different modes is called critical speed for that mode.

6.3.2 WHIRL SPEED AND CAMPBELL DIAGRAM FOR FIRST MODE

The forward whirl speed and backward whirl speed are clearly distinguishable and the trend is opposite to each other for the first mode. The spread between backward whirl and forward whirl is increasing with increase in the rotor spin speed. The values of the first mode are plotted in Figure 6-2.

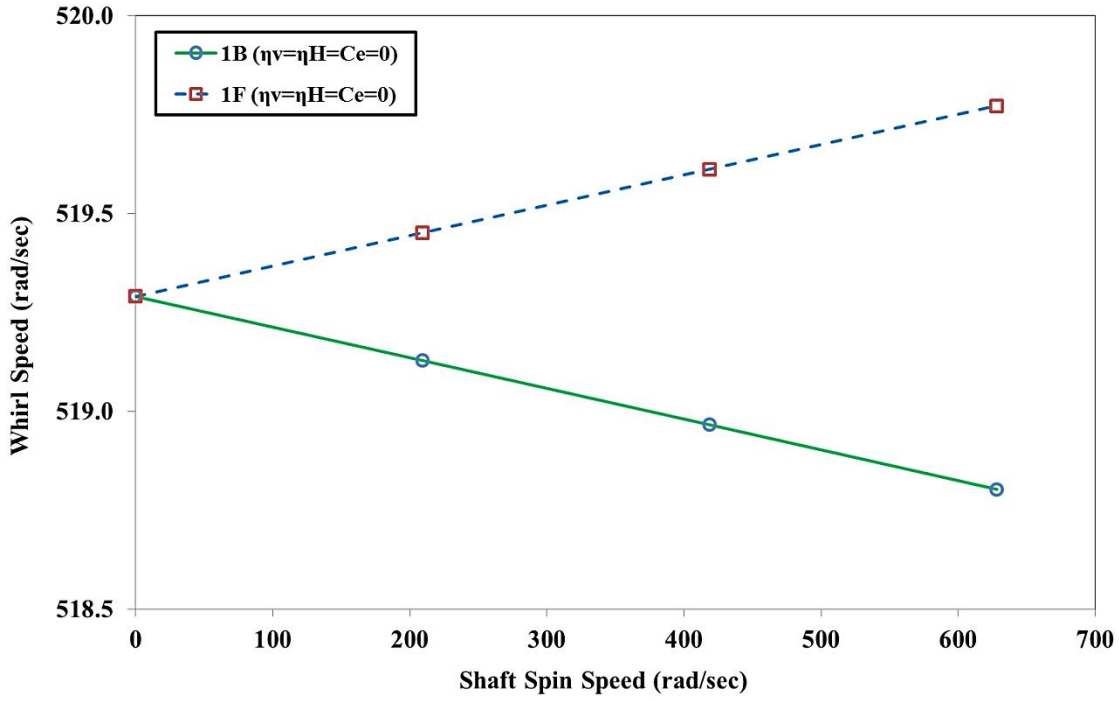

Figure 6-2 Whirl Speed Map for 1st Mode

The synchronous whirl excitation is intersecting at two different locations for the first mode. The details of intersection are shown in Figure 6-3. The range between backward critical speed and forward critical speed range is shown as ‘A’. If the rotor operating spin speed is within this range ‘A’, there will be the unbounded amplitude of vibration which results into

rotor failure. To mitigate this risk and to avoid resonance, only two options are available, either rotor should redesign in such a way that the range 'A' will get shifted from the operating rotor spin speed or operating rotor spin speed needs to change. This information is very useful in the design stage of the rotor.

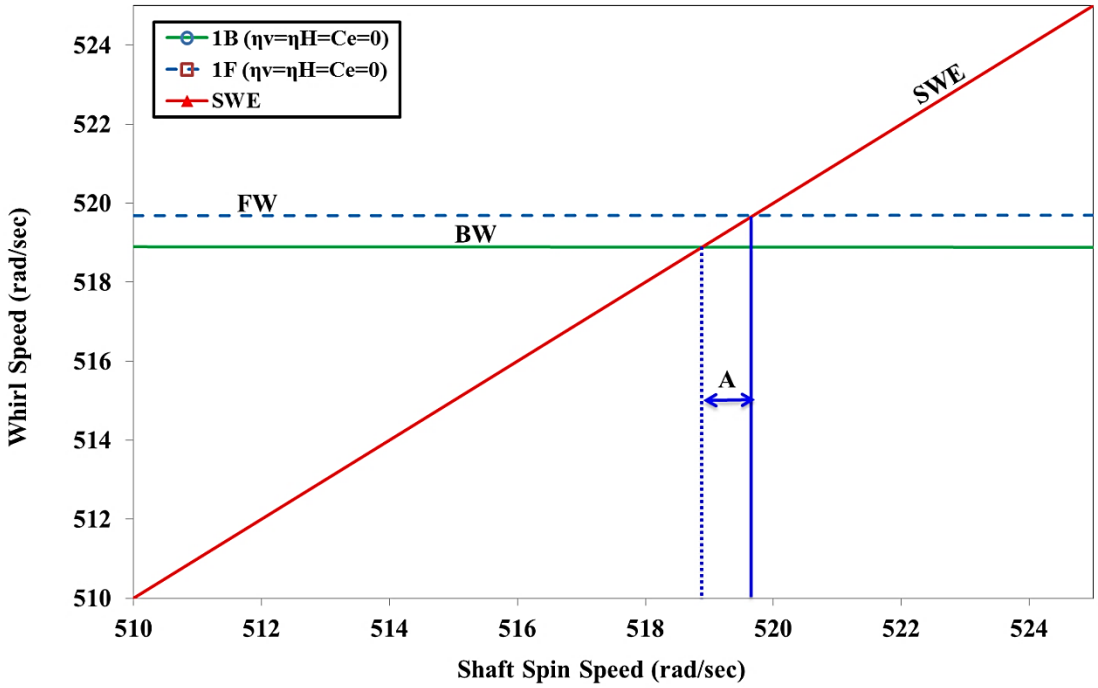

Figure 6-3 Campbell Diagram for 1st Mode

6.3.3 CHANGE IN WHIRL SPEED RATIO

The non-dimensional term 'change in whirl speed ratio' is calculated for each mode shape. The results are tabulated in Table 6-2 and shown in Figure 6-4.

Table 6-2 Change in whirl speed ratio for different rotor spin speeds

Mode	0 rpm (0 rad/sec)	2000 rpm (209.4 rad/sec)	4000 rpm (418.9 rad/sec)	6000 rpm (628.3 rad/sec)
1st Mode	0.000%	0.062%	0.125%	0.187%
2nd Mode	0.000%	0.147%	0.293%	0.440%
3rd Mode	0.000%	0.299%	0.597%	0.896%
4th Mode	0.000%	0.302%	0.604%	0.906%

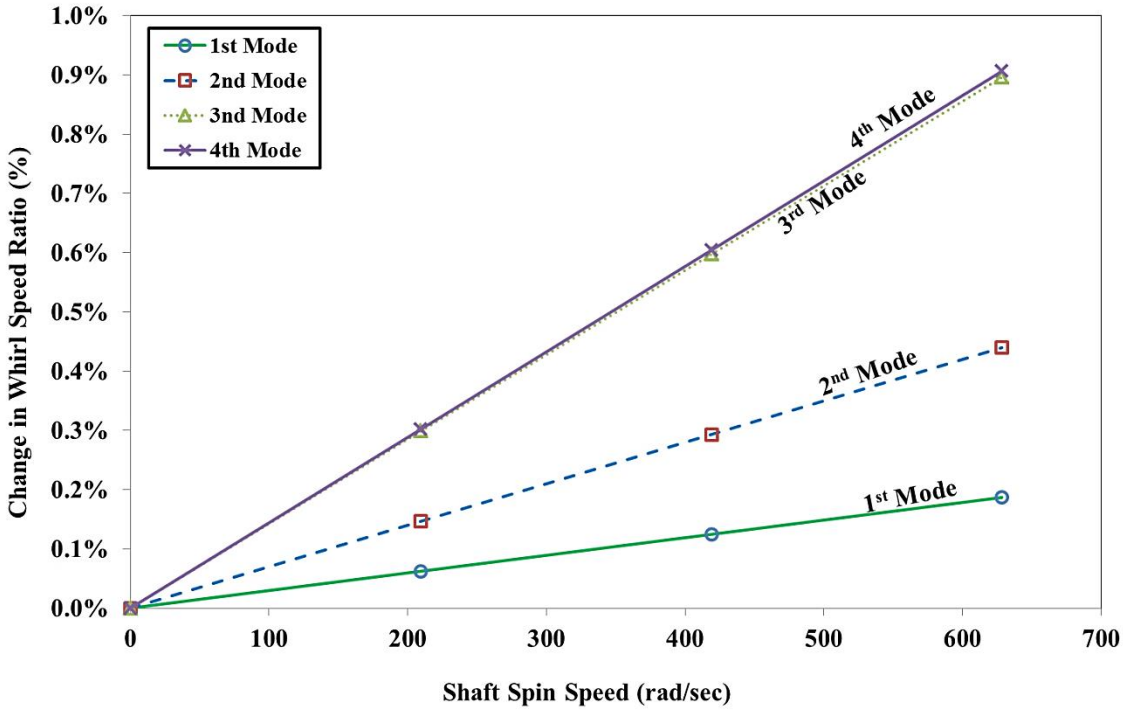

Figure 6-4 Change in Whirl Speed Ratio for Different Modes

The spread between backward whirl speed and forward whirl speed is increasing with increase in the rotor spin speed. This spread is also increasing with higher modes. This is clearly shown with the help of 'change in whirl speed ratio' in Figure 6-4. The change in the whirl speed ratio is clearly linear for all the modes. The gyroscopic effect will be predominant for higher modes.

6.3.4 CONCLUSION

As expected for the undamped rotor, the spread between forward whirl speed and backward whirl speed increases for all modes. This spread is also increasing at higher rotor spin speed. It is clearly observed in Figure 6-4 with the help of whirl speed ratio. This phenomenon is due to gyroscopic effect only. Critical speed range is plotted in Figure 6-3 with the rotor synchronous whirl excitation. A clear understanding of the undamped rotor is very important and it will be a baseline to study the influence of different forms of damping and operating temperature on rotor whirl speeds.

6.3.5 APPLICATION

The undamped rotor is pure theoretical rotor model. This model is a baseline to understand the rotor behavior under the influence of different forms of damping and operating temperature. The simple solid shaft is supported by anti-friction bearings and neglecting the hysteretic losses and operating temperature effect.

e.g. Lab test rig

6.4 INTERNAL VISCOUS DAMPING ACTING ALONE

This case study includes only internal viscous damping (η_v). It does not include internal hysteretic damping (η_H), operating temperature (T) and external viscous damping (C_e). Suppressing the operating temperature and different forms of damping in equations (4-75) and (4-86),

- External viscous damping, $C_{xx}=0$, $C_{yy}=0$, $C_{xy}=0$ and $C_{yx}=0$
- Internal hysteretic damping, $\eta_H=0$

$$\therefore \eta_a=\frac{1+\eta_H}{\sqrt{1+\eta_H{}^2}}=1; \text{ and } \therefore \eta_b=\frac{\eta_H}{\sqrt{1+\eta_H{}^2}}+\eta_v\Omega=\eta_v\Omega$$

The equations of motion for internal viscous damping becomes,

$$\left[\left[M_T^e\right]+\left[M_R^e\right]\right]\left\{\ddot{\bar{q}}_n^f\right\}+\left[\eta_v\left[K_B^e\right]-\Omega\left[G^e\right]\right]\left\{\dot{\bar{q}}_n^f\right\}+\left[\left[K_B^e\right]+\eta_v\Omega\left[K_C^e\right]\right]\left\{\bar{q}_n^f\right\}=\left\{\bar{F}_n^f\right\} \quad (6\text{-}3)$$

6.4.1 EFFECT ON WHIRL SPEEDS

Simulation is performed for different internal viscous damping values. As the internal viscous damping increases, both forward whirl and backward whirl speeds are also increases for the first and second mode only. For the higher modes, the forward whirl and backward whirl decreases with increasing this damping. Results are summarized in Table 6-3.

Table 6-3 Whirl Speeds (rad/sec) at rotor spin speed of 4000 (rpm)

Mode	η_v (0.0001 s)	η_v (0.00015 s)	η_v (0.0002 s)
1st BW	519.56	519.62	519.62
1st FW	519.62	520.29	521.31
2nd BW	1092.10	1093.32	1094.94
2nd FW	1094.45	1094.66	1094.96
3rd BW	2217.79	2211.01	2201.35
3rd FW	2231.11	2224.42	2215.00
4th BW	4799.30	4628.91	4379.38
4th FW	4829.57	4659.90	4411.65

6.4.2 WHIRL SPEED AND CAMPBELL DIAGRAM FOR ALL MODES

Simulation is performed at different rotor spin speeds and predicted the forward whirl and backward whirl speeds for first four modes with a constant internal viscous damping. Results are tabulated in Table 6-4 and shown in Figure 6-5.

Table 6-4 Whirl Speeds (rad/sec) for η_v = 0.0002 s, at different rotor spin speeds

Mode	0 rpm (0 rad/sec)	2000 rpm (209.4 rad/sec)	4000 rpm (418.9 rad/sec)	6000 rpm (628.3 rad/sec)
1st BW	519.89	519.61	519.62	519.93
1st FW	519.89	520.46	521.31	522.44
2nd BW	1094.63	1094.70	1094.94	1095.26
2nd FW	1094.63	1094.71	1094.96	1095.42
3rd BW	2207.18	2204.04	2201.35	2199.07
3rd FW	2207.18	2210.82	2215.00	2219.77
4th BW	4388.00	4382.02	4379.38	4379.77
4th FW	4388.00	4397.72	4411.65	4430.31

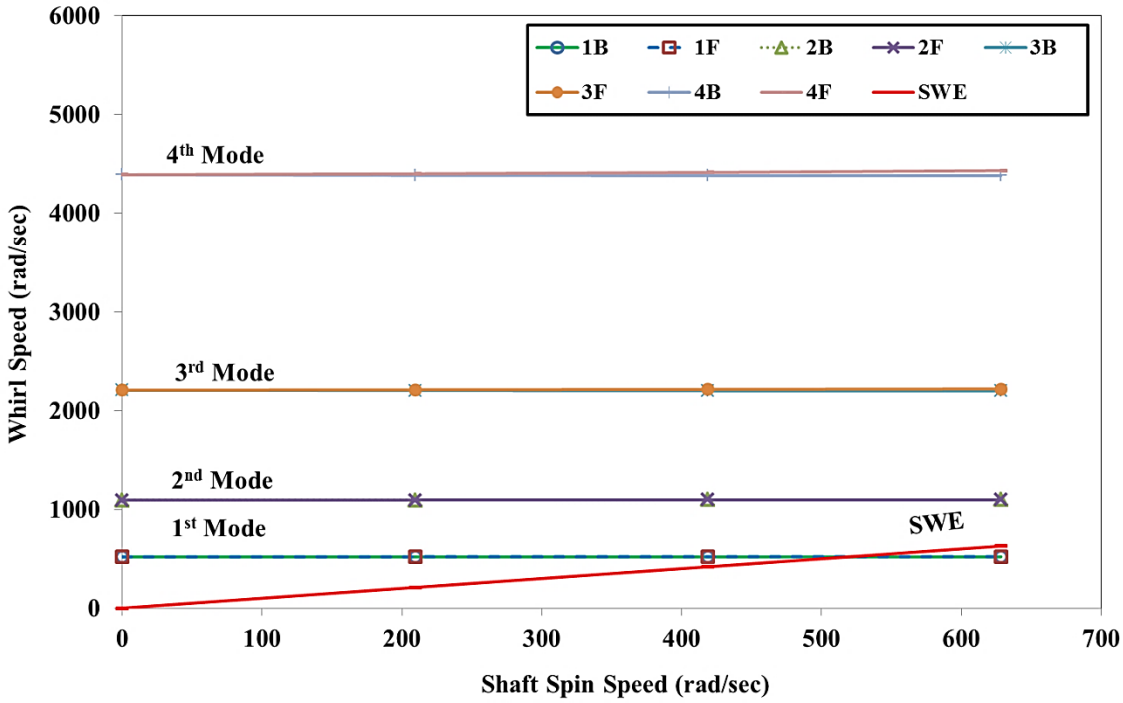

Figure 6-5 Campbell Diagram for Different Modes

Based on the results from the Table 6-4, the change in backward whirl speed is small for different rotor spin speeds. The clear trend is observed for forward whirl speed. The forward whirl speed is increasing with increase in rotor spin speed. The forward whirl speed and backward whirl speed are almost same for the second mode.

6.4.3 WHIRL SPEED AND CAMPBELL DIAGRAM FOR FIRST MODE

The forward whirl speed and backward whirl speed are clearly distinguishable for the first mode. The sensitivity analysis is carried out in detail with different internal viscous damping values. With the addition of this damping, the starting point of the forward whirl and backward whirl at zero spin speed gets offset. This offset of the forward whirl and/or backward whirl is increasing with increasing the damping. Due to this, the forward whirl and backward whirl speeds are increased with clear offset. Results are tabulated in ***Table 6-5*** and shown in Figure 6-6.

Table 6-5 Whirl Speeds (rad/sec) for different rotor spin speeds

	1st Mode	0 rpm (0 rad/sec)	2000 rpm (209.4 rad/sec)	4000 rpm (418.9 rad/sec)	6000 rpm (628.3 rad/sec)
η_v = 0.0001 s	BW	519.44	519.46	519.56	519.72
	FW	519.44	519.49	519.62	519.81
η_v = 0.00015 s	BW	519.63	519.54	519.62	519.86
	FW	519.63	519.88	520.29	520.86
η_v = 0.0002 s	BW	519.89	519.61	519.62	519.93
	FW	519.89	520.46	521.31	522.44

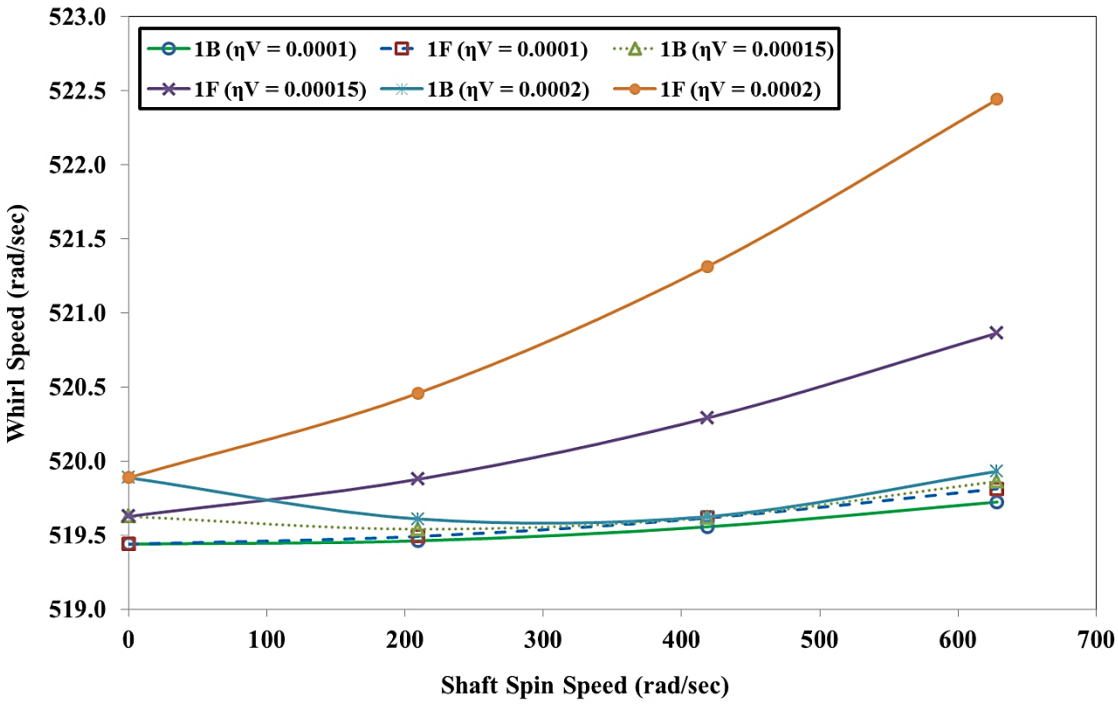

Figure 6-6 Whirl Speed Map for 1st Mode

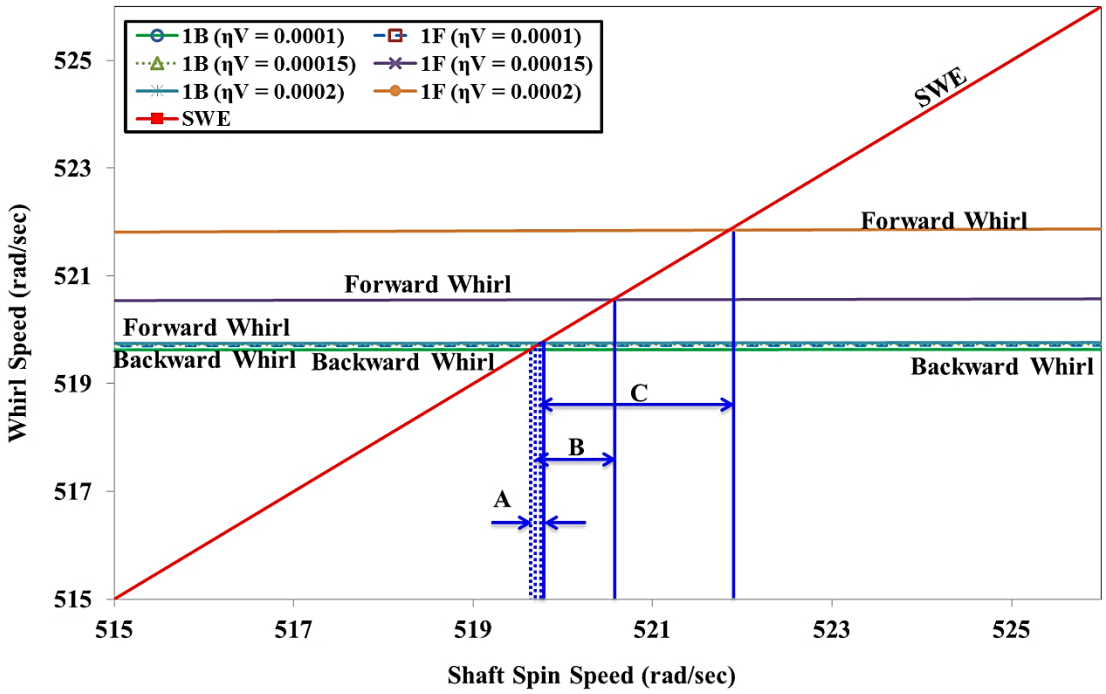

Figure 6-7 Campbell Diagram for 1st Mode

The synchronous whirl excitation is intersecting at two different locations for the first mode. The details of intersection are shown in Figure 6-7 for different internal viscous damping values. The range between backward critical speed and forward critical speed ranges are shown as 'A', 'B' and 'C'. These ranges are based on the contribution of internal viscous damping. As the internal viscous damping increases, these ranges are increasing. If the rotor operating spin speed is within this range 'A' 'B' and 'C', there will be the unbounded amplitude of vibration which results into rotor failure. To mitigate this risk and to avoid resonance, only two options are available, either rotor should redesign in such a way that the range 'A' 'B' and 'C' will get shifted from the operating spin speed or operate spin speed needs to change. This information is very useful in the design stage of the rotor.

6.4.4 CHANGE IN WHIRL SPEED RATIO

The non-dimensional term 'change in whirl speed ratio' is calculated for each mode shape with constant internal viscous damping. The change in whirl speed ratio is increasing as the spin speed increases for all the modes except the second mode; it means the spread between forward whirl and backward whirl increase as the spin speed increases. The whirl

speed ratio is more predominant at the higher modes and at higher speed. The results are tabulated in Table 6-6 and shown in Figure 6-8.

Table 6-6 Change in whirl speed ratio for η_v = 0.0002 s, at different rotor spin speeds

Mode	0 rpm (0 rad/sec)	2000 rpm (209.4 rad/sec)	4000 rpm (418.9 rad/sec)	6000 rpm (628.3 rad/sec)
1st Mode	0.000%	0.163%	0.325%	0.483%
2nd Mode	0.000%	0.001%	0.003%	0.015%
3rd Mode	0.000%	0.307%	0.619%	0.938%
4th Mode	0.000%	0.358%	0.325%	1.152%

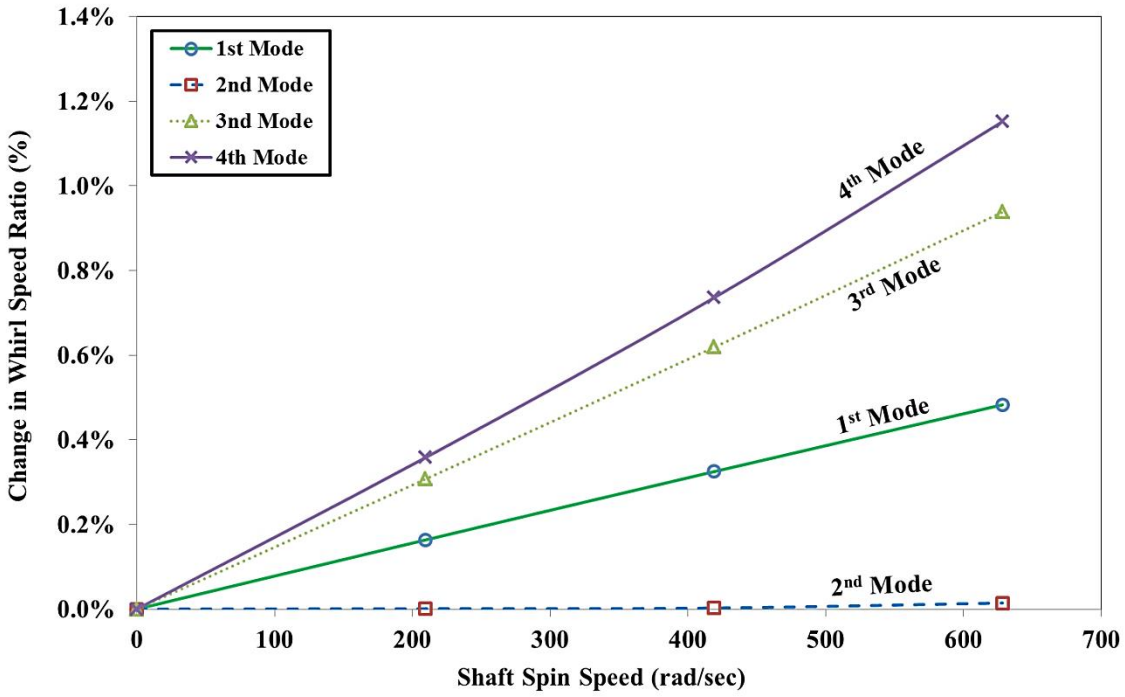

Figure 6-8 Change in Whirl Speed Ratio for Different Modes

The spread between backward whirl speed and forward whirl speed is increasing with increase in the rotor spin speed. This spread is also increasing with higher modes except for the second mode. This phenomenon is attributed to the nullifying effect of the gyroscopic couple for the second mode.

The sensitivity analysis is carried out on the change in whirl speed ratio with different internal viscous damping values. The results are tabulated in Table 6-7 and shown in Figure 6-9.

Table 6-7 Change in whirl speed ratio for different rotor spin speeds

	0 rpm (0 rad/sec)	2000 rpm (209.4 rad/sec)	4000 rpm (418.9 rad/sec)	6000 rpm (628.3 rad/sec)
η_v = 0.0001 s	0.000%	0.006%	0.011%	0.017%
η_v = 0.00015 s	0.000%	0.065%	0.129%	0.193%
η_v = 0.0002 s	0.000%	0.163%	0.325%	0.483%

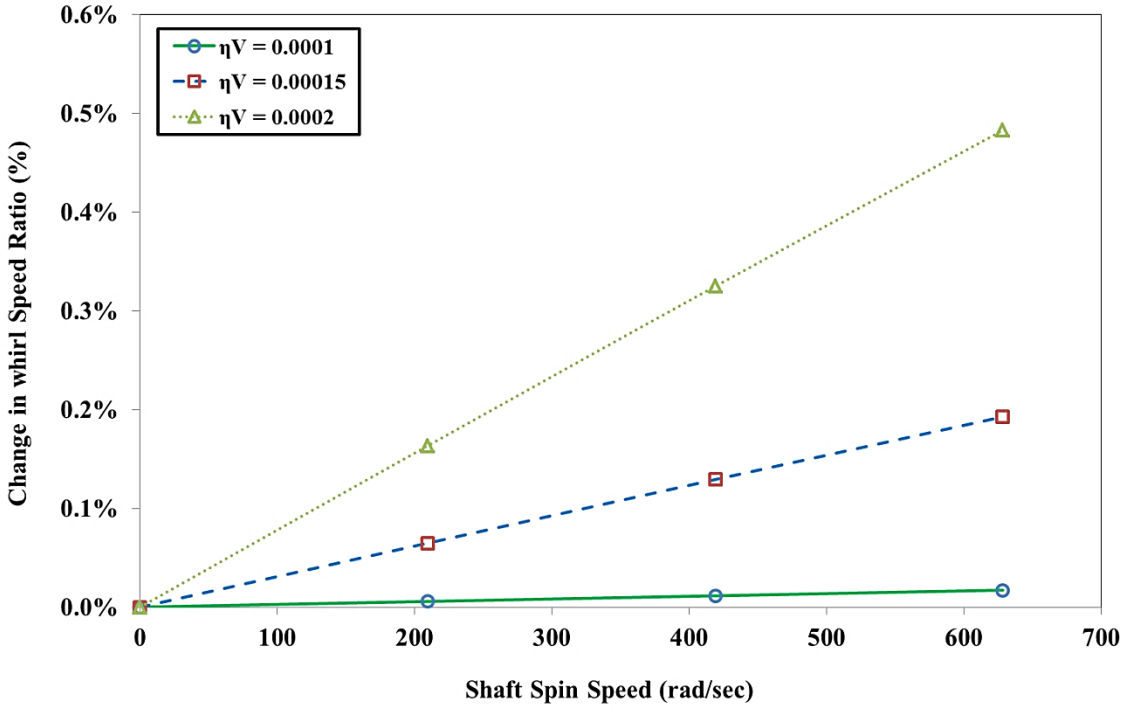

Figure 6-9 Change in Whirl Speed Ratio for 1st Mode

As the internal viscous damping increases, the change in whirl speed ratio increases as shown in Figure 6-9.

6.4.5 CONCLUSION

The spread between forward whirl speed and backward whirl speed increases with increase in rotor spin speed except for the second mode. This interesting phenomenon is

observed only for the second mode. The spread between forward whirl and backward whirl is small and this phenomenon is attributed to the nullifying effect of the gyroscopic couple. The spread is large for the first, third and fourth mode. It is clearly observed in Figure 6-8 with the help of whirl speed ratio. Critical speed range or spread is also increasing and shifting at higher side with an increase in internal viscous damping as shown in Figure 6-10. A clear understanding of the combined damping of internal viscous damping and external viscous damping is very useful while designing flexible and rigid rotors.

6.4.6 APPLICATION

Practical application or situation will be the different parts or components mounted on the shaft with shrink fit and operating temperature is not critical and external viscous damping is not present. The Fan, hub, coupling, balance ring etc are mounted on the shaft with shrink fit and it is supported by anti-friction bearings like ball bearings, roller bearings etc assuming no hysteretic losses in the shaft.

e.g. Lab test rig

6.5 INTERNAL HYSTERETIC DAMPING ACTING ALONE

This case study includes only internal hysteretic damping (η_H). It does not include internal viscous damping (η_v), operating temperature (T) and external viscous damping (C_e). Suppressing the operating temperature and different forms of damping in equations (4-75) and (4-86),

- External viscous damping, $C_{xx} = 0$, $C_{yy} = 0$, $C_{xy} = 0$ and $C_{yx} = 0$
- Internal viscous damping, $\eta_v = 0$

$\therefore \eta_a = \dfrac{1+\eta_H}{\sqrt{1+\eta_H{}^2}}$; and $\therefore \eta_b = \dfrac{\eta_H}{\sqrt{1+\eta_H{}^2}} + \eta_v\Omega = \dfrac{\eta_H}{\sqrt{1+\eta_H{}^2}}$

The equations of motion for internal hysteretic damping becomes,

$$\left[\left[M_T^e\right]+\left[M_R^e\right]\right]\left\{\ddot{\bar{q}}_n^f\right\}-\Omega\left[G^e\right]\left\{\dot{\bar{q}}_n^f\right\}+\left[\frac{1+\eta_H}{\sqrt{1+\eta_H{}^2}}\left[K_B^e\right]+\frac{\eta_H}{\sqrt{1+\eta_H{}^2}}\left[K_C^e\right]\right]\left\{\bar{q}_n^f\right\}=\left\{\bar{F}_n^f\right\} \quad (6\text{-}4)$$

6.5.1 EFFECT ON WHIRL SPEEDS

Simulation is performed for different internal hysteretic damping values. As the internal hysteretic damping increases, both forward whirl and backward whirl speeds are also increases for all the modes. Results are tabulated in Table 6-8.

Table 6-8 Whirl Speeds (rad/sec) at rotor spin speed of 4000 (rpm)

Mode	η_H (0.0002)	η_H (0.0025)	η_H (0.005)
1st BW	518.99	519.23	519.48
1st FW	519.63	519.87	520.13
2nd BW	1091.08	1091.18	1091.30
2nd FW	1094.28	1094.39	1094.50
3rd BW	2223.27	2224.87	2226.61
3rd FW	2236.59	2238.19	2239.93
4th BW	4931.77	4937.04	4942.76
4th FW	4961.64	4966.91	4972.63

6.5.2 WHIRL SPEED AND CAMPBELL DIAGRAM FOR ALL MODES

Simulation is performed at different rotor spin speeds and predicted the forward whirl and backward whirl speeds for first four modes with a constant internal hysteretic damping. Results are tabulated in Table 6-9.

Table 6-9 Whirl Speeds (rad/sec) for η_H = 0.005, at different rotor spin speeds

Mode	0 rpm (0 rad/sec)	2000 rpm (209.4 rad/sec)	4000 rpm (418.9 rad/sec)	6000 rpm (628.3 rad/sec)
1st BW	519.81	519.65	519.48	519.32
1st FW	519.81	519.97	520.13	520.29
2nd BW	1092.90	1092.10	1091.30	1090.50
2nd FW	1092.90	1093.70	1094.50	1095.30
3rd BW	2233.26	2229.93	2226.61	2223.29
3rd FW	2233.26	2236.59	2239.93	2243.28
4th BW	4957.68	4950.21	4942.76	4935.31
4th FW	4957.68	4965.15	4972.63	4980.13

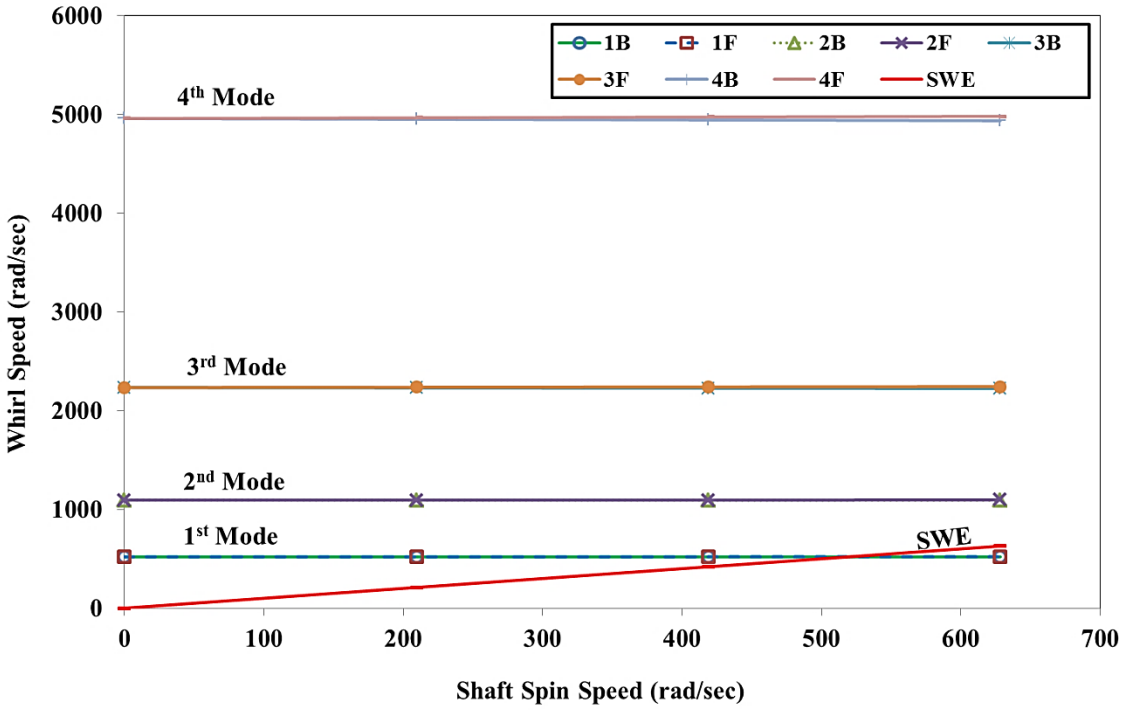

Figure 6-10 Campbell Diagram for Different Modes

Based on the results from the Table 6-9, there is a clear trend for backward whirl speed and forward whirls speed. The backward whirl speeds are decreasing and forward whirls speeds are increasing with increasing in rotor spin speed. This trend is like baseline or undamped rotor.

6.5.3 WHIRL SPEED AND CAMPBELL DIAGRAM FOR FIRST MODE

The forward whirl speed and backward whirl speed are clearly distinguishable. The sensitivity analysis is carried out to understand the effect of internal hysteretic damping on the forward whirl and backward whirl speeds. With the addition of this damping, the starting point of the forward whirl and backward whirl at zero spin speed gets offset. This offset is increasing with increasing the internal hysteretic damping. Results are summarized in Table 6-10 and shown in Figure 6-11.

Table 6-10 Whirl Speeds (rad/sec) for different rotor spin speeds

	1st Mode	0 rpm (0 rad/sec)	2000 rpm (209.4 rad/sec)	4000 rpm (418.9 rad/sec)	6000 rpm (628.3 rad/sec)
η_H = 0.0002	BW	519.31	519.15	518.99	518.82
	FW	519.31	519.47	519.63	519.79
η_H = 0.00025	BW	519.55	519.39	519.23	519.06
	FW	519.55	519.71	519.87	520.03
η_H = 0.0005	BW	519.81	519.65	519.48	519.32
	FW	519.81	519.97	520.13	520.29

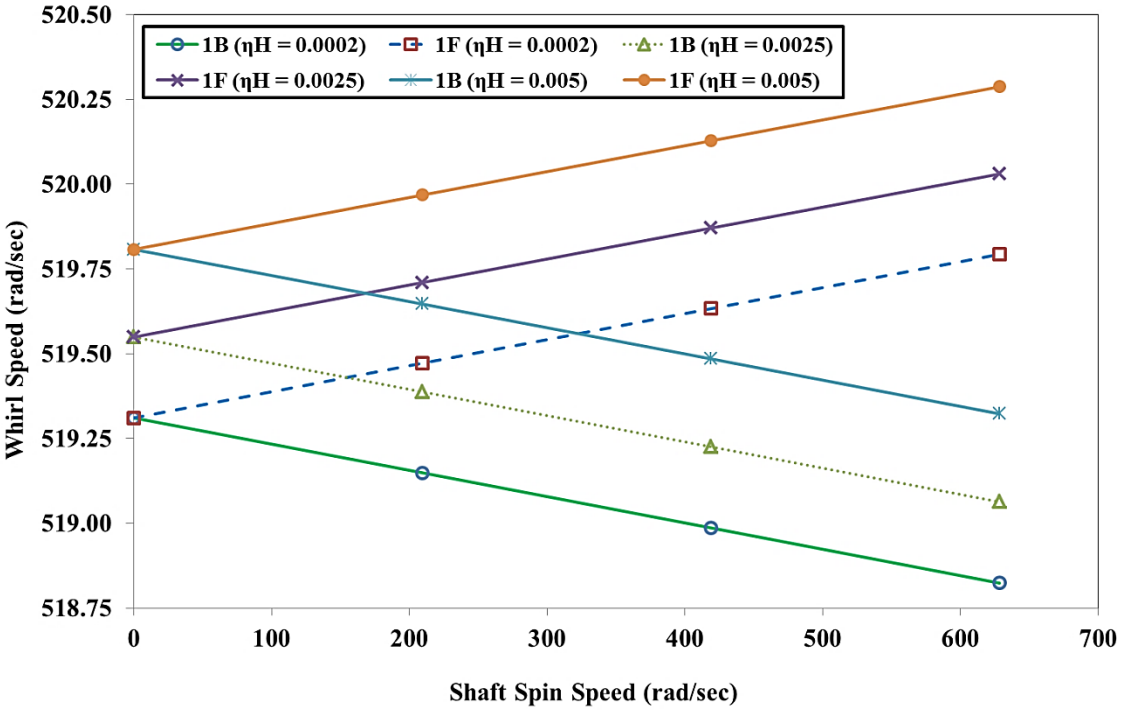

Figure 6-11 Whirl Speed Map for 1st Mode

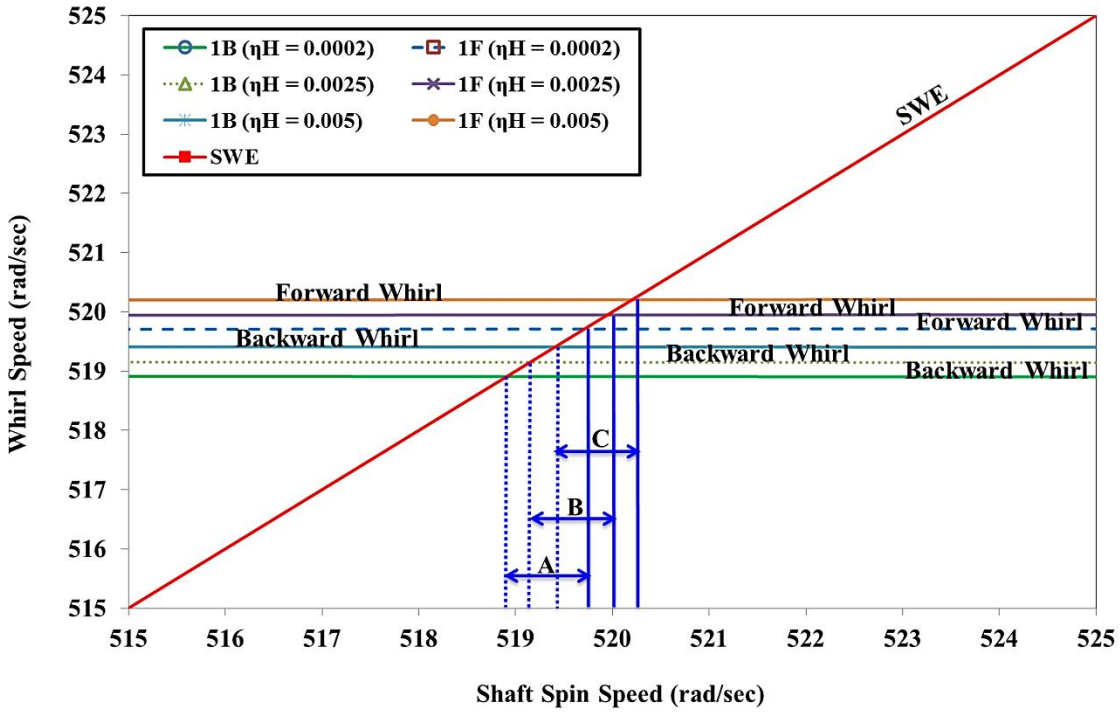

Figure 6-12 Campbell Diagram for 1st Mode

The synchronous whirl excitation is intersecting at two different locations for the first mode. The details of intersection are shown in Figure 6-12. The range between backward critical speed and forward critical speed ranges are shown as 'A', 'B' and 'C'. These ranges are based on the contribution of internal hysteretic damping. As the internal hysteretic damping increases, these ranges are shifting or moving at a high level. If the rotor operating spin speed is within this range 'A' 'B' and 'C', there will be the unbounded amplitude of vibration which results into rotor failure. To mitigate this risk and to avoid resonance, only two options are available, either rotor should redesign in such a way that the range 'A' 'B' and 'C' will get shifted from the operating speed or operate spin speed needs to change. This information is very useful in the design stage of the rotor.

6.5.4 CHANGE IN WHIRL SPEED RATIO

The non-dimensional term 'change in whirl speed ratio' is calculated for each mode shape with constant internal hysteretic damping. The change in whirl speed ratio is increasing with increase in rotor spin speed for all the modes, it means the spread between forward whirl and backward whirl increase as the spin speed increases. The whirl speed ratio is more

predominant at the higher modes and at higher speeds. The results are tabulated in Table 6-11 and shown in Figure 6-13.

Table 6-11 Change in whirl speed ratio for $\eta_H = 0.005$, at different rotor spin speeds

Mode	0 rpm (0 rad/sec)	2000 rpm (209.4 rad/sec)	4000 rpm (418.9 rad/sec)	6000 rpm (628.3 rad/sec)
1st Mode	0.000%	0.062%	0.124%	0.186%
2nd Mode	0.000%	0.147%	0.293%	0.440%
3rd Mode	0.000%	0.298%	0.597%	0.895%
4th Mode	0.000%	0.301%	0.603%	0.904%

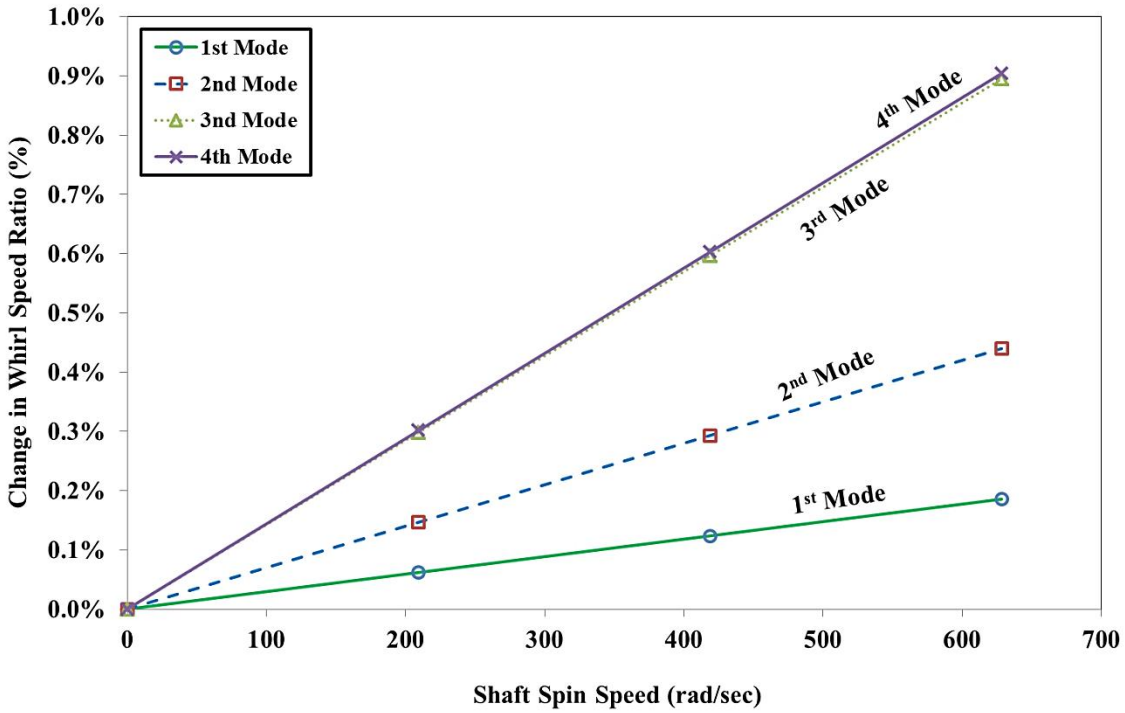

Figure 6-13 Change in Whirl Speed Ratio for Different Modes

The spread between backward whirl speed and forward whirl speed is increasing with increase in the rotor spin speed. This spread is also increasing with higher modes. This is clearly shown in Figure 6-13 with the help of a change in whirl speed ratio. This spreading effect is due to the contribution of internal hysteretic damping. This phenomenon is attributed to the adding effect of the gyroscopic couple.

The sensitivity analysis is carried out on the change in whirl speed ratio with different internal hysteretic damping. As the internal hysteretic damping increases, the change in whirl speed ratio reduces. In conclusion, the internal hysteretic damping is attributed to the nullifying effect of a gyroscopic couple with lesser magnitude. The results are tabulated in the below Table 6-12.

Table 6-12 Change in whirl speed ratio for different rotor spin speeds

	0 rpm (0 rad/sec)	2000 rpm (209.4 rad/sec)	4000 rpm (418.9 rad/sec)	6000 rpm (628.3 rad/sec)
$\eta_H = 0.0002$	0.0000%	0.0622%	0.1245%	0.1867%
$\eta_H = 0.00025$	0.0000%	0.0621%	0.1241%	0.1862%
$\eta_H = 0.0005$	0.0000%	0.0619%	0.1237%	0.1856%

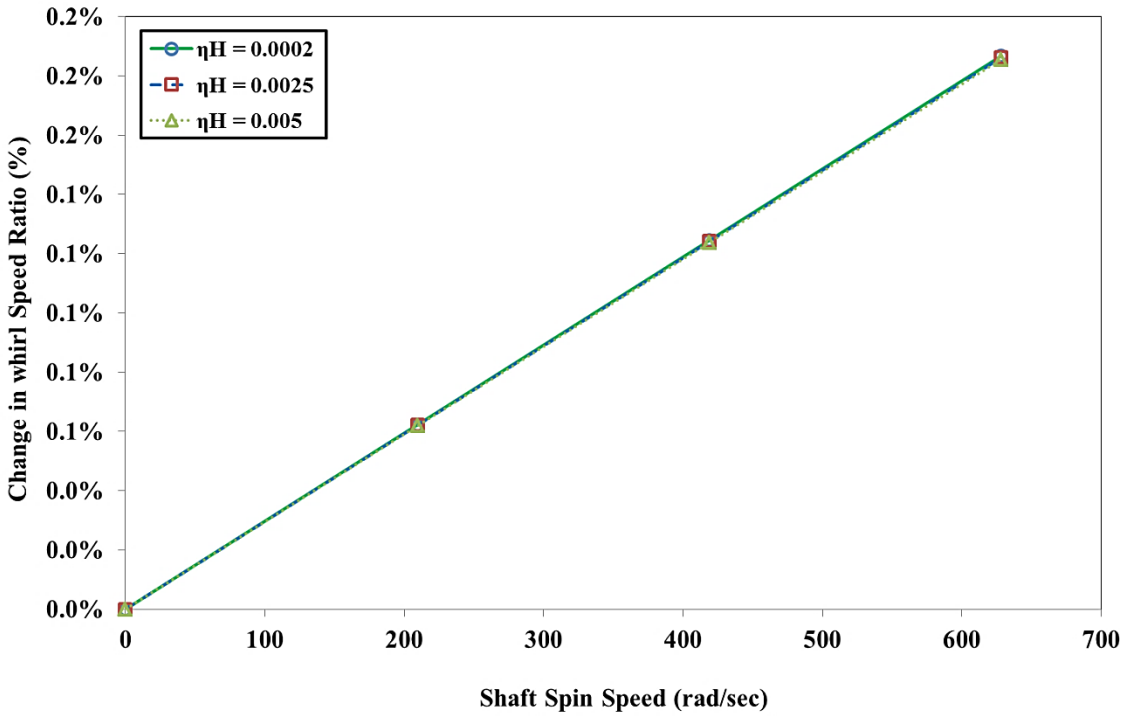

Figure 6-14 Change in Whirl Speed Ratio for 1st Mode

The effect of internal hysteretic damping on the change in whirls speed ratio is small as shown in Figure 6-14.

6.5.5 CONCLUSION

The spread between forward whirl speed and backward whirl speed increases with increase in rotor spin speed for all modes. This spread is larger for higher modes and at higher speeds. This is clearly observed in Figure 6-13 with the help of whirl speed ratio. Critical speed range or spread remains almost constant and shifting at higher side with an increase in internal hysteretic damping as shown in Figure 6-12. The effect of internal hysteretic damping is small. A clear understanding of the internal hysteretic damping is very useful while designing rigid and flexible and rigid rotors.

6.5.6 APPLICATION

Practical application or situation will be the simple shaft and operating temperature is not critical and external viscous damping is not present. e.g. shaft is supported with anti-friction bearings like ball bearings, roller bearings etc.

e.g. Lab test rig

6.6 EXTERNAL VISCOUS DAMPING ACTING ALONE

This case study includes only external viscous damping (C_e). It does not include internal viscous damping (η_v), internal hysteretic damping (η_H) and operating temperature (T).

Suppressing the operating temperature and different forms of damping in equations (4-75) and (4-86),

- Internal viscous damping, $\eta_v = 0$
- Internal hysteretic damping, $\eta_H = 0$

$$\therefore \eta_a = \frac{1+\eta_H}{\sqrt{1+\eta_H{}^2}} = 1; \text{ and } \therefore \eta_b = \frac{\eta_H}{\sqrt{1+\eta_H{}^2}} + \eta_v\Omega = 0$$

The equations of motion for external viscous damping becomes,

$$\left[\left[M_T^e\right] + \left[M_R^e\right]\right]\left\{\ddot{\bar{q}}_n^f\right\} - \Omega\left[G^e\right]\left\{\dot{\bar{q}}_n^f\right\} + \left[K_B^e\right]\left\{\bar{q}_n^f\right\} = \left\{\bar{F}_n^f\right\} \qquad (6\text{-}5)$$

$$\begin{bmatrix} C_{xx} & C_{xy} \\ C_{yx} & C_{yy} \end{bmatrix} \{\dot{\bar{q}}_n^f\} + \begin{bmatrix} K_{xx} & K_{xy} \\ K_{yx} & K_{yy} \end{bmatrix} \{\bar{q}_n^f\} = \{\bar{F}_b^f\} \quad (6\text{-}6)$$

6.6.1 EFFECT ON WHIRL SPEEDS

Simulation is performed for different external viscous damping values. As the external viscous damping increases, both forward whirl and backward whirl speeds are also increases for the first mode. For the higher modes, the forward whirl and backward whirl decreases with increasing this damping. Results are tabulated in Table 6-13.

Table 6-13 Whirl Speeds (rad/sec) at rotor spin speed of 4000 (rpm)

Mode	Ce = 500 (N-sec/m)	Ce = 1000 (N-sec/m)	Ce = 1752 (N-sec/m)
1st BW	518.97	519.00	519.08
1st FW	519.62	519.65	519.73
2nd BW	1091.00	1090.79	1090.21
2nd FW	1094.20	1093.99	1093.42
3rd BW	2222.96	2222.44	2221.00
3rd FW	2236.28	2235.76	2234.33
4th BW	4931.11	4930.53	4928.93
4th FW	4960.99	4960.41	4958.82

6.6.2 WHIRL SPEED AND CAMPBELL DIAGRAM FOR ALL MODES

Simulation is performed at different rotor spin speeds and predicted the forward whirl and backward whirl speeds for first four modes with a constant external viscous damping. Results are tabulated in Table 6-14 and shown in Figure 6-15.

Table 6-14 Whirl Speeds (rad/sec) for Ce = 1752 N-s/m, at different rotor spin speeds

Mode	0 rpm (0 rad/sec)	2000 rpm (209.4 rad/sec)	4000 rpm (418.9 rad/sec)	6000 rpm (628.3 rad/sec)
1st BW	519.40	519.24	519.08	518.92
1st FW	519.40	519.57	519.73	519.89
2nd BW	1091.81	1091.01	1090.21	1089.41
2nd FW	1091.81	1092.62	1093.42	1094.22
3rd BW	2227.66	2224.33	2221.00	2217.69
3rd FW	2227.66	2230.99	2234.33	2237.68
4th BW	4943.86	4936.39	4928.93	4921.49
4th FW	4943.86	4951.33	4958.82	4966.32

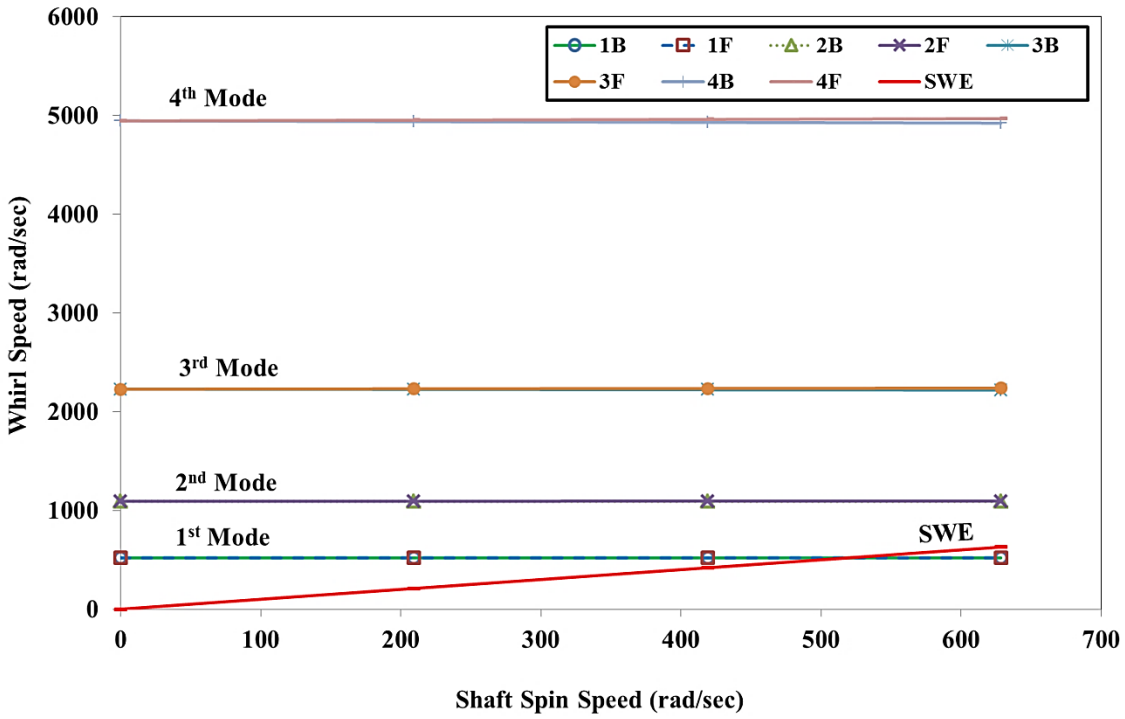

Figure 6-15 Campbell Diagram for Different Modes

Based on the results from Table 6-14 and Figure 6-15, the backward whirl speed decreases and forward whirl speed increases with increase in rotor spin speed for all modes. This is more predominant for higher modes.

6.6.3 WHIRL SPEED AND CAMPBELL DIAGRAM FOR FIRST MODE

The forward whirl speed and backward whirl speed are clearly distinguishable. The sensitivity analysis is carried out in detail with different external viscous damping values. With the addition of external viscous damping, the starting point of the forward whirl and backward whirl at zero spin speed gets higher offset. Results are summarized in Table 6-15 and shown in Figure 6-16.

Table 6-15 Whirl Speeds (rad/sec) for different rotor spin speeds

	1st Mode	0 rpm (0 rad/sec)	2000 rpm (209.4 rad/sec)	4000 rpm (418.9 rad/sec)	6000 rpm (628.3 rad/sec)
Ce = 500 N-s/m	BW	519.30	519.14	518.97	518.81
	FW	519.30	519.46	519.62	519.78
Ce = 1000 N-s/m	BW	519.33	519.17	519.00	518.84
	FW	519.33	519.49	519.65	519.81
Ce = 1752 N-s/m	BW	519.40	519.24	519.08	518.92
	FW	519.40	519.57	519.73	519.89

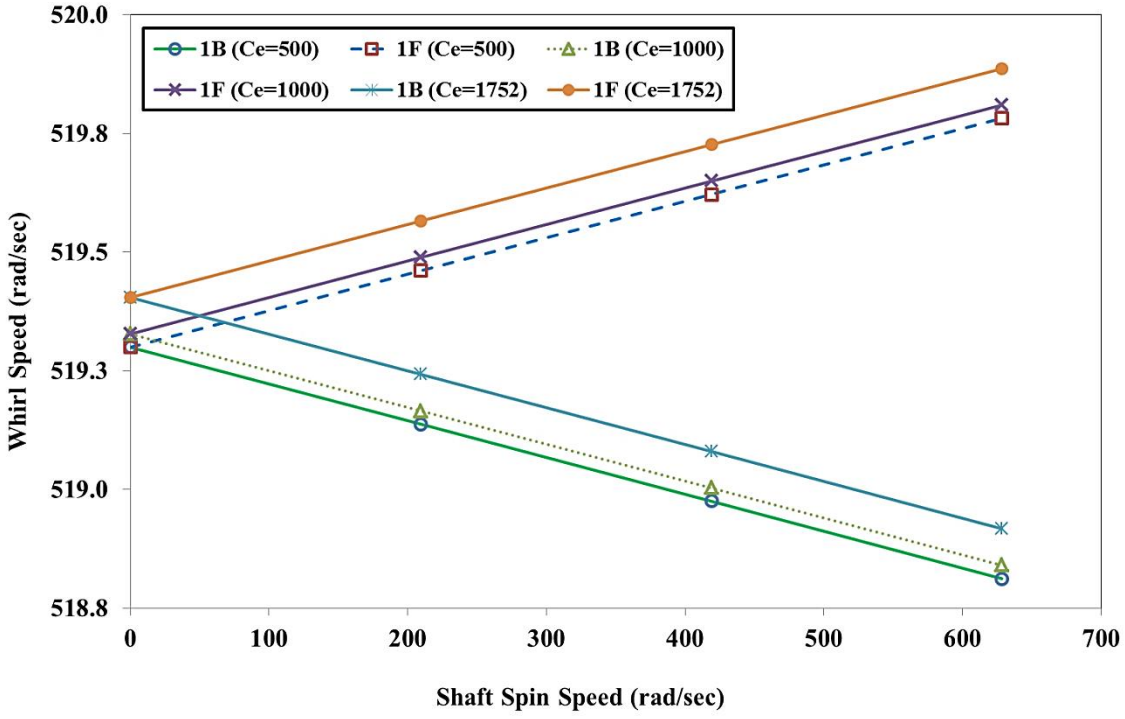

Figure 6-16 Whirl Speed Map for 1st Mode

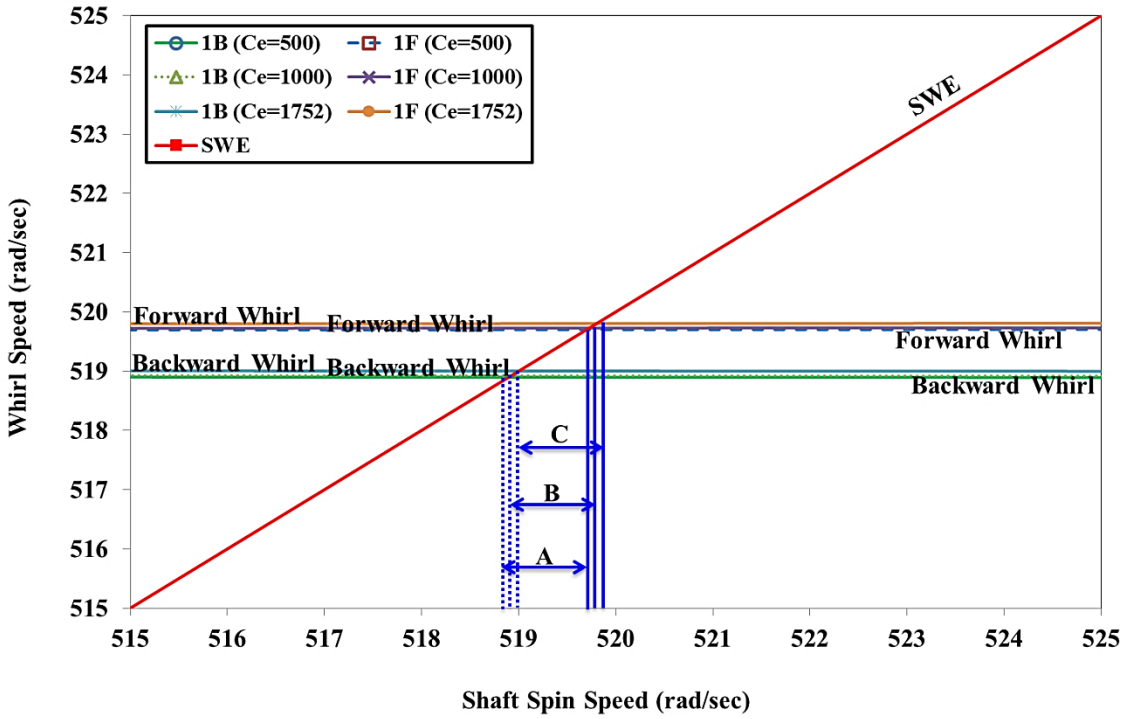

Figure 6-17 Campbell Diagram for 1st Mode

The synchronous whirl excitation is intersecting at two different locations for the first mode. The details of intersection are shown in Figure 6-17. The range between backward critical speed and forward critical speed ranges are shown as 'A', 'B' and 'C'. These ranges are based on the contribution of external viscous damping. As the external viscous damping increases, these ranges are shifting proportionately at a higher level. If the rotor operating spin speed is within this range 'A' 'B' and 'C', there will be the unbounded amplitude of vibration which results into rotor failure. To mitigate this risk and to avoid resonance, only two options are available, either rotor should redesign in such a way that the range 'A' 'B' and 'C' will get shifted from the operating speed or operate spin speed needs to change. This information is very useful in the design stage of the rotor.

6.6.4 CHANGE IN WHIRL SPEED RATIO

The non-dimensional term 'change in whirl speed ratio' is calculated for each mode shape with constant external viscous damping. The change in whirl speed ratio is increasing as the spin speed increases for all the modes; it means the spread between forward whirl and backward whirl is increasing with increase in rotor spin speed. The whirl speed ratio is more

predominant at the higher modes and at higher speed. The results are tabulated in Table 6-16 and shown in Figure 6-18.

Table 6-16 Change in whirl speed ratio for Ce = 1752 N-s/m, at different rotor spin speeds

Mode	0 rpm (0 rad/sec)	2000 rpm (209.4 rad/sec)	4000 rpm (418.9 rad/sec)	6000 rpm (628.3 rad/sec)
1st Mode	0.000%	0.062%	0.124%	0.187%
2nd Mode	0.000%	0.147%	0.294%	0.440%
3rd Mode	0.000%	0.299%	0.598%	0.897%
4th Mode	0.000%	0.302%	0.605%	0.907%

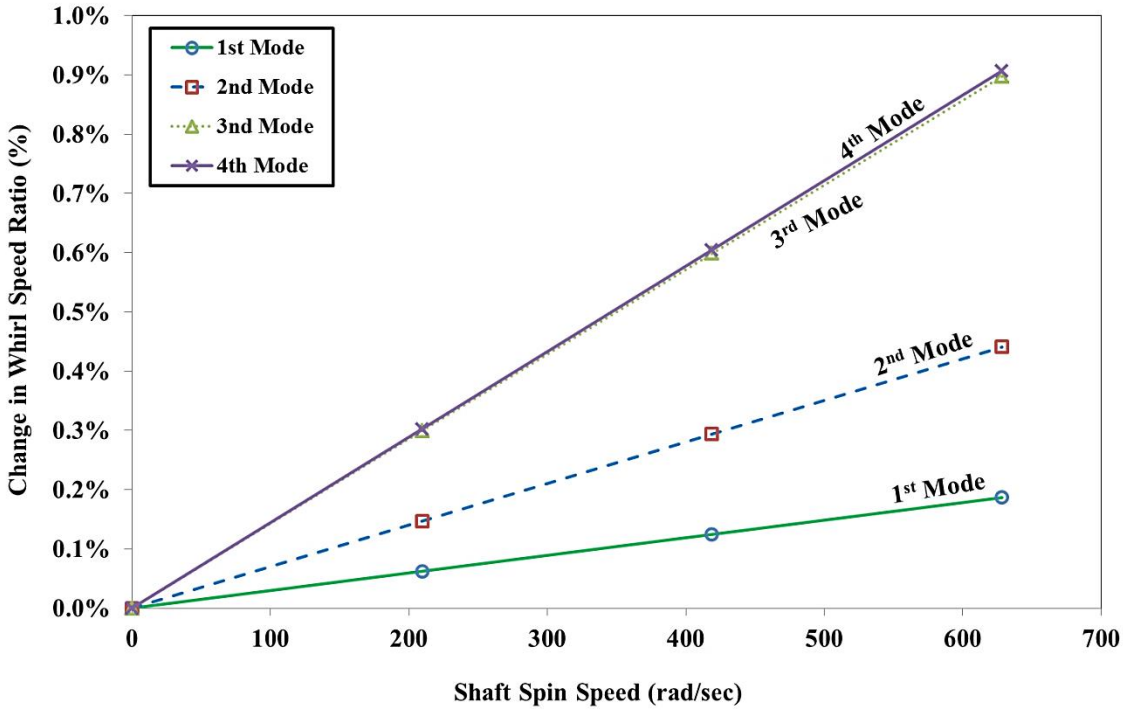

Figure 6-18 Change in Whirl Speed Ratio for Different Modes

The spread between backward whirl speed and forward whirl speed is increasing with increase in the rotor spin speed. This spread is also increasing with higher modes. This spreading effect is due to the contribution of external viscous damping. This phenomenon is attributed to the adding effect of the gyroscopic couple.

The sensitivity analysis is carried out on the change in whirl speed ratio with different external viscous damping values. As the external viscous damping increases, the change in whirl speed ratio decreases. In conclusion, the external viscous damping is attributed to the nullifying effect of the gyroscopic couple. The results are tabulated in Table 6-17. and shown in Figure 6-19.

Table 6-17 Change in whirl speed ratio for different rotor spin speeds

	0 rpm (0 rad/sec)	2000 rpm (209.4 rad/sec)	4000 rpm (418.9 rad/sec)	6000 rpm (628.3 rad/sec)
Ce = 500 N-s/m	0.00000%	0.06226%	0.12451%	0.18677%
Ce = 1000 N-s/m	0.00000%	0.06224%	0.12448%	0.18672%
Ce = 1752 N-s/m	0.00000%	0.06220%	0.12440%	0.18660%

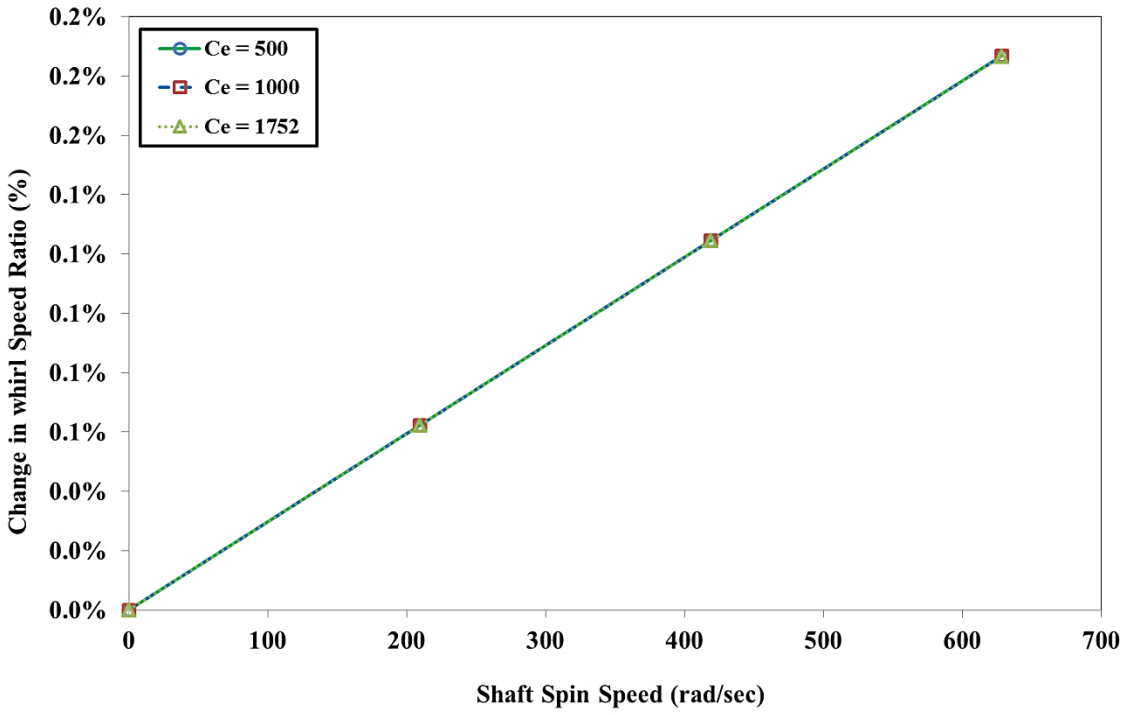

Figure 6-19 Change in Whirl Speed Ratio for 1st Mode

The effect of external viscous damping on the change in whirls speed ratio is small as shown in Figure 6-19.

6.6.5 CONCLUSION

The spread between forward whirl speed and backward whirl speed increases with increase in rotor spin speed for all modes. The spread is large for higher modes. It is clearly observed in Figure 6-18 with the help of whirl speed ratio. Critical speed range or spread remains constant and shifting at higher side with an increase in external viscous damping as shown in Figure 6-17. A clear understanding of the external viscous damping is very useful while designing flexible and rigid rotors.

6.6.6 APPLICATION

Practical application or situation will be the simple shaft supported with an external viscous damping. Operating temperature is not critical in this load case. e.g. shaft is supported with sleeve or journal bearings assuming no hysteretic losses in the shaft

e.g. Lab test rig

6.7 OPERATING TEMPERATURE ACTING ALONE

This case study includes only operating temperature (T). It does not include internal viscous damping (η_v), internal hysteretic damping (η_H) and external viscous damping (C_e).

Suppressing the different forms of damping in equations (4-75) and (4-86),

- External viscous damping, $C_{xx} = 0$, $C_{yy} = 0$, $C_{xy} = 0$ and $C_{yx} = 0$
- Internal viscous damping, $\eta_v = 0$
- Internal hysteretic damping, $\eta_H = 0$

$\therefore \eta_a = \dfrac{1+\eta_H}{\sqrt{1+\eta_H{}^2}} = 1$; and $\therefore \eta_b = \dfrac{\eta_H}{\sqrt{1+\eta_H{}^2}} + \eta_v\Omega = 0$

The equations of motion for operating temperature becomes,

$$\left[\left[M_{Tt}^{e}\right]+\left[M_{Rt}^{e}\right]\right]\left\{\ddot{\bar{q}}_{n}^{f}\right\}-\Omega\left[G_{t}^{e}\right]\left\{\dot{\bar{q}}_{n}^{f}\right\}+\left[K_{Bt}^{e}\right]\left\{\bar{q}_{n}^{f}\right\}=\left\{\bar{F}_{n}^{f}\right\} \tag{6-7}$$

6.7.1 EFFECT ON WHIRL SPEEDS

Simulation is performed for different operating temperature values. As the operating temperature increases, both forward whirl and backward whirl speeds are decreased for all modes. Results are tabulated in Table 6-18.

Table 6-18 Whirl Speeds (rad/sec) at rotor spin speed of 4000 (rpm)

Mode	T (50 °C)	T (100 °C)	T (150 °C)
1st BW	518.38	517.02	515.20
1st FW	519.03	517.68	515.87
2nd BW	1090.81	1090.22	1089.42
2nd FW	1094.02	1093.42	1092.61
3rd BW	2219.21	2210.25	2198.41
3rd FW	2232.52	2223.55	2211.69
4th BW	4918.35	4888.71	4849.48
4th FW	4948.22	4918.57	4879.34

6.7.2 WHIRL SPEED AND CAMPBELL DIAGRAM FOR ALL MODES

Simulation is performed at different rotor spin speeds and predicted the forward whirl and backward whirl speeds for first four modes with a constant operating temperature. Results are tabulated in Table 6-19 and shown in Figure 6-20.

Table 6-19 Whirl Speeds (rad/sec) for T = 150 °C, different rotor spin speeds

Mode	0 rpm (0 rad/sec)	2000 rpm (209.4 rad/sec)	4000 rpm (418.9 rad/sec)	6000 rpm (628.3 rad/sec)
1st BW	515.53	515.37	515.20	515.03
1st FW	515.53	515.70	515.87	516.04
2nd BW	1091.01	1090.21	1089.42	1088.62
2nd FW	1091.01	1091.81	1092.61	1093.41
3rd BW	2205.04	2201.72	2198.41	2195.11
3rd FW	2205.04	2208.36	2211.69	2215.03
4th BW	4864.39	4856.93	4849.48	4842.04
4th FW	4864.39	4871.86	4879.34	4886.83

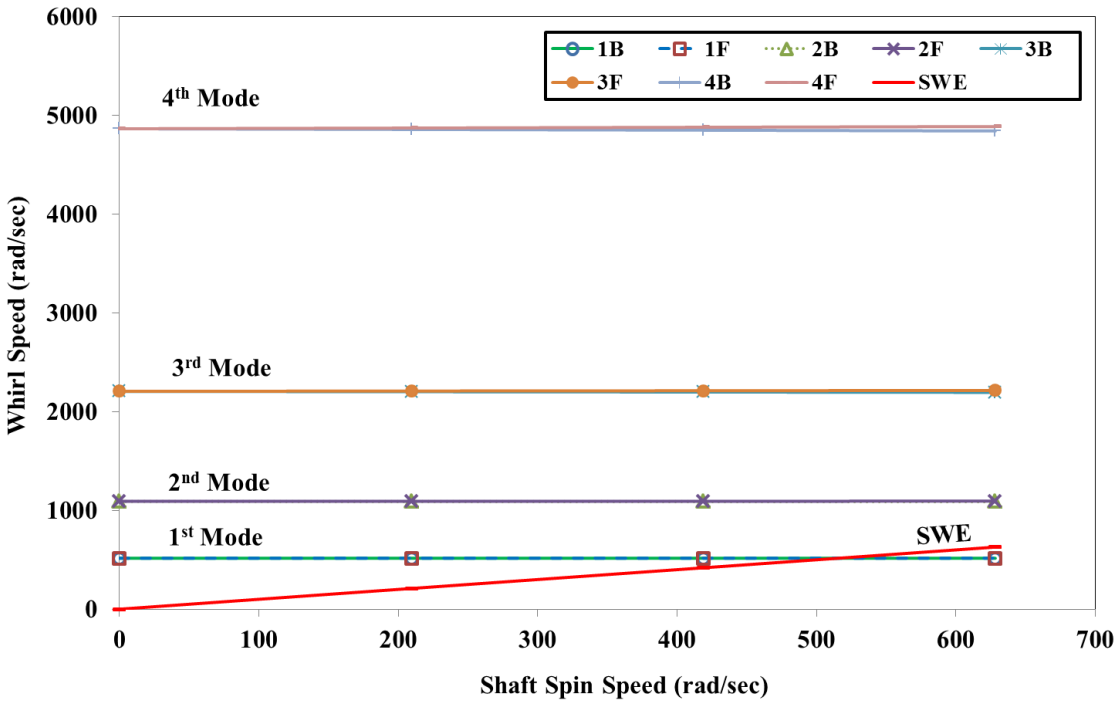

Figure 6-20 Campbell Diagram for Different Modes

Based on the results from Table 6-19 and Figure 6-20, the backward speeds are decreasing and forward speeds are increasing with increase in rotor spin speed for all modes. This is more predominant at higher modes.

6.7.3 WHIRL SPEED AND CAMPBELL DIAGRAM FOR FIRST MODE

The forward whirl speed and backward whirl speed are clearly distinguishable. The sensitivity analysis is carried out to understand the effect of operating temperature on the forward whirl and backward whirl speeds. With the addition of operating temperature, the starting point of the forward whirl and backward whirl at zero spin speed gets lower offset. This offset is more with an increase in the operating temperature. Results are summarized in Table 6-20 and shown in Figure 6-21.

Table 6-20 Whirl Speeds (rad/sec) for different rotor spin speeds

	1st Mode	0 rpm (0 rad/sec)	2000 rpm (209.4 rad/sec)	4000 rpm (418.9 rad/sec)	6000 rpm (628.3 rad/sec)
T = 50 °C	BW	518.71	518.54	518.38	518.21
	FW	518.71	518.87	519.03	519.19
T = 100 °C	BW	517.35	517.19	517.02	516.86
	FW	517.35	517.52	517.68	517.85
T = 150 °C	BW	515.53	515.37	515.20	515.03
	FW	515.53	515.70	515.87	516.04

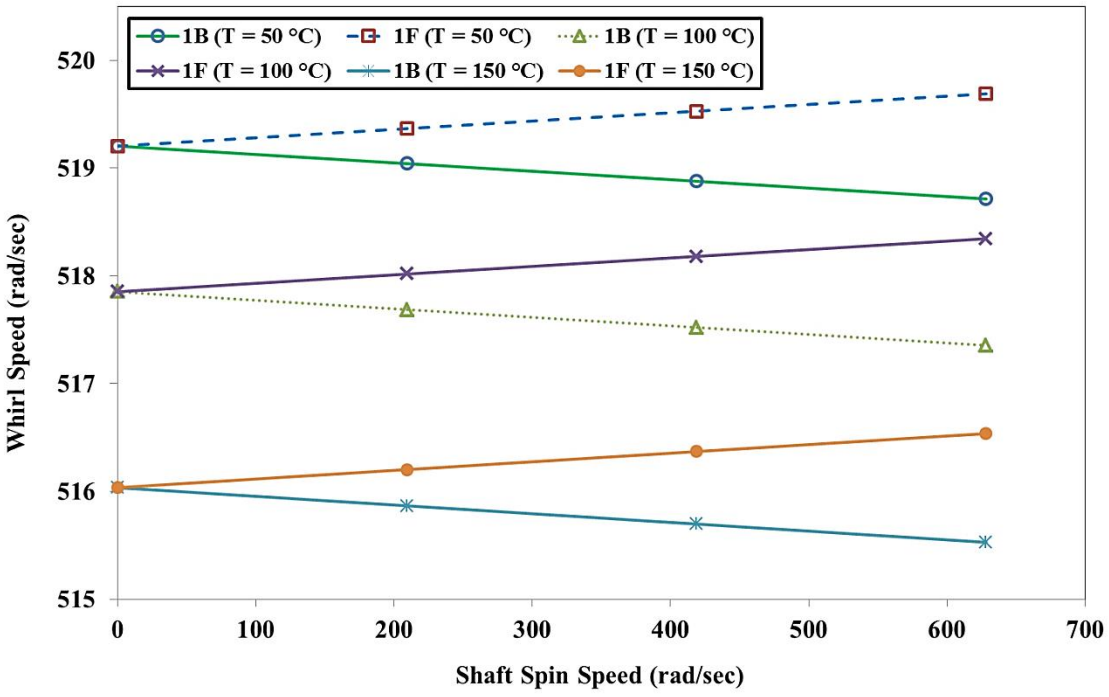

Figure 6-21 Whirl Speed Map for 1st Mode

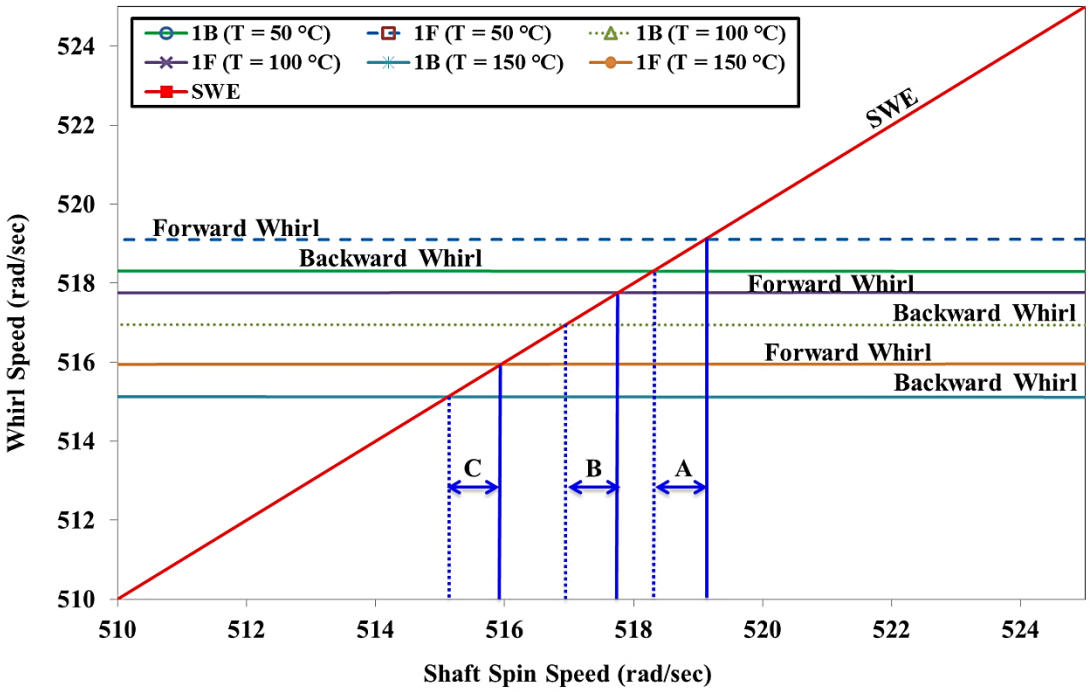

Figure 6-22 Campbell Diagram for 1st Mode

The synchronous whirl excitation is intersecting at two different locations for the first mode. The details of intersection are shown in Figure 6-22. The range between backward critical speed and forward critical speed ranges are shown as 'A', 'B' and 'C'. These ranges are based on the contribution of operating temperature. As the operating temperature increases, these ranges are shifting or moving at a lower level. If the rotor operating spin speed is within this range 'A' 'B' and 'C', there will be the unbounded amplitude of vibration which results into rotor failure. To mitigate this risk and to avoid resonance, only two options are available, either rotor should redesign in such a way that the range 'A' 'B' and 'C' will get shifted from the operating speed or operate spin speed needs to change. This information is very useful in the design stage of the rotor.

6.7.4 CHANGE IN WHIRL SPEED RATIO

The non-dimensional term 'change in whirl speed ratio' is calculated for each mode shape with constant operating temperature. The change in whirl speed ratio is increasing as the spin speed increases for all the modes, it means the spread between forward whirl and backward whirl increase as the spin speed increases. The whirl speed ratio is more

predominant at the higher modes and at higher speeds. The results are tabulated in Table 6-21 and shown in Figure 6-23.

Table 6-21 Change in whirl speed ratio for T = 150 °C, at different rotor spin speeds

Mode	0 rpm (0 rad/sec)	2000 rpm (209.4 rad/sec)	4000 rpm (418.9 rad/sec)	6000 rpm (628.3 rad/sec)
1st Mode	0.000%	0.065%	0.130%	0.196%
2nd Mode	0.000%	0.146%	0.293%	0.439%
3rd Mode	0.000%	0.301%	0.602%	0.903%
4th Mode	0.000%	0.307%	0.614%	0.921%

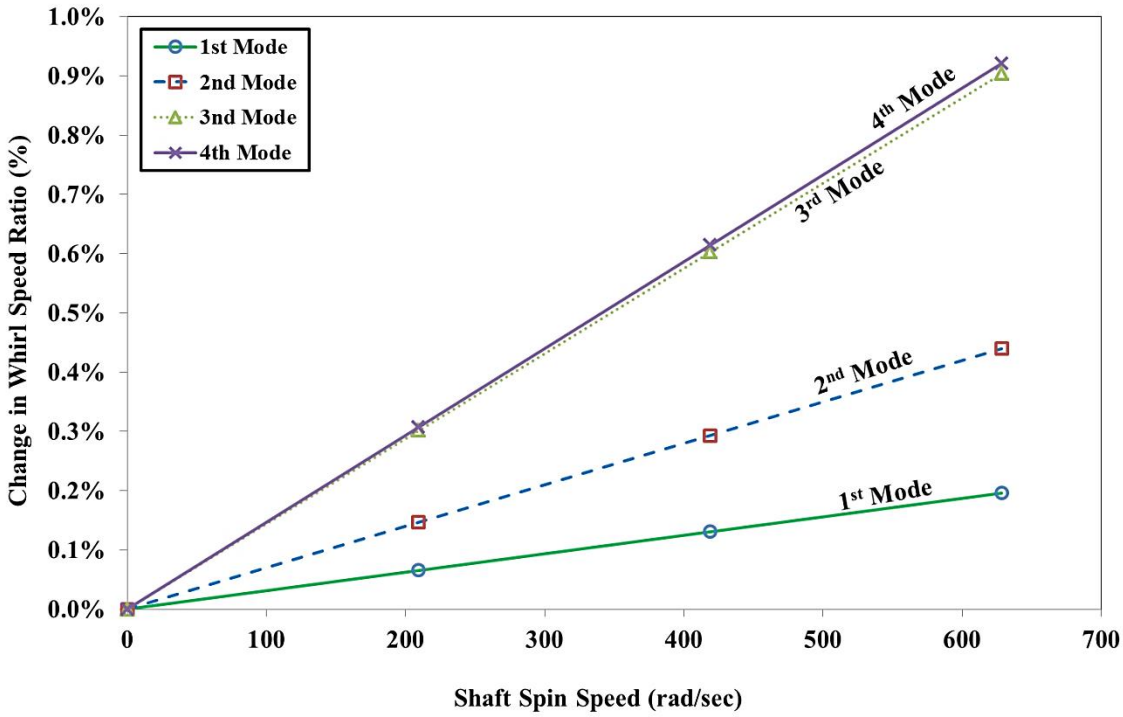

Figure 6-23 Change in Whirl Speed Ratio for Different Modes

The spread between backward whirl speed and forward whirl speed is increasing with increase in the rotor spin speed. This spread is also increasing for higher modes. This spreading effect is due to the contribution of operating temperature. This phenomenon is attributed to adding of the gyroscopic couple.

The sensitivity analysis is carried out on the change in whirl speed ratio with different operating temperature. As the operating temperature increases, the change in whirl speed ratio also increases. The results are tabulated in Table 6-22.

Table 6-22 Change in whirl speed ratio for different rotor spin speeds

	0 rpm (0 rad/sec)	2000 rpm (209.4 rad/sec)	4000 rpm (418.9 rad/sec)	6000 rpm (628.3 rad/sec)
T = 50 °C	0.000%	0.063%	0.125%	0.188%
T = 100 °C	0.000%	0.064%	0.128%	0.191%
T = 150 °C	0.000%	0.065%	0.130%	0.196%

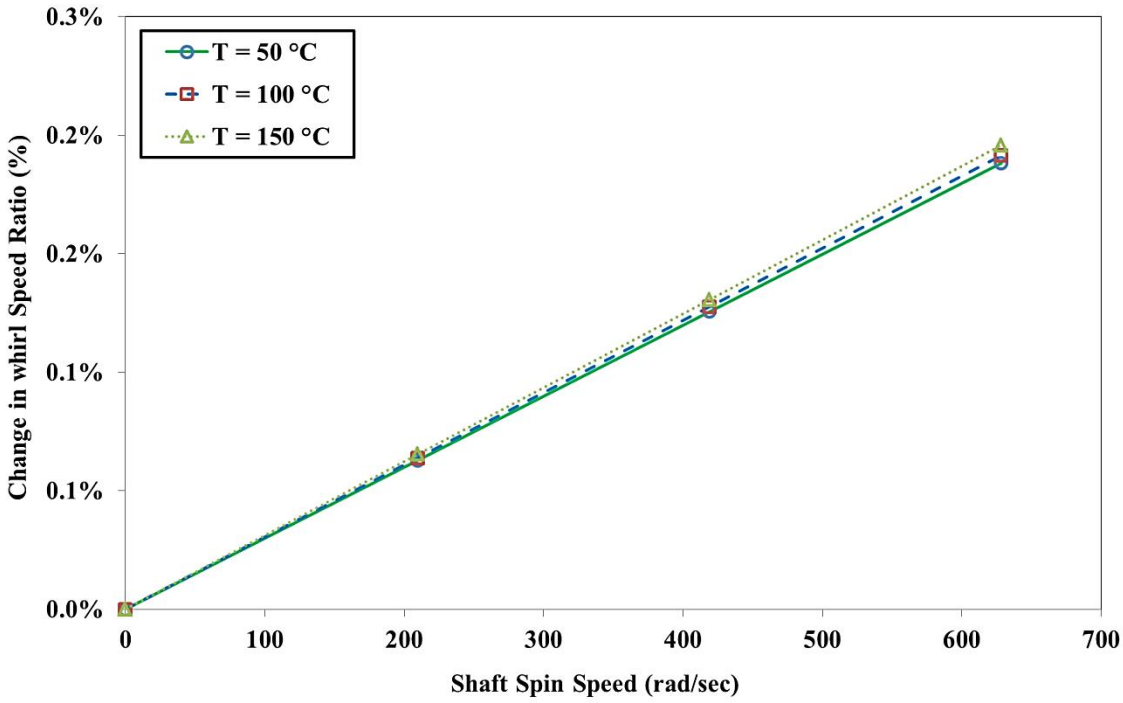

Figure 6-24 Change in Whirl Speed Ratio for 1st Mode

The effect of operating temperature on the change in whirls speed ratio is small as shown in Figure 6-24.

6.7.5 CONCLUSION

The spread between forward whirl speed and backward whirl speed increases with increase in rotor spin speed for all modes. It is clearly observed in Figure 6-23 with the help of whirl speed ratio. The effect of operating temperature is considerable on whirl speeds and critical speeds. Critical speed range or spread is almost same and shifting at the lower side with an increase in operating temperature as shown in Figure 6-22. A clear understanding of operating temperature is very useful while designing rigid and flexible rotors.

6.7.6 APPLICATION

Practical application or situation will be the simple shaft assuming no hysteretic losses and high-temperature ambient conditions supported with anti-friction bearings like ball bearings, roller bearings etc.

e.g. Lab test rig

CHAPTER 7

STUDY ON COMBINED INFLUENCE OF PARAMETERS ON WHIRLING SPEEDS OF ROTOR

Different forms of damping with individual parameters and its effect on rotor backward whirl speed, forward whirl speed and critical speed are studied in the previous chapter. In this chapter, the different forms of damping and operating temperature with all the combinations are discussed. All the forms of damping viz. internal viscous damping, internal hysteretic damping, external viscous damping and operating temperature are simulated with different combinations. The main intension of this chapter is to understand the behavior of the rotor with different forms of damping and operating temperatures acting simultaneously. Computations are done to predict the forward whirl, backward whirl and critical speeds.

7.1 CRITICAL PARAMETERS AND COMBINATIONS

There are different parameters which are the inputs for the rotor dynamic analysis. Below are the lists of parameters or factors (*f*),

1. Internal Viscous Damping (η_v)
2. Internal Hysteretic Damping (η_H)
3. External Viscous Damping (C_e)
4. Operating Temperature (T)

For the simulation studies, the above factors are categorized as "include" and "not include" for the different load cases. These are called as levels (L). There are two levels as,

1. Include
2. Not – Include

The total number of all combinations (N) are calculated as,

$$N = [L]^f \tag{7-1}$$

$$\therefore N = 2^4 = 16$$

All the combinations are listed in Table 7-1,

Table 7-1 Summary of all load cases and its combinations

Sr. No.	External Viscous Damping	Internal Viscous Damping	Internal Hysteresis Damping	Operating Temperature	Combinations Summary
	Ce	η_v	η_H	T	
1	Not - Include	Not - Include	Not - Include	Not - Include	*Baseline**
2	Not - Include	Include	Not - Include	Not - Include	η_v*
3	Not - Include	Not - Include	Include	Not - Include	η_H*
4	Not - Include	Not - Include	Not - Include	Include	T
5	Include	Not - Include	Not - Include	Not - Include	Ce
6	Include	Include	Not - Include	Not - Include	$Ce + \eta_v$
7	Include	Not - Include	Include	Not - Include	$Ce + \eta_H$
8	Include	Not - Include	Not - Include	Include	$Ce + T$
9	Not - Include	Include	Not - Include	Include	$\eta_v + T$
10	Not - Include	Include	Include	Not - Include	$\eta_v + \eta_H$
11	Not - Include	Not - Include	Include	Include	$\eta_H + T$
12	Not - Include	Include	Include	Include	$\eta_v + \eta_H + T$
13	Include	Include	Not - Include	Include	$Ce + \eta_v + T$
14	Include	Not - Include	Include	Include	$Ce + \eta_H + T$
15	Include	Include	Include	Not - Include	$Ce + \eta_v + \eta_H$
16	Include	Include	Include	Include	$Ce + \eta_v + \eta_H + T$

** Models are validated with published data [13]*

In the previous chapter, the influence of individual parameters on rotor whirl speeds and critical speeds are studied. In this chapter, the influence of combined forms of critical parameters with all the possible combination is discussed.

7.2 INTERNAL VISCOUS DAMPING AND EXTERNAL VISCOUS DAMPING ACTING IN COMBINED FORM

This case study includes internal viscous damping (η_v) and external viscous damping (C_e). It does not include internal hysteretic damping (η_H) and operating temperature (T).

Suppressing the operating temperature and different forms of damping in equations (4-75) and (4-86),

- Internal hysteretic damping, $\eta_H = 0$

$$\therefore \eta_a = \frac{1+\eta_H}{\sqrt{1+\eta_H{}^2}} = 1 \text{ and } \therefore \eta_b = \frac{\eta_H}{\sqrt{1+\eta_H{}^2}} + \eta_v\Omega = \eta_v\Omega$$

The equations of motion for internal viscous damping and external viscous damping are expressed,

$$\left[\left[M_T^e\right]+\left[M_R^e\right]\right]\left\{\ddot{\bar{q}}_n^f\right\}+\left[\eta_v\left[K_B^e\right]-\Omega[G]\right]\left\{\dot{\bar{q}}_n^f\right\}+\left[\left[K_B^e\right]+\eta_v\Omega\left[K_C^e\right]\right]\left\{\bar{q}_n^f\right\}=\left\{\bar{F}_n^f\right\} \tag{7-2}$$

$$\begin{bmatrix} C_{xx} & C_{xy} \\ C_{yx} & C_{yy} \end{bmatrix}\left\{\dot{\bar{q}}_n^f\right\}+\begin{bmatrix} K_{xx} & K_{xy} \\ K_{yx} & K_{yy} \end{bmatrix}\left\{\bar{q}_n^f\right\}=\left\{\bar{F}_b^f\right\} \tag{7-3}$$

7.2.1 EFFECT ON WHIRL SPEEDS

Simulation is performed for different internal viscous damping and external viscous damping values in combined form. As the combination of internal viscous damping and external viscous damping increases, the forward whirl and backward whirl speeds are changing based on the contribution of internal viscous damping and external viscous damping. Results are tabulated in Table 7-2.

Table 7-2 Whirl Speeds (rad/sec) at rotor spin speed of 4000 (rpm)

Mode	Ce = 500 N-s/m; η_v = 0.0001 s	Ce = 1000 N-s/m; η_v = 0.00015 s	Ce = 1752 N-s/m; η_v = 0.0002 s
1st BW	519.36	519.53	519.45
1st FW	519.58	519.70	519.96
2nd BW	1091.55	1091.63	1090.85
2nd FW	1094.14	1093.66	1092.42
3rd BW	2215.87	2205.09	2187.02
3rd FW	2229.18	2218.44	2200.47
4th BW	4794.10	4612.52	4338.18
4th FW	4824.28	4643.25	4369.85

7.2.2 WHIRL SPEED AND CAMPBELL DIAGRAM FOR ALL MODES

Simulation is performed at different rotor spin speeds and predicted the forward whirl and backward whirl speeds for a constant combined form of external viscous damping and internal viscous damping to understand the spread between whirl speed for each mode. Results are tabulated in Table 7-3 and shown in Figure 7-1.

Table 7-3 Whirl Speeds (rad/sec) for Ce = 1752 N-s/m and η_v = 0.0002 s, at different rotor spin speeds

Mode	0 rpm (0 rad/sec)	2000 rpm (209.4 rad/sec)	4000 rpm (418.9 rad/sec)	6000 rpm (628.3 rad/sec)
1st BW	519.12	519.14	519.45	520.05
1st FW	519.12	519.40	519.96	520.80
2nd BW	1091.27	1090.98	1090.85	1090.86
2nd FW	1091.27	1091.74	1092.42	1093.31
3rd BW	2192.67	2189.60	2187.02	2184.88
3rd FW	2192.67	2196.28	2200.47	2205.27
4th BW	4346.30	4340.53	4338.18	4338.92
4th FW	4346.30	4355.91	4369.85	4388.70

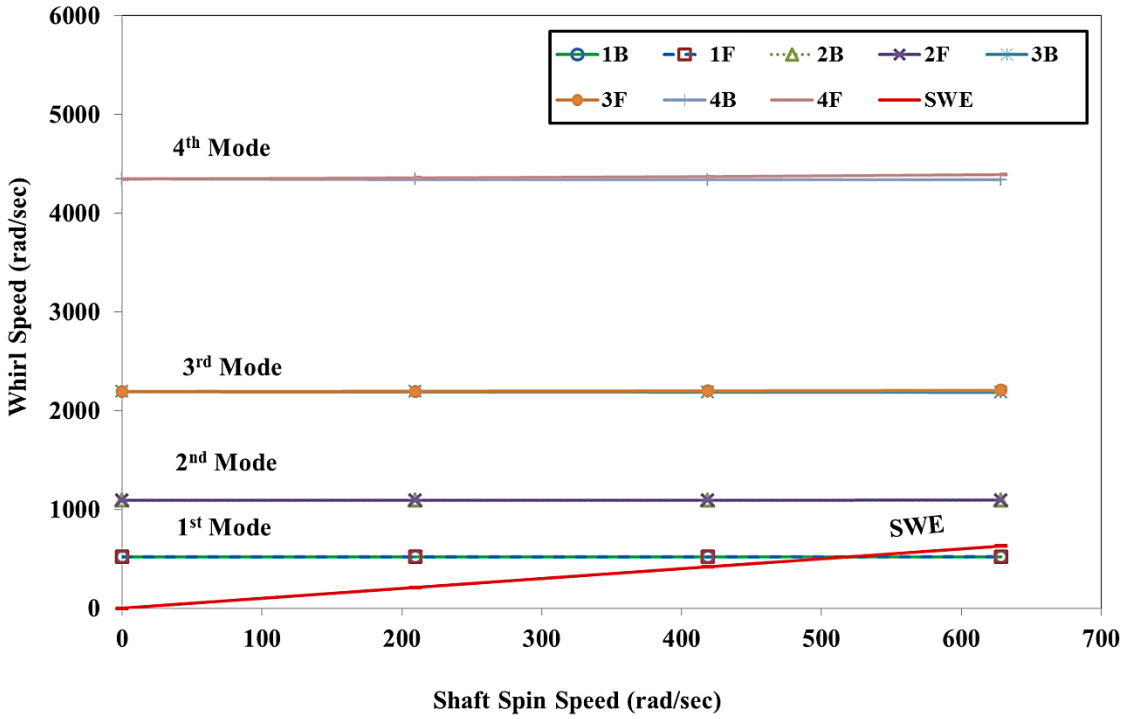

Figure 7-1 Campbell Diagram for Different Modes

Based on the results from Table 7-3 and in Figure 7-1, change in backward whirl speed is small for different rotor spin speeds. The clear trend is observed for forward whirl speed. The forward whirl speed is increasing with increase in rotor spin speed. The forward whirl speed and backward whirl speed are almost same for the first mode.

7.2.3 WHIRL SPEED AND CAMPBELL DIAGRAM FOR FIRST MODE

The forward whirl speed and backward whirl speed are clearly distinguishable. The spread between backward whirl and forward whirl is increasing with increase in the rotor spin speed. The sensitivity analysis is carried out to understand the combined effect of external viscous damping and internal viscous damping on the forward whirl and backward whirl speeds. Results are summarized in Table 7-4 and shown in Figure 7-2.

Table 7-4 Whirl Speeds (rad/sec) for different rotor spin speeds

	1st Mode	0 rpm (0 rad/sec)	2000 rpm (209.4 rad/sec)	4000 rpm (418.9 rad/sec)	6000 rpm (628.3 rad/sec)
Ce = 500 N-s/m; η_v = 0.0001 s	BW	519.32	519.30	519.36	519.48
	FW	519.32	519.42	519.58	519.82
Ce = 1000 N-s/m; η_v = 0.00015 s	BW	519.29	519.33	519.53	519.90
	FW	519.29	519.41	519.70	520.15
Ce = 1752 N-s/m; η_v = 0.0002 s	BW	519.12	519.14	519.45	520.05
	FW	519.12	519.40	519.96	520.80

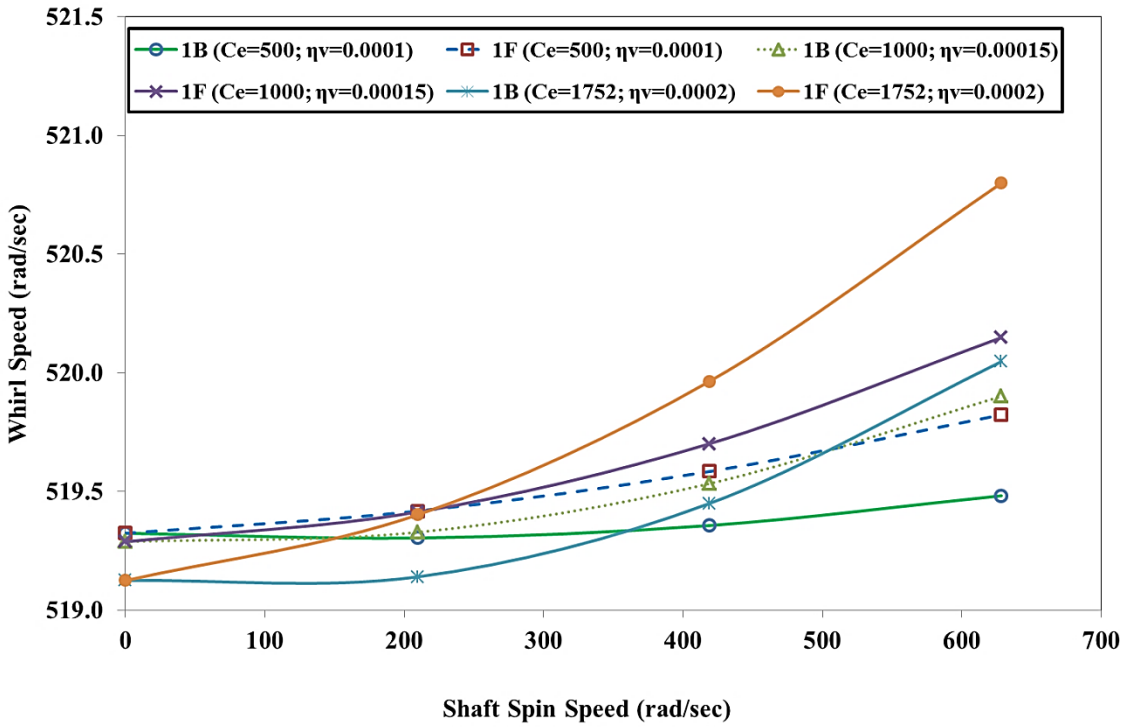

Figure 7-2 Whirl Speed Map for 1st Mode

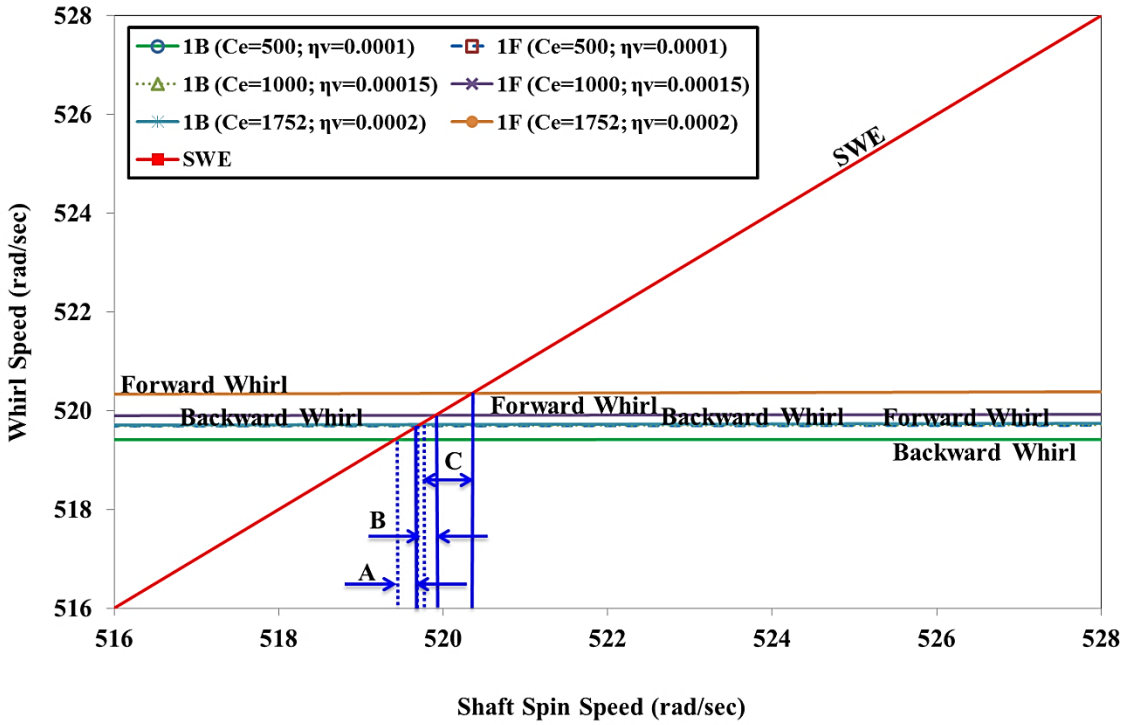

Figure 7-3 Campbell Diagram for 1st Mode

The synchronous whirl excitation is intersecting at two different locations for the first mode. The details of intersection are shown in Figure 7-3 for different combined form of internal viscous damping and external viscous damping values. The range between backward critical speed and forward critical speed ranges are shown as 'A', 'B' and 'C'. These ranges are based on the contribution of internal viscous damping and external viscous damping. As the internal viscous damping and external viscous damping increases, these ranges are increasing and shifting proportionately at a higher level. If the rotor operating spin speed is within this range 'A' 'B' and 'C', there will be the unbounded amplitude of vibration which results into rotor failure. To mitigate this risk and to avoid resonance, only two options are available, either rotor should redesign in such a way that the range 'A' 'B' and 'C' will get shifted from the operating speed or operate spin speed needs to change. This information is very useful in the design stage of the rotor.

7.2.4 CHANGE IN WHIRL SPEED RATIO

The non-dimensional term 'change in whirl speed ratio' is calculated for each mode for a given constant combined form of internal viscous damping and external viscous damping values. This parameter is increasing as the spin speed increases; it means the spread

between forward whirl and backward increases as the spin speed increases. The whirl speed ratio is more predominant at the higher modes as shown in Figure 7-4. The results are tabulated in Table 7-5.

Table 7-5 Change in whirl speed ratio for Ce = 1752 N-sec/m and η_v=0.0002 s, at different rotor spin speeds

Mode	0 rpm (0 rad/sec)	2000 rpm (209.4 rad/sec)	4000 rpm (418.9 rad/sec)	6000 rpm (628.3 rad/sec)
1st Mode	0.000%	0.050%	0.099%	0.145%
2nd Mode	0.000%	0.070%	0.144%	0.224%
3rd Mode	0.000%	0.304%	0.613%	0.930%
4th Mode	0.000%	0.354%	0.729%	1.145%

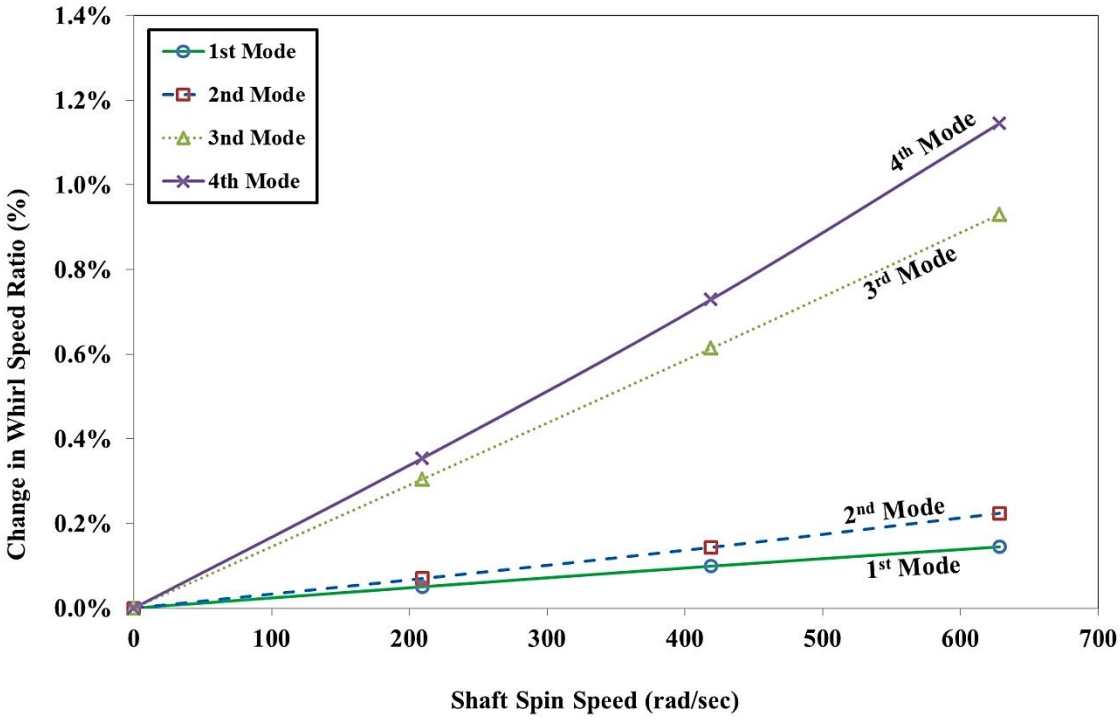

Figure 7-4 Change in Whirl Speed Ratio for Different Modes

The spread between backward whirl speed and forward whirl speed is increasing with increasing the rotor spin speed. This spread is also increasing with higher modes. This spreading effect is due to the contribution of combined form of internal viscous damping and external viscous damping. This phenomenon is attributed for adding the effect of the gyroscopic couple.

The sensitivity analysis is carried out on the change in whirl speed ratio with the combined effect of increasing external viscous damping and internal viscous damping. As these combined form of damping increases, the change in whirl speed ratio changes. The results are tabulated in Table 7-6 and shown in Figure 7-5.

Table 7-6 Change in whirl speed ratio for different rotor spin speeds

	0 rpm (0 rad/sec)	2000 rpm (209.4 rad/sec)	4000 rpm (418.9 rad/sec)	6000 rpm (628.3 rad/sec)
Ce = 500 N-s/m; η_v = 0.0001 s	0.000%	0.022%	0.044%	0.066%
Ce = 1000 N-s/m; η_v = 0.00015 s	0.000%	0.016%	0.032%	0.048%
Ce = 1752 N-s/m; η_v = 0.0002 s	0.000%	0.050%	0.099%	0.145%

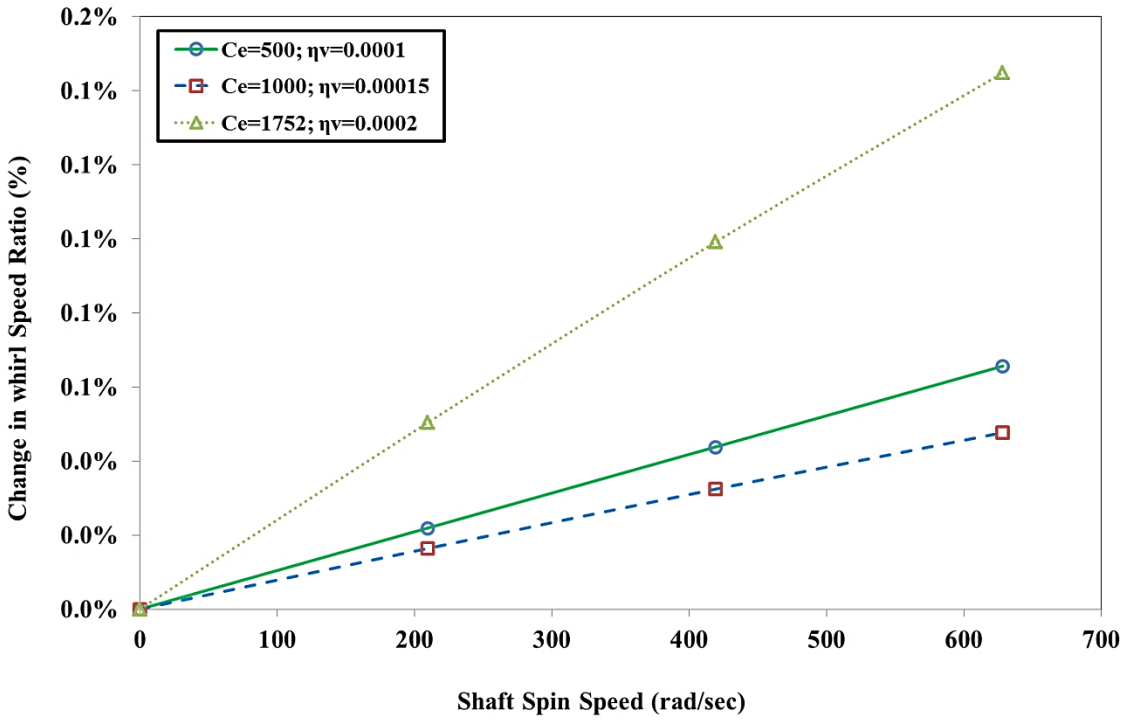

Figure 7-5 Change in Whirl Speed Ratio for 1st Mode

7.2.5 CONCLUSION

The spread between forward whirl speed and backward whirl speed increases with increase in rotor spin speed for all modes. This spread is larger for higher modes and at higher speeds. This is clearly observed in Figure 7-4 with the help of whirl speed ratio. Critical speed

range or spread is also increasing and shifting at higher side with an increase in combined form of internal viscous damping and external viscous damping as shown in Figure 7-3. A clear understanding of the combined damping of internal viscous damping and external viscous damping is very useful while designing the rotors.

7.2.6 APPLICATION

Practical application or situation will be the different parts or components mounted on the shaft with shrink fit and supported by sleeve bearings. The hysteretic losses in the shaft are assumed to be negligible. The operating temperature is not critical. e.g. Fan, hub, coupling, balance ring etc mounted on the shaft with shrink fit and shaft is supported by sleeve bearings.

e.g. Belt conveyor shaft.

7.3 INTERNAL HYSTERETIC DAMPING AND EXTERNAL VISCOUS DAMPING ACTING IN COMBINED FORM

This case study includes internal hysteretic damping (η_H) and external viscous damping (C_e). It does not include internal viscous damping (η_v) and operating temperature (T).

Suppressing the operating temperature and different forms of damping in equations (4-75) and (4-86),

- Internal viscous damping, $\eta_v = 0$

$$\therefore \eta_a = \frac{1+\eta_H}{\sqrt{1+\eta_H{}^2}} \text{ ; and } \therefore \eta_b = \frac{\eta_H}{\sqrt{1+\eta_H{}^2}} + \eta_v\Omega = \frac{\eta_H}{\sqrt{1+\eta_H{}^2}}$$

The equations of motion for internal hysteretic damping and external viscous damping are expressed,

$$\left[\left[M_T^e\right]+\left[M_R^e\right]\right]\left\{\ddot{\bar{q}}_n^f\right\}-\Omega\left[G^e\right]\left\{\dot{\bar{q}}_n^f\right\}+\left[\frac{1+\eta_H}{\sqrt{1+\eta_H^2}}\left[K_B^e\right]+\frac{\eta_H}{\sqrt{1+\eta_H^2}}\left[K_C^e\right]\right]\left\{\bar{q}_n^f\right\}=\left\{\bar{F}_n^f\right\} \quad (7\text{-}4)$$

$$\begin{bmatrix} C_{xx} & C_{xy} \\ C_{yx} & C_{yy} \end{bmatrix}\left\{\dot{\bar{q}}_n^f\right\}+\begin{bmatrix} K_{xx} & K_{xy} \\ K_{yx} & K_{yy} \end{bmatrix}\left\{\bar{q}_n^f\right\}=\left\{\bar{F}_b^f\right\} \quad (7\text{-}5)$$

7.3.1 EFFECT ON WHIRL SPEEDS

Simulation is performed for different internal hysteretic damping and external viscous damping values. As these combined forms of internal hysteretic damping and external viscous damping increases, the forward whirl and backward whirl speeds are also increasing for all the modes. Results are tabulated in Table 7-7.

Table 7-7 Whirl Speeds (rad/sec) at rotor spin speed of 4000 (rpm)

Mode	Ce = 500 (N-s/m); η_H = 0.0002	Ce = 1000 (N-s/m); η_H = 0.0025	Ce = 1752 (N-s/m); η_H = 0.005
1st BW	519.00	519.25	519.56
1st FW	519.64	519.92	520.28
2nd BW	1091.01	1090.89	1090.38
2nd FW	1094.21	1094.12	1093.69
3rd BW	2223.10	2224.18	2224.48
3rd FW	2236.42	2237.50	2237.82
4th BW	4931.57	4936.27	4940.40
4th FW	4961.45	4966.14	4970.26

7.3.2 WHIRL SPEED AND CAMPBELL DIAGRAM FOR ALL MODES

Simulation is performed at different rotor spin speeds and predicted the forward whirl and backward whirl speeds. This involves constant combined forms of external viscous damping and internal hysteretic damping to understand the spread between whirl speed for each mode. Results are tabulated in Table 7-8 and shown in shown in Figure 7-6.

Table 7-8 Whirl Speeds (rad/sec) for Ce = 1752 N-s/m and η_H = 0.005, at different rotor spin speeds

Mode	0 rpm (0 rad/sec)	2000 rpm (209.4 rad/sec)	4000 rpm (418.9 rad/sec)	6000 rpm (628.3 rad/sec)
1st BW	519.96	519.73	519.56	519.40
1st FW	519.96	520.12	520.28	520.44
2nd BW	1092.09	1091.18	1090.38	1089.58
2nd FW	1092.09	1092.89	1093.69	1094.49
3rd BW	2231.14	2227.80	2224.48	2221.16
3rd FW	2231.14	2234.47	2237.82	2241.16
4th BW	4955.30	4947.86	4940.40	4932.96
4th FW	4955.30	4962.78	4970.26	4977.76

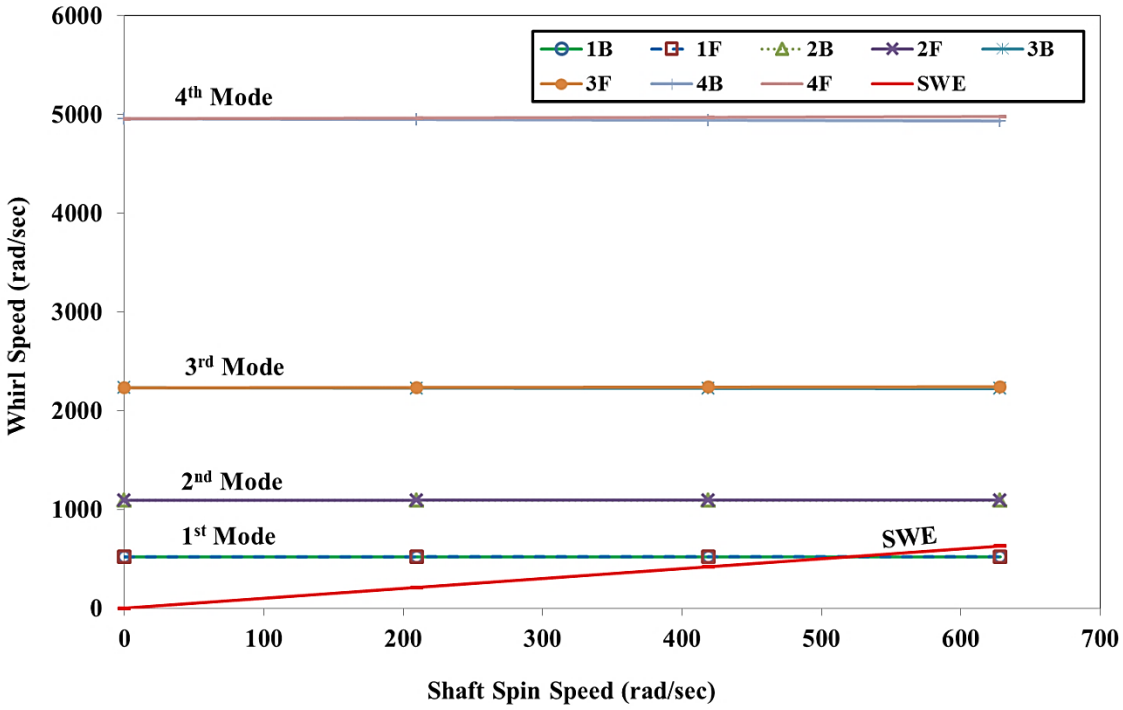

Figure 7-6 Campbell Diagram for Different Modes

7.3.3 WHIRL SPEED AND CAMPBELL DIAGRAM FOR FIRST MODE

The forward whirl speed and backward whirl speed are clearly distinguishable. The spread between backward whirl speed and forward whirl speed is increasing with increase in the rotor spin speed. The sensitivity analysis is carried out to understand the combined effect of external viscous damping and internal hysteretic damping on the forward whirl and backward whirl speeds. Results are summarized in Table 7-9.

Table 7-9 Whirl Speeds (rad/sec) for different rotor spin speeds

	1st Mode	0 rpm (0 rad/sec)	2000 rpm (209.4 rad/sec)	4000 rpm (418.9 rad/sec)	6000 rpm (628.3 rad/sec)
Ce = 500 N-s/m; η_H = 0.0002	BW	519.32	519.16	519.00	518.83
	FW	519.32	519.48	519.64	519.80
Ce = 1000 N-s/m; η_H = 0.0025	BW	519.60	519.41	519.25	519.09
	FW	519.60	519.76	519.92	520.08
Ce = 1752 N-s/m; η_H = 0.005	BW	519.96	519.73	519.56	519.40
	FW	519.96	520.12	520.28	520.44

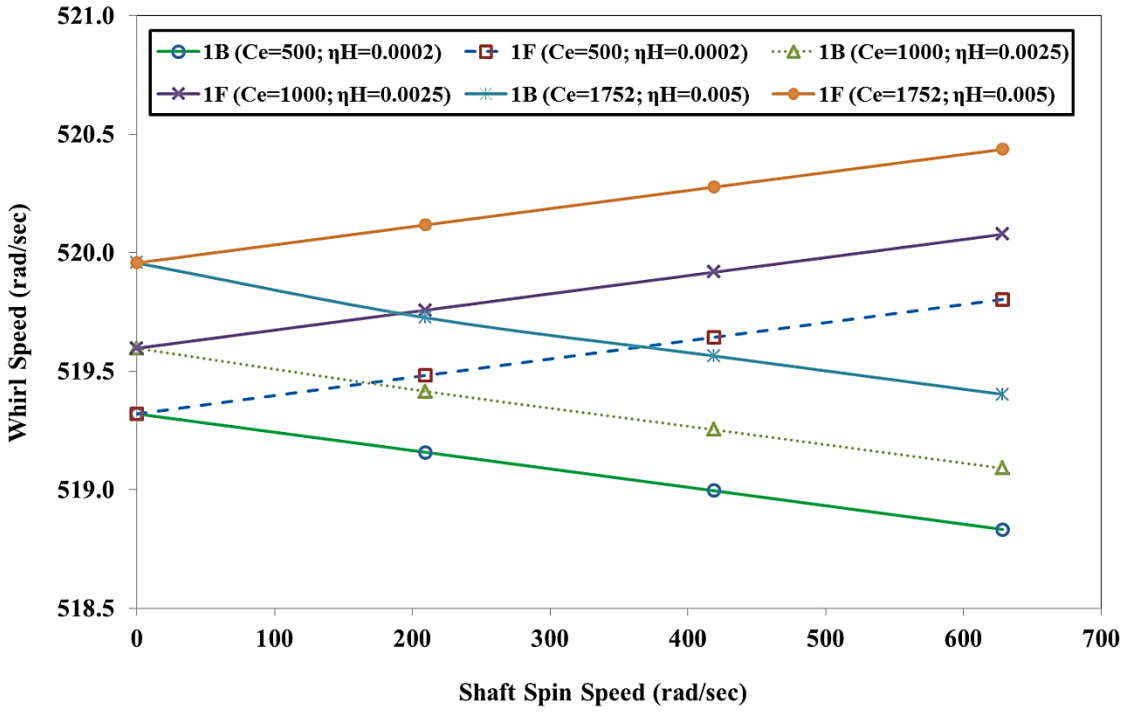

Figure 7-7 Whirl Speed Map for 1st Mode

With the addition of these damping, the starting point of the forward whirl and backward whirl at zero spin speed gets offset. This offset is increasing higher level with increasing these combined damping. Results are shown in Figure 7-7.

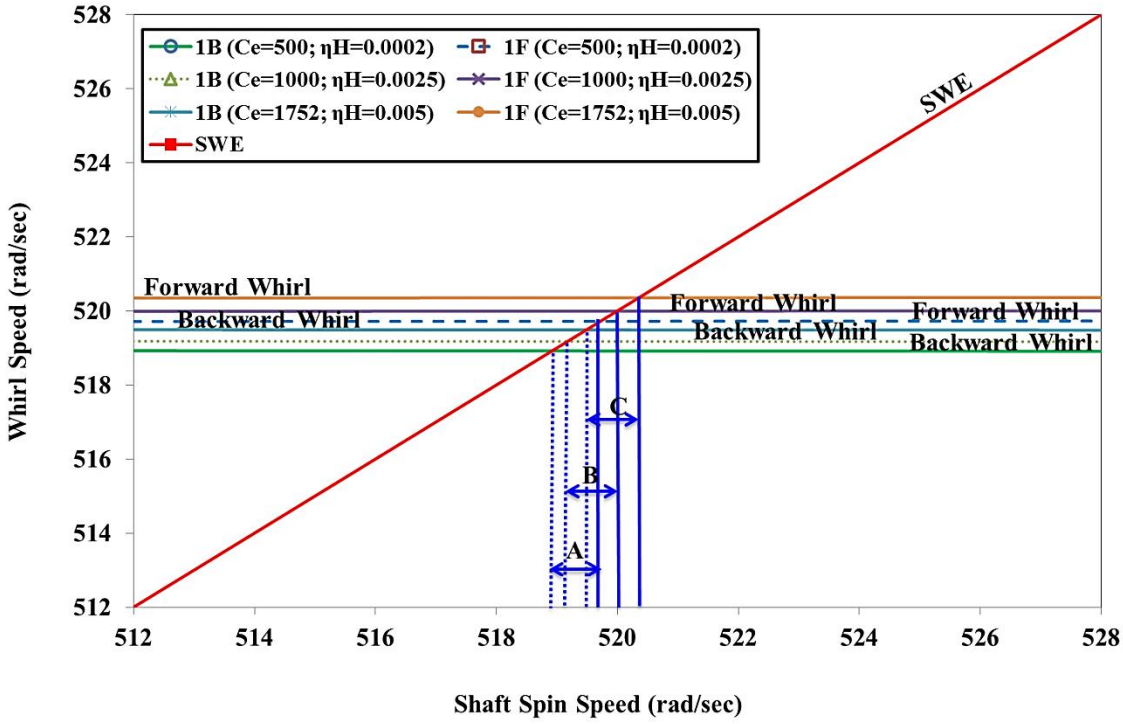

Figure 7-8 Campbell Diagram for 1st Mode

The synchronous whirl excitation is intersecting at two different locations for the first mode. The details of intersection are shown in Figure 7-8 for different combined form of internal hysteretic damping and external viscous damping values. The range between backward critical speed and forward critical speed ranges are shown as ‘A’, ‘B’ and ‘C’. These ranges are based on the contribution of combined form of internal hysteretic damping and external viscous damping. As the combination of internal hysteretic damping and external viscous damping increases, these ranges are increasing and shifting proportionately at a higher level. If the rotor operating spin speed is within this range ‘A’ ‘B’ and ‘C’, there will be the unbounded amplitude of vibration which results into rotor failure. To mitigate this risk and to avoid resonance, only two options are available, either rotor should redesign in such a way that the range ‘A’ ‘B’ and ‘C’ will get shifted from the operating speed or operate spin speed needs to change. This information is very useful in the design stage of the rotor.

7.3.4 CHANGE IN WHIRL SPEED RATIO

The non-dimensional term 'change in whirl speed ratio' is calculated for each mode with constant internal hysteretic damping and external viscous damping. This parameter is increasing as the spin speed increases; it means the gap between forward whirl and backward increase as the spin speed increases. The whirl speed ratio is more predominant in the higher modes. The results are tabulated in Table 7-10 and shown in Figure 7-9.

Table 7-10 Change in whirl speed ratio for Ce = 1752 N-s/m; η_H = 0.005, at different rotor spin speeds

Mode	0 rpm (0 rad/sec)	2000 rpm (209.4 rad/sec)	4000 rpm (418.9 rad/sec)	6000 rpm (628.3 rad/sec)
1st Mode	0.000%	0.075%	0.137%	0.199%
2nd Mode	0.000%	0.156%	0.303%	0.450%
3rd Mode	0.000%	0.299%	0.598%	0.897%
4th Mode	0.000%	0.301%	0.603%	0.904%

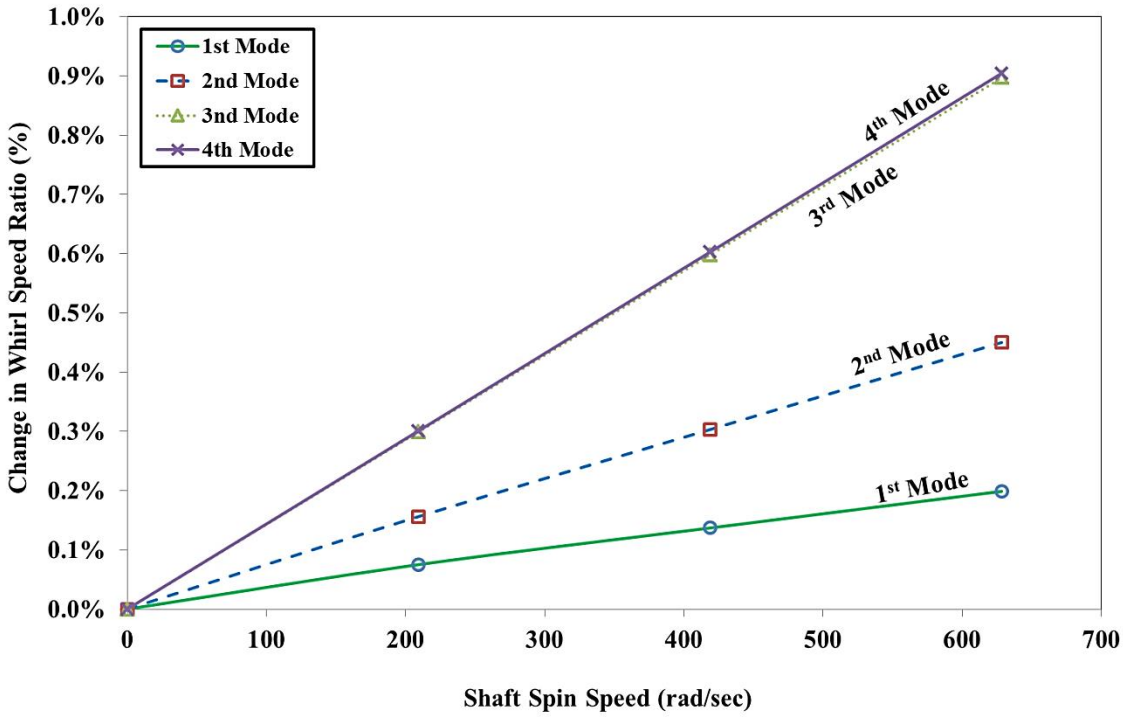

Figure 7-9 Change in Whirl Speed Ratio for Different Modes

This spreading effect is due to the contribution of combined form of internal hysteretic damping and external viscous damping. This phenomenon is attributed for adding effect for a gyroscopic couple.

The sensitivity analysis also carried out on the change in whirl speed ratio with increasing the combination of external viscous damping and internal hysteretic damping. As this combination increases, the change in whirl speed ratio increases. In conclusion, this combination is contributing to the gyroscopic effect. The results are tabulated in Table 7-11 and shown in Figure 7-10.

Table 7-11 Change in whirl speed ratio for different rotor spin speeds

	0 rpm (0 rad/sec)	2000 rpm (209.4 rad/sec)	4000 rpm (418.9 rad/sec)	6000 rpm (628.3 rad/sec)
Ce = 500 N-s/m; η_H = 0.0002	0.000%	0.062%	0.125%	0.187%
Ce = 1000 N-s/m; η_H = 0.0025	0.000%	0.066%	0.128%	0.190%
Ce = 1752 N-s/m; η_H = 0.005	0.000%	0.075%	0.137%	0.199%

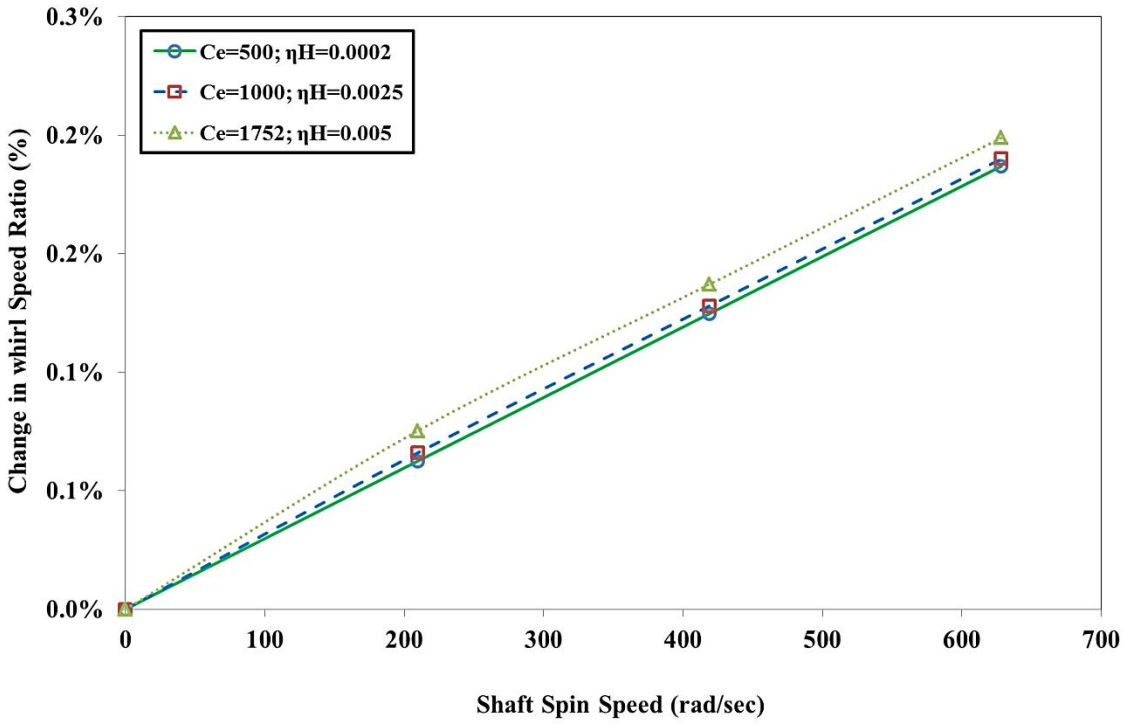

Figure 7-10 Change in Whirl Speed Ratio for 1st Mode

7.3.5 CONCLUSION

The spread between forward whirl speed and backward whirl speed increases with increase in rotor spin speed for all modes. This spread is larger for higher modes and at higher speeds. This is clearly observed in Figure 7-9 with the help of whirl speed ratio. Critical speed range or spread remains constant and shifting at higher side with an increase in combined form of internal hysteretic damping and external viscous damping as shown in Figure 7-8. A clear understanding of the combined damping of internal hysteretic damping and external viscous damping is very useful while designing flexible and rigid rotors.

7.3.6 APPLICATION

Practical application or situation will be the simple shaft supported on sleeve bearings. The operating temperature is not critical.

e.g. Large drive shaft.

7.4 INTERNAL VISCOUS DAMPING AND INTERNAL HYSTERETIC DAMPING ACTING IN COMBINED FORM

This case study includes internal viscous damping (η_v) and internal hysteretic damping (η_H). It does not include external viscous damping (C_e) and operating temperature (T).

Suppressing the operating temperature and different forms of damping in equations (4-75) and (4-86),

- External viscous damping, $C_{xx} = 0$, $C_{yy} = 0$, $C_{xy} = 0$ and $C_{yx} = 0$

$\therefore \eta_a = \dfrac{1+\eta_H}{\sqrt{1+\eta_H{}^2}}$; and $\therefore \eta_b = \dfrac{\eta_H}{\sqrt{1+\eta_H{}^2}} + \eta_v \Omega$

The equations of motion for internal viscous damping and internal hysteretic damping is expressed,

$$\left[\left[M_T^e\right]+\left[M_R^e\right]\right]\left\{\ddot{\bar{q}}_n^f\right\}+\left[\eta_v\left[K_B^e\right]-\Omega[G]\right]\left\{\dot{\bar{q}}_n^f\right\}+\left[\eta_a\left[K_B^e\right]+\eta_b\left[K_C^e\right]\right]\left\{\bar{q}_n^f\right\}=\left\{\bar{F}_n^f\right\} \quad (7\text{-}6)$$

7.4.1 EFFECT ON WHIRL SPEEDS

Simulation is performed for different internal viscous damping and internal hysteretic damping values. As the combination of internal viscous damping and internal hysteretic damping increases, the forward and backward whirl speeds are also increasing for the first and second mode only. For the higher modes, the forward whirl and backward whirl decreases with increasing these damping. Results are tabulated in Table 7-12.

Table 7-12 Whirl Speeds (rad/sec) at rotor spin speed of 4000 (rpm)

Mode	η_v = 0.0001 s; η_H = 0.0002	η_v = 0.00015 s; η_H = 0.0025	η_v = 0.0002 s; η_H = 0.005
1st BW	519.58	519.88	520.14
1st FW	519.64	520.60	521.95
2nd BW	1092.11	1093.47	1095.13
2nd FW	1094.45	1094.75	1095.24
3rd BW	2217.93	2212.80	2204.95
3rd FW	2231.25	2226.21	2218.65
4th BW	4799.79	4635.30	4393.06
4th FW	4830.05	4666.36	4425.58

7.4.2 WHIRL SPEED AND CAMPBELL DIAGRAM FOR ALL MODES

Simulation is performed at different rotor spin speeds and predicted the forward whirl and backward whirl speeds for constant internal viscous damping and internal hysteretic damping to understand the spread between whirl speed for each mode. Results are tabulated in Table 7-13.

Table 7-13 Whirl Speeds (rad/sec) for η_V = 0.0002 s and η_H=0.005, at different rotor spin speeds

Mode	0 rpm (0 rad/sec)	2000 rpm (209.4 rad/sec)	4000 rpm (418.9 rad/sec)	6000 rpm (628.3 rad/sec)
1st BW	520.33	520.09	520.14	520.48
1st FW	520.33	521.07	521.95	523.09
2nd BW	1094.73	1094.84	1095.13	1095.56
2nd FW	1094.73	1095.01	1095.24	1095.62
3rd BW	2210.68	2207.59	2204.95	2202.71
3rd FW	2210.68	2214.39	2218.65	2223.48
4th BW	4400.90	4395.34	4393.06	4393.75
4th FW	4400.90	4411.15	4425.58	4444.75

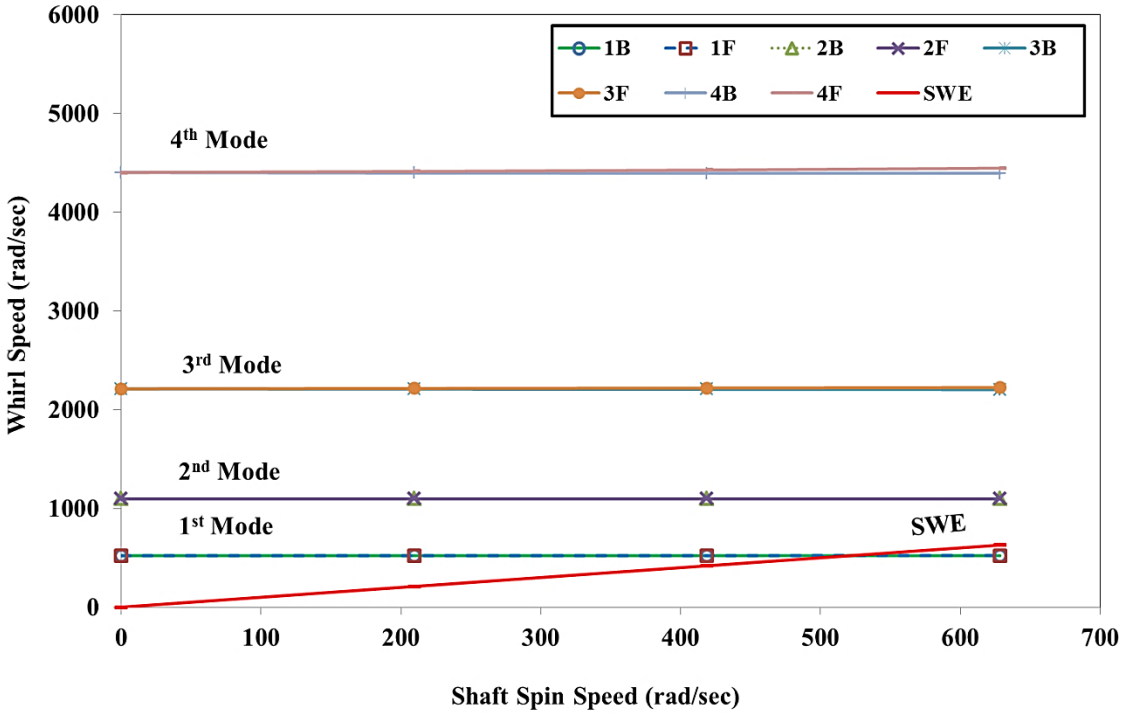

Figure 7-11 Campbell Diagram for Different Modes

7.4.3 WHIRL SPEED AND CAMPBELL DIAGRAM FOR FIRST MODE

The forward whirl speeds and backward whirl speeds are clearly distinguishable. The sensitivity analysis is carried out to understand the combined effect of internal viscous damping and internal hysteretic damping. Results are summarized in Table 7-14.

Table 7-14 Whirl Speeds (rad/sec) for different rotor spin speeds

	1st Mode	0 rpm (0 rad/sec)	2000 rpm (209.4 rad/sec)	4000 rpm (418.9 rad/sec)	6000 rpm (628.3 rad/sec)
η_v = 0.0001 s; η_H = 0.0002	BW	519.46	519.48	519.58	519.75
	FW	519.46	519.51	519.64	519.83
η_v = 0.00015 s; η_H = 0.0025	BW	519.86	519.79	519.88	520.13
	FW	519.86	520.17	520.60	521.18
η_v = 0.0002 s; η_H = 0.005	BW	520.33	520.09	520.14	520.48
	FW	520.33	521.07	521.95	523.09

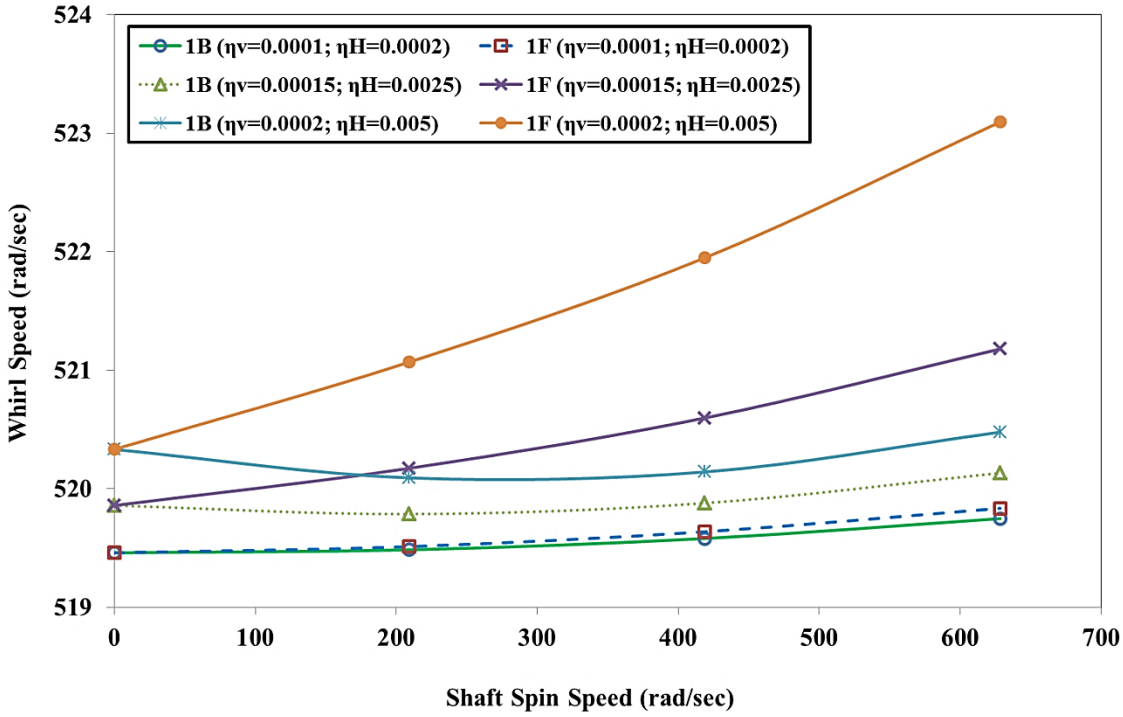

Figure 7-12 Whirl Speed Map for 1st Mode

With the addition of these damping, the starting point of the forward whirl and backward whirl at zero spin speed gets offset. This offset is increasing with increasing these combined damping. Results are shown in Figure 7-12.

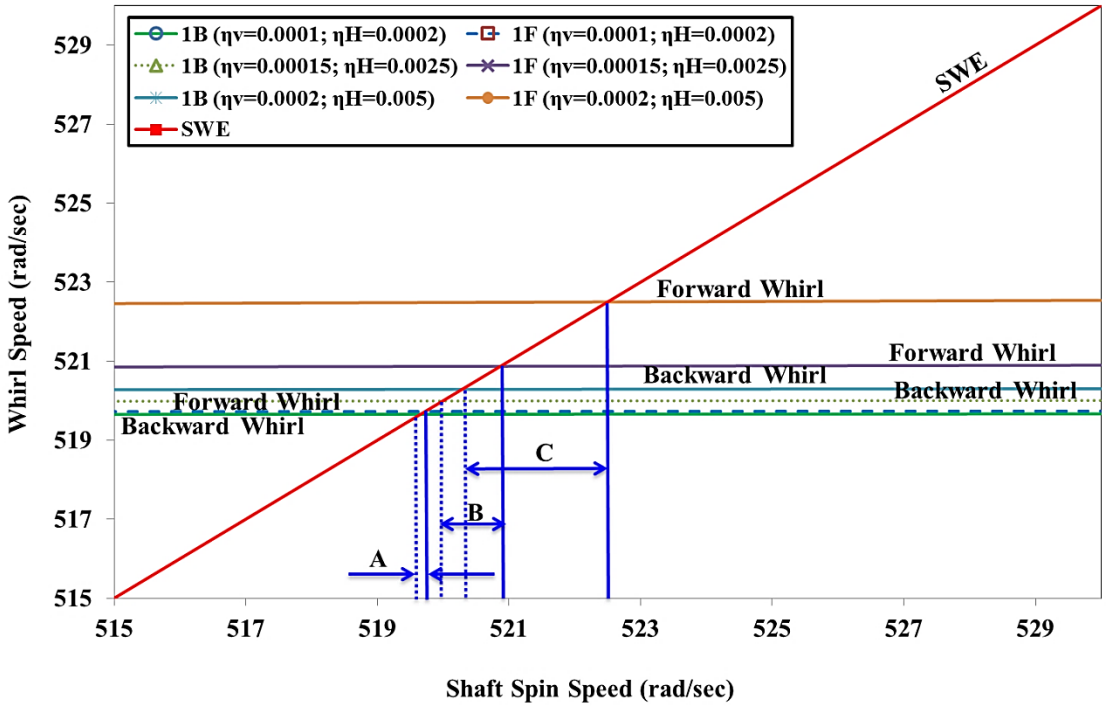

Figure 7-13 Campbell Diagram for 1st Mode

The synchronous whirl excitation is intersecting at two different locations for the first mode. The details of intersection are shown in Figure 7-13 for different combined form of internal viscous damping and internal hysteretic damping. The range between backward critical speed and forward critical speed ranges are shown as 'A', 'B' and 'C'. These ranges are based on the contribution of internal viscous damping and internal hysteretic damping. As the internal viscous damping and internal hysteretic damping increases, these ranges are increasing and shifting proportionately at a higher level. If the rotor operating spin speed is within this range 'A' 'B' and 'C', there will be the unbounded amplitude of vibration which results into rotor failure. To mitigate this risk and to avoid resonance, only two options are available, either rotor should redesign in such a way that the range 'A' 'B' and 'C' will get shifted from the operating speed or operate spin speed needs to change. This information is very useful in the design stage of the rotor.

7.4.4 CHANGE IN WHIRL SPEED RATIO

The non-dimensional term 'change in whirl speed ratio' is calculated for each mode shape with combined form of constant internal viscous damping and internal hysteretic damping. This parameter is increasing as the spin speed increases for all the modes; it means the spread between forward whirl and backward increases as the spin speed increases. The whirl speed ratio is more predominant at higher modes and at a higher speed. The results are tabulated in Table 7-15 and shown in Figure 7-14.

Table 7-15 Change in whirl speed ratio for $\eta_v = 0.0002$ s and $\eta_H = 0.005$, at different rotor spin speeds

Mode	0 rpm (0 rad/sec)	2000 rpm (209.4 rad/sec)	4000 rpm (418.9 rad/sec)	6000 rpm (628.3 rad/sec)
1st Mode	0.000%	0.188%	0.347%	0.503%
2nd Mode	0.000%	0.016%	0.010%	0.005%
3rd Mode	0.000%	0.308%	0.619%	0.939%
4th Mode	0.000%	0.359%	0.739%	1.159%

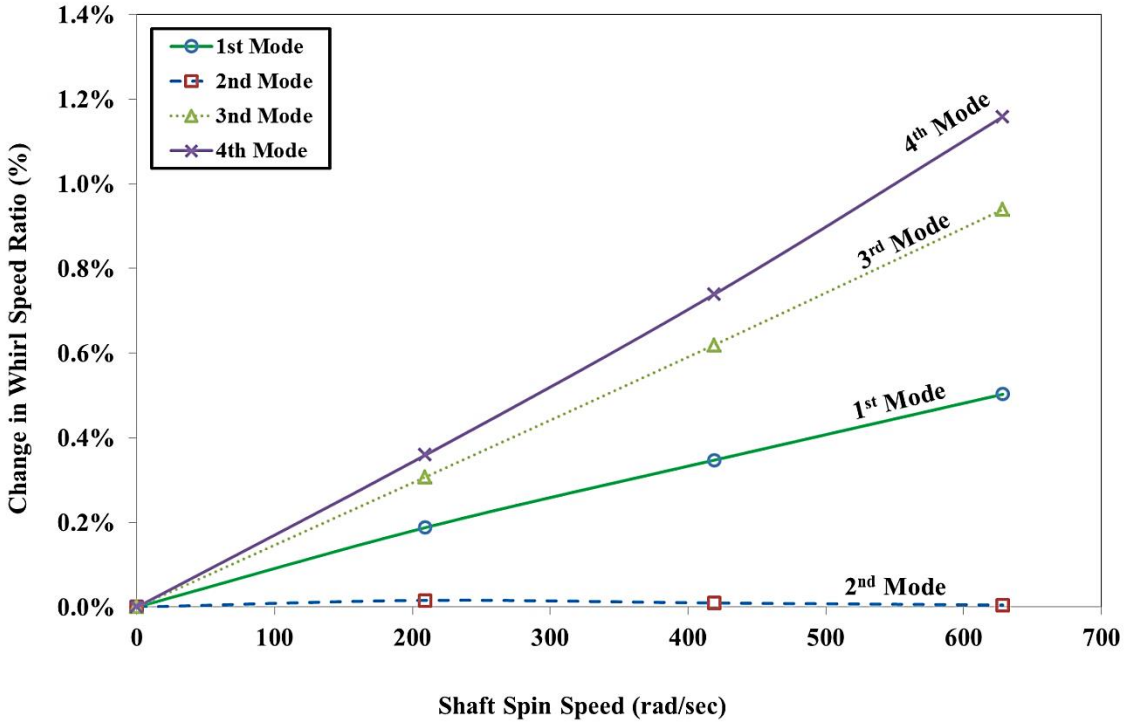

Figure 7-14 Change in Whirl Speed Ratio for Different Modes

The spread between backward whirl speed and forward whirl speed is increasing with increase in the rotor spin speed. This spread is also increasing with higher modes. This spreading effect is due to the contribution of the combination of internal viscous damping and internal hysteretic damping. This phenomenon is attributed to the adding effect for the gyroscopic couple.

The sensitivity analysis also carried out on the change in whirl speed ratio with increasing the combination of internal viscous damping and internal hysteretic damping. As the internal viscous damping and internal hysteretic damping increases, the change in whirl speed ratio increases. The results are tabulated in Table 7-16 and shown in Figure 7-15.

Table 7-16 Change in whirl speed ratio for different rotor spin speeds

	0 rpm (0 rad/sec)	2000 rpm (209.4 rad/sec)	4000 rpm (418.9 rad/sec)	6000 rpm (628.3 rad/sec)
η_v = 0.0001 s; η_H = 0.0002	0.000%	0.005%	0.011%	0.017%
η_v = 0.00015 s; η_H = 0.0025	0.000%	0.074%	0.138%	0.201%
η_v = 0.0002 s; η_H = 0.005	0.000%	0.188%	0.347%	0.503%

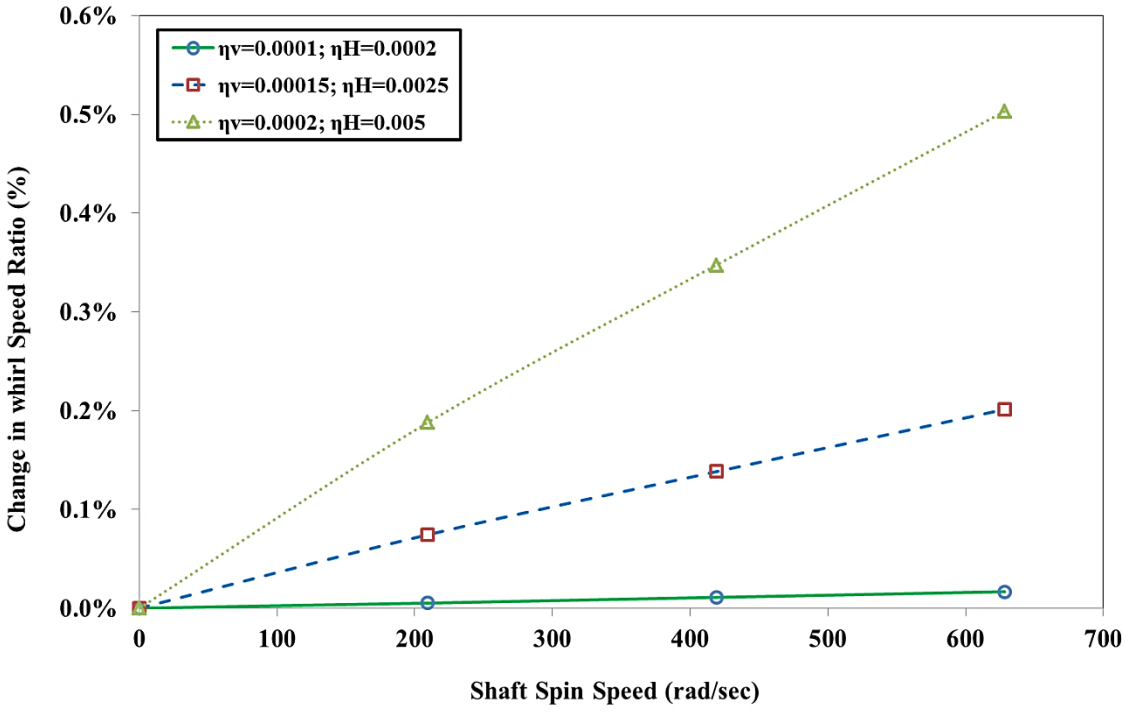

Figure 7-15 Change in Whirl Speed Ratio for 1st Mode

This combined damping is contributing to the gyroscopic effect as shown in Figure 7-15.

7.4.5 CONCLUSION

The spread between forward whirl speed and backward whirl speed increases with increase in rotor spin speed for all modes except for the second mode. This interesting phenomenon is observed only for the second mode. The spread between forward whirl and backward whirl for second is very small and this phenomenon is attributed towards nullifying the effect of the gyroscopic couple. The spread is large for the first, third and fourth mode. It is clearly observed in Figure 7-14 with the help of whirl speed ratio. Critical speed range or spread is increasing with the larger magnitude and shifting at higher side with an increase in combined form of internal viscous damping and internal hysteretic viscous damping as shown in Figure 7-13. A clear understanding of the combined form of internal viscous damping and internal hysteretic viscous damping is very useful while designing the rotors.

7.4.6 APPLICATION

Practical application or situation will be the different parts or components mounted on the shaft with shrink fit and operating temperature is not critical and external viscous damping is not present. e.g. Fan, hub, coupling, balance ring etc mounted on the shaft with shrink fit, the shaft itself is having hysteretic loss and shaft is supported with anti-friction bearings like ball bearings, roller bearings.
e.g. Marine propeller shaft

7.5 OPERATING TEMPERATURE AND INTERNAL VISCOUS DAMPING ACTING IN COMBINED FORM

This case study includes operating temperature (T) and internal viscous damping (η_v). It does not include internal hysteretic damping (η_H) and external viscous damping (C_e).

Suppressing the different forms of damping in equations (4-75) and (4-86),

- External viscous damping, $C_{xx} = 0$, $C_{yy} = 0$, $C_{xy} = 0$ and $C_{yx} = 0$

- Internal hysteretic damping, $\eta_H = 0$

$$\therefore \eta_a = \frac{1+\eta_H}{\sqrt{1+\eta_H{}^2}} = 1; \text{ and } \therefore \eta_b = \frac{\eta_H}{\sqrt{1+\eta_H{}^2}} + \eta_v \Omega = \eta_v \Omega$$

The equations of motion for operating temperature and internal viscous damping is expressed,

$$\left[\left[M_{Tt}^e\right] + \left[M_{Rt}^e\right]\right]\left\{\ddot{\bar{q}}_n^f\right\} + \left[\eta_v\left[K_{Bt}^e\right] - \Omega\left[G_t^e\right]\right]\left\{\dot{\bar{q}}_n^f\right\} + \left[\left[K_{Bt}^e\right] + \eta_v\Omega\left[K_{Ct}^e\right]\right]\left\{\bar{q}_n^f\right\} = \left\{\bar{F}_n^f\right\} \quad (7\text{-}7)$$

7.5.1 EFFECT ON WHIRL SPEEDS

Simulation is performed for different operating temperature and internal viscous damping values. As the combinations of operating temperature and internal viscous damping increases, the forward whirl and backward whirl speeds changes based on the contribution of operating temperature and internal viscous damping. Results are tabulated in Table 7-17.

Table 7-17 Whirl Speeds (rad/sec) at rotor spin speed of 4000 (rpm)

Mode	T = 50 °C; η_v = 0.0001 s	T = 100 °C; η_v = 0.00015 s	T = 150 °C; η_v = 0.0002 s
1st BW	518.97	517.69	515.88
1st FW	519.03	518.34	517.53
2nd BW	1091.85	1092.51	1093.32
2nd FW	1094.19	1093.81	1093.40
3rd BW	2213.93	2198.55	2178.05
3rd FW	2227.24	2211.91	2191.58
4th BW	4787.50	4595.03	4328.42
4th FW	4817.76	4626.03	4360.72

7.5.2 WHIRL SPEED AND CAMPBELL DIAGRAM FOR ALL MODES

Simulation is performed at different rotor spin speeds and predicted the forward whirl and backward whirl speeds for constant operating temperature and internal viscous damping to understand the spread between whirl speeds for each mode. Results are tabulated in Table 7-18 and shown in Figure 7-16.

Table 7-18 Whirl Speeds (rad/sec) for T = 150 °C and η_v = 0.0002 s, at different rotor spin speeds

Mode	0 rpm (0 rad/sec)	2000 rpm (209.4 rad/sec)	4000 rpm (418.9 rad/sec)	6000 rpm (628.3 rad/sec)
1st BW	516.12	515.85	515.88	516.20
1st FW	516.12	516.68	517.53	518.65
2nd BW	1093.03	1093.08	1093.32	1093.77
2nd FW	1093.03	1093.15	1093.40	1093.77
3rd BW	2183.85	2180.73	2178.05	2175.76
3rd FW	2183.85	2187.45	2191.58	2196.29
4th BW	4337.26	4331.22	4328.42	4328.56
4th FW	4337.26	4346.94	4360.72	4379.11

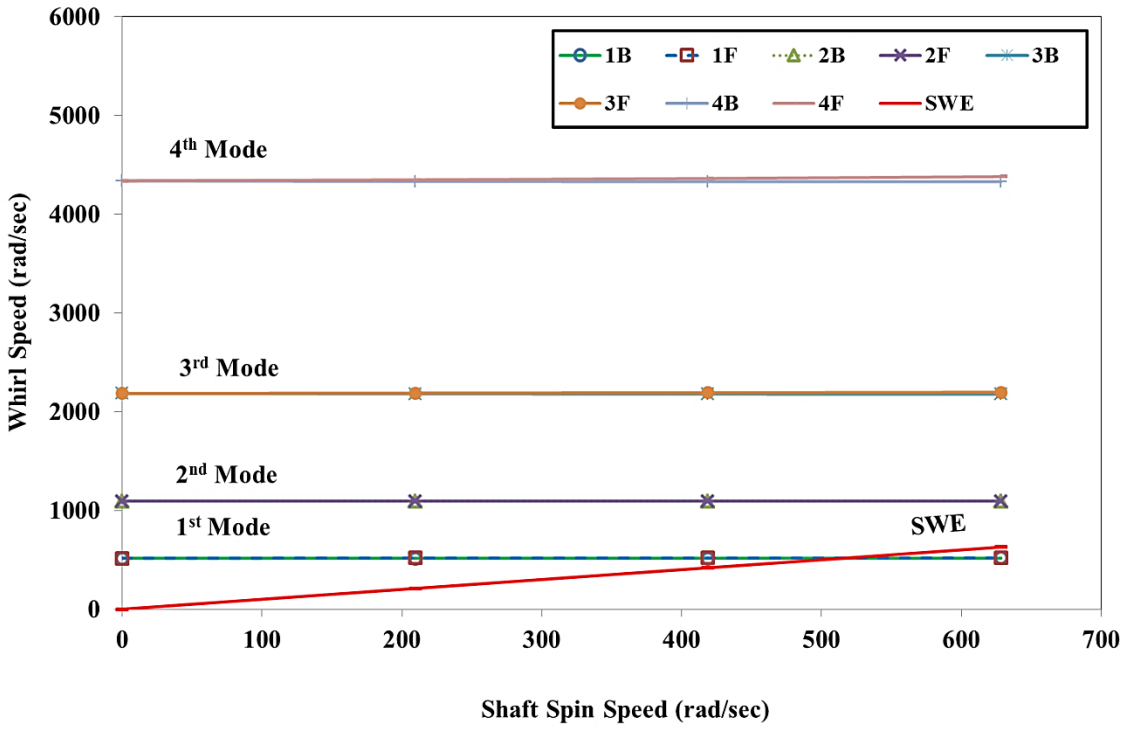

Figure 7-16 Campbell Diagram for Different Modes

7.5.3 WHIRL SPEED AND CAMPBELL DIAGRAM FOR FIRST MODE

The forward whirl speed and backward whirl speed are clearly distinguishable. The sensitivity analysis is carried out to understand the combined effect of operating temperature and internal viscous damping on the forward whirl and backward whirl speeds. Results are summarized in Table 7-19 and shown in Figure 7-17.

Table 7-19 Whirl Speeds (rad/sec) for different rotor spin speeds

	1st Mode	0 rpm (0 rad/sec)	2000 rpm (209.4 rad/sec)	4000 rpm (418.9 rad/sec)	6000 rpm (628.3 rad/sec)
T = 50 °C; η_v = 0.0001 s	BW	518.85	518.87	518.97	519.13
	FW	518.85	518.91	519.03	519.23
T = 100 °C; η_v = 0.00015 s	BW	517.68	517.60	517.69	517.94
	FW	517.68	517.93	518.34	518.91
T = 150 °C; η_v = 0.0002 s	BW	516.12	515.85	515.88	516.20
	FW	516.12	516.68	517.53	518.65

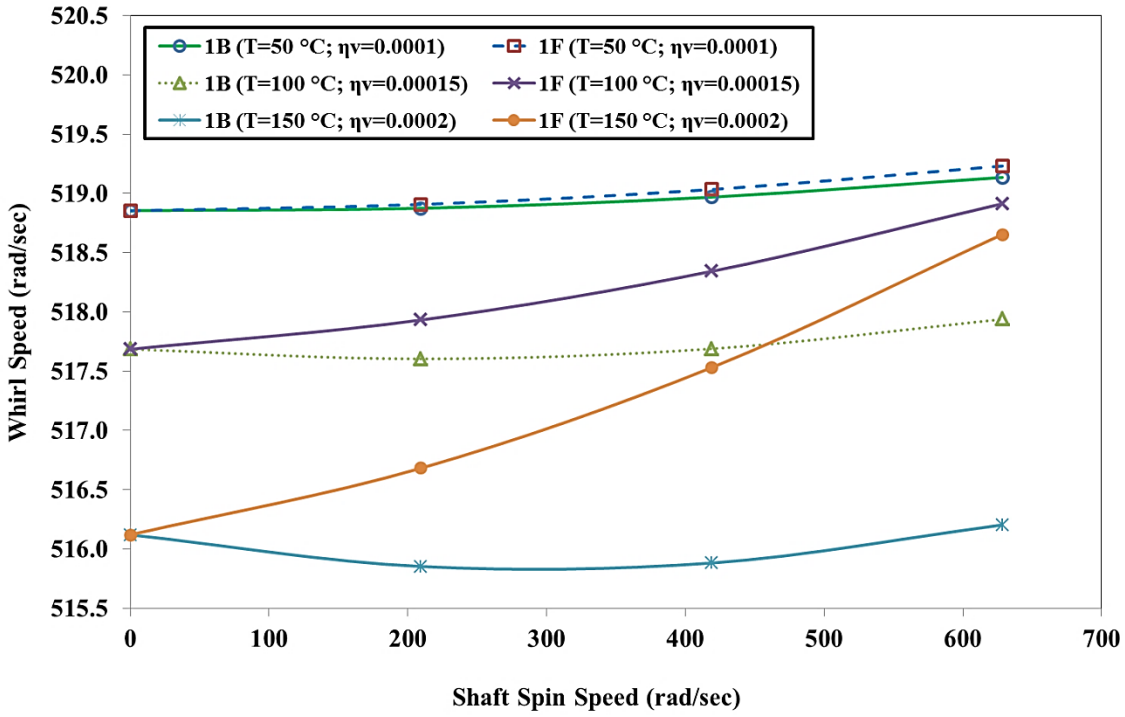

Figure 7-17 Whirl Speed Map for 1st Mode

The offset of the forward whirl and/or backward whirl is increasing with increasing the damping. Due to this, the forward whirl and backward whirl speeds are increased with clear offset. Results are shown in Figure 7-17.

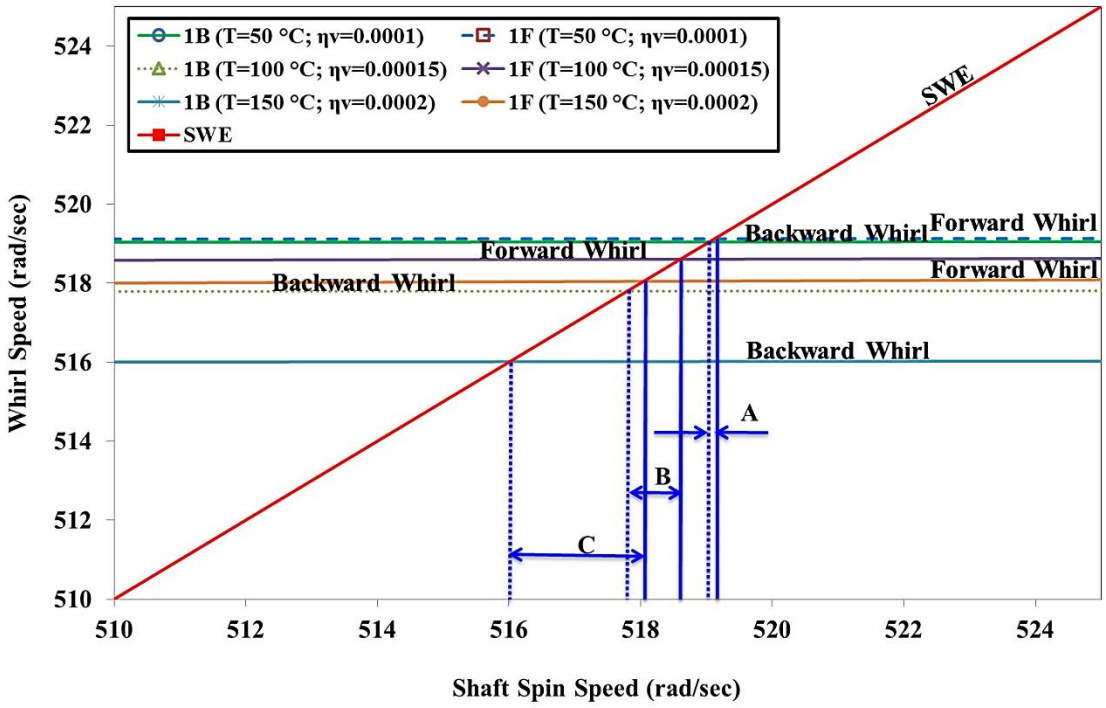

Figure 7-18 Campbell Diagram for 1st Mode

The synchronous whirl excitation is intersecting at two different locations for the first mode. The details of intersection are shown in Figure 7-18. The range between backward critical speed and forward critical speed ranges are shown as 'A', 'B' and 'C'. These ranges are based on the contribution of combined form of operating temperature and internal viscous damping. As the operating temperature and internal viscous damping increases, these ranges are shifting proportionately at a lower level. If the rotor operating spin speed is within this range 'A' 'B' and 'C', there will be the unbounded amplitude of vibration which results into rotor failure. To mitigate this risk and to avoid resonance, only two options are available, either rotor should redesign in such a way that the range 'A' 'B' and 'C' will get shifted from the operating speed or operate spin speed needs to change. This information is very useful in the design stage of the rotor.

7.5.4 CHANGE IN WHIRL SPEED RATIO

The non-dimensional term 'change in whirl speed ratio' is calculated for each mode shape with constant combined form of operating temperature and internal viscous damping. This parameter is increasing as the spin speed increases; it means the gap between forward whirl and backward increase as the spin speed increases. The whirl speed ratio is more predominant in the higher modes. The results are tabulated in Table 7-20 and shown in Figure 7-19.

Table 7-20 Change in whirl speed ratio for T = 150 °C and η_v = 0.0002 s, at different rotor spin speeds

Mode	0 rpm (0 rad/sec)	2000 rpm (209.4 rad/sec)	4000 rpm (418.9 rad/sec)	6000 rpm (628.3 rad/sec)
1st Mode	0.000%	0.161%	0.319%	0.475%
2nd Mode	0.000%	0.006%	0.008%	0.000%
3rd Mode	0.000%	0.308%	0.620%	0.940%
4th Mode	0.000%	0.362%	0.745%	1.165%

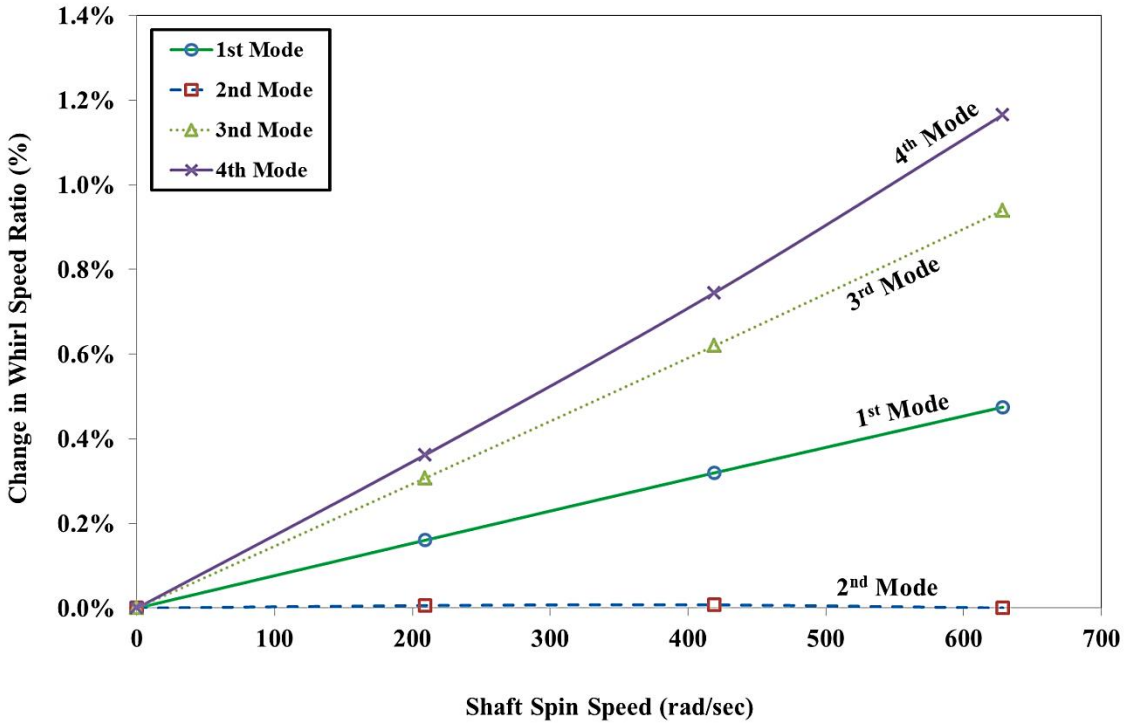

Figure 7-19 Change in Whirl Speed Ratio for Different Modes

The spread between backward whirl speed and forward whirl speed is increasing with increasing the rotor spin speed. This spread is also increasing with higher modes except for the second mode.

The sensitivity analysis also carried out on the change in whirl speed ratio with the combined effect of increasing the operating temperature and internal viscous damping. As the operating temperature and internal viscous damping increases, the change in whirl speed ratio changes. The results are tabulated in the below Table 7-21 and shown in Figure 7-20.

Table 7-21 Change in whirl speed ratio for different rotor spin speeds

	0 rpm (0 rad/sec)	2000 rpm (209.4 rad/sec)	4000 rpm (418.9 rad/sec)	6000 rpm (628.3 rad/sec)
T = 50 °C; η_v = 0.0001 s	0.000%	0.006%	0.012%	0.019%
T = 100 °C; η_v = 0.00015 s	0.000%	0.063%	0.126%	0.188%
T = 150 °C; η_v = 0.0002 s	0.000%	0.161%	0.319%	0.475%

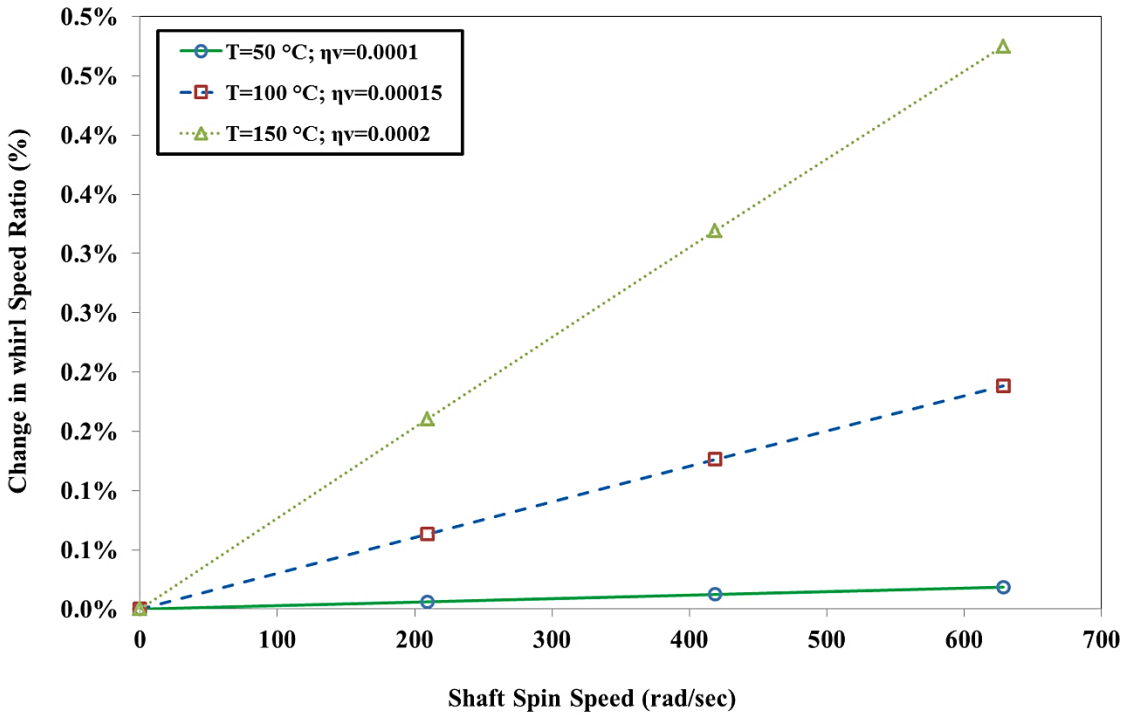

Figure 7-20 Change in Whirl Speed Ratio for 1st Mode

7.5.5 CONCLUSION

The spread between forward whirl speed and backward whirl speed increases with increase in the rotor spin speed for all modes except for the second mode. This interesting phenomenon is observed only for the second mode. The spread between forward whirl and backward whirl for second is small and this phenomenon is attributed to the nullifying effect for the gyroscopic couple. The spread is large for the first, third and fourth mode. It is clearly observed in Figure 7-19 with the help of whirl speed ratio. Critical speed range or spread is increasing with the larger magnitude and shifting at the lower side with an increase in combined form of operating temperature and internal viscous damping as shown in Figure 7-18. A clear understanding of operating temperature and internal viscous damping is very useful while designing flexible and rigid rotors.

7.5.6 APPLICATION

Practical application or situation will be the different parts or components mounted on the shaft with shrink fit and operating temperature is critical. The external viscous damping is not present. e.g. Fan, hub, coupling, balance ring etc mounted on the shaft with shrink fit and shaft is supported with anti-friction bearings like ball bearings, roller bearings. This is operated at high temperature.

e.g. Slow speed gear box.

7.6 OPERATING TEMPERATURE AND INTERNAL HYSTERETIC DAMPING ACTING IN COMBINED FORM

This case study includes operating temperature (T) and internal hysteretic damping (η_H). It does not include internal viscous damping (η_v) and external viscous damping (C_e).

Suppressing the different forms of damping in equations (4-75) and (4-86),

- External viscous damping, $C_{xx} = 0$, $C_{yy} = 0$, $C_{xy} = 0$ and $C_{yx} = 0$
- Internal viscous damping, $\eta_v = 0$

$$\therefore \eta_a = \frac{1+\eta_H}{\sqrt{1+\eta_H{}^2}} \text{ ; and } \therefore \eta_b = \frac{\eta_H}{\sqrt{1+\eta_H{}^2}} + \eta_v\Omega = \frac{\eta_H}{\sqrt{1+\eta_H{}^2}}$$

The equations of motion for operating temperature and internal hysteretic damping is expressed,

$$\left[\left[M_{Tt}^e\right]+\left[M_{Rt}^e\right]\right]\left\{\ddot{\bar{q}}_n^f\right\}-\Omega\left[G_t^e\right]\left\{\dot{\bar{q}}_n^f\right\}+\left[\frac{1+\eta_H}{\sqrt{1+\eta_H{}^2}}\left[K_{Bt}^e\right]+\frac{\eta_H}{\sqrt{1+\eta_H{}^2}}\left[K_{Ct}^e\right]\right]\left\{\bar{q}_n^f\right\}=\left\{\bar{F}_n^f\right\} \quad (7\text{-}8)$$

7.6.1 EFFECT ON WHIRL SPEEDS

Simulation is performed for different operating temperature and internal hysteretic damping values. As the operating temperature and the internal hysteretic damping increases, the forward whirl and backward whirl speeds are decreases for all the modes. Results are tabulated in Table 7-22.

Table 7-22 Whirl Speeds (rad/sec) at rotor spin speed of 4000 (rpm)

Mode	T = 50 °C; η_H = 0.0002	T = 100 °C; η_H = 0.0025	T = 150 °C; η_H = 0.005
1st BW	518.40	517.28	515.72
1st FW	519.05	517.94	516.39
2nd BW	1090.82	1090.33	1089.65
2nd FW	1094.02	1093.53	1092.85
3rd BW	2219.35	2211.97	2201.80
3rd FW	2232.66	2225.27	2215.09
4th BW	4918.81	4894.38	4860.71
4th FW	4948.68	4924.25	4890.57

7.6.2 WHIRL SPEED AND CAMPBELL DIAGRAM FOR ALL MODES

Simulation is performed at different rotor spin speeds and predicted the forward whirl and backward whirl speeds for constant combined form of operating temperature and internal hysteretic damping to understand the spread between whirl speed for each mode. Results are tabulated in ***Table 7-23*** and shown in Figure 7-21.

Table 7-23 Whirl Speeds (rad/sec) for T = 150 °C; η_H = 0.005, at different rotor spin speeds

Mode	0 rpm (0 rad/sec)	2000 rpm (209.4 rad/sec)	4000 rpm (418.9 rad/sec)	6000 rpm (628.3 rad/sec)
1st BW	516.06	515.89	515.72	515.56
1st FW	516.06	516.23	516.39	516.56
2nd BW	1091.25	1090.45	1089.65	1088.85
2nd FW	1091.25	1092.05	1092.85	1093.65
3rd BW	2208.43	2205.12	2201.80	2198.50
3rd FW	2208.43	2211.76	2215.09	2218.42
4th BW	4875.62	4868.16	4860.71	4853.27
4th FW	4875.62	4883.09	4890.57	4898.06

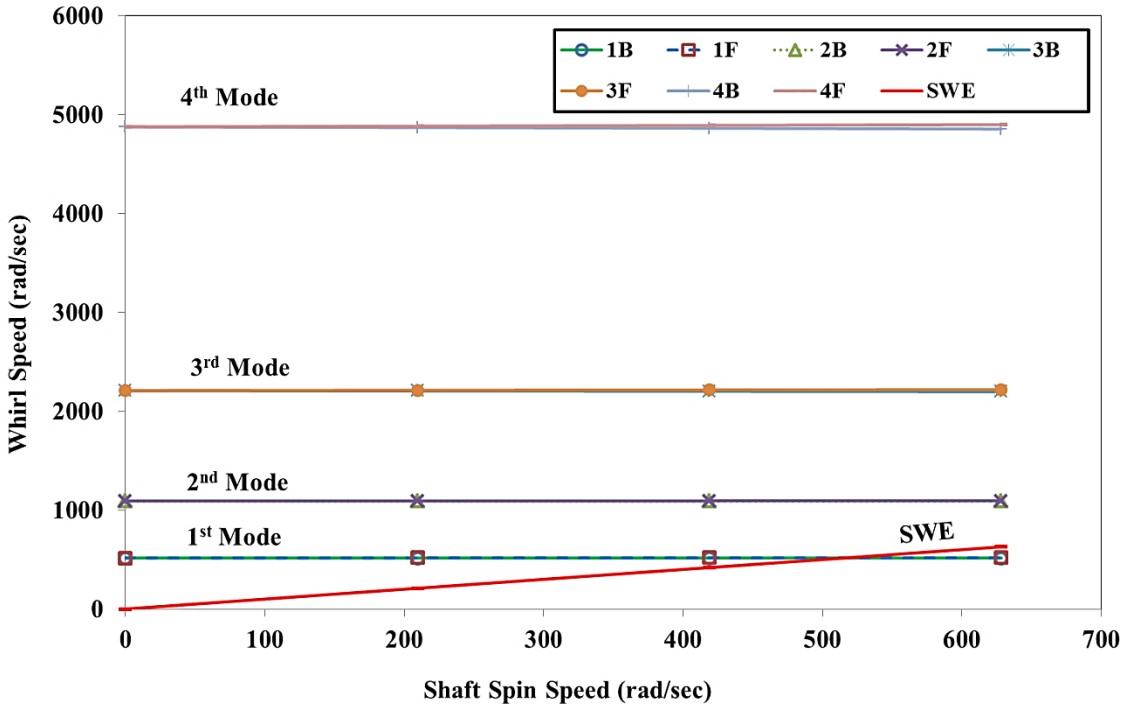

Figure 7-21 Campbell Diagram for Different Modes

7.6.3 WHIRL SPEED AND CAMPBELL DIAGRAM FOR FIRST MODE

The forward whirl speed and backward whirl speed are clearly distinguishable. The spread between backward whirl and forward whirl is increasing with increase in the rotor spin speed. The sensitivity analysis is carried out to understand the combined effect of operating temperature and internal hysteretic damping on the forward whirl and backward whirl speeds. Results are summarized in Table 7-24 and shown in Figure 7-22.

Table 7-24 Whirl Speeds (rad/sec) for different rotor spin speeds

(For different T and η_H)

	1st Mode	0 rpm (0 rad/sec)	2000 rpm (209.4 rad/sec)	4000 rpm (418.9 rad/sec)	6000 rpm (628.3 rad/sec)
T = 50 °C; η_H = 0.0002	BW	518.73	518.56	518.40	518.24
	FW	518.73	518.89	519.05	519.21
T = 100 °C; η_H = 0.0025	BW	517.61	517.45	517.28	517.12
	FW	517.61	517.78	517.94	518.11
T = 150 °C; η_H = 0.005	BW	516.06	515.89	515.72	515.56
	FW	516.06	516.23	516.39	516.56

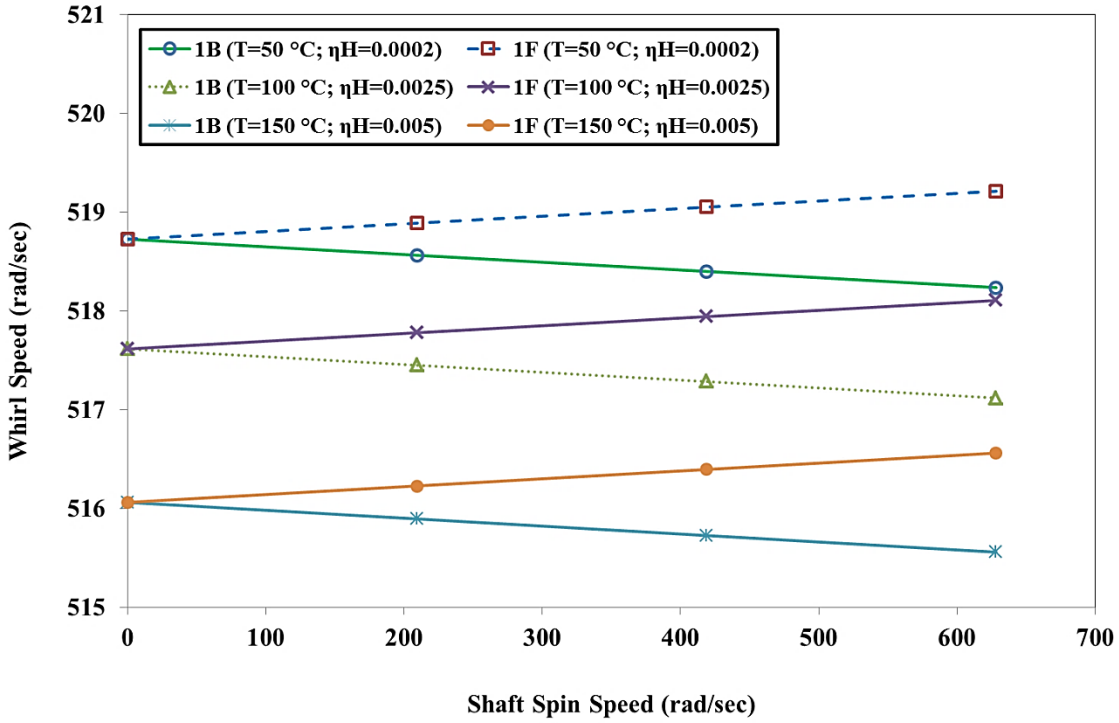

Figure 7-22 Whirl Speed Map for 1st Mode

With the addition of combined form of operating temperature and internal hysteretic damping, the starting point of the forward whirl and backward whirl at zero spin speed gets offset. This offset is increasing with increasing the operating temperature and internal hysteretic damping. Due to this, the forward whirl and backward whirl speeds are decreased with clear offset.

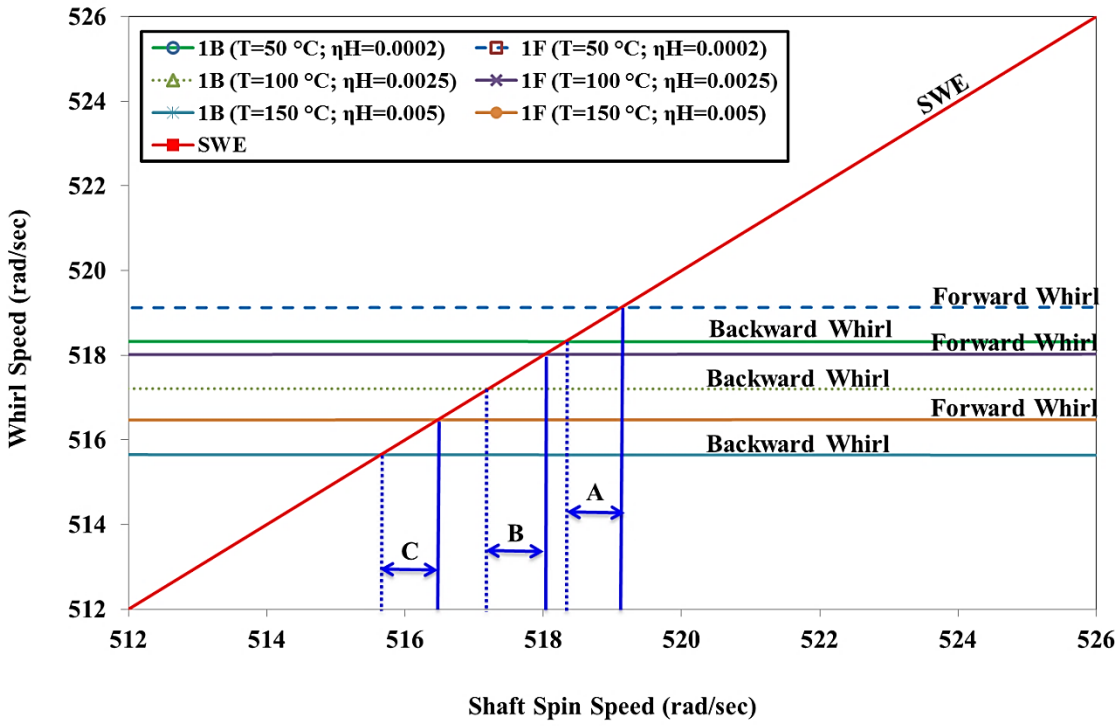

Figure 7-23 Campbell Diagram for 1st Mode

The synchronous whirl excitation is intersecting at two different locations for the first mode. The details of intersection are shown in Figure 7-23. The range between backward critical speed and forward critical speed ranges are shown as 'A', 'B' and 'C'. These ranges are based on the combination of the contribution of operating temperature and internal hysteretic damping. As the operating temperature and internal hysteretic damping increases, these ranges are shifting proportionately at a lower level. If the rotor operating spin speed is within this range 'A' 'B' and 'C', there will be the unbounded amplitude of vibration which results into rotor failure. To mitigate this risk and to avoid resonance, only two options are available, either rotor should redesign in such a way that the range 'A' 'B' and 'C' will get shifted from the operating speed or operate spin speed needs to change. This information is very useful in the design stage of the rotor.

7.6.4 CHANGE IN WHIRL SPEED RATIO

The non-dimensional term 'change in whirl speed ratio' is calculated for each mode shape with constant operating temperature and internal hysteretic damping. This parameter is increasing as the spin speed increases; it means the gap between forward whirl and backward increase as the spin speed increases. The whirl speed ratio is more predominant in the higher modes. The results are tabulated in Table 7-25 and shown in Figure 7-24.

Table 7-25 Change in whirl speed ratio for T = 150 °C; η_H = 0.005, at different rotor spin speeds

Mode	0 rpm (0 rad/sec)	2000 rpm (209.4 rad/sec)	4000 rpm (418.9 rad/sec)	6000 rpm (628.3 rad/sec)
1st Mode	0.000%	0.065%	0.130%	0.194%
2nd Mode	0.000%	0.146%	0.293%	0.439%
3rd Mode	0.000%	0.301%	0.601%	0.902%
4th Mode	0.000%	0.306%	0.613%	0.919%

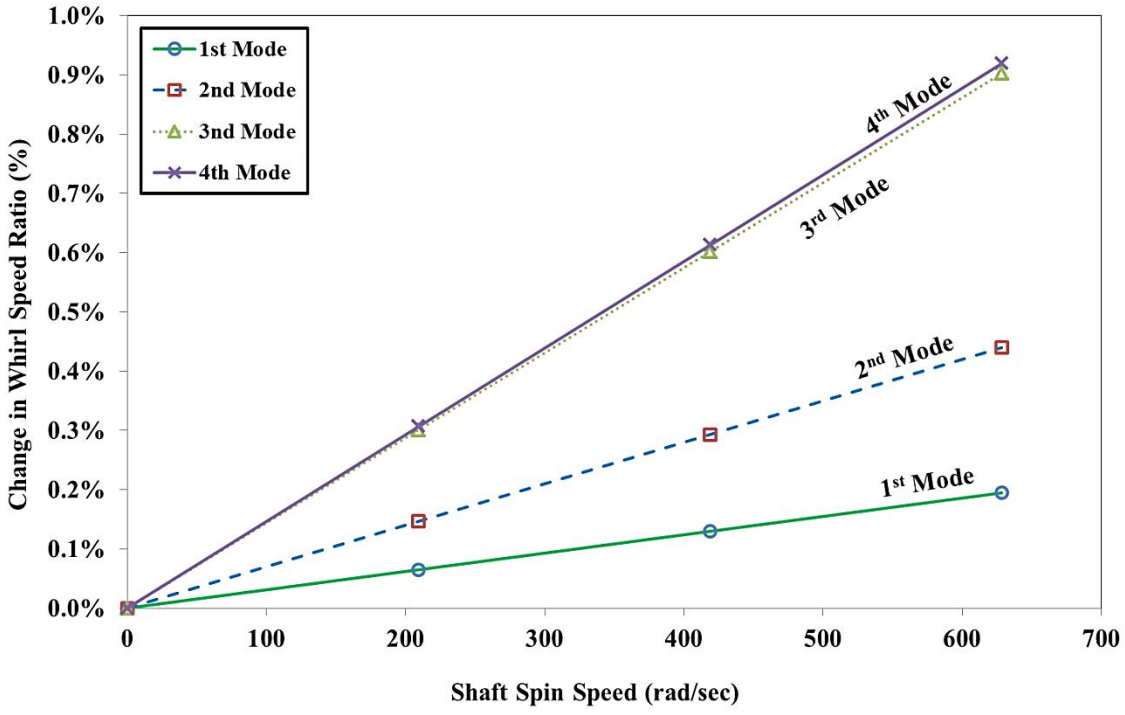

Figure 7-24 Change in Whirl Speed Ratio for Different Modes

The spread between backward whirl speed and forward whirl speed is increasing with increasing the rotor spin speed. This spread is also increasing with higher modes. This spreading effect is due to the contribution of the combination of operating temperature and internal hysteretic damping. This phenomenon is adding to the gyroscopic effect.

The sensitivity analysis also carried out on the change in whirl speed ratio with increasing the combination of operating temperature and internal hysteretic damping. As this combination increases, the change in whirl speed ratio increases. In conclusion, this combination is contributing to the gyroscopic effect. The results are tabulated in the below Table 7-26 and shown in Figure 7-25.

Table 7-26 Change in whirl speed ratio for different rotor spin speeds

	0 rpm (0 rad/sec)	2000 rpm (209.4 rad/sec)	4000 rpm (418.9 rad/sec)	6000 rpm (628.3 rad/sec)
T = 50 °C; η_H = 0.0002	0.000%	0.063%	0.125%	0.188%
T = 100 °C; η_H = 0.0025	0.000%	0.064%	0.127%	0.191%
T = 150 °C; η_H = 0.005	0.000%	0.065%	0.130%	0.194%

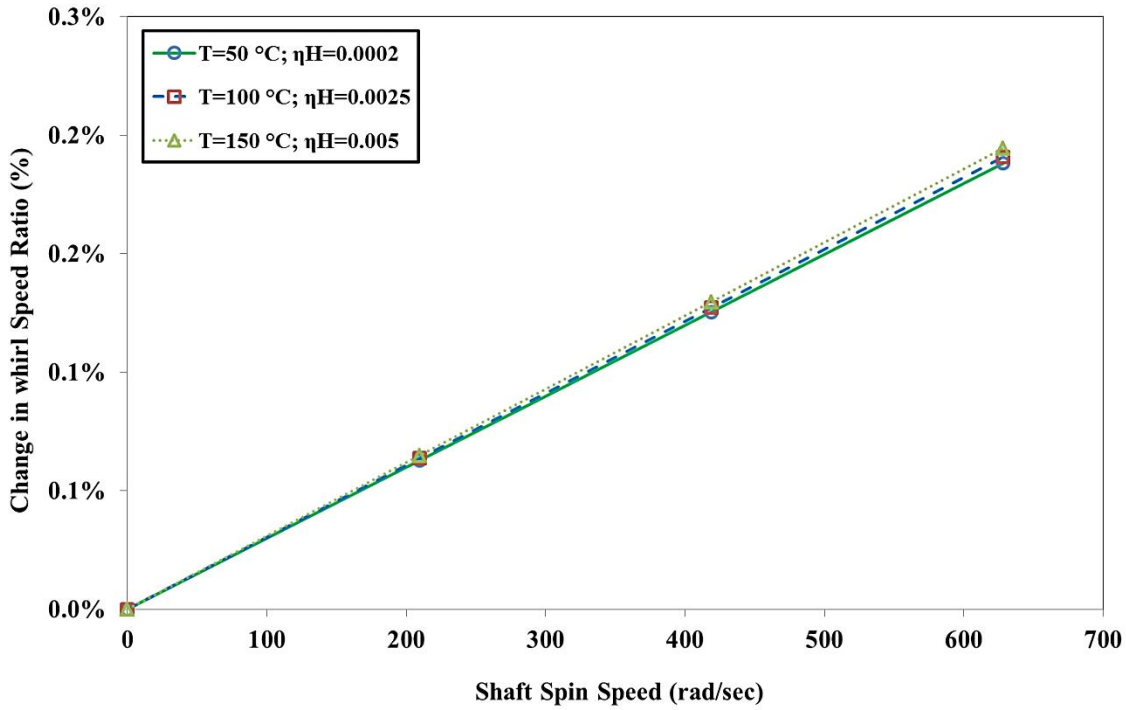

Figure 7-25 Change in Whirl Speed Ratio for 1st Mode

7.6.5 CONCLUSION

The spread between forward whirl speed and backward whirl speed increases with increase in rotor spin speed for all modes. It is clearly observed in Figure 7-24 with the help of whirl speed ratio. Critical speed range or spread remains same and shifting at the lower side with an increase in combined form of operating temperature and internal hysteretic damping as shown in Figure 7-23. A clear understanding of operating temperature and internal hysteretic damping is very useful while designing flexible and rigid rotors.

7.6.6 APPLICATION

Practical application or situation will be the simple shaft and high-temperature ambient conditions supported with anti-friction bearings like ball bearings, roller bearings etc.

e.g. Exhaust fan shaft

7.7 OPERATING TEMPERATURE AND EXTERNAL VISCOUS DAMPING ACTING IN COMBINED FORM

This case study includes operating temperature (T) and external viscous damping (C_e). It does not include internal viscous damping (η_v) and internal hysteretic damping (η_H).

Suppressing the different forms of damping in equations (4-75) and (4-86),

- Internal viscous damping, $\eta_v = 0$
- Internal hysteretic damping, $\eta_H = 0$

$\therefore \eta_a = \dfrac{1+\eta_H}{\sqrt{1+\eta_H{}^2}} = 1$; and $\therefore \eta_b = \dfrac{\eta_H}{\sqrt{1+\eta_H{}^2}} + \eta_v \Omega = 0$

The equations of motion for operating temperature and external viscous damping are expressed,

$$\left[\left[M_{Tt}^{e}\right]+\left[M_{Rt}^{e}\right]\right]\left\{\ddot{\bar{q}}_{n}^{f}\right\}-\Omega\left[G_{t}^{e}\right]\left\{\dot{\bar{q}}_{n}^{f}\right\}+\left[K_{Bt}^{e}\right]\left\{\bar{q}_{n}^{f}\right\}=\left\{\bar{F}_{n}^{f}\right\} \tag{7-9}$$

$$\begin{bmatrix} C_{xx} & C_{xy} \\ C_{yx} & C_{yy} \end{bmatrix}\left\{\dot{\bar{q}}_{n}^{f}\right\}+\begin{bmatrix} K_{xx} & K_{xy} \\ K_{yx} & K_{yy} \end{bmatrix}\left\{\bar{q}_{n}^{f}\right\}=\left\{\bar{F}_{b}^{f}\right\} \tag{7-10}$$

7.7.1 EFFECT ON WHIRL SPEEDS

Simulation is performed for different operating temperature and external viscous damping values. As the operating temperature and external viscous damping increases, the forward whirl and backward whirl speeds are decreases for all the modes. Results are tabulated in Table 7-27.

Table 7-27 Whirl Speeds (rad/sec) at rotor spin speed of 4000 (rpm)

Mode	Ce=500 N-s/m; T=50 °C	Ce=1000 N-s/m; T=100 °C	Ce=1752 N-s/m; T=150 °C
1st BW	518.39	517.06	515.31
1st FW	519.04	517.72	515.98
2nd BW	1090.74	1089.95	1088.59
2nd FW	1093.95	1093.15	1091.79
3rd BW	2219.04	2209.56	2196.29
3rd FW	2232.35	2222.86	2209.58
4th BW	4918.16	4887.93	4847.07
4th FW	4948.03	4917.80	4876.95

7.7.2 WHIRL SPEED AND CAMPBELL DIAGRAM FOR ALL MODES

Simulation is performed at different rotor spin speeds and predicted the forward whirl and backward whirl speeds for constant combined form of operating temperature and external viscous damping to understand the spread between whirl speed for each mode. Results are tabulated in Table 7-28 and shown in Figure 7-26.

Table 7-28 Whirl Speeds (rad/sec) for Ce=1752 N-s/m; T=150 °C, at different rotor spin speeds

Mode	0 rpm (0 rad/sec)	2000 rpm (209.4 rad/sec)	4000 rpm (418.9 rad/sec)	6000 rpm (628.3 rad/sec)
1st BW	515.65	515.48	515.31	515.14
1st FW	515.65	515.82	515.98	516.15
2nd BW	1090.19	1089.39	1088.59	1087.79
2nd FW	1090.19	1090.99	1091.79	1092.59
3rd BW	2202.92	2199.60	2196.29	2192.98
3rd FW	2202.92	2206.25	2209.58	2212.92
4th BW	4861.99	4854.53	4847.07	4839.63
4th FW	4861.99	4869.46	4876.95	4884.44

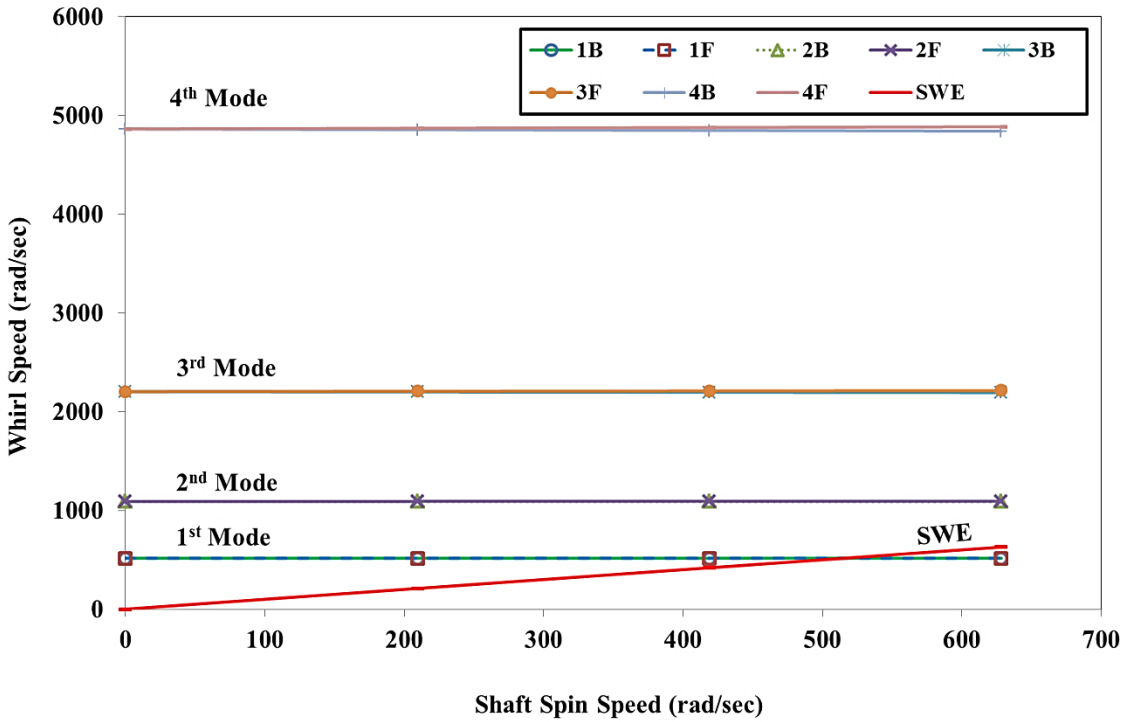

Figure 7-26 Campbell Diagram for Different Modes

7.7.3 WHIRL SPEED AND CAMPBELL DIAGRAM FOR FIRST MODE

The forward whirl speed and backward whirl speed are clearly distinguishable. The spread between backward whirl and forward whirl is increasing with increase in the rotor spin speed. The sensitivity analysis is carried out to understand the combined effect of external viscous damping and operating temperature on the forward whirl and backward whirl speeds. Results are summarized in Table 7-29 and shown in Figure 7-27.

Table 7-29 Whirl Speeds (rad/sec) for different rotor spin speeds

	1st Mode	0 rpm (0 rad/sec)	2000 rpm (209.4 rad/sec)	4000 rpm (418.9 rad/sec)	6000 rpm (628.3 rad/sec)
Ce = 500 N-s/m; T = 50 °C	BW	518.71	518.55	518.39	518.22
	FW	518.71	518.88	519.04	519.20
Ce = 1000 N-s/m; T = 100 °C	BW	517.39	517.22	517.06	516.89
	FW	517.39	517.55	517.72	517.88
Ce = 1752 N-s/m; T = 150 °C	BW	515.65	515.48	515.31	515.14
	FW	515.65	515.82	515.98	516.15

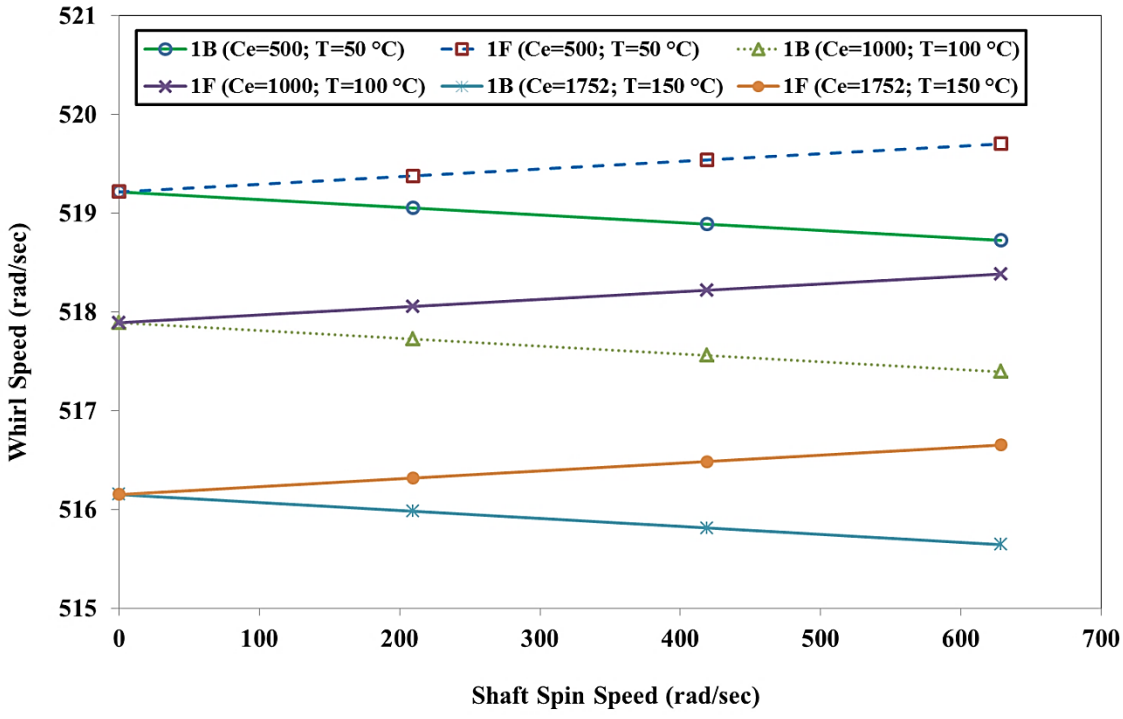

Figure 7-27 Whirl Speed Map for 1st Mode

With the addition of the external viscous damping and operating temperature, the starting point of the forward whirl and backward whirl speed at zero spin speed gets lower offset. This offset is increasing with increasing the external viscous damping and operating temperature.

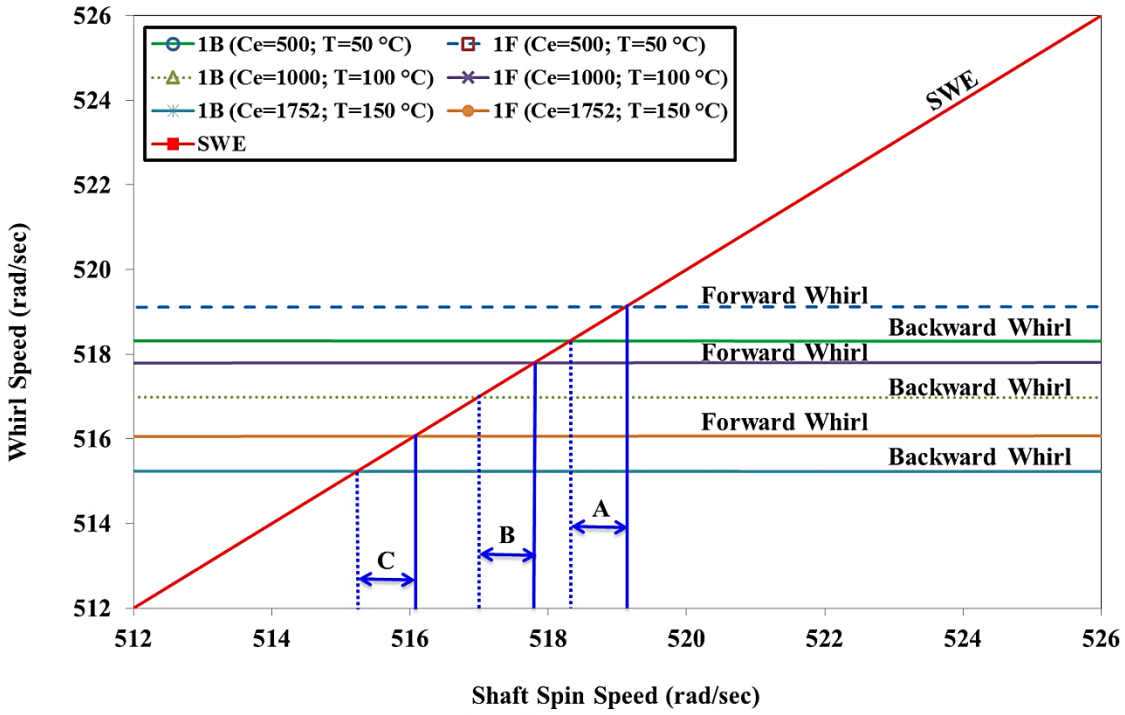

Figure 7-28 Campbell Diagram for 1st Mode

The synchronous whirl excitation is intersecting at two different locations for the first mode. The details of intersection are shown in Figure 7-28. The range between backward critical speed and forward critical speed ranges are shown as 'A', 'B' and 'C'. These ranges are based on the contribution of combined form of operating temperature and external viscous damping. As the operating temperature and external viscous damping increases, these ranges are shifting proportionately at a lower level. If the rotor operating spin speed is within this range 'A' 'B' and 'C', there will be the unbounded amplitude of vibration which results into rotor failure. To mitigate this risk and to avoid resonance, only two options are available, either rotor should redesign in such a way that the range 'A' 'B' and 'C' will get shifted from the operating speed or operate spin speed needs to change. This information is very useful in the design stage of the rotor

7.7.4 CHANGE IN WHIRL SPEED RATIO

The non-dimensional term 'change in whirl speed ratio' is calculated for each mode shape with constant operating temperature and external viscous damping. This parameter is increasing as the spin speed increases; it means the gap between forward whirl and backward increase as the spin speed increases. The whirl speed ratio is more predominant in the higher modes. The results are tabulated in Table 7-30 and shown in Figure 7-29.

Table 7-30 Change in whirl speed ratio for Ce=1752 N-s/m; T=150 °C, at different rotor spin speeds

Mode	0 rpm (0 rad/sec)	2000 rpm (209.4 rad/sec)	4000 rpm (418.9 rad/sec)	6000 rpm (628.3 rad/sec)
1st Mode	0.000%	0.065%	0.130%	0.196%
2nd Mode	0.000%	0.147%	0.294%	0.440%
3rd Mode	0.000%	0.302%	0.603%	0.905%
4th Mode	0.000%	0.307%	0.614%	0.922%

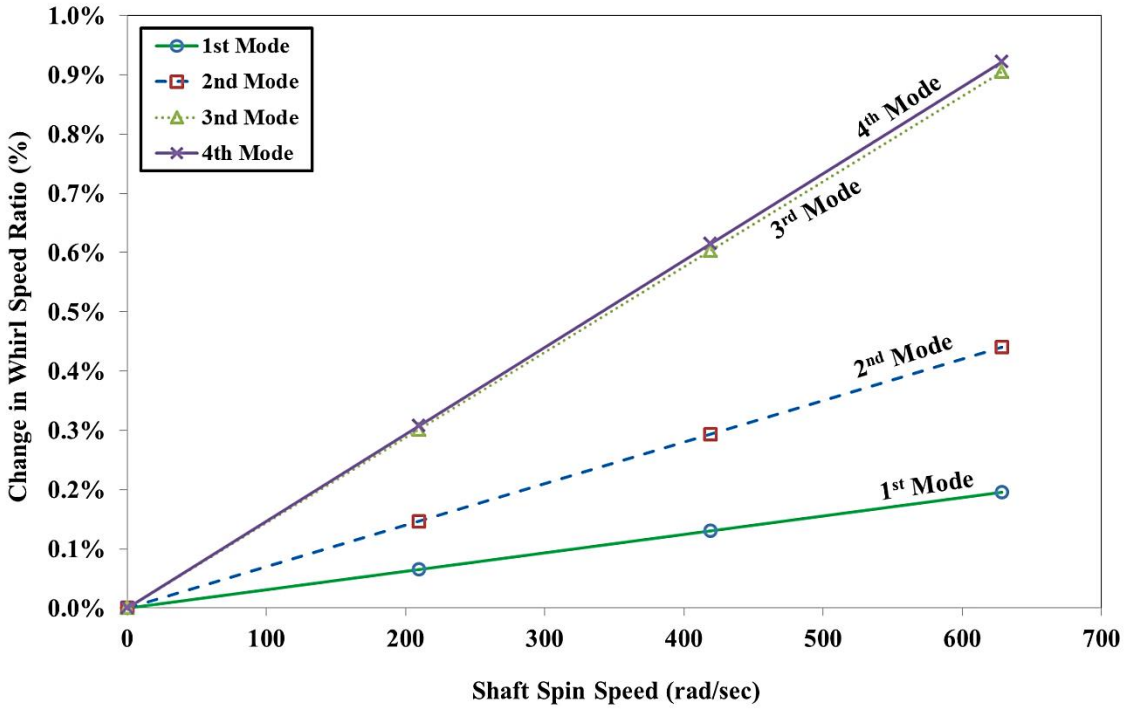

Figure 7-29 Change in Whirl Speed Ratio for Different Modes

The spread between backward whirl speed and forward whirl speed is increasing with increasing the rotor spin speed. This spread is also increasing with higher modes. This spreading effect is due to the contribution of operating temperature and external viscous damping. This phenomenon is adding to the gyroscopic effect.

The sensitivity analysis is carried out on the change in whirl speed ratio with increasing the combined form of external viscous damping and operating temperature. As this combination increases, the change in whirl speed ratio increases. In conclusion, this combination is attributed to contributing towards the gyroscopic couple. The results are tabulated in the below Table 7-31 also shown in Figure 7-30.

Table 7-31 Change in whirl speed ratio for different rotor spin speeds

	0 rpm (0 rad/sec)	2000 rpm (209.4 rad/sec)	4000 rpm (418.9 rad/sec)	6000 rpm (628.3 rad/sec)
Ce = 500 N-s/m; T = 50 °C	0.000%	0.063%	0.125%	0.188%
Ce = 1000 N-s/m; T = 100 °C	0.000%	0.064%	0.128%	0.191%
Ce = 1752 N-s/m; T = 150 °C	0.000%	0.065%	0.130%	0.196%

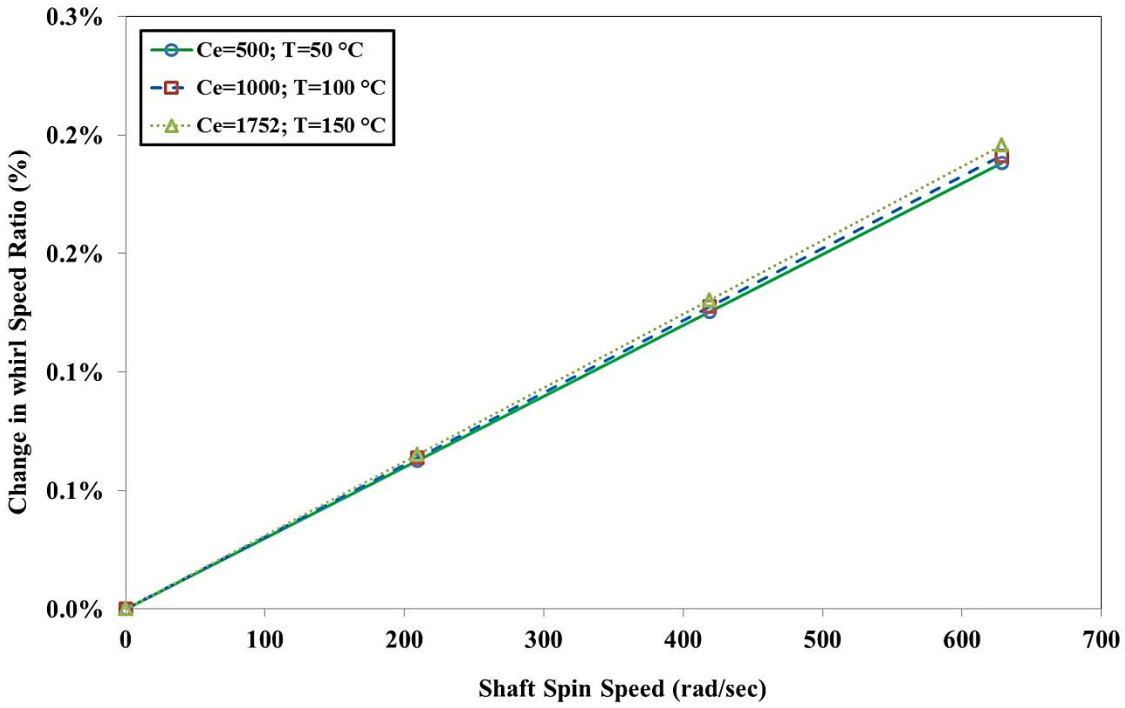

Figure 7-30 Change in Whirl Speed Ratio for 1st Mode

7.7.5 CONCLUSION

The spread between forward whirl speed and backward whirl speed increases with increase in rotor spin speed for all modes. This spread is larger for higher modes and at higher speeds. This is clearly observed in Figure 7-29 with the help of whirl speed ratio. Critical speed range or spread remains constant and shifting at the lower side with an increase in combined form of operating temperature and external viscous damping as shown in Figure 7-28. A clear understanding of the combined form of operating temperature and external viscous damping is very useful while designing flexible and rigid rotors.

7.7.6 APPLICATION

Practical application or situation will be the simple shaft and high-temperature ambient conditions supported with sleeve bearings.

e.g. Drive shaft.

7.8 INTERNAL VISCOUS DAMPING, INTERNAL HYSTERETIC DAMPING AND EXTERNAL VISCOUS DAMPING ACTING IN COMBINED FORM

This case study includes internal viscous damping (η_v), internal hysteretic damping (η_H) and external viscous damping (C_e). It does not include operating temperature (T).

Suppressing the operating temperature in equations (4-75) and (4-86),

$$\therefore \eta_a = \frac{1+\eta_H}{\sqrt{1+\eta_H{}^2}} \text{; and } \therefore \eta_b = \frac{\eta_H}{\sqrt{1+\eta_H{}^2}} + \eta_v \Omega$$

The equations of motion for internal viscous damping, internal hysteretic damping and external viscous damping are expressed,

$$\left[\left[M_T^e\right]+\left[M_R^e\right]\right]\left\{\ddot{\bar{q}}_n^f\right\}+\left[\eta_v\left[K_B^e\right]-\Omega[G]\right]\left\{\dot{\bar{q}}_n^f\right\}+\left[\eta_a\left[K_B^e\right]+\eta_b\left[K_C^e\right]\right]\left\{\bar{q}_n^f\right\}=\left\{\bar{F}_n^f\right\} \quad (7\text{-}11)$$

$$\begin{bmatrix} C_{xx} & C_{xy} \\ C_{yx} & C_{yy} \end{bmatrix}\left\{\dot{\bar{q}}_n^f\right\}+\begin{bmatrix} K_{xx} & K_{xy} \\ K_{yx} & K_{yy} \end{bmatrix}\left\{\bar{q}_n^f\right\}=\left\{\bar{F}_b^f\right\} \quad (7\text{-}12)$$

7.8.1 EFFECT ON WHIRL SPEEDS

Simulation is performed for different internal viscous damping, internal hysteretic damping and external viscous damping values. As these combined form of damping increases, the forward whirl and backward whirl speeds are also increased for the first mode only. For the higher modes, the forward and backward whirl decreases with increasing in these damping. Results are tabulated in Table 7-32.

Table 7-32 Whirl Speeds (rad/sec) at rotor spin speed of 4000 (rpm)

Mode	Ce = 500 N-s/m; η_v = 0.0001 s; η_H = 0.0002	Ce = 1000 N-s/m; η_v = 0.00015 s; η_H = 0.0025	Ce = 1752 N-s/m; η_v = 0.0002 s; η_H = 0.005
1st BW	519.38	519.80	520.00
1st FW	519.60	520.00	520.57
2nd BW	1091.56	1091.77	1091.14
2nd FW	1094.14	1093.77	1092.65
3rd BW	2216.01	2206.89	2190.66
3rd FW	2229.33	2220.25	2204.14
4th BW	4794.59	4618.93	4352.00
4th FW	4824.77	4649.72	4383.91

7.8.2 WHIRL SPEED AND CAMPBELL DIAGRAM FOR ALL MODES

Simulation is performed at different rotor spin speeds and predicted the forward whirl and backward whirl speeds for constant combined form of internal viscous damping, internal hysteretic damping and external viscous damping to understand the spread between whirl speed for each mode. Results are tabulated in ***Table 7-33*** and shown in Figure 7-31.

Table 7-33 Whirl Speeds (rad/sec) for Ce=1752 N-s/m; η_v = 0.0002 s; η_H = 0.005, at different rotor spin speeds

Mode	0 rpm (0 rad/sec)	2000 rpm (209.4 rad/sec)	4000 rpm (418.9 rad/sec)	6000 rpm (628.3 rad/sec)
1st BW	519.67	519.66	520.00	520.63
1st FW	519.67	519.98	520.57	521.42
2nd BW	1091.53	1091.26	1091.14	1091.15
2nd FW	1091.53	1091.94	1092.65	1093.56
3rd BW	2196.20	2193.19	2190.66	2188.56
3rd FW	2196.20	2199.88	2204.14	2209.01
4th BW	4359.33	4353.99	4352.00	4353.04
4th FW	4359.33	4369.45	4383.91	4403.27

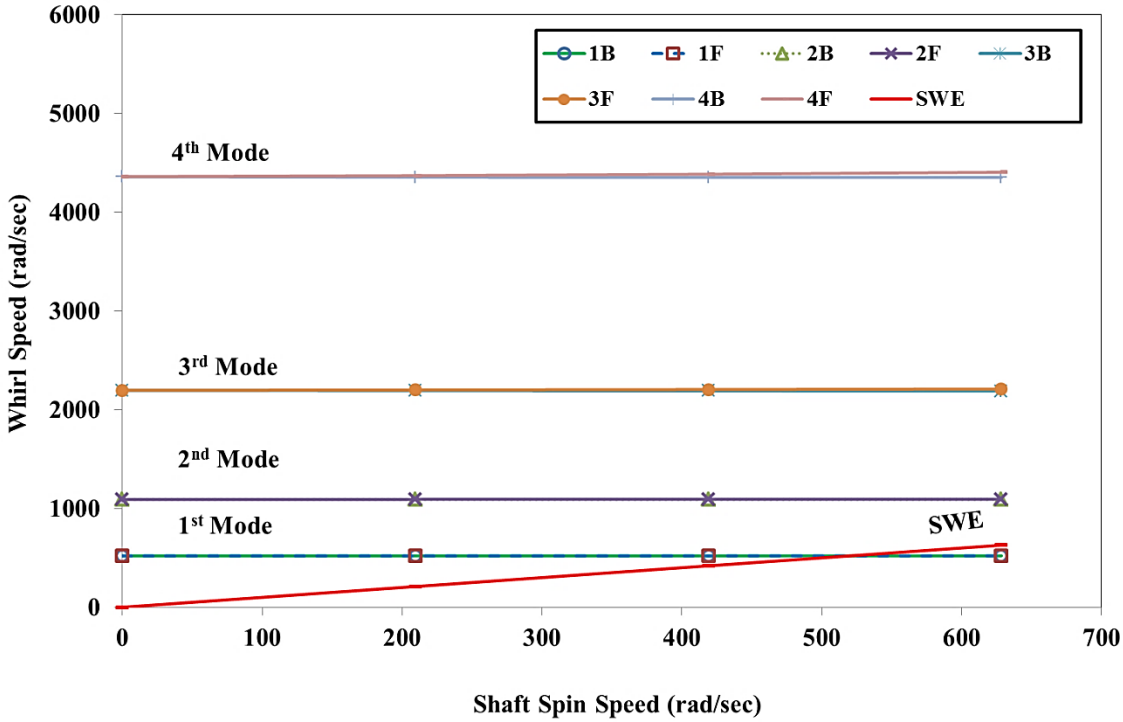

Figure 7-31 Campbell Diagram for Different Modes

7.8.3 WHIRL SPEED AND CAMPBELL DIAGRAM FOR FIRST MODE

The forward whirl speed and backward whirl speed are clearly distinguishable. The spread between backward whirl and forward whirl is increasing with increase in the rotor spin speed. The sensitivity analysis is carried out to understand the combined effect of all damping on the forward whirl and backward whirl speeds. With the addition of all these damping, the starting point of the forward whirl and backward whirl at zero spin speed gets offset. This offset is increasing with increasing these damping. Results are summarized in Table 7-34 and shown in Figure 7-32.

Table 7-34 Whirl Speeds (rad/sec) for different rotor spin speeds

	1st Mode	0 rpm (0 rad/sec)	2000 rpm (209.4 rad/sec)	4000 rpm (418.9 rad/sec)	6000 rpm (628.3 rad/sec)
Ce = 500 N-s/m; η_v = 0.0001 s; η_H = 0.0002	BW	519.34	519.33	519.38	519.50
	FW	519.34	519.44	519.60	519.84
Ce = 1000 N-s/m; η_v = 0.00015 s; η_H = 0.0025	BW	519.53	519.58	519.80	520.18
	FW	519.53	519.70	520.00	520.45
Ce=1752 N-s/m; η_v = 0.0002 s; η_H = 0.005	BW	519.67	519.66	520.00	520.63
	FW	519.67	519.98	520.57	521.42

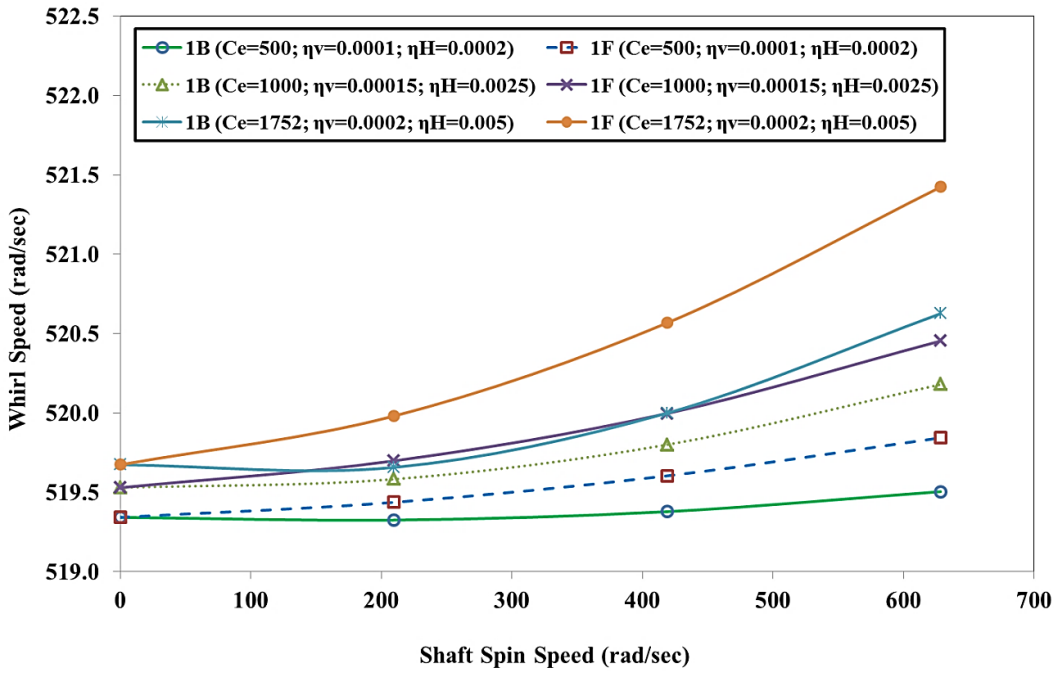

Figure 7-32 Whirl Speed Map for 1st Mode

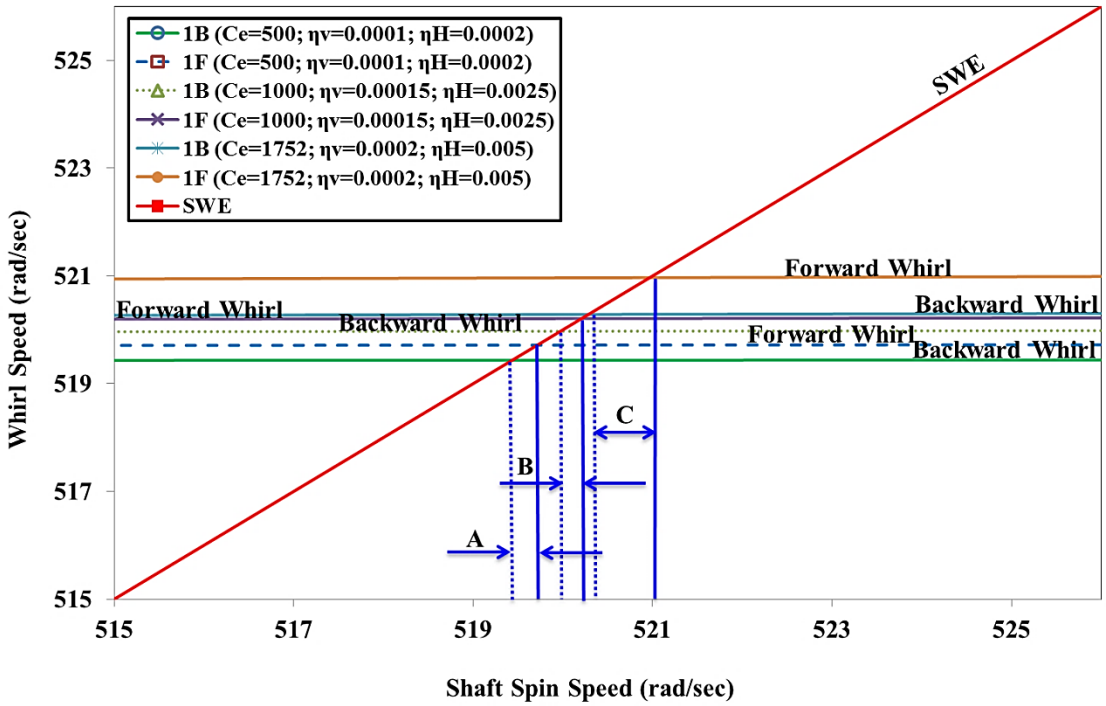

Figure 7-33 Campbell Diagram for 1st Mode

The synchronous whirl excitation is intersecting at two different locations for the first mode. The details of intersection are shown in Figure 7-33. The range between backward critical speed and forward critical speed ranges are shown as 'A', 'B' and 'C'. These ranges are based on the contribution of combined form of internal viscous damping, internal hysteretic damping and external viscous damping. As the internal viscous damping, internal hysteretic damping and external viscous damping increases, these ranges are shifting proportionately at a higher level. If the rotor operating spin speed is within this range 'A' 'B' and 'C', there will be the unbounded amplitude of vibration which results into rotor failure. To mitigate this risk and to avoid resonance, only two options are available, either rotor should redesign in such a way that the range 'A' 'B' and 'C' will get shifted from the operating speed or operate spin speed needs to change. This information is very useful in the design stage of the rotor

7.8.4 CHANGE IN WHIRL SPEED RATIO

The non-dimensional term 'change in whirl speed ratio' is calculated for each mode shape with constant combined form of internal viscous damping, internal hysteretic damping and external viscous damping. This parameter is increasing as the spin speed increases; it means the gap between forward whirl and backward increase as the spin speed increases. The

whirl speed ratio is more predominant in the higher modes. The results are tabulated in Table 7-35 and shown in Figure 7-34.

Table 7-35 Change in whirl speed ratio for Ce=1752 N-s/m; η_v = 0.0002 s; η_H = 0.005, at different rotor spin speeds

Mode	0 rpm (0 rad/sec)	2000 rpm (209.4 rad/sec)	4000 rpm (418.9 rad/sec)	6000 rpm (628.3 rad/sec)
1st Mode	0.000%	0.062%	0.109%	0.153%
2nd Mode	0.000%	0.063%	0.138%	0.221%
3rd Mode	0.000%	0.304%	0.614%	0.931%
4th Mode	0.000%	0.355%	0.732%	1.152%

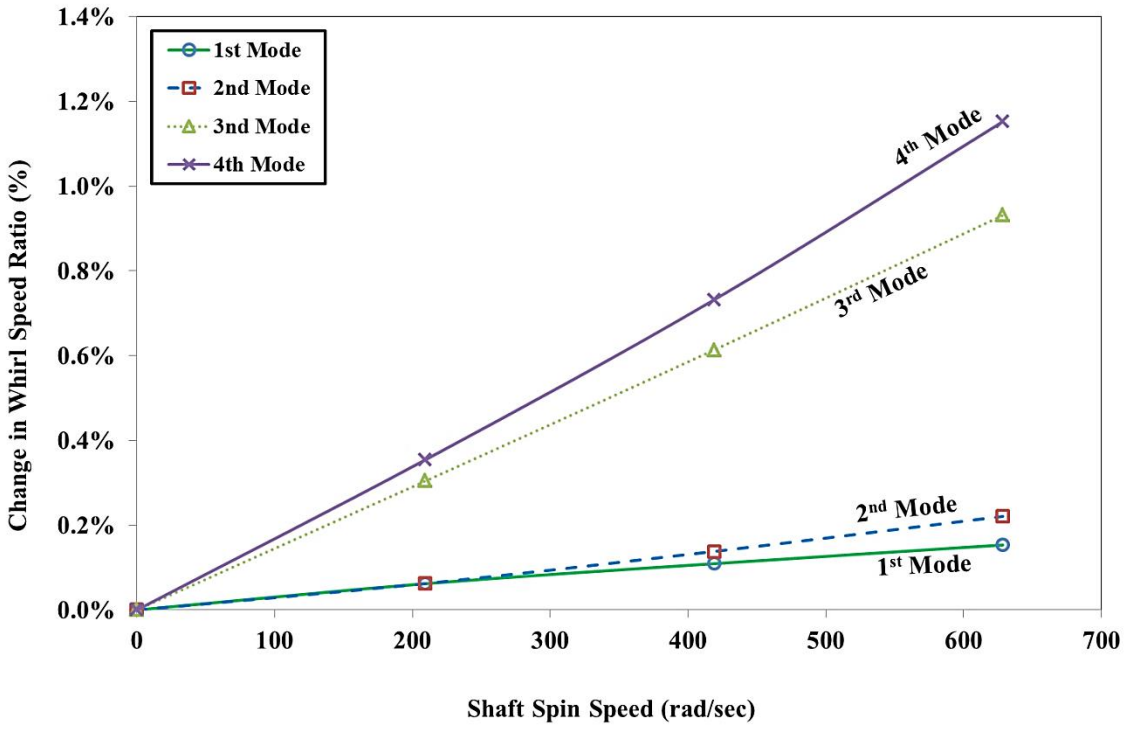

Figure 7-34 Change in Whirl Speed Ratio for Different Modes

The spread between backward whirl speed and forward whirl speed is increasing with increasing the rotor spin speed. This spread is also increasing with higher modes. This spreading effect is due to the contribution of internal viscous damping, internal hysteretic damping and external viscous damping. This phenomenon is adding to the gyroscopic effect.

The sensitivity analysis is carried out on the change in whirl speed ratio with increasing the all combined damping. The results are tabulated in Table 7-36 and shown in Figure 7-35.

Table 7-36 Change in whirl speed ratio for different rotor spin speeds

	0 rpm (0 rad/sec)	2000 rpm (209.4 rad/sec)	4000 rpm (418.9 rad/sec)	6000 rpm (628.3 rad/sec)
Ce = 500 N-s/m; η_v = 0.0001 s; η_H = 0.0002	0.000%	0.022%	0.043%	0.065%
Ce = 1000 N-s/m; η_v = 0.00015 s; η_H = 0.0025	0.000%	0.022%	0.038%	0.053%
Ce=1752 N-s/m; η_v = 0.0002 s; η_H = 0.005	0.000%	0.062%	0.109%	0.153%

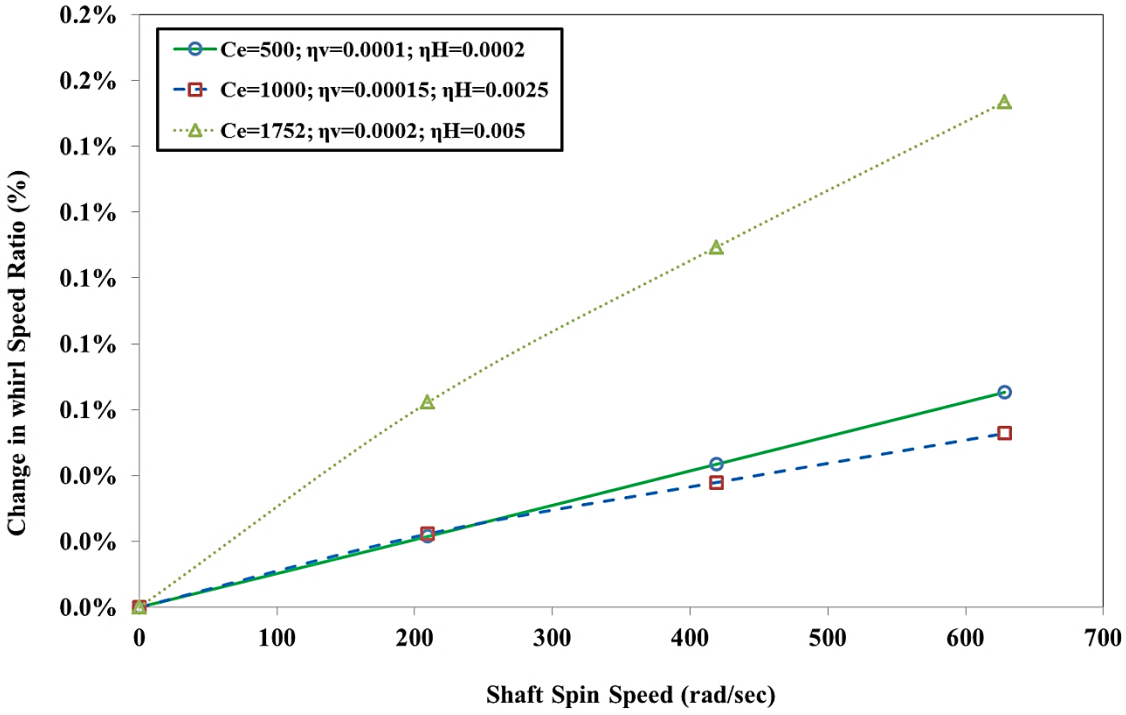

Figure 7-35 Change in Whirl Speed Ratio for 1st Mode

7.8.5 CONCLUSION

The spread between forward whirl speed and backward whirl speed increases with increase in rotor spin speed for all modes. This spread is larger for higher modes and at higher speeds. This is clearly observed in Figure 7-34 with the help of whirl speed ratio. Critical

speed range or spread increases and shifting at higher side with an increase in combined form of external viscous damping internal viscous damping and internal hysteretic damping, as shown in Figure 7-33. A clear understanding of the combined form of external viscous damping internal viscous damping and internal hysteretic damping is very useful while designing flexible and rigid rotors.

7.8.6 APPLICATION

Practical application or situation will be the different parts or components mounted on the shaft with shrink fit and supported on sleeve bearings. The operating temperature is not critical. e.g. Fan, hub, coupling, balance ring etc mounted on the shaft with shrink fit and shaft is supported with sleeve bearings.
e.g. Large vertical water pumps.

7.9 OPERATING TEMPERATURE, INTERNAL VISCOUS DAMPING AND INTERNAL HYSTERETIC DAMPING ACTING IN COMBINED FORM

This case study includes operating temperature (T), internal viscous damping (η_v) and internal hysteretic damping (η_H). It does not include external viscous damping (C_e).

Suppressing the different forms of damping in equations (4-75) and (4-86),

- External viscous damping, $C_{xx} = 0$, $C_{yy} = 0$, $C_{xy} = 0$ and $C_{yx} = 0$

$\therefore \eta_a = \dfrac{1+\eta_H}{\sqrt{1+\eta_H{}^2}}$; and $\therefore \eta_b = \dfrac{\eta_H}{\sqrt{1+\eta_H{}^2}} + \eta_v \Omega$

The equations of motion for operating temperature, internal viscous damping and internal hysteretic damping is expressed,

$$\left[\left[M_{Tt}^{e}\right]+\left[M_{Rt}^{e}\right]\right]\left\{\ddot{\bar{q}}_{n}^{f}\right\}+\left[\eta_{v}\left[K_{Bt}^{e}\right]-\Omega\left[G_{t}^{e}\right]\right]\left\{\dot{\bar{q}}_{n}^{f}\right\}+\left[\eta_{a}\left[K_{Bt}^{e}\right]+\eta_{b}\left[K_{Ct}^{e}\right]\right]\left\{\bar{q}_{n}^{f}\right\}=\left\{\bar{F}_{n}^{f}\right\} \quad (7\text{-}13)$$

7.9.1 EFFECT ON WHIRL SPEEDS

Simulation is performed for different operating temperature, internal viscous damping and internal hysteretic damping values. As these combined damping and operating temperature increases, the forward whirl and backward whirl speeds are changed. Results are tabulated in Table 7-37.

Table 7-37 Whirl Speeds (rad/sec) at rotor spin speed of 4000 (rpm)

Mode	T = 50 °C; η_v = 0.0001 s; η_H = 0.0002	T = 100 °C; η_v = 0.00015 s; η_H = 0.0025	T = 150 °C; η_v = 0.0002 s; η_H = 0.005
1st BW	518.99	517.95	516.41
1st FW	519.05	518.65	518.17
2nd BW	1091.86	1092.66	1093.49
2nd FW	1094.20	1093.91	1093.72
3rd BW	2214.07	2200.31	2181.56
3rd FW	2227.38	2213.68	2195.13
4th BW	4787.98	4601.35	4341.76
4th FW	4818.25	4632.41	4374.31

7.9.2 WHIRL SPEED AND CAMPBELL DIAGRAM FOR ALL MODES

Simulation is performed at different rotor spin speeds and predicted the forward whirl and backward whirl speeds for constant combined form of operating temperature, internal viscous damping and internal hysteretic damping to understand the spread between whirl speed for each mode. Results are tabulated in Table 7-38.

Table 7-38 Whirl Speeds (rad/sec) for T = 150 °C; η_v = 0.0002 s; η_H = 0.005, at different rotor spin speeds

Mode	0 rpm (0 rad/sec)	2000 rpm (209.4 rad/sec)	4000 rpm (418.9 rad/sec)	6000 rpm (628.3 rad/sec)
1st BW	516.71	516.34	516.41	516.76
1st FW	516.71	517.30	518.17	519.32
2nd BW	1093.13	1093.22	1093.49	1093.97
2nd FW	1093.13	1093.46	1093.72	1094.08
3rd BW	2187.26	2184.20	2181.56	2179.31
3rd FW	2187.26	2190.93	2195.13	2199.90
4th BW	4349.85	4344.22	4341.76	4342.19
4th FW	4349.85	4360.05	4374.31	4393.19

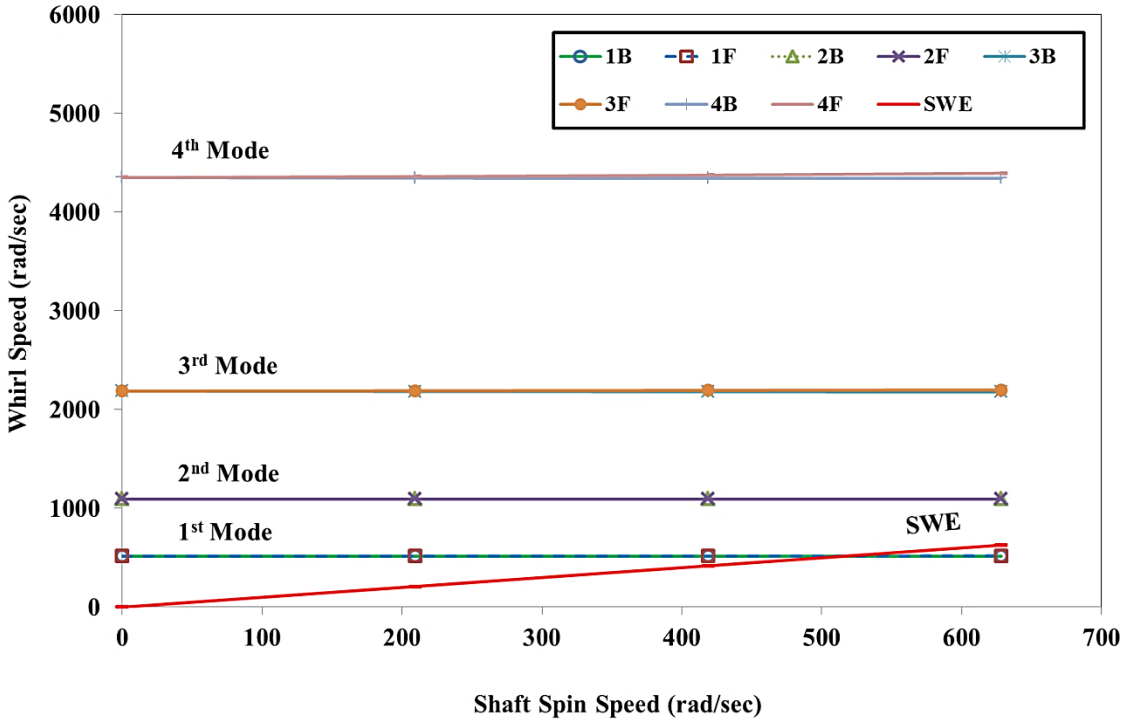

Figure 7-36 Campbell Diagram for Different Modes

7.9.3 WHIRL SPEED AND CAMPBELL DIAGRAM FOR FIRST MODE

The forward whirl speed and backward whirl speed are clearly distinguishable. The spread between backward whirl and forward whirl is increasing with increase in the rotor spin speed. The sensitivity analysis is carried out to understand the combined effect of operating temperature and all forms of damping on the forward whirl and backward whirl speeds. Results are summarized in Table 7-39 and shown in Figure 7-37.

Table 7-39 Whirl Speeds (rad/sec) for different rotor spin speeds

	1st Mode	0 rpm (0 rad/sec)	2000 rpm (209.4 rad/sec)	4000 rpm (418.9 rad/sec)	6000 rpm (628.3 rad/sec)
T = 50 °C; η_v = 0.0001 s; η_H = 0.0002	BW	518.87	518.90	518.99	519.16
	FW	518.87	518.93	519.05	519.25
T = 100 °C; η_v = 0.00015 s; η_H = 0.0025	BW	517.92	517.85	517.95	518.21
	FW	517.92	518.23	518.65	519.23
T = 150 °C; η_v = 0.0002 s; η_H = 0.005	BW	516.71	516.34	516.41	516.76
	FW	516.71	517.30	518.17	519.32

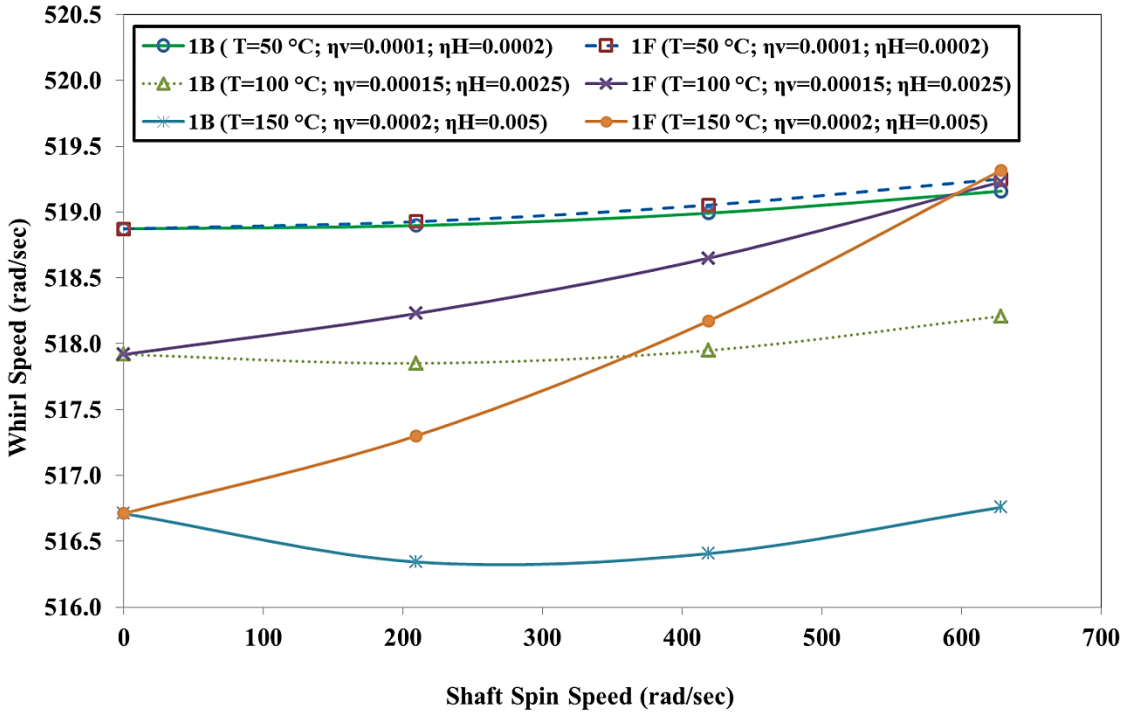

Figure 7-37 Whirl Speed Map for 1st Mode

With the addition of all these damping and operating temperature, the starting point of the forward whirl and backward whirl at zero spin speed gets offset. This offset is increasing with increasing these combinations. Due to this, the forward whirl and backward whirl speeds are increased with clear offset.

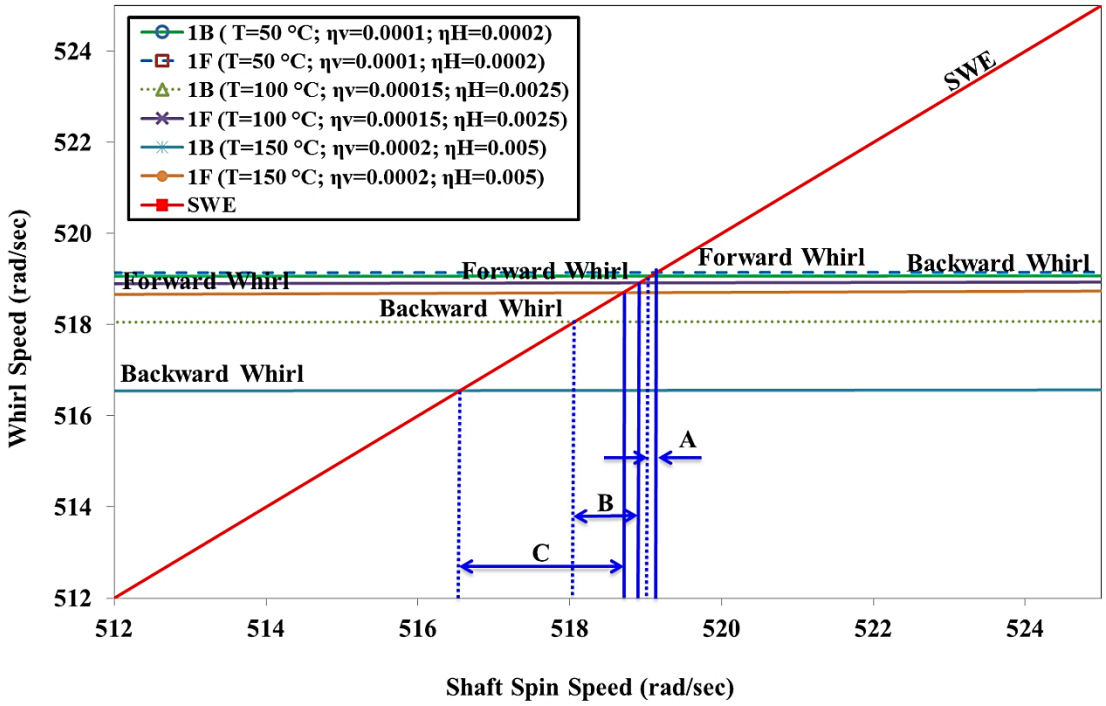

Figure 7-38 Campbell Diagram for 1st Mode

The synchronous whirl excitation is intersecting at two different locations for the first mode. The details of intersection are shown in Figure 7-38. The range between backward critical speed and forward critical speed ranges are shown as ‘A’, ‘B’ and ‘C’. These ranges are based on the contribution of operating temperature, internal viscous damping and internal hysteretic damping. As the operating temperature, internal viscous damping and internal hysteretic damping increases, these ranges are shifting at a lower level with an increase in the range. If the rotor operating spin speed is within this range ‘A’ ‘B’ and ‘C’, there will be the unbounded amplitude of vibration which results into rotor failure. To mitigate this risk and to avoid resonance, only two options are available, either rotor should redesign in such a way that the range ‘A’ ‘B’ and ‘C’ will get shifted from the operating speed or operate spin speed needs to change. This information is very useful in the design stage of the rotor

7.9.4 CHANGE IN WHIRL SPEED RATIO

The non-dimensional term 'change in whirl speed ratio' is calculated for each mode shape with constant combined form of operating temperature, internal viscous damping and internal hysteretic damping. This parameter is increasing as the spin speed increases; it means the gap between forward whirl and backward increases as the spin speed increases. The whirl speed ratio is more predominant in the higher modes. The results are tabulated in Table 7-40 and shown in Figure 7-39.

Table 7-40 Change in whirl speed ratio for T = 150 °C; η_v = 0.0002 s; η_H = 0.005, at different rotor spin speeds

Mode	0 rpm (0 rad/sec)	2000 rpm (209.4 rad/sec)	4000 rpm (418.9 rad/sec)	6000 rpm (628.3 rad/sec)
1st Mode	0.000%	0.185%	0.342%	0.495%
2nd Mode	0.000%	0.022%	0.021%	0.010%
3rd Mode	0.000%	0.308%	0.620%	0.941%
4th Mode	0.000%	0.364%	0.748%	1.172%

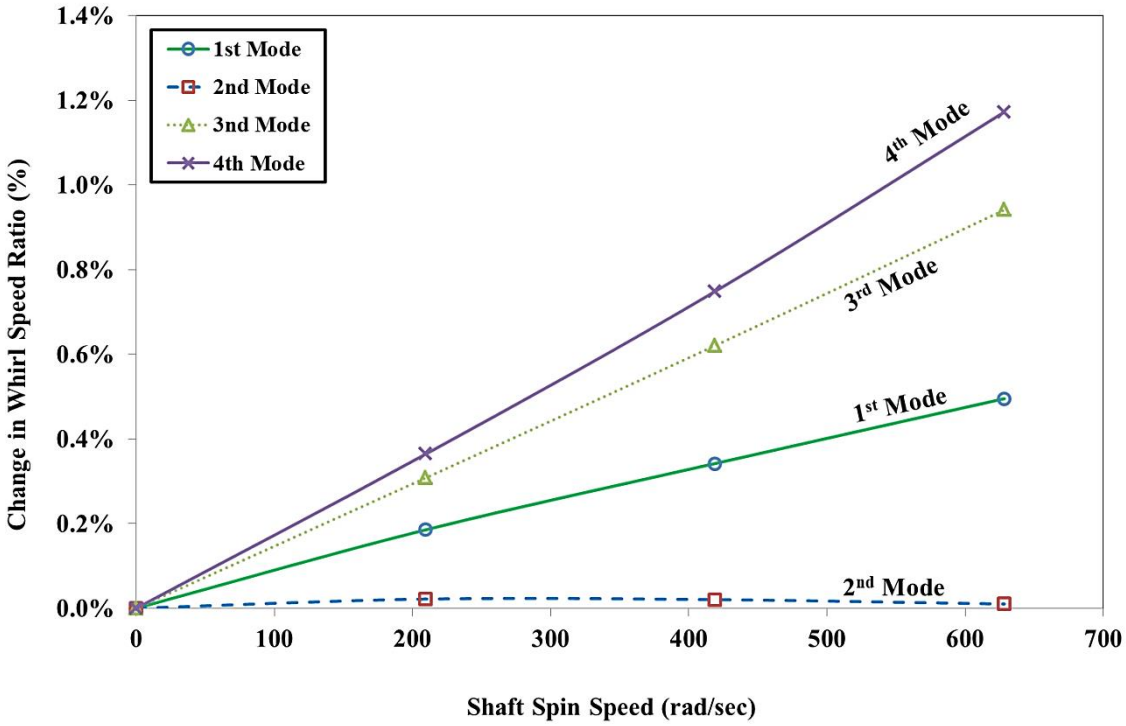

Figure 7-39 Change in Whirl Speed Ratio for Different Modes

The spread between backward whirl speed and forward whirl speed is increasing with increasing the rotor spin speed. This spread is also increasing with higher modes. This spreading effect is due to the contribution of operating temperature, internal viscous damping and internal hysteretic damping. This phenomenon is adding to the gyroscopic effect.

The sensitivity analysis also carried out on the change in whirl speed ratio with increasing operating temperature and all combined damping. The results are tabulated in Table 7-41 and shown in Figure 7-40.

Table 7-41 Change in whirl speed ratio for different rotor spin speeds

	0 rpm (0 rad/sec)	2000 rpm (209.4 rad/sec)	4000 rpm (418.9 rad/sec)	6000 rpm (628.3 rad/sec)
T = 50 °C; η_v = 0.0001 s; η_H = 0.0002	0.000%	0.006%	0.012%	0.018%
T = 100 °C; η_v = 0.00015 s; η_H = 0.0025	0.000%	0.073%	0.135%	0.197%
T = 150 °C; η_v = 0.0002 s; η_H = 0.005	0.000%	0.185%	0.342%	0.495%

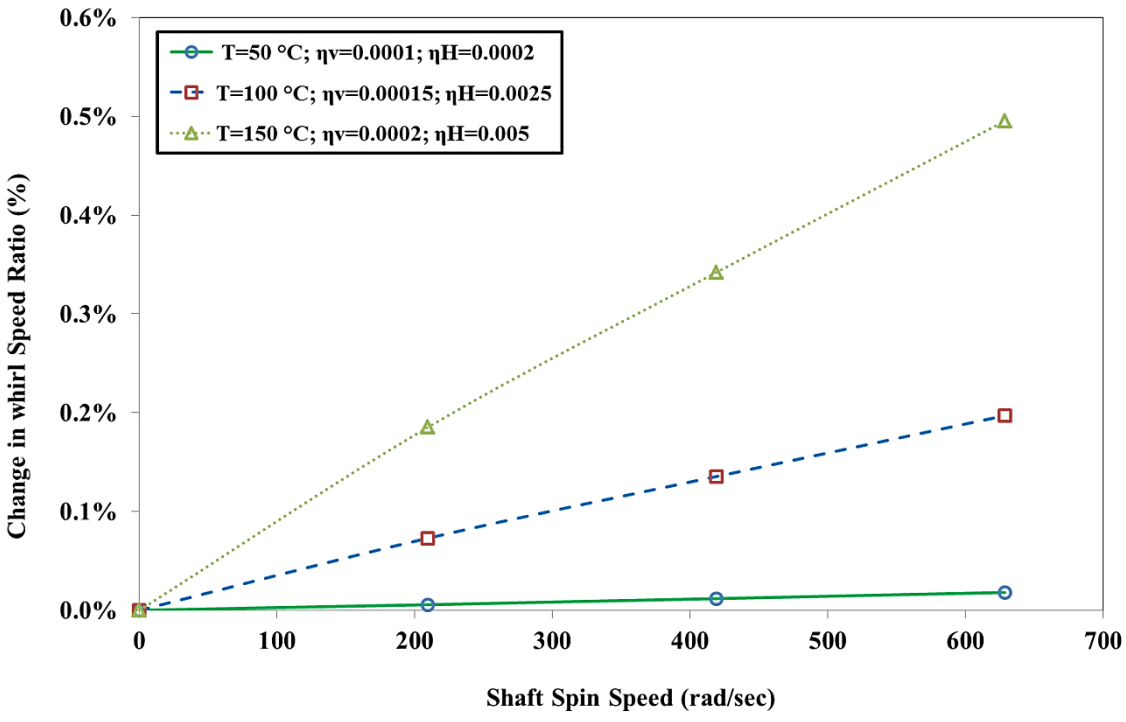

Figure 7-40 Change in Whirl Speed Ratio for 1st Mode

7.9.5 CONCLUSION

The spread between forward whirl speed and backward whirl speed increases with increase in rotor spin speed for all modes except for the second mode. This interesting phenomenon is observed only for the second mode. The spread between forward whirl and backward whirl for second is small and this phenomenon is attributed towards nullifying the gyroscopic effect. The spread is large for the first, third and fourth mode. It is clearly observed in Figure 7-39 with the help of whirl speed ratio. Critical speed range or spread is increasing with the larger magnitude and shifting at the lower side with an increase in combined form of operating temperature, internal viscous damping and internal hysteretic damping as shown in Figure 7-38. A clear understanding of operating temperature, internal viscous damping and internal hysteretic damping is very useful while designing flexible and rigid rotors.

7.9.6 APPLICATION

Practical application or situation will be the different parts or components mounted on the shaft with shrink fit and operating temperature is critical. The external viscous damping is not present. e.g. Fan, hub, coupling, balance ring etc mounted on the shaft with shrink fit and shaft is supported with anti-friction bearings like ball bearings, roller bearings. This is operated at high temperature.

e.g. Furnace conveyor shaft with different mountings.

7.10 OPERATING TEMPERATURE, INTERNAL VISCOUS DAMPING AND EXTERNAL VISCOUS DAMPING ACTING IN COMBINED FORM

This case study includes operating temperature (T), internal viscous damping (η_v) and external viscous damping (C_e). It does not include internal hysteretic damping (η_H).

Suppressing the different forms of damping in equations (4-75) and (4-86),

- Internal hysteretic damping, $\eta_H = 0$

$$\therefore \eta_a = \frac{1+\eta_H}{\sqrt{1+\eta_H{}^2}} = 1 \text{; and } \therefore \eta_b = \frac{\eta_H}{\sqrt{1+\eta_H{}^2}} + \eta_v\Omega = \eta_v\Omega$$

The equations of motion for operating temperature, internal viscous damping and external viscous damping are expressed,

$$\left[\left[M_{Tt}^e\right]+\left[M_{Rt}^e\right]\right]\left\{\ddot{\bar{q}}_n^f\right\}+\left[\eta_v\left[K_{Bt}^e\right]-\Omega\left[G_t^e\right]\right]\left\{\dot{\bar{q}}_n^f\right\}+\left[\left[K_{Bt}^e\right]+\eta_v\Omega\left[K_{Ct}^e\right]\right]\left\{\bar{q}_n^f\right\}=\left\{\bar{F}_n^f\right\} \quad (7\text{-}14)$$

$$\begin{bmatrix} C_{xx} & C_{xy} \\ C_{yx} & C_{yy} \end{bmatrix}\left\{\dot{\bar{q}}_n^f\right\}+\begin{bmatrix} K_{xx} & K_{xy} \\ K_{yx} & K_{yy} \end{bmatrix}\left\{\bar{q}_n^f\right\}=\left\{\bar{F}_b^f\right\} \quad (7\text{-}15)$$

7.10.1 EFFECT ON WHIRL SPEEDS

Simulation is performed for different operating temperature, internal viscous damping and external viscous damping values. As these combined damping and operating temperature increases, the forward whirl and backward whirl speeds are decreased for all the modes. Results are tabulated in Table 7-42.

Table 7-42 Whirl Speeds (rad/sec) at rotor spin speed of 4000 (rpm)

Mode	Ce = 500 N-s/m T = 50 °C; η_v = 0.0001 s	Ce = 1000 N-s/m T = 100 °C; η_v = 0.00015 s	Ce = 1752 N-s/m T = 150 °C; η_v = 0.0002 s
1st BW	518.77	517.60	515.71
1st FW	519.00	517.76	516.20
2nd BW	1091.29	1090.80	1089.25
2nd FW	1093.88	1092.81	1090.76
3rd BW	2212.01	2192.67	2163.93
3rd FW	2225.32	2205.99	2177.29
4th BW	4782.31	4578.84	4288.27
4th FW	4812.49	4609.57	4319.94

7.10.2 WHIRL SPEED AND CAMPBELL DIAGRAM FOR ALL MODES

Simulation is performed at different rotor spin speeds and predicted the forward whirl and backward whirl speeds for constant combined form of damping and operating temperature to understand the spread between the forward whirl speed and backward whirl speed for each mode. Results are tabulated in Table 7-43 and shown in Figure 7-41

Table 7-43 Whirl Speeds (rad/sec) for Ce = 1752 N-s/m; T = 150 °C; η_v = 0.0002 s, at different rotor spin speeds

Mode	0 rpm (0 rad/sec)	2000 rpm (209.4 rad/sec)	4000 rpm (418.9 rad/sec)	6000 rpm (628.3 rad/sec)
1st BW	515.37	515.39	515.71	516.33
1st FW	515.37	515.64	516.20	517.03
2nd BW	1089.62	1089.35	1089.25	1089.29
2nd FW	1089.62	1090.09	1090.76	1091.65
3rd BW	2169.56	2166.51	2163.93	2161.77
3rd FW	2169.56	2173.14	2177.29	2182.04
4th BW	4296.60	4290.77	4288.27	4288.75
4th FW	4296.60	4306.15	4319.94	4338.49

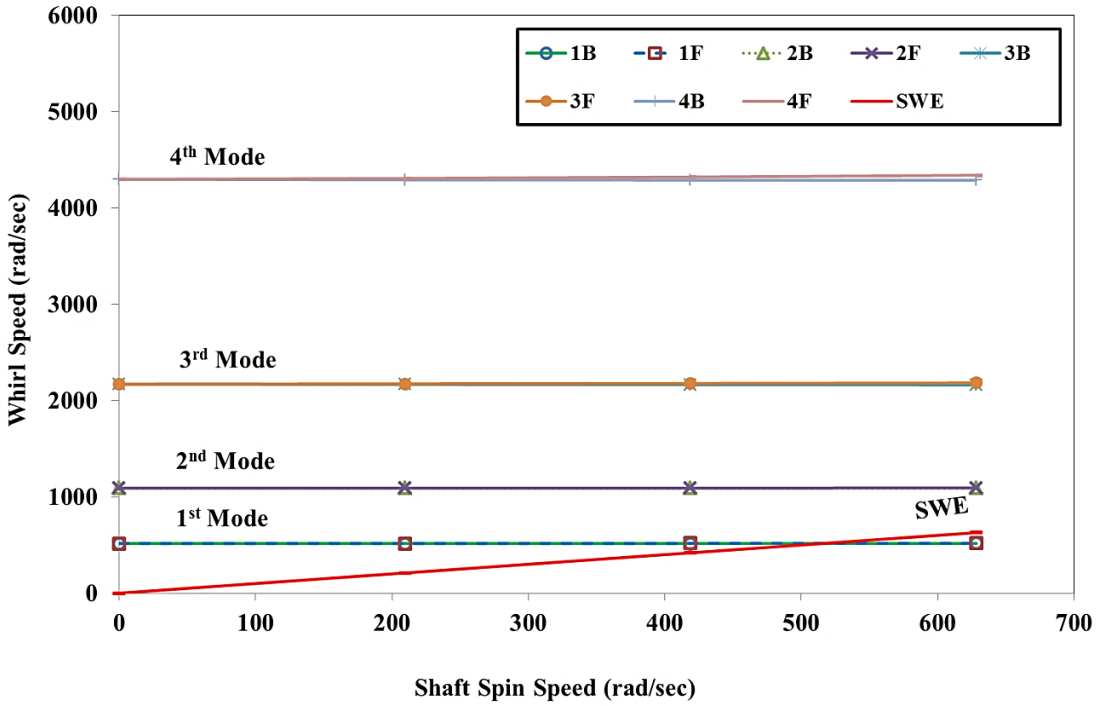

Figure 7-41 Campbell Diagram for Different Modes

7.10.3 WHIRL SPEED AND CAMPBELL DIAGRAM FOR FIRST MODE

The forward whirl speed and backward whirl speed are clearly distinguishable. The spread between backward whirl and forward whirl is increasing with increase in the rotor spin speed. The sensitivity analysis is carried out to understand the combined effect of operating temperature and all damping on the forward whirl and backward whirl speeds. Results are summarized in Table 7-44 and shown in Figure 7-42.

Table 7-44 Whirl Speeds (rad/sec) for different rotor spin speeds

	1st Mode	0 rpm (0 rad/sec)	2000 rpm (209.4 rad/sec)	4000 rpm (418.9 rad/sec)	6000 rpm (628.3 rad/sec)
Ce = 500 N-s/m; T = 50 °C; η_v = 0.0001 s	BW	518.74	518.72	518.77	518.89
	FW	518.74	518.83	519.00	519.24
Ce = 1000 N-s/m; T = 100 °C; η_v = 0.00015 s	BW	517.35	517.39	517.60	517.98
	FW	517.35	517.47	517.76	518.20
Ce = 1752 N-s/m; T = 150 °C; η_v = 0.0002 s	BW	515.37	515.39	515.71	516.33
	FW	515.37	515.64	516.20	517.03

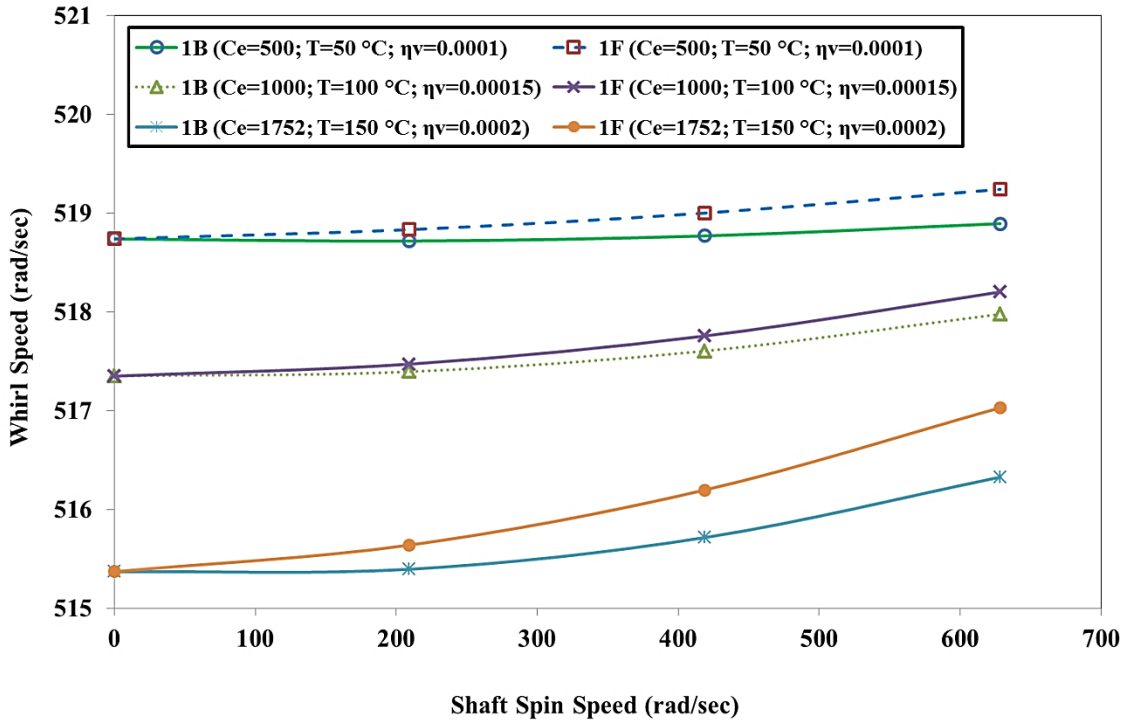

Figure 7-42 Whirl Speed Map for 1st Mode

With the addition of all these damping and operating temperature, the starting point of the forward whirl and backward whirl at zero spin speed gets offset. This offset is increasing with increasing operating temperature and these damping. Due to this, the forward whirl and backward whirl speeds are increased with clear offset.

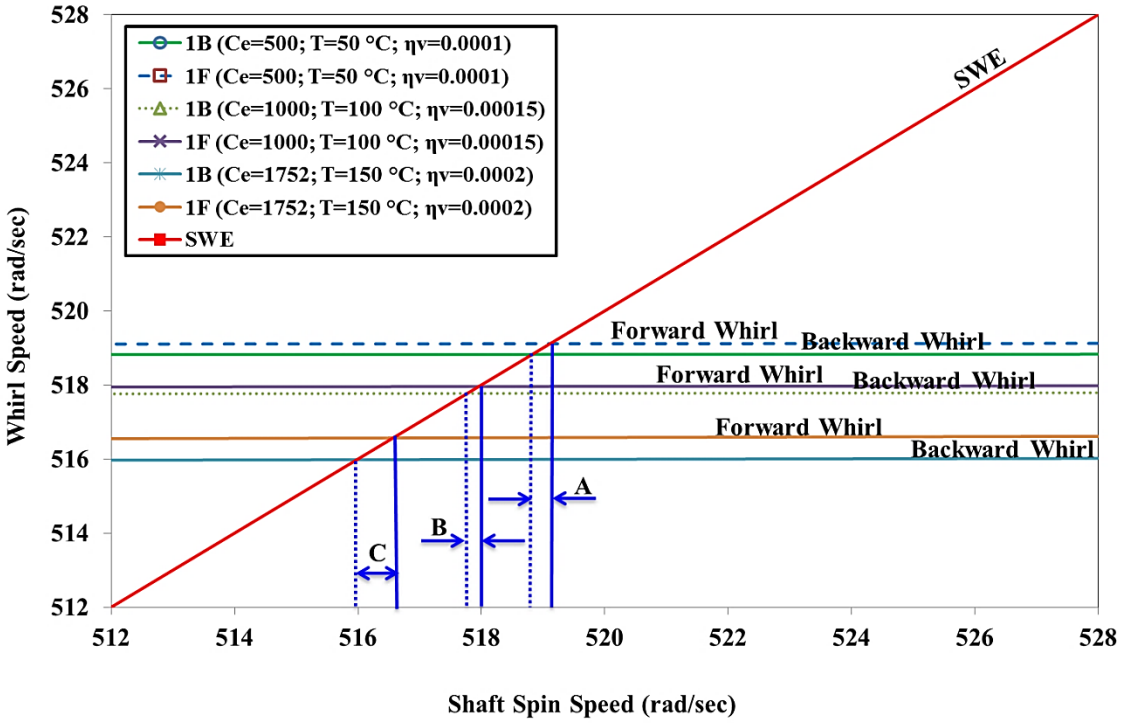

Figure 7-43 Campbell Diagram for 1st Mode

The synchronous whirl excitation is intersecting at two different locations for the first mode. The details of intersection are shown in Figure 7-43. The range between backward critical speed and forward critical speed ranges are shown as 'A', 'B' and 'C'. These ranges are based on the contribution of combined form of operating temperature, internal viscous damping and external viscous damping. As the operating temperature, internal viscous damping and internal hysteretic damping increases, these ranges are shifting at a lower level with an increase in the range. If the rotor operating spin speed is within this range 'A' 'B' and 'C', there will be the unbounded amplitude of vibration which results into rotor failure. To mitigate this risk and to avoid resonance, only two options are available, either rotor should redesign in such a way that the range 'A' 'B' and 'C' will get shifted from the operating speed or operate spin speed needs to change. This information is very useful in the design stage of the rotor.

7.10.4 CHANGE IN WHIRL SPEED RATIO

The non-dimensional term 'change in whirl speed ratio' is calculated for each mode shape with constant operating temperature, internal viscous damping and external viscous damping. This parameter is increasing as the spin speed increases; it means the gap between forward whirl and backward increase as the spin speed increases. The whirl speed ratio is more predominant in the higher modes. The results are tabulated in Table 7-45 and shown in Figure 7-44.

Table 7-45 Change in whirl speed ratio for Ce = 1752 N-s/m; T = 150 °C; η_v = 0.0002 s, at different rotor spin speeds

Mode	0 rpm (0 rad/sec)	2000 rpm (209.4 rad/sec)	4000 rpm (418.9 rad/sec)	6000 rpm (628.3 rad/sec)
1st Mode	0.000%	0.047%	0.093%	0.136%
2nd Mode	0.000%	0.067%	0.138%	0.217%
3rd Mode	0.000%	0.306%	0.616%	0.934%
4th Mode	0.000%	0.358%	0.737%	1.157%

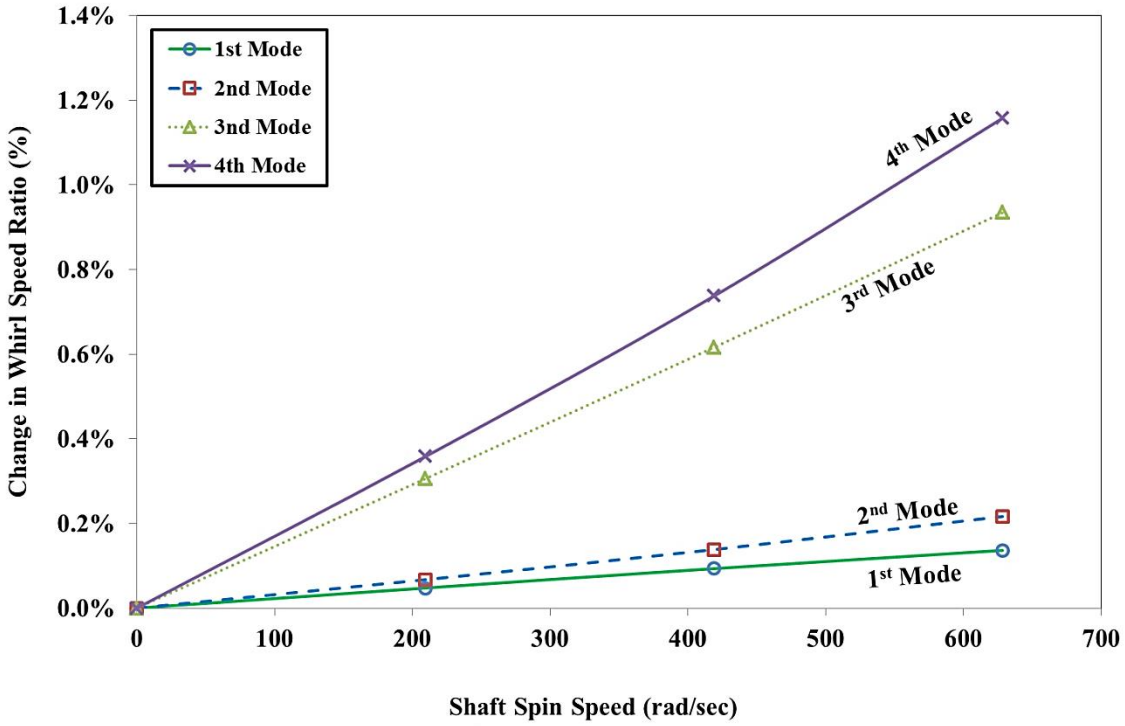

Figure 7-44 Change in Whirl Speed Ratio for Different Modes

The spread between backward whirl speed and forward whirl speed is increasing with increasing the rotor spin speed. This spread is also increasing with higher modes. This spreading effect is due to the contribution of operating temperature, internal viscous damping and external viscous damping. This phenomenon is adding to the gyroscopic effect.

The sensitivity analysis also carried out on the change in whirl speed ratio with increasing operating temperature and all combined damping. The results are tabulated in Table 7-46 and shown in Figure 7-45.

Table 7-46 Change in whirl speed ratio for different rotor spin speeds

	0 rpm (0 rad/sec)	2000 rpm (209.4 rad/sec)	4000 rpm (418.9 rad/sec)	6000 rpm (628.3 rad/sec)
Ce = 500 N-s/m; T = 50 °C; η_v = 0.0001 s	0.000%	0.022%	0.045%	0.067%
Ce = 1000 N-s/m; T = 100 °C; η_v = 0.00015 s	0.000%	0.015%	0.029%	0.043%
Ce = 1752 N-s/m; T = 150 °C; η_v = 0.0002 s	0.000%	0.047%	0.093%	0.136%

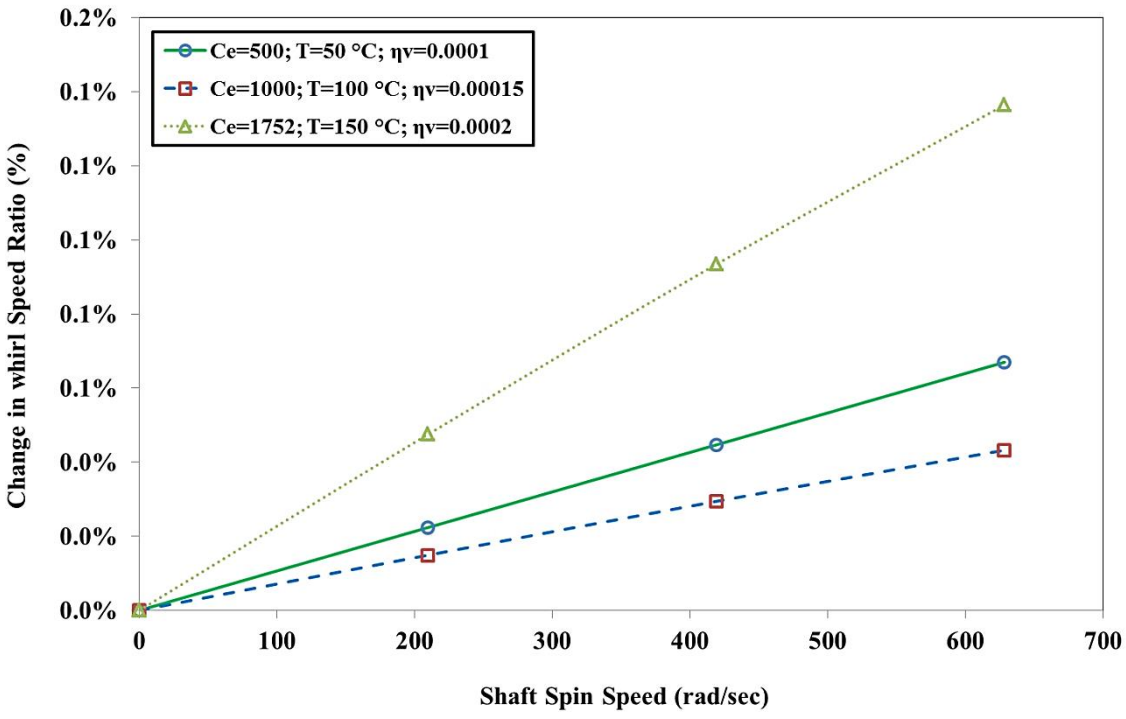

Figure 7-45 Change in Whirl Speed Ratio for 1st Mode

7.10.5 CONCLUSION

The spread between forward whirl speed and backward whirl speed increases with increase in rotor spin speed for all modes. This spread is larger for higher modes and at higher speeds. This is clearly observed in Figure 7-44 with the help of whirl speed ratio. Critical speed range or spread changes slightly and shifting at the lower side with an increase in combined form of operating temperature, external viscous damping and internal viscous damping as shown in Figure 7-43. A clear understanding of the combined form of operating temperature, external viscous damping and internal viscous damping is very useful while designing flexible and rigid rotors.

7.10.6 APPLICATION

Practical application or situation will be the different parts or components mounted on the shaft with shrink fit and operating temperature is critical. The external viscous damping is also present. e.g. Fan, hub, coupling, balance ring etc mounted on the shaft with shrink fit and shaft is supported with sleeve bearings like ball bearings, roller bearings. This is operated at high temperature.

e.g. Gearbox.

7.11 OPERATING TEMPERATURE, INTERNAL HYSTERETIC DAMPING AND EXTERNAL VISCOUS DAMPING ACTING IN COMBINED FORM

This case study includes operating temperature (T), internal hysteretic damping (η_H) and external viscous damping (C_e). It does not include internal viscous damping (η_v).

Suppressing the different forms of damping in equations (4-75) and (4-86),

- Internal viscous damping, $\eta_v = 0$

$\therefore \eta_a = \dfrac{1+\eta_H}{\sqrt{1+\eta_H{}^2}}$; and $\therefore \eta_b = \dfrac{\eta_H}{\sqrt{1+\eta_H{}^2}} + \eta_v\Omega = \dfrac{\eta_H}{\sqrt{1+\eta_H{}^2}}$

The equations of motion for operating temperature, internal hysteretic damping and external viscous damping are expressed,

$$\left[\left[M_{Tt}^{e}\right]+\left[M_{Rt}^{e}\right]\right]\left\{\ddot{\bar{q}}_{n}^{f}\right\}-\Omega\left[G_{t}^{e}\right]\left\{\dot{\bar{q}}_{n}^{f}\right\}+\left[\frac{1+\eta_{H}}{\sqrt{1+\eta_{H}^{2}}}\left[K_{Bt}^{e}\right]+\frac{\eta_{H}}{\sqrt{1+\eta_{H}^{2}}}\left[K_{Ct}^{e}\right]\right]\left\{\bar{q}_{n}^{f}\right\}=\left\{\bar{F}_{n}^{f}\right\} \tag{7-16}$$

$$\begin{bmatrix} C_{xx} & C_{xy} \\ C_{yx} & C_{yy} \end{bmatrix}\left\{\dot{\bar{q}}_{n}^{f}\right\}+\begin{bmatrix} K_{xx} & K_{xy} \\ K_{yx} & K_{yy} \end{bmatrix}\left\{\bar{q}_{n}^{f}\right\}=\left\{\bar{F}_{b}^{f}\right\} \tag{7-17}$$

7.11.1 EFFECT ON WHIRL SPEEDS

Simulation is performed for different operating temperature, internal hysteretic damping and external viscous damping values. As these combined damping and operating temperature increases, the forward whirl and backward whirl speeds are changed. Results are tabulated in Table 7-47.

Table 7-47 Whirl Speeds (rad/sec) at rotor spin speed of 4000 (rpm)

Mode	Ce = 500 N-s/m; T = 50 °C; η_H = 0.0002	Ce = 1000 N-s/m; T = 100 °C; η_H = 0.0025	Ce = 1752 N-s/m; T = 150 °C; η_H = 0.005
1st BW	518.41	517.31	515.81
1st FW	519.06	517.99	516.54
2nd BW	1090.75	1090.04	1088.76
2nd FW	1093.96	1093.28	1092.07
3rd BW	2219.18	2211.28	2199.67
3rd FW	2232.49	2224.58	2212.98
4th BW	4918.61	4893.60	4858.32
4th FW	4948.49	4923.47	4888.17

7.11.2 WHIRL SPEED AND CAMPBELL DIAGRAM FOR ALL MODES

Simulation is performed at different rotor spin speeds and predicted the forward whirl and backward whirl speeds for constant operating temperature, internal hysteretic damping and external viscous damping to understand the spread between whirl speed for each mode. Results are tabulated in Table 7-48 and shown in Figure 7-46.

Table 7-48 Whirl Speeds (rad/sec) for Ce = 1752 N-s/m; T = 150 °C; η_H = 0.005, at different rotor spin speeds

Mode	0 rpm (0 rad/sec)	2000 rpm (209.4 rad/sec)	4000 rpm (418.9 rad/sec)	6000 rpm (628.3 rad/sec)
1st BW	516.14	515.97	515.81	515.64
1st FW	516.14	516.38	516.54	516.71
2nd BW	1090.36	1089.56	1088.76	1087.96
2nd FW	1090.36	1091.27	1092.07	1092.87
3rd BW	2206.32	2202.99	2199.67	2196.37
3rd FW	2206.32	2209.64	2212.98	2216.32
4th BW	4873.21	4865.78	4858.32	4850.88
4th FW	4873.21	4880.68	4888.17	4895.66

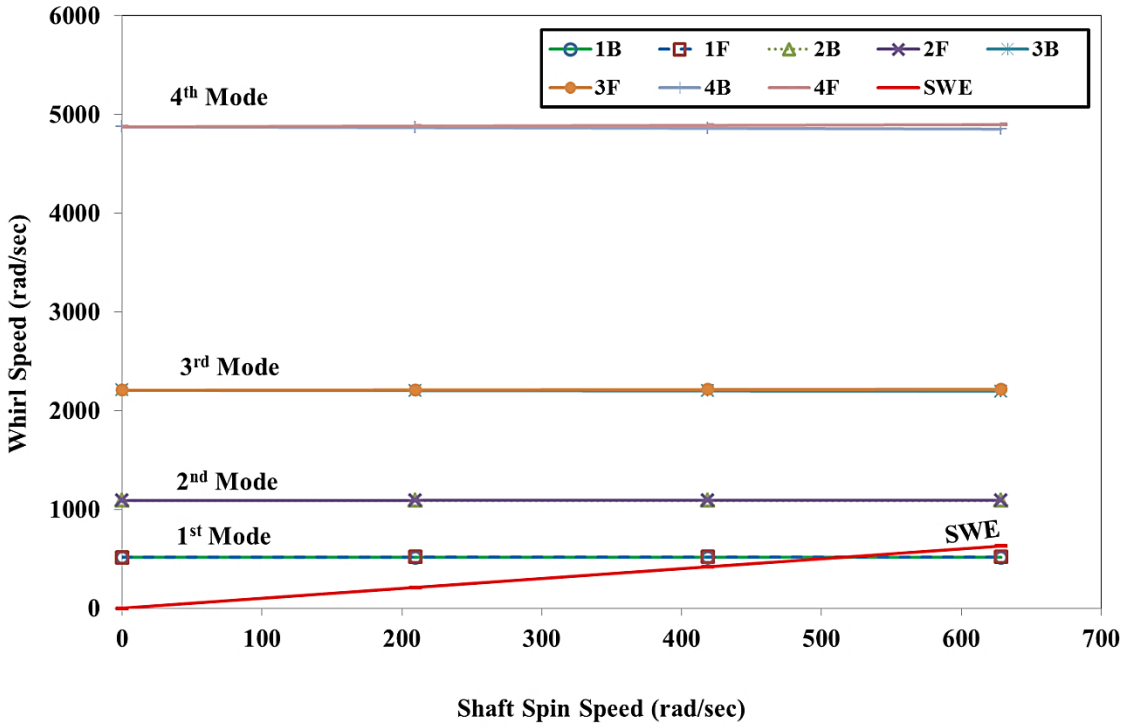

Figure 7-46 Campbell Diagram for Different Modes

7.11.3 WHIRL SPEED AND CAMPBELL DIAGRAM FOR FIRST MODE

The forward whirl speed and backward whirl speed are clearly distinguishable. The spread between backward whirl and forward whirl is increasing with increase in the rotor spin speed. The sensitivity analysis is carried out to understand the combined effect of external viscous damping, operating temperature and internal hysteretic damping on the forward whirl and backward whirl speeds. Results are summarized in Table 7-49 and shown in Figure 7-47.

Table 7-49 Whirl Speeds (rad/sec) for different rotor spin speeds

	1st Mode	0 rpm (0 rad/sec)	2000 rpm (209.4 rad/sec)	4000 rpm (418.9 rad/sec)	6000 rpm (628.3 rad/sec)
Ce = 500 N-s/m; T = 50 °C; η_H = 0.0002	BW	518.73	518.57	518.41	518.24
	FW	518.73	518.90	519.06	519.22
Ce = 1000 N-s/m; T = 100 °C; η_H = 0.0025	BW	517.64	517.48	517.31	517.15
	FW	517.64	517.83	517.99	518.15
Ce = 1752 N-s/m; T=150 °C; η_H = 0.005	BW	516.14	515.97	515.81	515.64
	FW	516.14	516.38	516.54	516.71

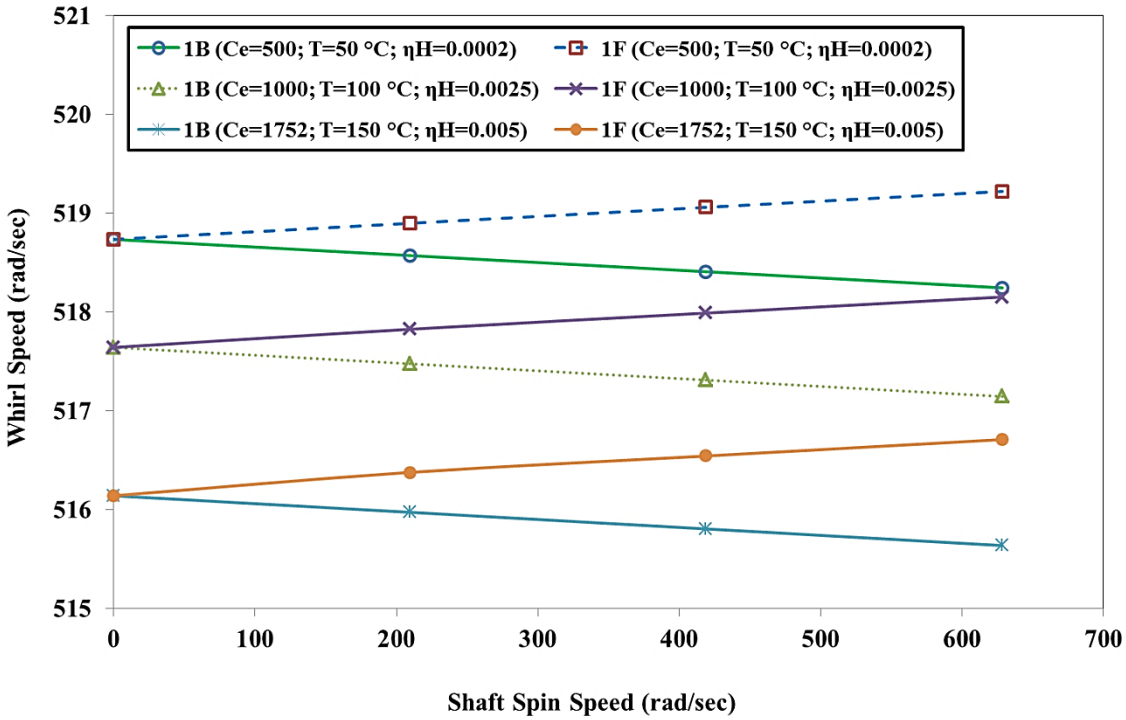

Figure 7-47 Whirl Speed Map for 1st Mode

With the addition of all these damping and operating temperature, the starting point of the forward whirl and backward whirl at zero spin speed gets offset. This offset is increasing with increasing these combinations. Due to this, the forward whirl and backward whirl speeds are increased with clear offset.

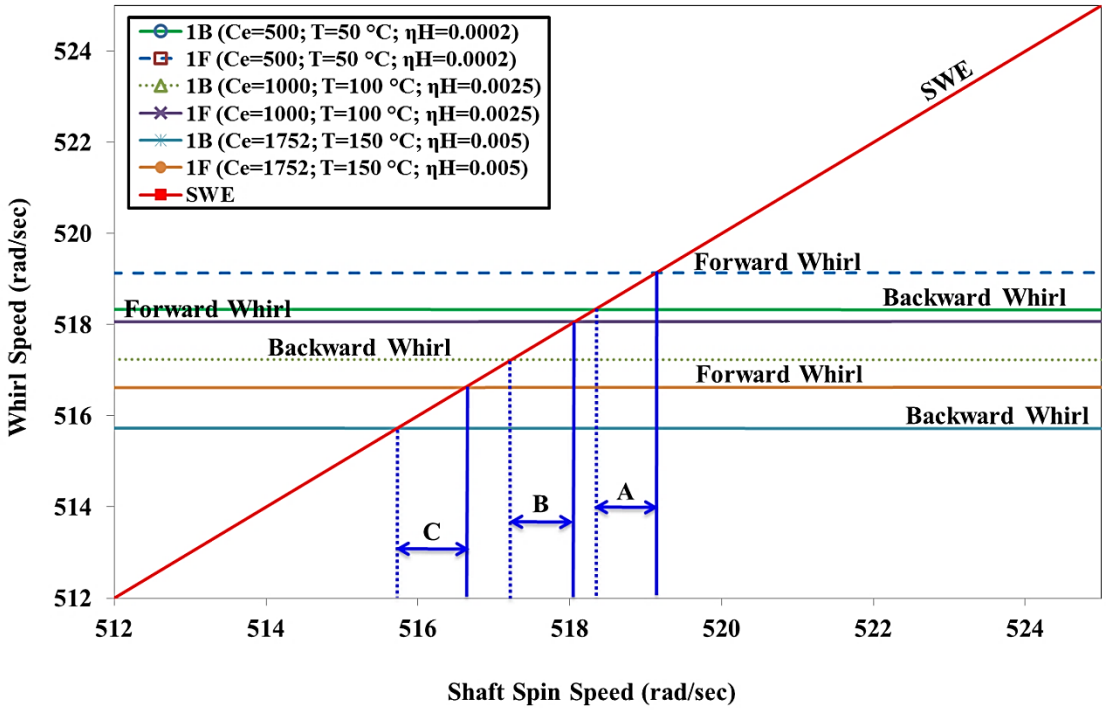

Figure 7-48 Campbell Diagram for 1st Mode

The synchronous whirl excitation is intersecting at two different locations for the first mode. The details of intersection are shown in Figure 7-48. The range between backward critical speed and forward critical speed ranges are shown as 'A', 'B' and 'C'. These ranges are based on the contribution of operating temperature, internal hysteretic damping and external viscous damping. As the operating temperature, internal hysteretic damping and external viscous damping increases, these ranges are shifting at a lower level with an increase in the range. If the rotor operating spin speed is within this range 'A' 'B' and 'C', there will be the unbounded amplitude of vibration which results into rotor failure. To mitigate this risk and to avoid resonance, only two options are available, either rotor should redesign in such a way that the range 'A' 'B' and 'C' will get shifted from the operating speed or operate spin speed needs to change. This information is very useful in the design stage of the rotor.

7.11.4 CHANGE IN WHIRL SPEED RATIO

The non-dimensional term 'change in whirl speed ratio' is calculated for each mode shape with constant combined form of operating temperature, internal hysteretic damping and external viscous damping. This parameter is increasing as the spin speed increases; it means the gap between forward whirl and backward increases as the spin speed increases. The whirl speed ratio is more predominant in the higher modes. The results are tabulated in Table 7-50 and shown in Figure 7-49.

Table 7-50 Change in whirl speed ratio for Ce = 1752 N-s/m; T = 150 °C; η_H = 0.005, at different rotor spin speeds

Mode	0 rpm (0 rad/sec)	2000 rpm (209.4 rad/sec)	4000 rpm (418.9 rad/sec)	6000 rpm (628.3 rad/sec)
1st Mode	0.000%	0.078%	0.143%	0.208%
2nd Mode	0.000%	0.157%	0.303%	0.450%
3rd Mode	0.000%	0.302%	0.603%	0.904%
4th Mode	0.000%	0.306%	0.612%	0.919%

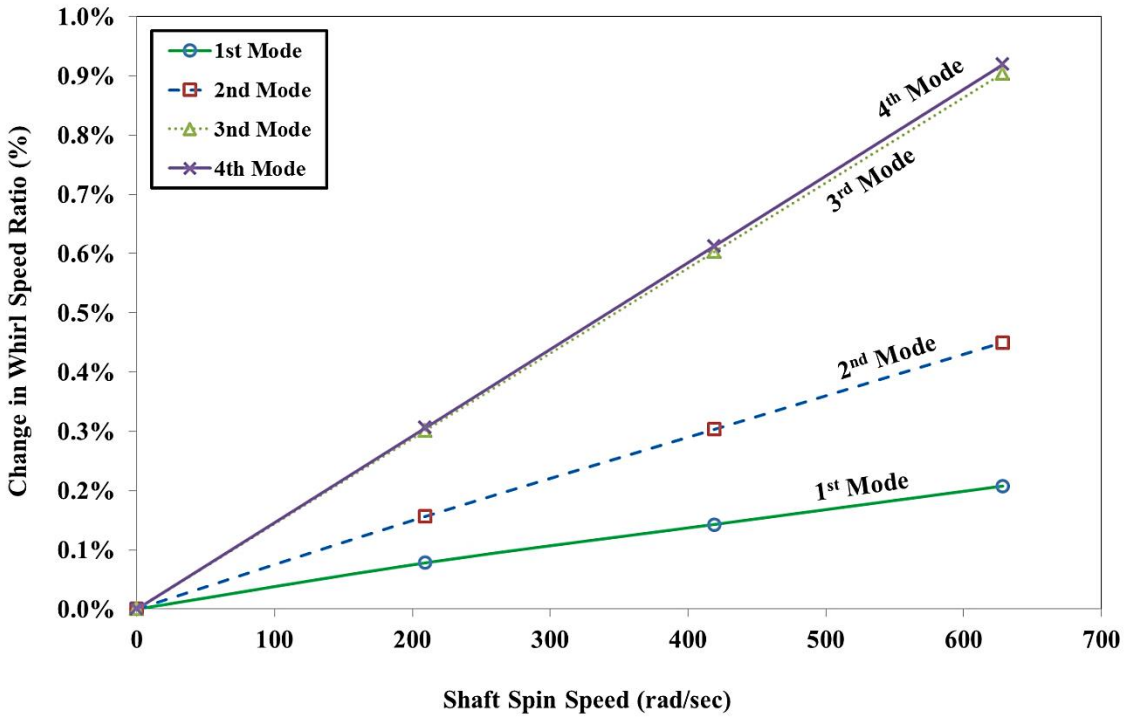

Figure 7-49 Change in Whirl Speed Ratio for Different Modes

The spread between backward whirl speed and forward whirl speed is increasing with increasing the rotor spin speed. This spread is also increasing with higher modes. This spreading effect is due to the contribution of operating temperature, internal hysteretic damping and external viscous damping. This phenomenon is adding to the gyroscopic effect.

The sensitivity analysis also carried out on the change in whirl speed ratio with increasing external viscous damping, operating temperature and internal hysteretic damping. The results are tabulated in Table 7-51 and shown in Figure 7-50.

Table 7-51 Change in whirl speed ratio for different rotor spin speeds

	0 rpm (0 rad/sec)	2000 rpm (209.4 rad/sec)	4000 rpm (418.9 rad/sec)	6000 rpm (628.3 rad/sec)
Ce = 500 N-s/m; T = 50 °C; η_H = 0.0002	0.000%	0.063%	0.126%	0.188%
Ce = 1000 N-s/m; T = 100 °C; η_H = 0.0025	0.000%	0.067%	0.131%	0.195%
Ce = 1752 N-s/m; T=150 °C; η_H = 0.005	0.000%	0.078%	0.143%	0.208%

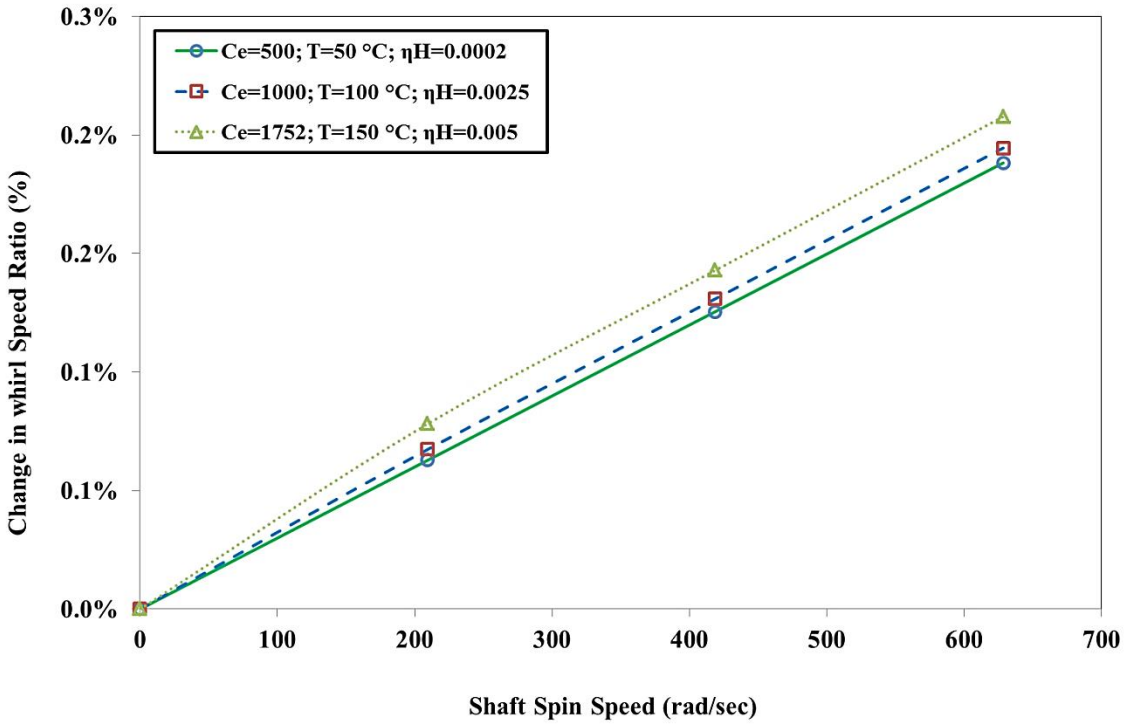

Figure 7-50 Change in Whirl Speed Ratio for 1st Mode

7.11.5 CONCLUSION

The spread between forward whirl speed and backward whirl speed increases with increase in rotor spin speed for all modes. This spread is larger for higher modes and at higher speeds. This is clearly observed in Figure 7-49 with the help of whirl speed ratio. Critical speed range or spread changes slightly and shifting at the lower side with an increase in combined form of operating temperature, external viscous damping and internal hysteretic damping as shown in Figure 7-48. A clear understanding of the combined form of operating temperature, external viscous damping and internal hysteretic damping is very useful while designing flexible and rigid rotors.

7.11.6 APPLICATION

Practical application or situation will be the simple shaft and high-temperature ambient conditions supported with sleeve bearings.

e.g. Drive shafts in power train.

7.12 OPERATING TEMPERATURE, INTERNAL VISCOUS DAMPING, INTERNAL HYSTERETIC DAMPING AND EXTERNAL VISCOUS DAMPING ACTING IN COMBINED FORM

This case study includes operating temperature (T), internal viscous damping (η_v), internal hysteretic damping (η_H) and external viscous damping (C_e),

The equations of motion from equation (4-75) and external viscous damping (4-86) as,

$$\left[\left[M_{Tt}^{e}\right]+\left[M_{Rt}^{e}\right]\right]\left\{\ddot{\bar{q}}_{n}^{f}\right\}+\left[\eta_{v}\left[K_{Bt}^{e}\right]-\Omega\left[G_{t}^{e}\right]\right]\left\{\dot{\bar{q}}_{n}^{f}\right\}+\left[\eta_{a}\left[K_{Bt}^{e}\right]+\eta_{b}\left[K_{Ct}^{e}\right]\right]\left\{\bar{q}_{n}^{f}\right\}=\left\{\bar{F}_{n}^{f}\right\}$$

$$\begin{bmatrix} C_{xx} & C_{xy} \\ C_{yx} & C_{yy} \end{bmatrix}\left\{\dot{\bar{q}}_{n}^{f}\right\}+\begin{bmatrix} K_{xx} & K_{xy} \\ K_{yx} & K_{yy} \end{bmatrix}\left\{\bar{q}_{n}^{f}\right\}=\left\{\bar{F}_{b}^{f}\right\}$$

7.12.1 EFFECT ON WHIRL SPEEDS

Simulation is performed for different operating temperature, internal viscous damping, internal hysteretic damping and external viscous damping values. As these combined damping and operating temperature increases, the forward whirl and backward whirl speeds are changed. Results are tabulated in Table 7-52.

Table 7-52 Whirl Speeds (rad/sec) at rotor spin speed of 4000 (rpm)

Mode	Ce = 500 N-s/m; T = 50 °C; η_v = 0.0001 s; η_H = 0.0002	Ce = 1000 N-s/m; T =100 °C; η_v = 0.00015 s; η_H = 0.0025	Ce = 1752 N-s/m; T = 150 °C; η_v = 0.0002 s; η_H = 0.005
1st BW	518.79	517.87	516.27
1st FW	519.02	518.06	516.81
2nd BW	1091.30	1090.94	1089.55
2nd FW	1093.89	1092.92	1090.99
3rd BW	2212.15	2194.45	2167.48
3rd FW	2225.46	2207.77	2180.87
4th BW	4782.80	4585.18	4301.74
4th FW	4812.98	4615.97	4333.65

7.12.2 WHIRL SPEED AND CAMPBELL DIAGRAM FOR ALL MODES

Simulation is performed at different rotor spin speeds and predicted the forward whirl and backward whirl speeds for constant operating temperature, internal viscous damping, internal hysteretic damping and external viscous damping to understand the spread between whirl speed for each mode. Results are tabulated in Table 7-53 and shown in Figure 7-51.

Table 7-53 Whirl Speeds (rad/sec) for Ce = 1752 N-s/m; T = 150 °C; η_v = 0.0002 s; η_H = 0.005, at different rotor spin speeds

Mode	0 rpm (0 rad/sec)	2000 rpm (209.4 rad/sec)	4000 rpm (418.9 rad/sec)	6000 rpm (628.3 rad/sec)
1st BW	515.93	515.92	516.27	516.92
1st FW	515.93	516.23	516.81	517.66
2nd BW	1089.90	1089.64	1089.55	1089.59
2nd FW	1089.90	1090.29	1090.99	1091.91
3rd BW	2173.01	2170.01	2167.48	2165.36
3rd FW	2173.01	2176.65	2180.87	2185.68
4th BW	4309.31	4303.90	4301.74	4302.52
4th FW	4309.31	4319.37	4333.65	4352.71

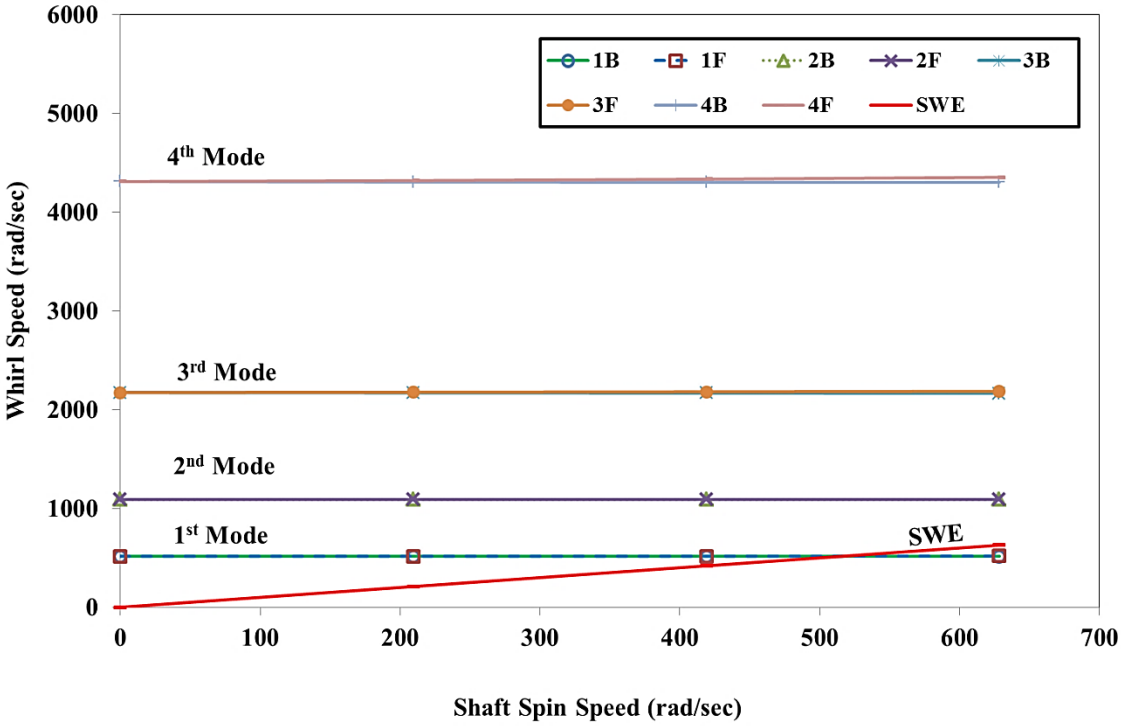

Figure 7-51 Campbell Diagram for Different Modes

7.12.3 WHIRL SPEED AND CAMPBELL DIAGRAM FOR FIRST MODE

The forward whirl speed and backward whirl speed are clearly distinguishable. The spread between backward whirl and forward whirl is increasing with increase in the rotor spin speed. The sensitivity analysis is carried out to understand the combined damping and operating temperature on the forward whirl and backward whirl speeds. Results are summarized in Table 7-54 and shown in Figure 7-52.

Table 7-54 Whirl Speeds (rad/sec) for different rotor spin speeds

	1st Mode	0 rpm (0 rad/sec)	2000 rpm (209.4 rad/sec)	4000 rpm (418.9 rad/sec)	6000 rpm (628.3 rad/sec)
Ce = 500 N-s/m; T = 50 °C; η_v = 0.0001 s; η_H = 0.0002	BW	518.76	518.74	518.79	518.92
	FW	518.76	518.85	519.02	519.26
Ce = 1000 N-s/m; T = 100 °C; η_v = 0.00015 s; η_H = 0.0025	BW	517.63	517.65	517.87	518.26
	FW	517.63	517.76	518.06	518.51
Ce = 1752 N-s/m; T = 150 °C; η_v = 0.0002 s; η_H = 0.005	BW	515.93	515.92	516.27	516.92
	FW	515.93	516.23	516.81	517.66

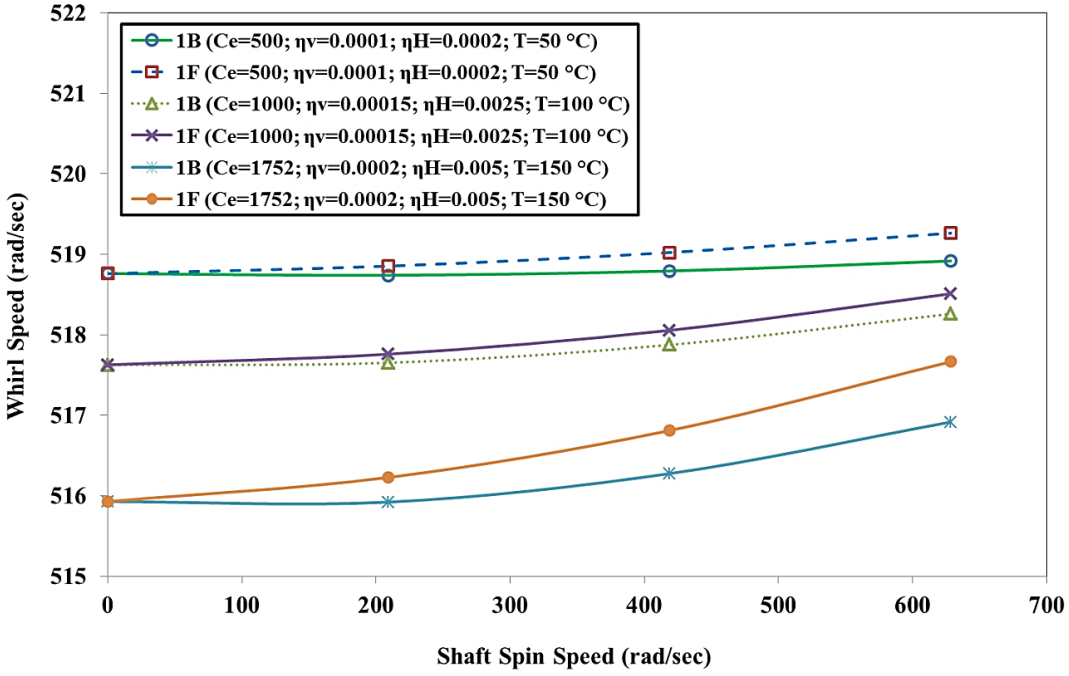

Figure 7-52 Whirl Speed Map for 1st Mode

With the addition of all these damping and operating temperature, the starting point of the forward whirl and backward whirl at zero spin speed gets offset. This offset is increasing with increasing these damping. Due to this, the forward whirl and backward whirl speeds are increased with clear offset.

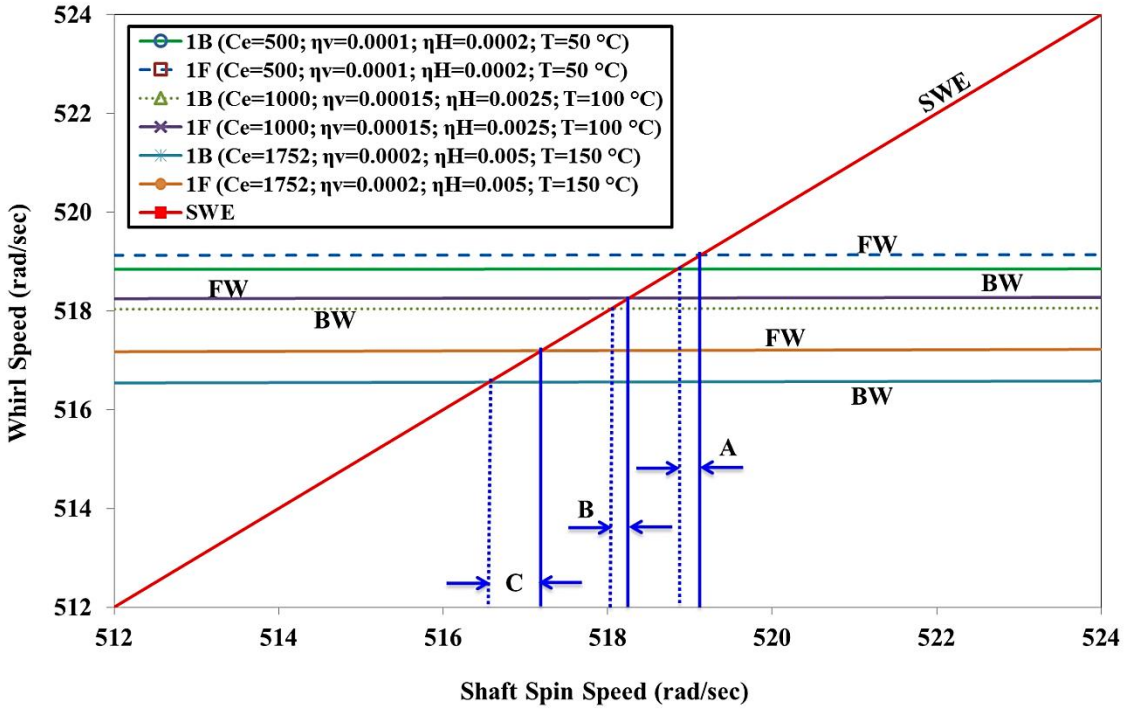

Figure 7-53 Campbell Diagram for 1st Mode

The synchronous whirl excitation is intersecting at two different locations for the first mode. The details of intersection are shown in Figure 7-53. The range between backward critical speed and forward critical speed ranges are shown as ‘A’, ‘B’ and ‘C’. These ranges are based on the contribution of operating temperature, internal viscous damping, internal hysteretic damping and external viscous damping. As the combined form of operating temperature, internal viscous damping, internal hysteretic damping and external viscous damping increases, these ranges are shifting at a lower level with an increase in the range. If the rotor operating spin speed is within this range ‘A’ ‘B’ and ‘C’, there will be the unbounded amplitude of vibration which results into rotor failure. To mitigate this risk and to avoid resonance, only two options are available, either rotor should redesign in such a way that the range ‘A’ ‘B’ and ‘C’ will get shifted from the operating speed or operate spin speed needs to change. This information is very useful in the design stage of the rotor.

7.12.4 CHANGE IN WHIRL SPEED RATIO

The non-dimensional term 'change in whirl speed ratio' is calculated for each mode shape with constant combined form of operating temperature, internal viscous damping, internal hysteretic damping and external viscous damping. This parameter is increasing as the spin speed increases; it means the gap between forward whirl and backward increase as the spin speed increases. The whirl speed ratio is more predominant in the higher modes. The results are tabulated in Table 7-55 and shown in Figure 7-54.

Table 7-55 Change in whirl speed ratio for Ce= 1752 N-s/m; T = 150 °C; η_v = 0.0002 s; η_H = 0.005, at different rotor spin speeds

Mode	0 rpm (0 rad/sec)	2000 rpm (209.4 rad/sec)	4000 rpm (418.9 rad/sec)	6000 rpm (628.3 rad/sec)
1st Mode	0.000%	0.059%	0.104%	0.145%
2nd Mode	0.000%	0.060%	0.133%	0.213%
3rd Mode	0.000%	0.306%	0.616%	0.935%
4th Mode	0.000%	0.359%	0.740%	1.165%

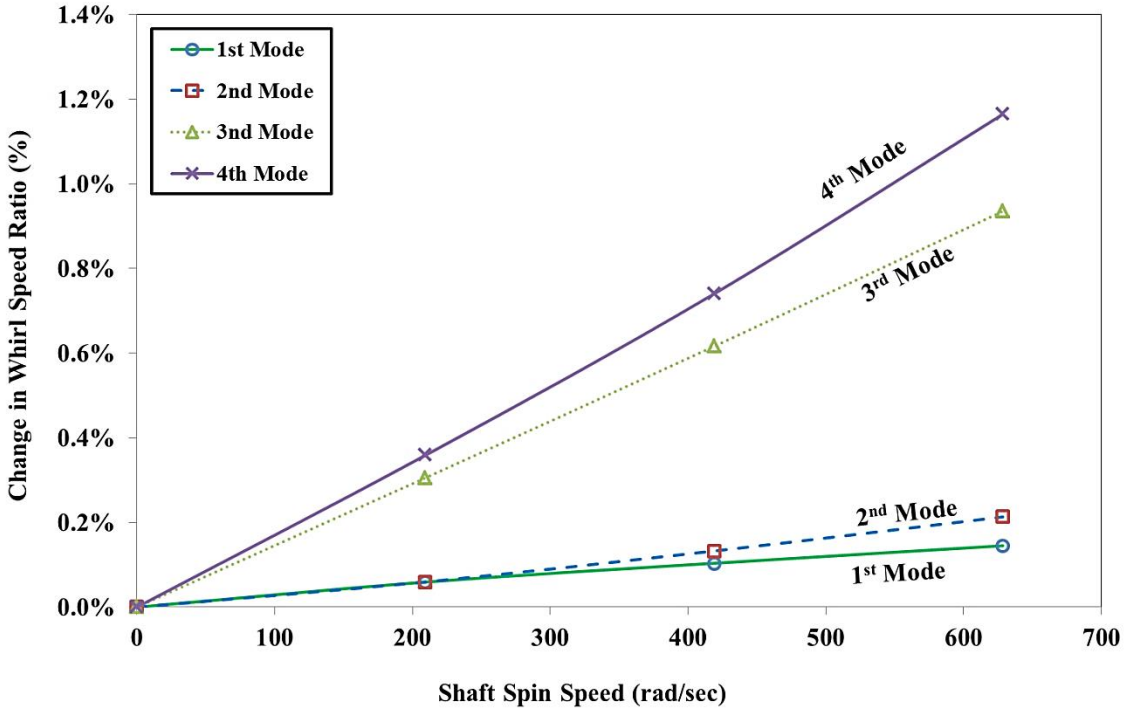

Figure 7-54 Change in Whirl Speed Ratio for Different Modes

The spread between backward whirl speed and forward whirl speed is increasing with increasing the rotor spin speed. This spread is also increasing with higher modes. This spreading effect is due to the contribution of operating temperature, internal viscous damping, internal hysteretic damping and external viscous damping

The sensitivity analysis also carried out on the change in whirl speed ratio with increasing the combined form of damping and operating temperature. The results are tabulated in Table 7-56 and shown in Figure 7-55.

Table 7-56 Change in whirl speed ratio for different rotor spin speeds

	0 rpm (0 rad/sec)	2000 rpm (209.4 rad/sec)	4000 rpm (418.9 rad/sec)	6000 rpm (628.3 rad/sec)
Ce = 500 N-s/m; T = 50 °C; η_v = 0.0001 s; η_H = 0.0002	0.000%	0.022%	0.044%	0.067%
Ce = 1000 N-s/m; T = 100 °C; η_v = 0.00015 s; η_H = 0.0025	0.000%	0.021%	0.035%	0.048%
Ce = 1752 N-s/m; T = 150 °C; η_v = 0.0002 s; η_H = 0.005	0.000%	0.059%	0.104%	0.145%

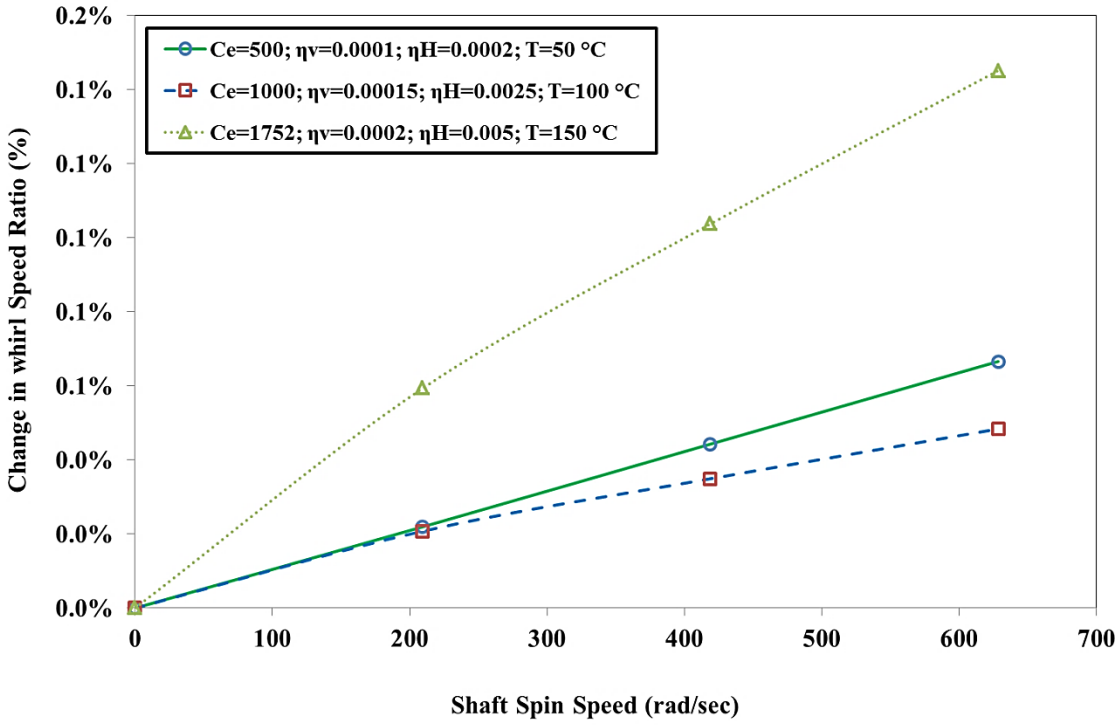

Figure 7-55 Change in Whirl Speed Ratio for 1st Mode

7.12.5 CONCLUSION

The spread between forward whirl speed and backward whirl speed increases with increase in rotor spin speed for all modes. This spread is larger for higher modes and at higher speeds. This is clearly observed in Figure 7-54 with the help of whirl speed ratio. Critical speed range or spread changes slightly and shifting at the lower side with an increase in combined form of operating temperature, external viscous damping, internal viscous damping and internal hysteretic damping as shown in Figure 7-53. A clear understanding of the combined form of operating temperature, external viscous damping, internal viscous damping and internal hysteretic damping is very useful while designing flexible and rigid rotors.

7.12.6 APPLICATION

Practical application or situation will be the different parts or components mounted on the shaft with shrink fit and supported on sleeve bearings. The operating temperature is also critical. e.g. Fan, hub, coupling, balance ring etc mounted on the shaft with shrink fit and shaft is supported with sleeve bearings along with high ambient temperature.

e.g. Gas turbines, Steam turbines, Motors, Generators, Compressors etc

CHAPTER 8

SENSITIVITY ANALYSIS

The design of experiments (DOE) is the statistical method of doing the sensitivity analysis with six sigma methodology. The design of experiments is a method which can make purposeful changes in the input factors of the process to observe the effects on the output. Traditionally, experimentation has been done in a haphazard one factor in a time manner. This method is inefficient and very often yields misleading results. The factorial designs are a very basic type of DOE, require only a minimal number of runs, yet they allow identifying the interactions in the process. In other words, it is used to find cause-and-effect relationships. This information is needed to manage process inputs to optimize the output. This methodology is used to understand the output (critical speeds, whirl speeds and deflection) for each input sources of variations (internal viscous damping, internal hysteretic damping and operating temperature) as shown in Figure 8-1.

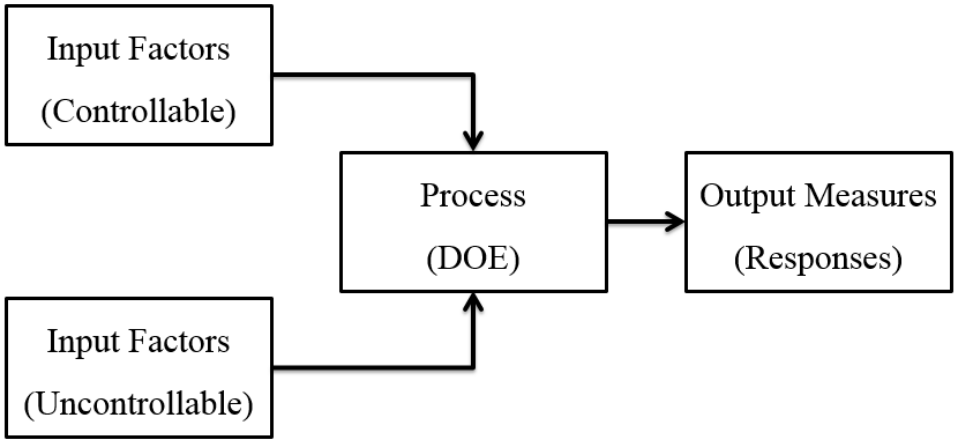

Figure 8-1 Design of Experiments

8.1 INPUTS FACTORS AND OUTPUT MEASURES

Input factors are nothing but the input parameters for the rotor dynamic analysis. These factors are classified as controllable and uncontrollable factors. Outputs of the rotor dynamic analysis are the response/results.

8.1.1 INPUT FACTORS - CONTROLLABLE

Below are the input factors which can be controlled directly or indirectly,

- Physical dimensions of the shaft
- Stiffness of the rotor
- Mass of the rotor
- Material properties of the Rotor
- Bearings stiffness
- Bearing damping / External damping (Ce)
- Internal viscous damping (IVD)
- Internal hysteretic damping (IHD)
- Operating temperature of the rotor (TEMP)

8.1.2 INPUT FACTORS - UNCONTROLLABLE

Below are the input factors which can't be controlled directly,

- Material properties variation due to manufacturing process
- Stiffness of the rotor due to complicated structure

8.1.3 OUTPUT MEASURES - RESPONSES

Below are the output measures,

- Rotor Backward Whirl Speed
- Rotor Forward Whirl Speed
- Rotor Critical Speed

In the design of experiments, different types of plots are used to understand the effect of different parameters and their interactions. ‘MiniTab’ tool is used to show the different types of plots for design of experiments. The simulation results of chapter 6 & 7 are considered for the design of experiments.

8.2 EFFECT PLOTS

These plots are shown with whirl speeds on ordinate and change in critical parameters on abscissa. The range of ‘change in critical parameters’ are considered as ‘zero (0) to one (1)’. Zero indicates the absence of critical parameters and one indicates the presence of critical parameters for all the load cases.

The effect plot helps us to understand the important parameters which affect the backward whirl and forward whirl speeds. These plots give the effect of each input parameter on the output results. The slope of the line decides the influence of the parameter. Maximum slope line decides the maximum influence and minimum slope line decides the minimum influence. The horizontal line indicates no influence. These plots are shown at different rotor spin speeds for backward whirl speed and forward whirl speed.

8.2.1 EFFECT PLOTS FOR BACKWARD WHIRL SPEEDS

The effect of all the critical parameters on backward whirl speed at different rotor spin speeds is shown in Figure 8-2, Figure 8-3 and Figure 8-4. Operating temperature variation is the main critical parameter for backward whirl speed at different rotor spin speeds. The slope of the operating temperature variation line is more as compared other parameters. The other parameters like external viscous damping, internal viscous damping and internal hysteretic damping are less important. The direction is same for external viscous damping and operating temperature while it is opposite for internal viscous damping and internal hysteretic damping. The slope of the internal viscous damping increases as the rotor spin speed increases and it is predominant at high rotor spin speed. The slope of the external viscous damping is small as compared to other parameters at different rotor spin speeds.

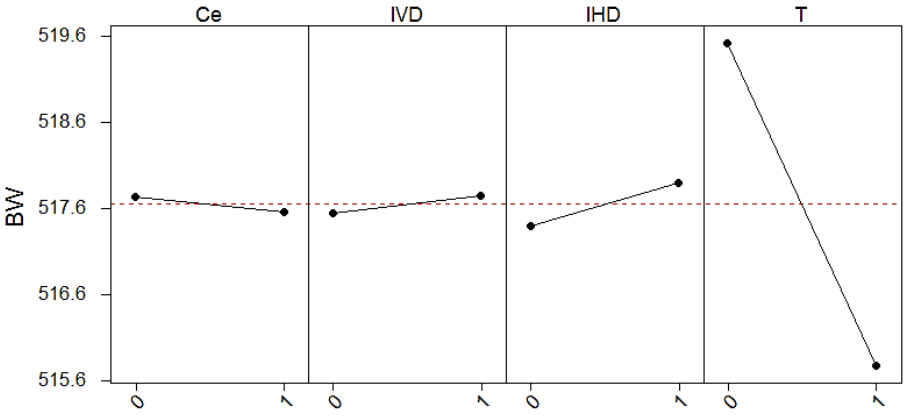

Figure 8-2 Effect plot for BW speeds at 2000 rpm rotor spin speed

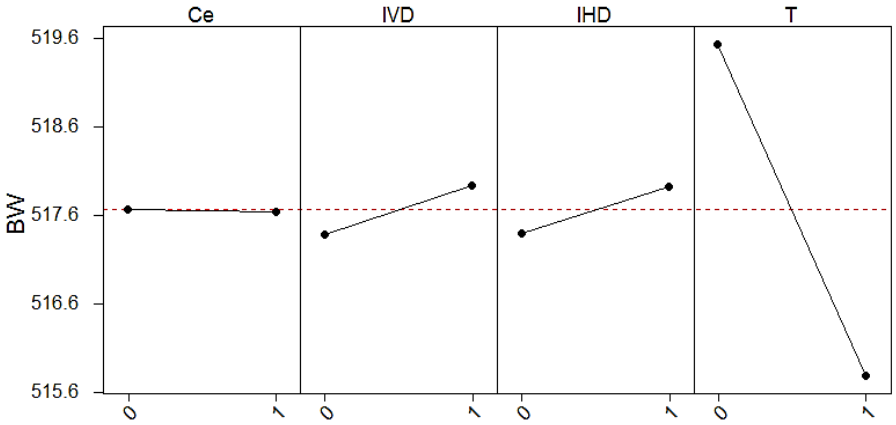

Figure 8-3 Effect plot for BW speeds at 4000 rpm rotor spin speed

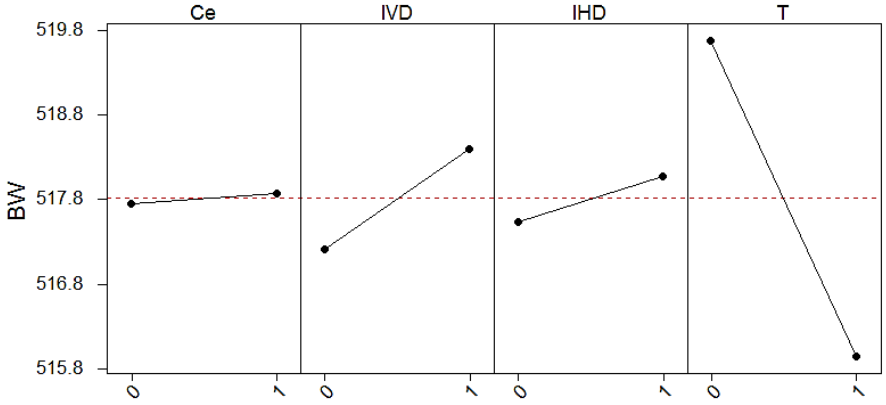

Figure 8-4 Effect plot for BW speeds at 6000 rpm rotor spin speed

8.2.2 EFFECT SUMMARY FOR BACKWARD WHIRL SPEEDS

- The slope and the direction of the external viscous damping are changing as the rotor spin speed increases which mean the effect of external viscous damping is changing due to the rotor spin speed. The slope is also negligible which shows that the effect is very small.
- The internal viscous damping is directly proportional to the rotor spin speed. The slope is considerable which shows that the influence of internal viscous damping is predominant at high rotor spin speed.
- The internal hysteretic damping is directly proportional to the rotor spin speed. The slope is almost constant at different rotor spin speed which shows that the influence of internal hysteretic damping is almost constant at different rotor spin speeds.
- The operating temperature variation is inversely proportional to the backward whirl speed. The slope is almost constant at different rotor spin speed which shows that the influence of operating temperature variation is almost constant at different rotor spin speeds.

8.2.3 EFFECT PLOTS FOR FORWARD WHIRL SPEEDS

The effect of all the critical parameters on backward whirl speed at different rotor spin speeds is shown in Figure 8-5, Figure 8-6 and Figure 8-7. Operating temperature variation is the main critical parameter for forward whirl speed at different rotor spin speeds. The slope of the operating temperature variation line is more as compared other parameters. The other parameters like external viscous damping, internal viscous damping and internal hysteretic damping are less important. The direction is same for external viscous damping and operating temperature while it is opposite for internal viscous damping and internal hysteretic damping. The slope of the internal viscous damping increases as the rotor spin speed increases and it is predominant at high rotor spin speed.

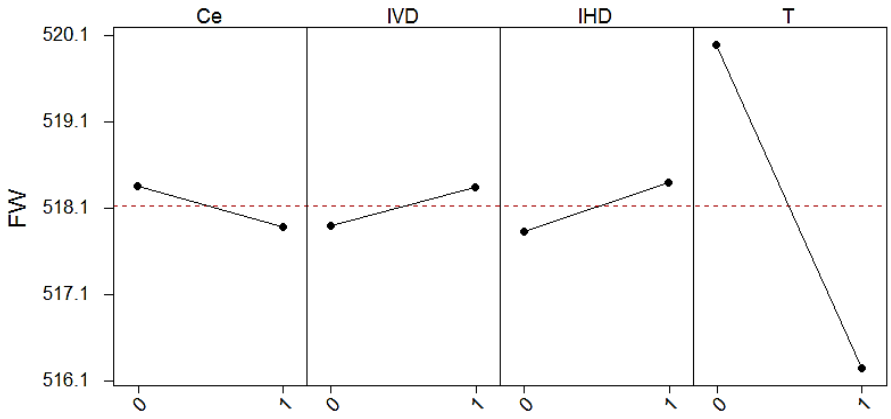

Figure 8-5 Effect plot for FW speeds at 2000 rpm rotor spin speed

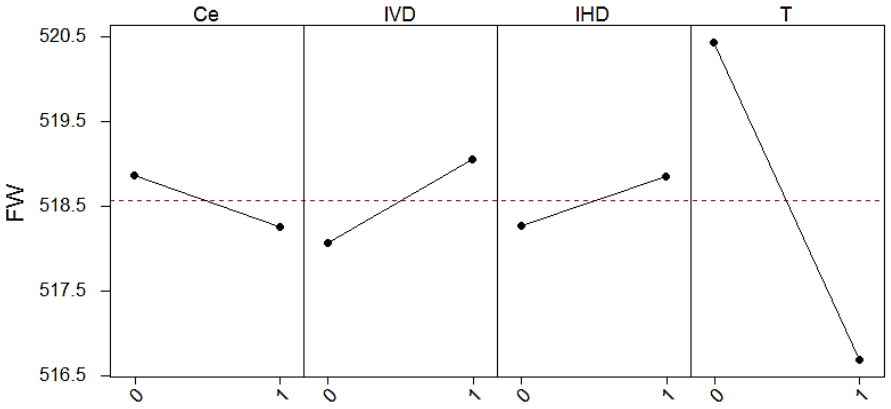

Figure 8-6 Effect plot for FW speeds at 4000 rpm rotor spin speed

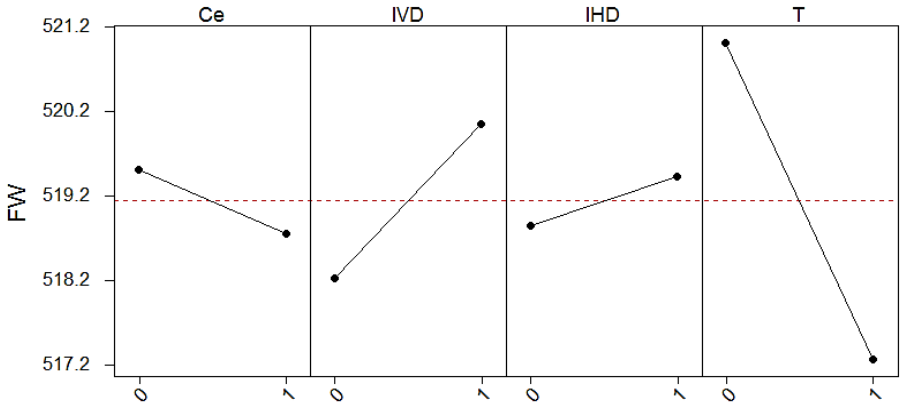

Figure 8-7 Effect plot for FW speeds at 6000 rpm rotor spin speed

8.2.4 EFFECT SUMMARY FOR FORWARD WHIRL SPEEDS

- The external viscous damping is inversely proportional to the rotor spin speed. The slope is almost constant at different rotor spin speed which shows that the influence of external viscous damping is almost constant at different rotor spin speeds.
- The internal viscous damping is directly proportional to the rotor spin speed. The slope is considerable which shows that the influence of internal viscous damping is predominant at high rotor spin speed.
- The internal hysteretic damping is directly proportional to the rotor spin speed. The slope is almost constant at different rotor spin speed which shows that the influence of internal hysteretic damping is almost constant at different rotor spin speeds.
- The operating temperature variation is inversely proportional to the backward whirl speed. The slope is almost constant at different rotor spin speed which shows that the influence of operating temperature variation is almost constant at different rotor spin speeds.

8.3 INTERACTION PLOTS

These plots are shown with whirl speeds on ordinate and change in critical parameters on abscissa. The range of 'change in critical parameters' are considered as 'zero (0) to one (1)'. Zero indicates the absence of critical parameters and one indicates the presence of critical parameters for all the load cases.

Interactions are when the effect of two or more variables is not simply additive. It is possible to examine the interactions of the two or more variables. These plots give the interaction within each input parameter on the output results. If the lines are not parallel, the plot indicates that there is an interaction between the two factors. Interaction plots are shown for a backward whirl and forward whirl speeds in the following sections.

8.3.1 INTERACTION PLOTS FOR BACKWARD WHIRL SPEEDS

The lines of external viscous damping and internal viscous damping are intersecting which indicates that there is a strong interaction between external viscous damping and internal viscous damping. The lines for external damping versus internal hysteretic damping,

external viscous damping versus operating temperature, internal viscous damping versus internal hysteretic damping, internal viscous damping versus operating temperature and internal hysteretic damping versus operating temperature variation are almost parallel and non-intersecting. There is no interaction between these parameters. The interactions between all the critical parameters at different rotor spin speeds are shown in Figure 8-8, Figure 8-9 and Figure 8-10.

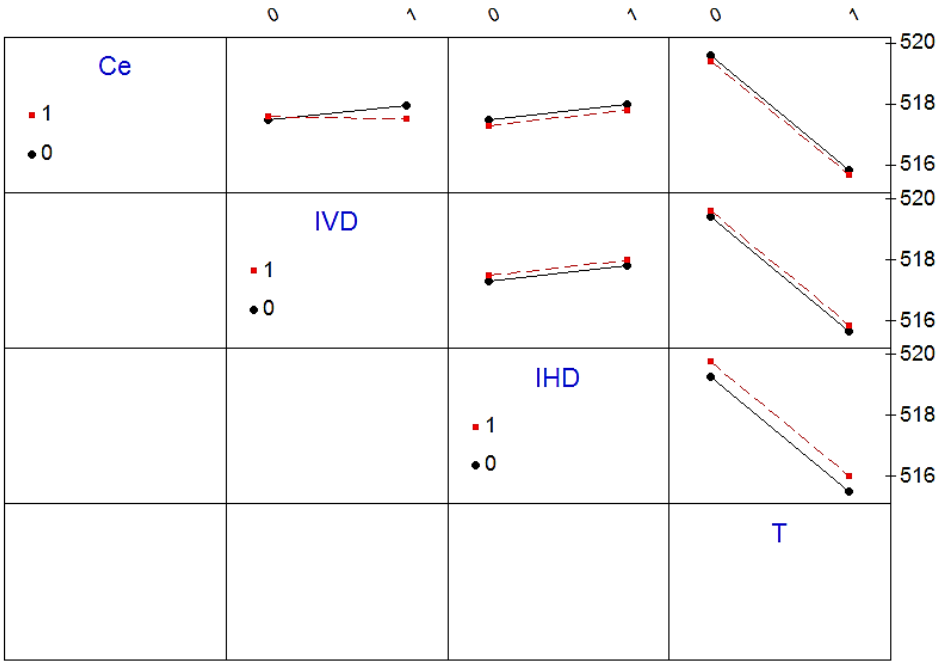

Figure 8-8 Interaction plot for BW speeds at 2000 rpm rotor spin speed

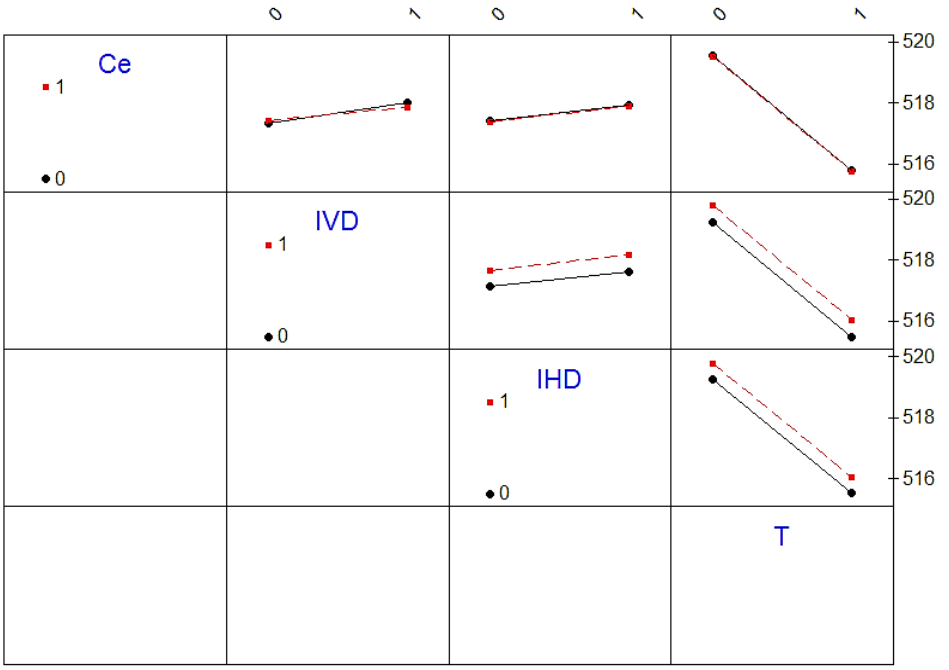

Figure 8-9 Interaction plot for BW speeds at 4000 rpm rotor spin speed

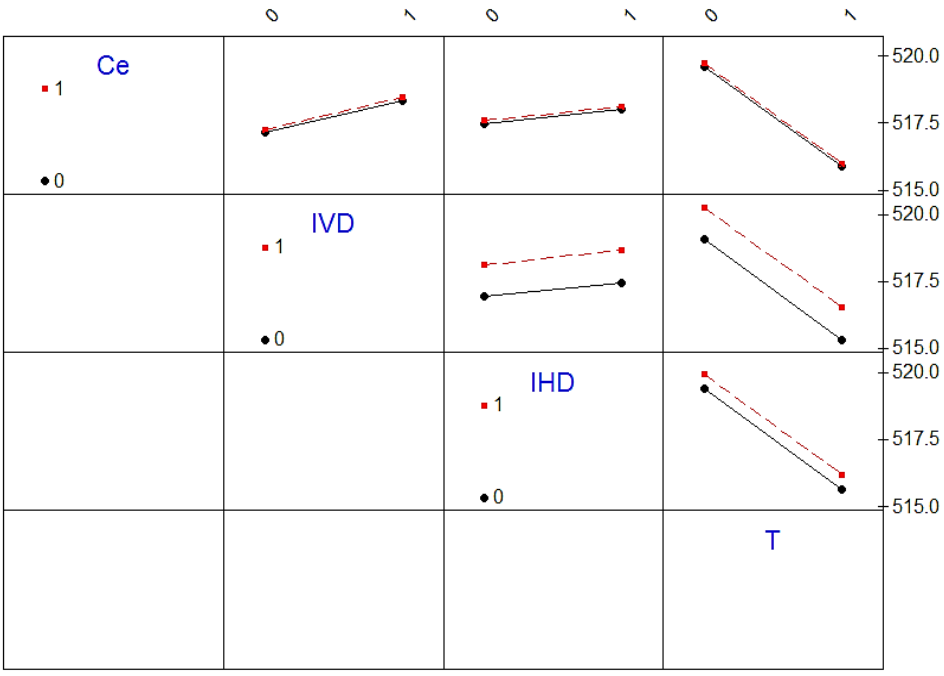

Figure 8-10 Interaction plot for BW speeds at 6000 rpm rotor spin speed

8.3.2 INTERACTION SUMMARY OF BACKWARD WHIRL SPEEDS

- There is strong interaction between external viscous damping and internal viscous damping with respect to rotor spin speed. The slope of the lines is changing with respect to rotor spin speed. The physical significance of this interaction is the effect of internal viscus damping is counteracting the effect of external viscous damping. This effect is more predominant at lower rotor spin speed and it is lesser at higher rotor spin speed.
- There is no interaction between external viscous damping and internal hysteretic damping because the lines are parallel and non-intersecting. The distance between these parallel line changing at different rotor spin speeds. The physical significance of these parameters is the effect of external viscous damping and internal hysteretic damping acts independently.
- There is no interaction between external viscous damping and operating temperature because the lines are parallel and non-intersecting. The distance between these parallel line changing at different rotor spin speeds. The physical significance of these parameters is the effect of external viscous damping and operating temperature act independently.
- These are no interaction between internal viscous damping and internal hysteretic damping because the lines are parallel throughout the speed range. The distance between these parallel line is increasing with respect to rotor spin speeds. The physical significance of these parameters is the effect of internal viscous damping and internal hysteretic damping act independently.
- There is no interaction between internal viscous damping and operating temperature because the lines are parallel throughout the speed range. The distance between these parallel line is increasing with respect to rotor spin speeds. The physical significance of these parameters is the effect of internal viscous damping and operating temperature act independently.
- There is no interaction between internal hysteretic damping and operating temperature because the lines are parallel throughout the speed range. The physical significance of these parameters is the effect of internal hysteretic damping and operating temperature act independently.

8.3.3 INTERACTION PLOTS FOR FORWARD WHIRL SPEEDS

The lines of external viscous damping and internal viscous damping are intersecting which indicates that there is a strong interaction between external viscous damping and internal viscous damping. The lines for external damping versus internal hysteretic damping, external viscous damping versus operating temperature, internal viscous damping versus internal hysteretic damping, internal viscous damping versus operating temperature and internal hysteretic damping versus operating temperature variation are almost parallel and non-intersecting. There is no interaction between these parameters. The interactions between all the critical parameters at different rotor spin speeds are shown in Figure 8-11, Figure 8-12 and Figure 8-13.

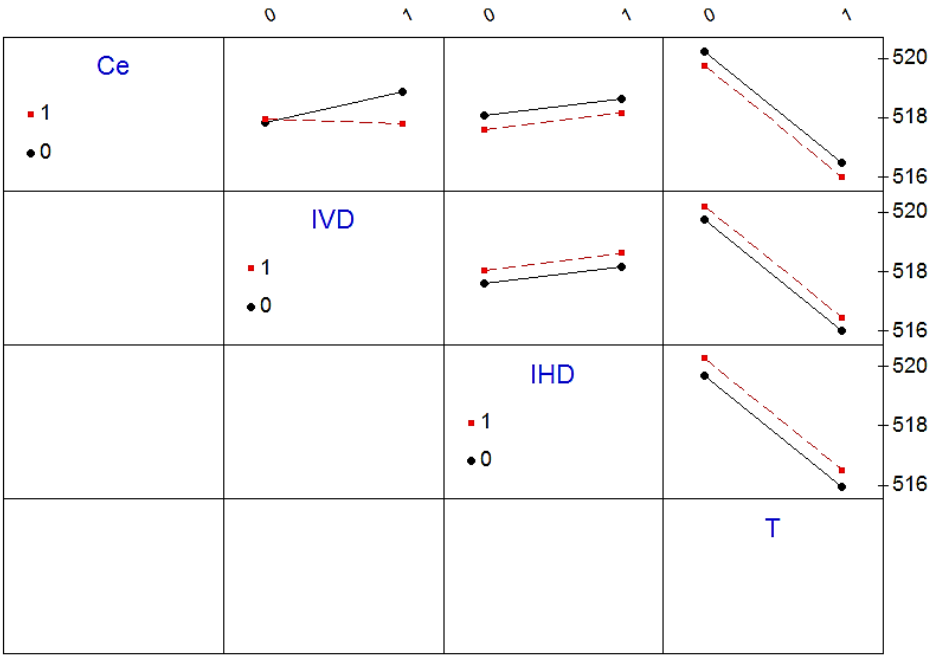

Figure 8-11 Interaction plot for FW speeds at 2000 rpm rotor spin speed

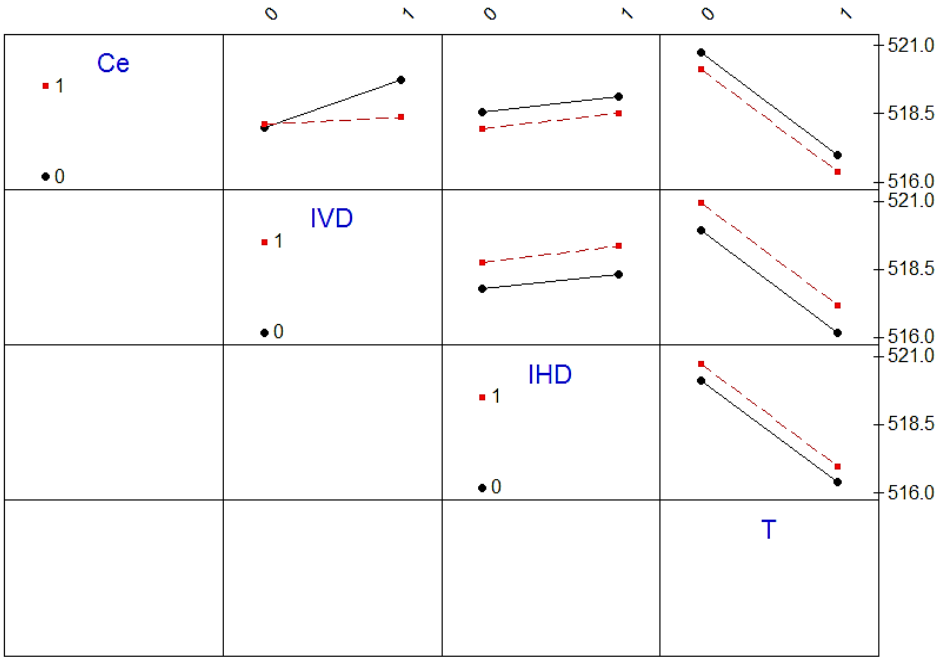

Figure 8-12 Interaction plot for FW speeds at 4000 rpm rotor spin speed

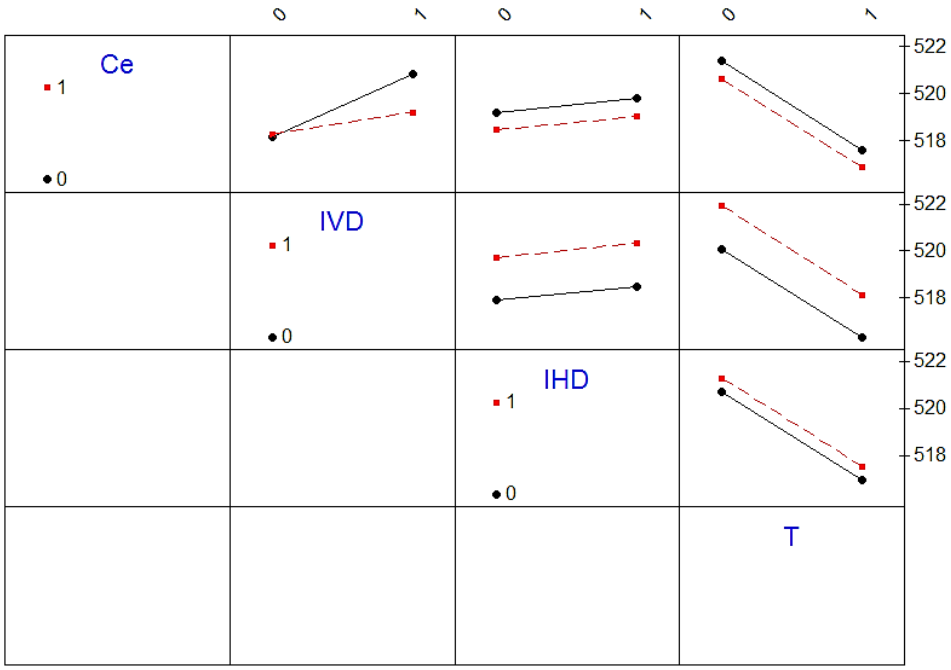

Figure 8-13 Interaction plot for FW speeds at 6000 rpm rotor spin speed

8.3.4 INTERACTION SUMMARY OF FORWARD WHIRL SPEEDS

- There is strong interaction between external viscous damping and internal viscous damping with respect to rotor spin speed. The slope of the lines is changing with respect to rotor speed. The physical significance of this interaction is the effect of internal viscus damping is counteracting the effect of external viscous damping. This effect is more predominant at lower rotor spin speed and it is lesser at higher rotor spin speed.
- There is no interaction between external viscous damping and internal hysteretic damping because the lines are parallel and non-intersecting. The distance between these parallel line changing at different rotor spin speeds. The physical significance of these parameters is the effect of external viscous damping and internal hysteretic damping acts independently.
- There is no interaction between external viscous damping and operating temperature because the lines are parallel and non-intersecting. The distance between these parallel line increasing at different rotor spin speeds. The physical significance of these parameters is the effect of external viscous damping and operating temperature acts independently.
- These are no interaction between internal viscous damping and internal hysteretic damping because the lines are parallel throughout the speed range. The distance between these parallel line is increasing with respect to rotor spin speeds. The physical significance of these parameters is the effect of internal viscous damping and internal hysteretic damping act independently.
- There is no interaction between internal viscous damping and operating temperature because the lines are parallel throughout the speed range. The distance between these parallel line is increasing with respect to rotor spin speeds. The physical significance of these parameters is the effect of internal viscous damping and operating temperature act independently.
- There is no interaction between internal hysteretic damping and operating temperature because the lines are parallel throughout the speed range. The physical significance of these parameters is the effect of internal hysteretic damping and operating temperature act independently.

8.4 RESPONSE SURFACE AND CONTOUR PLOTS

Response Surface (RS) plots are shown with whirl speeds on ordinate and change in critical parameters on abscissa. The range of ‘change in critical parameters’ are considered as ‘zero (0) to one (1)’. Zero indicates the absence of critical parameters and one indicates the presence of critical parameters for all the load cases. This is a three-dimensional plot.

Response Contour (RC) plots are shown with change in critical parameters on ordinate and abscissa with contours of constant whirl speeds. The range of ‘change in critical parameters’ are considered as ‘zero (0) to one (1)’. Zero indicates the absence of critical parameters and one indicates the presence of critical parameters for all the load cases.

Response surfaces and Response contours are plotted for the backward whirl speed and forward whirl speed for a given critical parameters like internal viscous damping, internal hysteretic damping, external viscous damping and operating temperature. These plots are used to understand the effect of parameters on the forward whirl and backward whirl speeds.

8.4.1 RS AND RC PLOTS FOR BACKWARD WHIRL SPEEDS

Backward whirl speed is a response and different critical parameters are the input parameters.

8.4.1.1 RESPONSE FOR TEMPERATURE AND INTERNAL HYSTERETIC DAMPING

Response surface of backward whirl speed is plotted against operating temperature and internal hysteretic damping. The operating temperature is predominant as compared to internal hysteretic damping. The contour plot is showing with constant backward whirl speed lines. These lines are almost horizontal at different rotor spin speeds which show that the effect of internal hysteretic damping is small and it is almost same with different rotor spin speeds. Details are shown in Figure 8-14, Figure 8-15 and Figure 8-16.

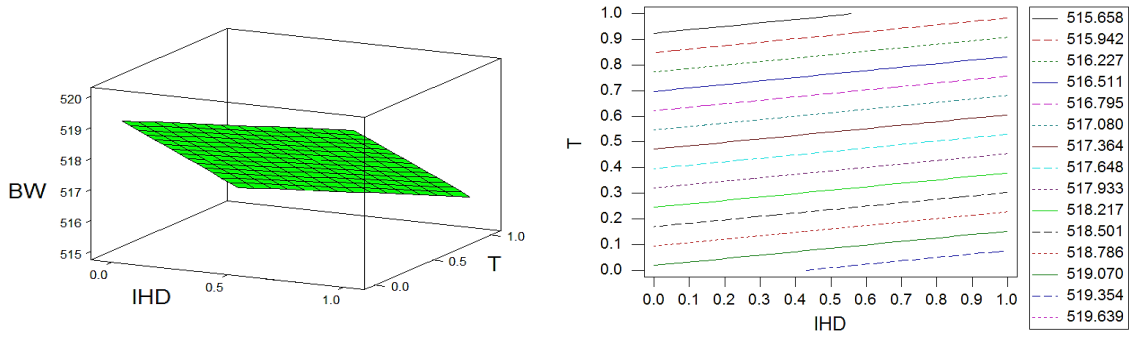

Figure 8-14 RS and RC plots for BW speeds at 2000 rpm rotor spin speed

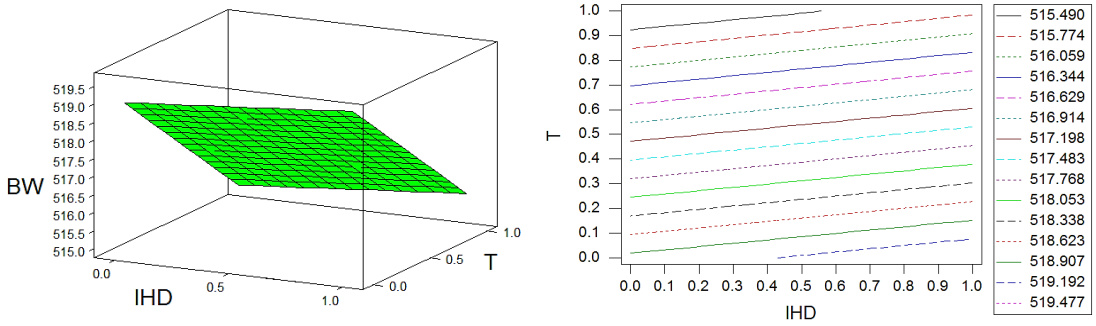

Figure 8-15 RS and RC plots for BW speeds at 4000 rpm rotor spin speed

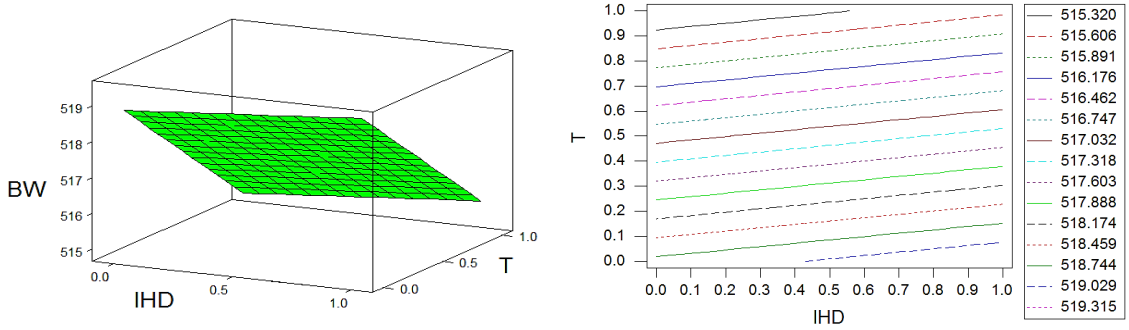

Figure 8-16 RS and RC plots for BW speeds at 6000 rpm rotor spin speed

8.4.1.2 RESPONSE FOR TEMPERATURE AND INTERNAL VISCOUS DAMPING

Response surface of backward whirl speed is plotted against operating temperature and internal viscous damping. The operating temperature is predominant as compared to internal viscous damping. The contour plot is showing with constant backward whirl speed lines. These lines are almost horizontal at lower rotor spin speed which show that the effect of internal viscous damping is small. The slope of the lines is increasing at higher rotor spin

speeds which means that the effect of internal viscous damping is predominant at higher rotor spin speeds. Details are shown in Figure 8-17, Figure 8-18 and Figure 8-19.

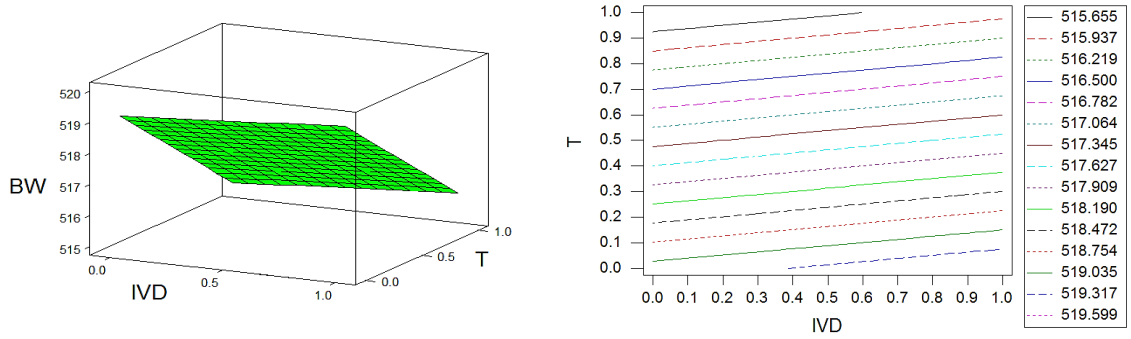

Figure 8-17 RS and RC plots for BW speeds at 2000 rpm rotor spin speed

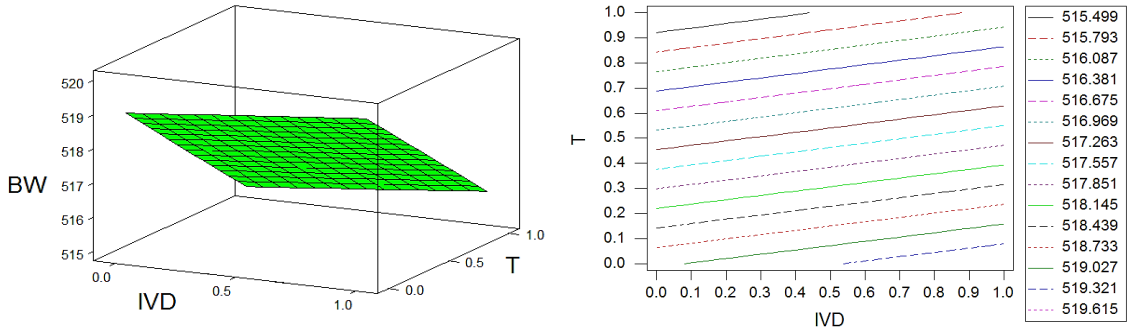

Figure 8-18 RS and RC plots for BW speeds at 4000 rpm rotor spin speed

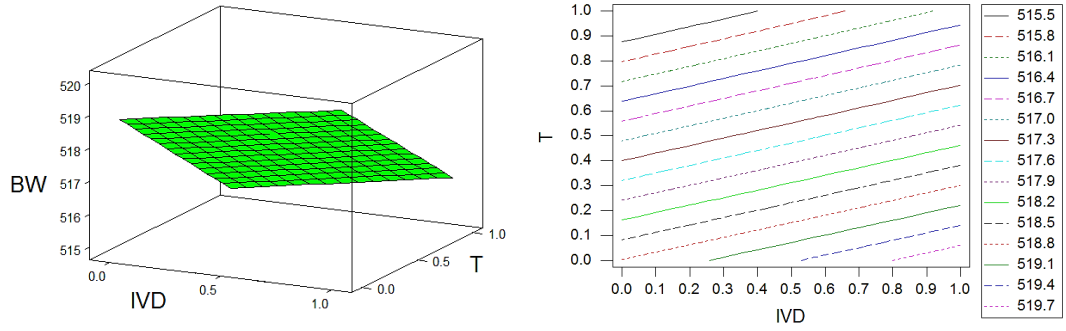

Figure 8-19 RS and RC plots for BW speeds at 6000 rpm rotor spin speed

8.4.1.3 RESPONSE FOR INTERNAL HYSTERETIC DAMPING AND INTERNAL VISCOUS DAMPING

Response surface of backward whirl speed is plotted against internal hysteretic damping and internal viscous damping. The contour plot is showing with constant backward

whirl speed lines. These lines are inclined uniformly with horizontal and vertical at different rotor spin speeds. The slope of the lines is increasing at higher rotor spin speeds which means that the effect of internal viscous damping is predominant at higher rotor spin speeds. Details are shown in Figure 8-20, Figure 8-21 and Figure 8-22.

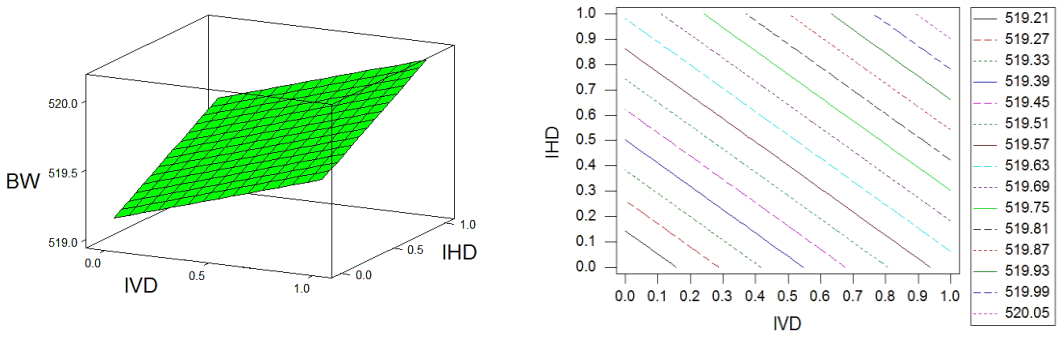

Figure 8-20 RS and RC plots for BW speeds at 2000 rpm rotor spin speed

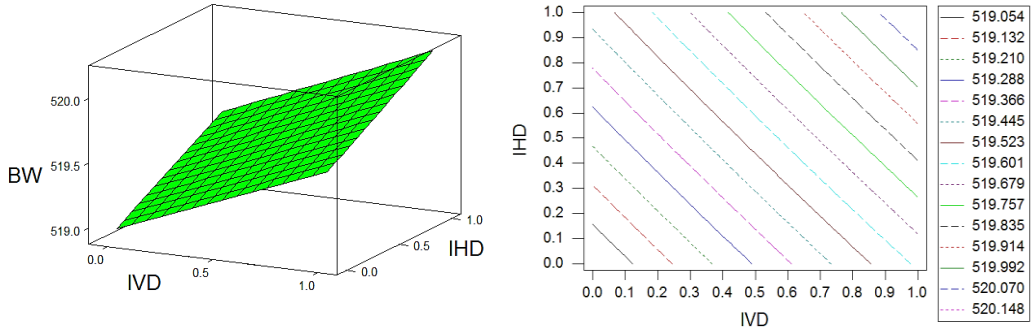

Figure 8-21 RS and RC plots for BW speeds at 4000 rpm rotor spin speed

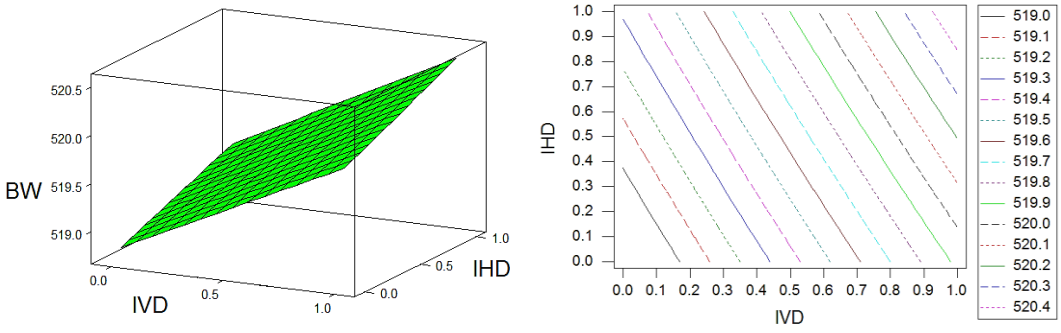

Figure 8-22 RS and RC plots for BW speeds at 6000 rpm rotor spin speed

8.4.1.4 RESPONSE FOR TEMPERATURE AND EXTERNAL VISCOUS DAMPING

Response surface of backward whirl speed is plotted against operating temperature and external viscous damping. The operating temperature is predominant as compared to external viscous damping. The contour plot is showing with constant backward whirl speed lines. These lines are almost horizontal at different rotor spin speeds which show that the effect of external damping is small and it is almost same with different rotor spin speeds which is shown in Figure 8-23, Figure 8-24 and Figure 8-25.

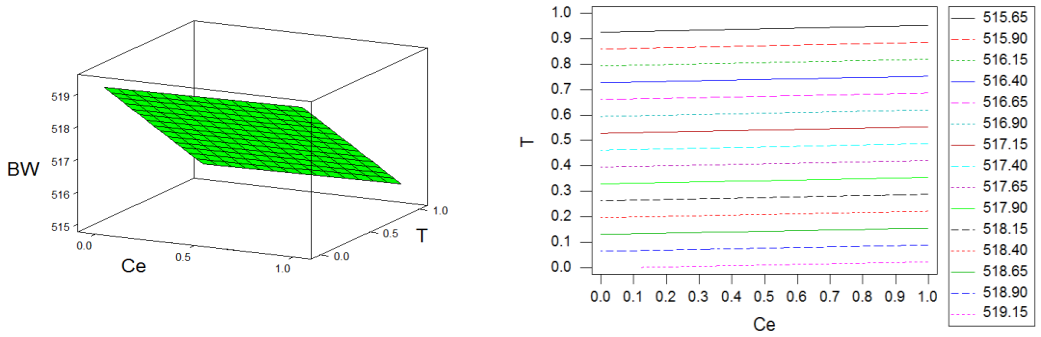

Figure 8-23 RS and RC plots for BW speeds at 2000 rpm rotor spin speed

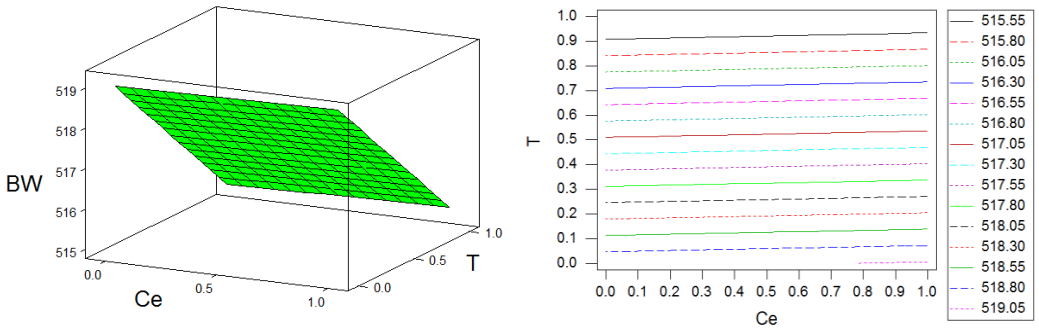

Figure 8-24 RS and RC plots for BW speeds at 4000 rpm rotor spin speed

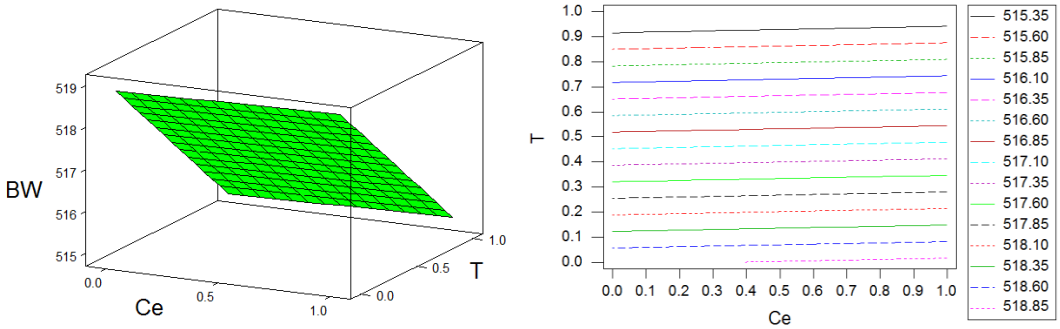

Figure 8-25 RS and RC plots for BW speeds at 6000 rpm rotor spin speed

8.4.1.5 RESPONSE FOR INTERNAL HYSTERETIC DAMPING AND EXTERNAL VISCOUS DAMPING

Response surface of backward whirl speed is plotted against internal hysteretic damping and external viscous damping. The contour plot is showing with constant backward whirl speed lines. These lines are almost horizontal at different rotor spin speeds which show that the effect of external viscous damping is small and it is almost same with different rotor spin speeds. Details are shown in Figure 8-26, Figure 8-27 and Figure 8-28.

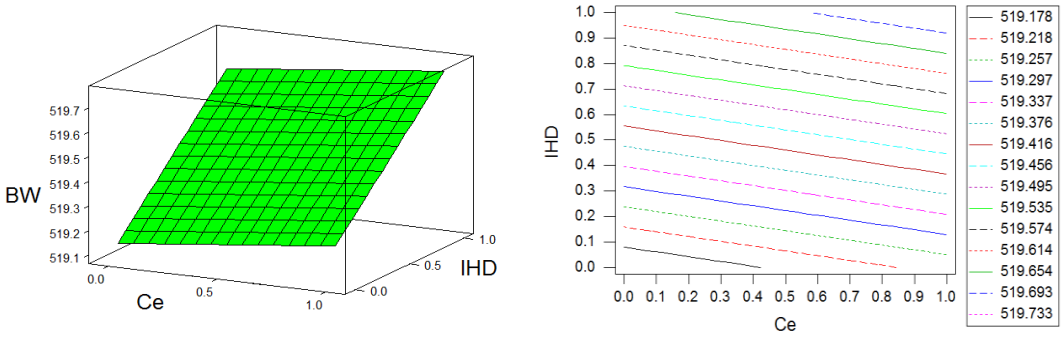

Figure 8-26 RS and RC plots for BW speeds at 2000 rpm rotor spin speed

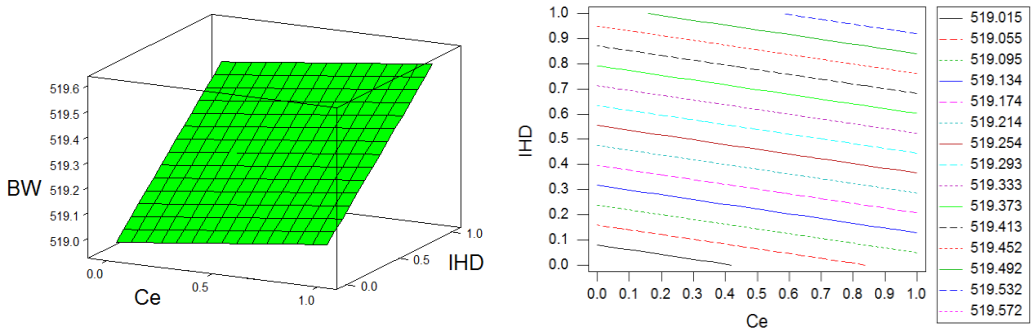

Figure 8-27 RS and RC plots for BW speeds at 4000 rpm rotor spin speed

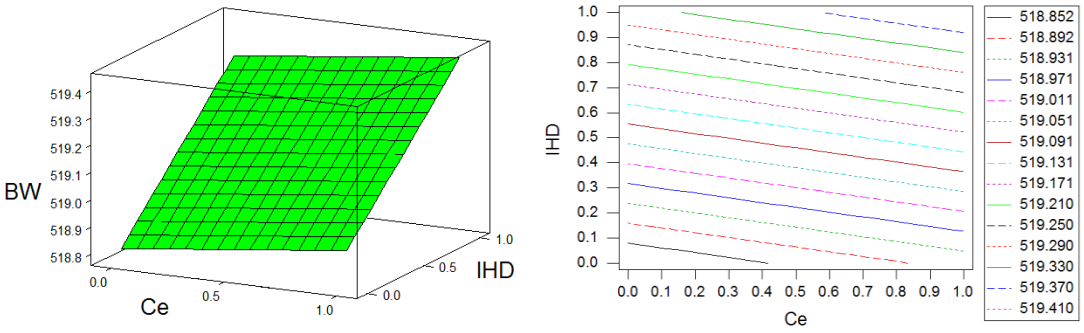

Figure 8-28 RS and RC plots for BW speeds at 6000 rpm rotor spin speed

8.4.1.6 RESPONSE FOR INTERNAL VISCOUS DAMPING AND EXTERNAL VISCOUS DAMPING

Response surface of backward whirl speed is plotted against internal viscous damping and external viscous damping. The contour plot is showing with constant backward whirl speed lines. These lines are curved at different rotor spin speeds. There is strong interaction between external viscous damping and internal viscous damping with respect to rotor spin speed. The slope of the lines is changing with respect to rotor spin speed. The physical significance of this interaction is the effect of internal viscus damping is counteracting the effect of external viscous damping. This effect is more predominant at lower rotor spin speed which shows the curved lines and it is lesser at higher rotor spin speed which shows almost straight lines. Details are shown in Figure 8-29, Figure 8-30 and Figure 8-31.

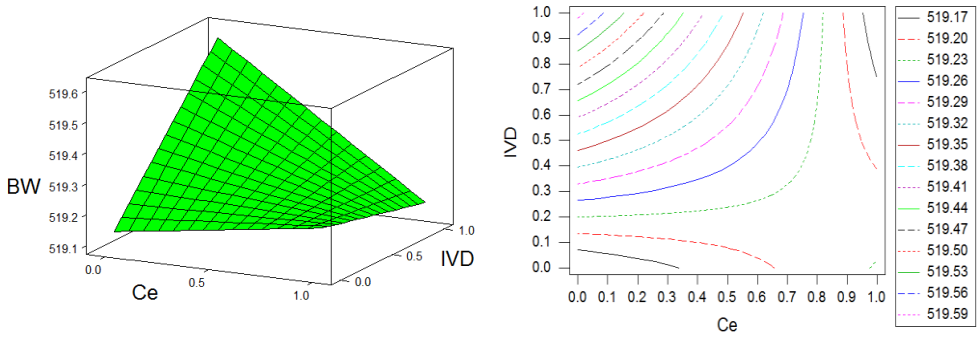

Figure 8-29 RS and RC plots for BW speeds at 2000 rpm rotor spin speed

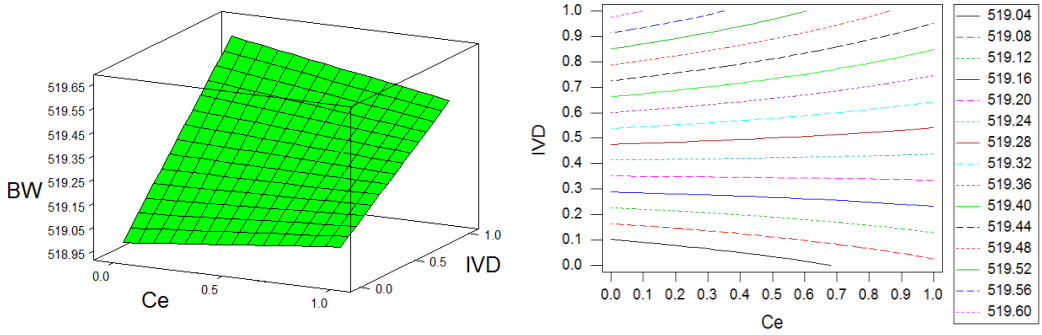

Figure 8-30 RS and RC plots for BW speeds at 4000 rpm rotor spin speed

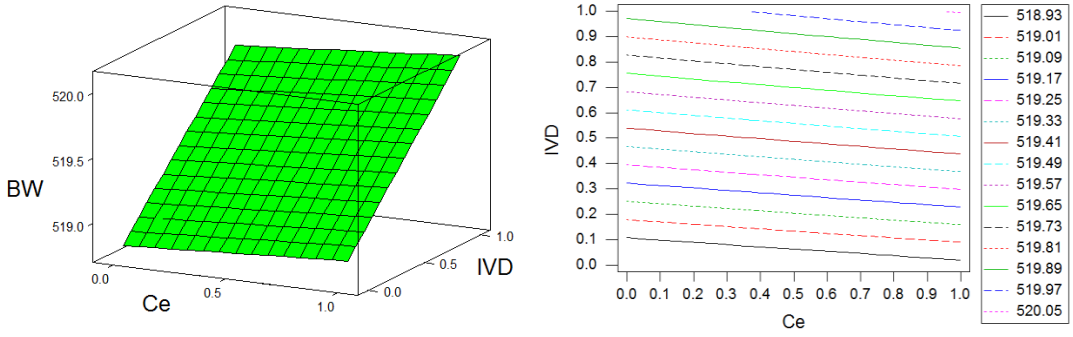

Figure 8-31 RS and RC plots for BW speeds at 6000 rpm rotor spin speed

8.4.2 RS AND RC PLOTS FOR FORWARD WHIRL SPEED

Forward whirl speed is a response and different critical parameters are the input parameters.

8.4.2.1 RESPONSE FOR TEMPERATURE AND INTERNAL HYSTERETIC DAMPING

Response surface of forward whirl speed is plotted against operating temperature and internal hysteretic damping. The operating temperature is predominant as compared to internal hysteretic damping. The contour plot is showing with constant forward whirl speed lines. These lines are almost horizontal at different rotor spin speeds which show that the effect of internal hysteretic damping is small. These lines are almost horizontal at different rotor spin speeds which show that the effect of internal hysteretic damping is small and it is almost same with different rotor spin speeds. Details are shown in Figure 8-32, Figure 8-33 and Figure 8-34.

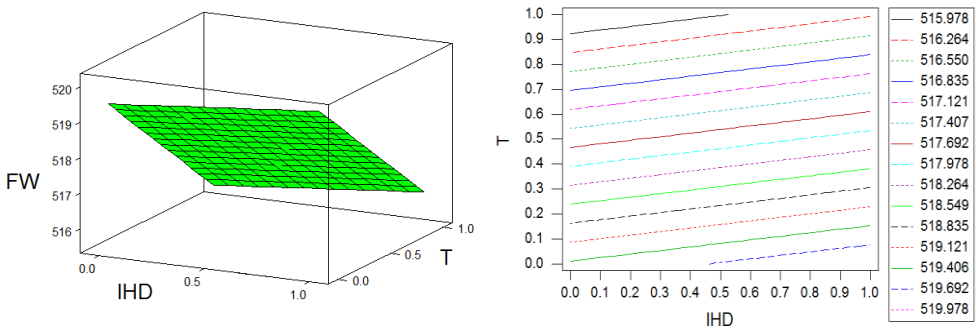

Figure 8-32 RS and RC plots for FW speeds at 2000 rpm rotor spin speed

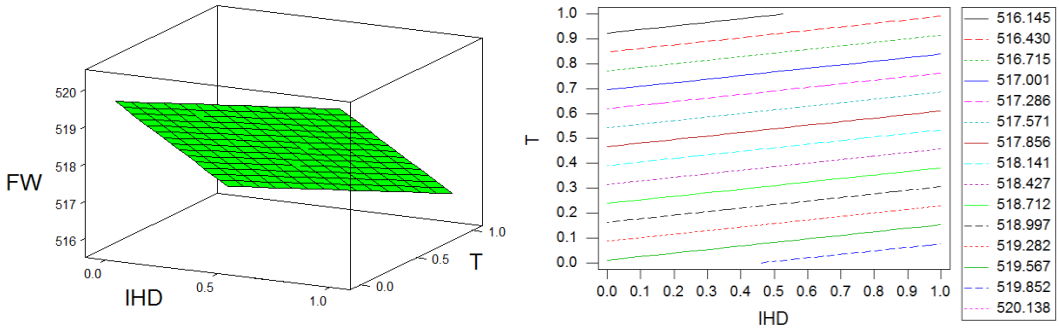

Figure 8-33 RS and RC plots for FW speeds at 4000 rpm rotor spin speed

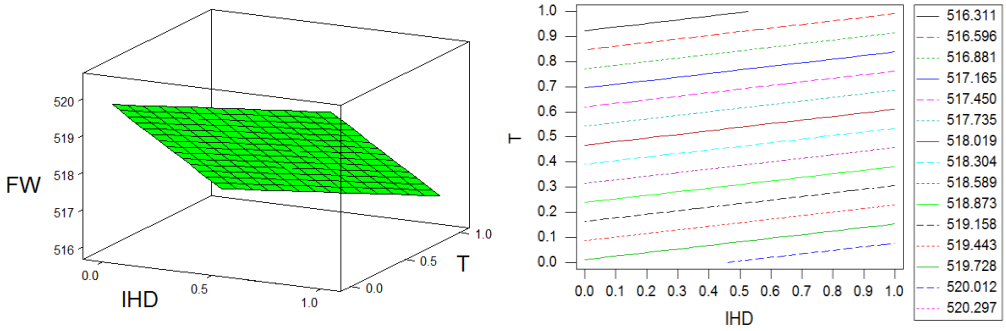

Figure 8-34 RS and RC plots for FW speeds at 6000 rpm rotor spin speed

8.4.2.2 RESPONSE FOR TEMPERATURE AND INTERNAL VISCOUS DAMPING

Response surface of forward whirl speed is plotted against operating temperature and internal viscous damping. The operating temperature is predominant as compared to internal viscous damping. The contour plot is showing with constant forward whirl speed lines. These lines are almost horizontal at lower rotor spin speed which show that the effect of internal viscous damping is small. The slope of the lines is increasing at higher rotor spin speeds which means that the effect of internal viscous damping is predominant at higher rotor spin speeds. Details are shown in Figure 8-35, Figure 8-36 and Figure 8-37.

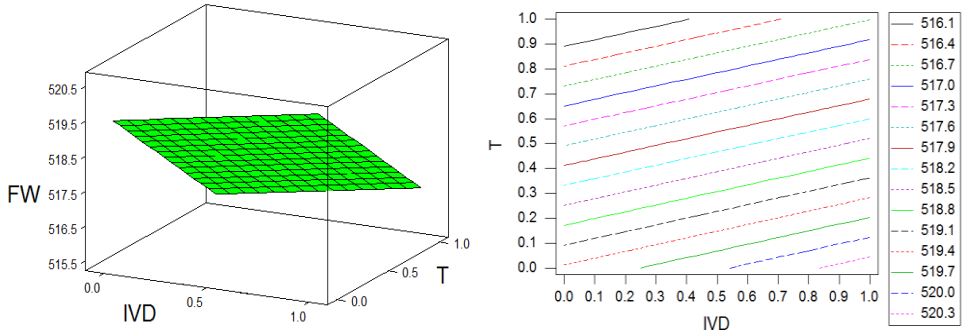

Figure 8-35 RS and RC plots for FW speeds at 2000 rpm rotor spin speed

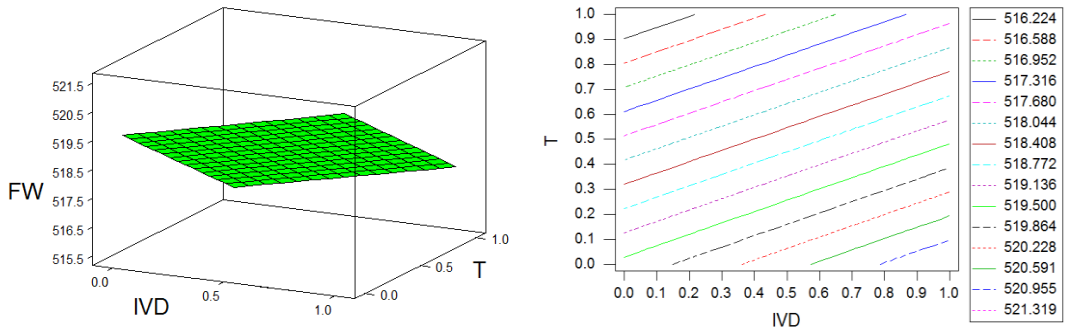

Figure 8-36 RS and RC plots for FW speeds at 4000 rpm rotor spin speed

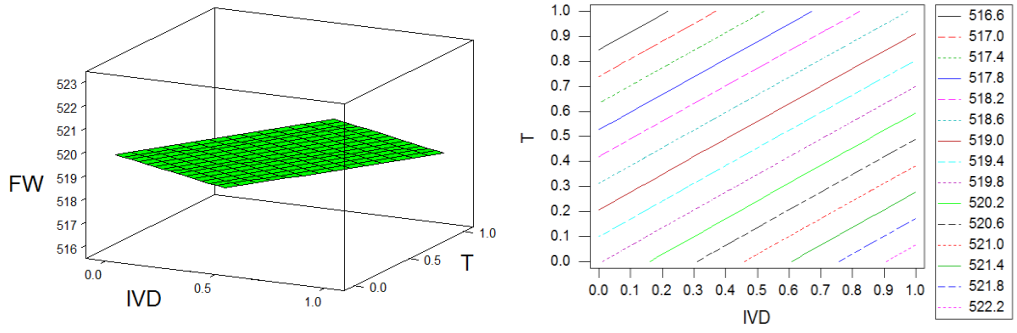

Figure 8-37 RS and RC plots for FW speeds at 6000 rpm rotor spin speed

8.4.2.3 RESPONSE FOR INTERNAL HYSTERETIC DAMPING AND INTERNAL VISCOUS DAMPING

Response surface of forward whirl speed is plotted against internal hysteretic damping and internal viscous damping. The contour plot is showing with constant forward whirl speed lines. These lines are inclined uniformly with horizontal and vertical at different rotor spin speeds. The slope of the lines is increasing at higher rotor spin speeds which means that the effect of internal viscous damping is predominant at higher rotor spin speeds. Details are shown in Figure 8-38, Figure 8-39 and Figure 8-40.

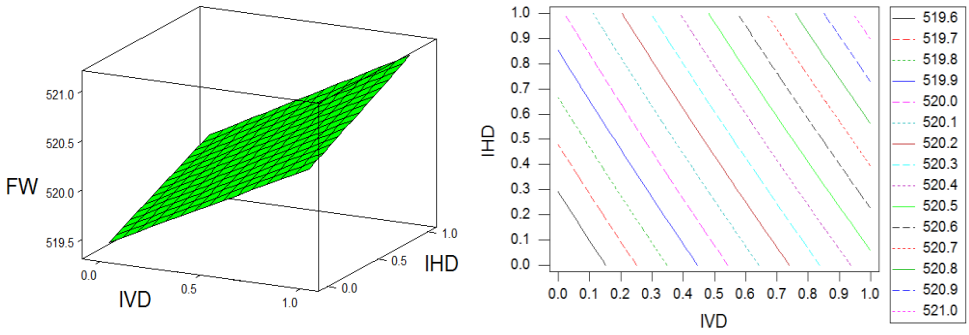

Figure 8-38 RS and RC plots for FW speeds at 2000 rpm rotor spin speed

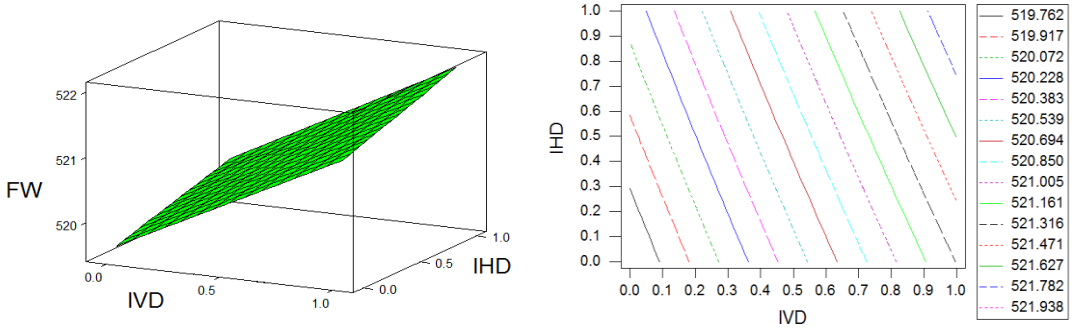

Figure 8-39 RS and RC plots for FW speeds at 4000 rpm rotor spin speed

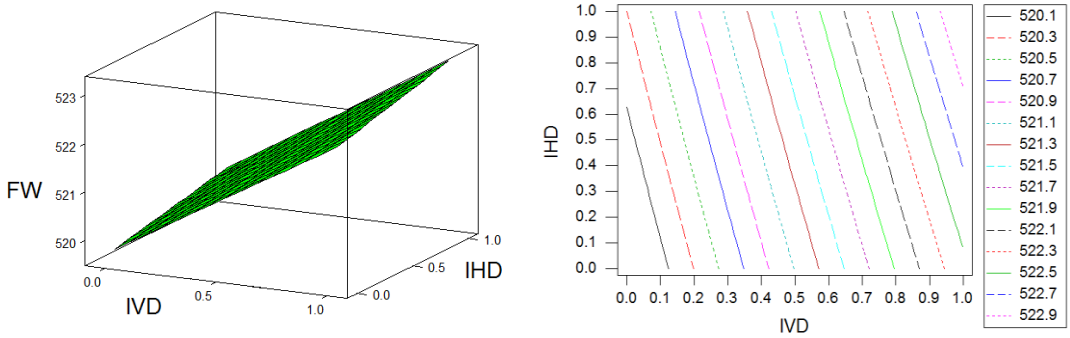

Figure 8-40 RS and RC plots for FW speeds at 6000 rpm rotor spin speed

8.4.2.4 RESPONSE FOR TEMPERATURE AND EXTERNAL VISCOUS DAMPING

Response surface of backward whirl speed is plotted against operating temperature and external viscous damping. The operating temperature is predominant as compared to external viscous damping. The contour plot is showing with constant backward whirl speed lines. These lines are almost horizontal at different rotor spin speeds which show that the effect of external damping is small and it is almost same with different rotor spin speeds. Details are shown in Figure 8-41, Figure 8-42 and Figure 8-43.

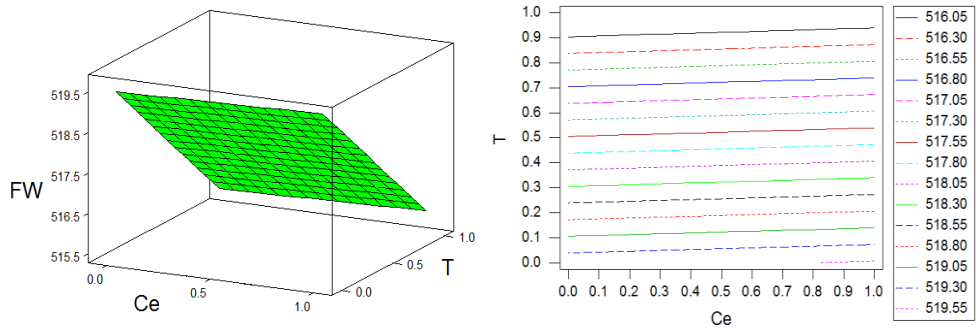

Figure 8-41 RS and RC plots for FW speeds at 2000 rpm rotor spin speed

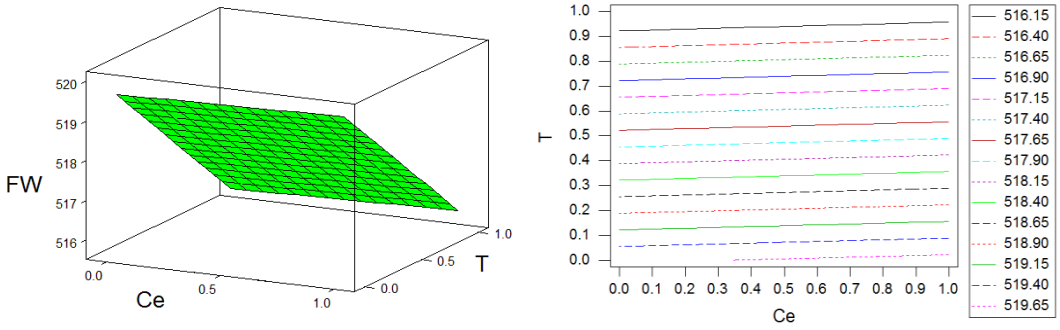

Figure 8-42 RS and RC plots for FW speeds at 4000 rpm rotor spin speed

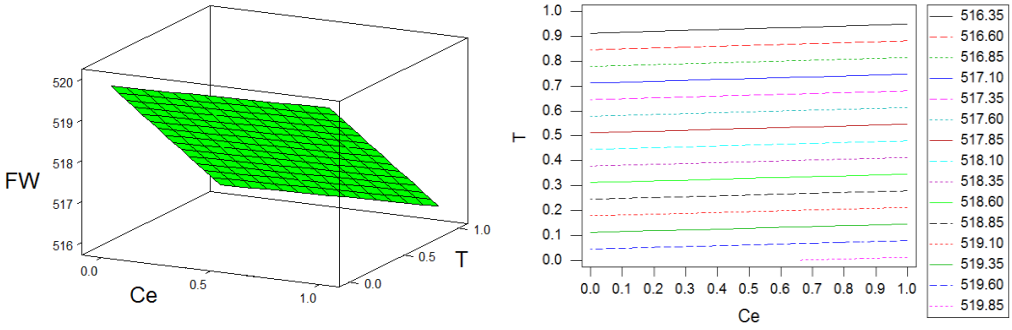

Figure 8-43 RS and RC plots for FW speeds at 6000 rpm rotor spin speed

8.4.2.5 RESPONSE FOR INTERNAL HYSTERETIC DAMPING AND EXTERNAL VISCOUS DAMPING

Response surface of forward whirl speed is plotted against internal hysteretic damping and external viscous damping. The contour plot is showing with constant forward whirl speed lines. These lines are almost horizontal at different rotor spin speeds which show that the effect of external viscous damping is small and it is almost same with different rotor spin speeds. Details are shown in Figure 8-44, Figure 8-45 and Figure 8-46.

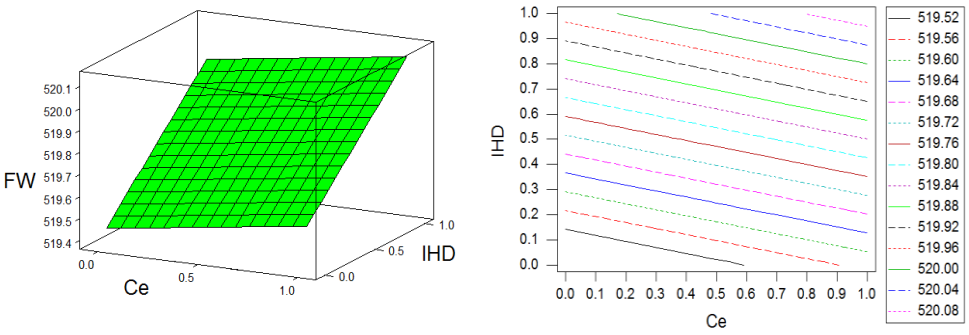

Figure 8-44 RS and RC plots for FW speeds at 2000 rpm rotor spin speed

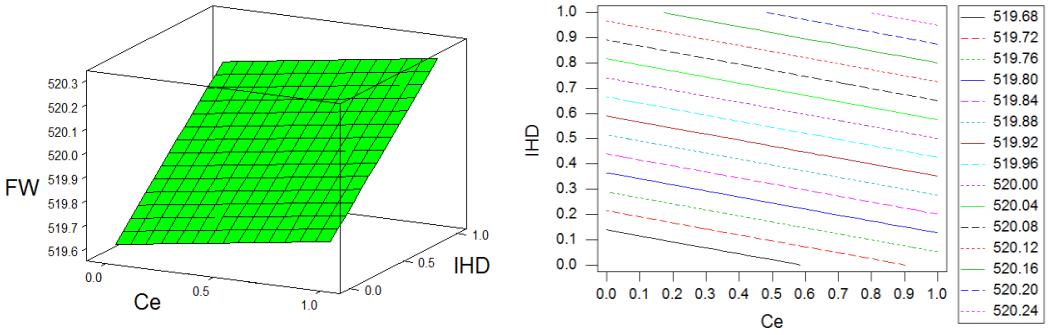

Figure 8-45 RS and RC plots for FW speeds at 4000 rpm rotor spin speed

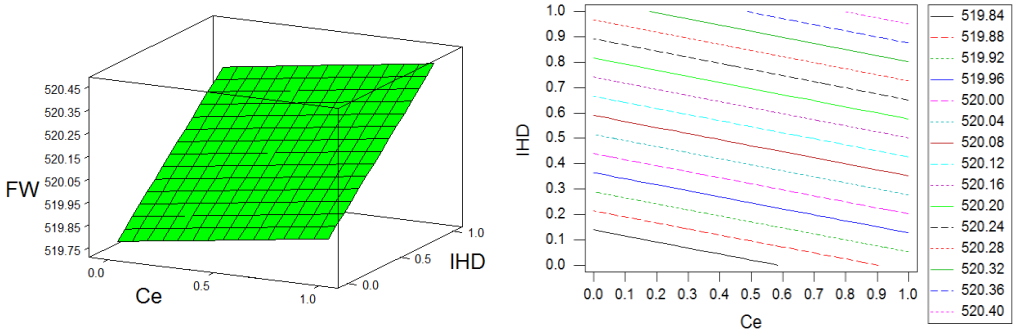

Figure 8-46 RS and RC plots for FW speeds at 6000 rpm rotor spin speed

8.4.2.6 RESPONSE FOR INTERNAL VISCOUS DAMPING AND EXTERNAL VISCOUS DAMPING

Response surface of forward whirl speed is plotted against internal viscous damping and external viscous damping. The contour plot is showing with constant forward whirl speed lines. These lines are curved at different rotor spin speeds. There is strong interaction between external viscous damping and internal viscous damping with respect to rotor spin speed. The slope of the lines is changing with respect to rotor spin speed. The physical significance of

this interaction is the effect of internal viscus damping is counteracting the effect of external viscous damping. This effect is more predominant at lower rotor spin speed which shows the curved lines and it is lesser at higher rotor spin speed which shows almost straight lines. Details are shown in Figure 8-47, Figure 8-48 and Figure 8-49.

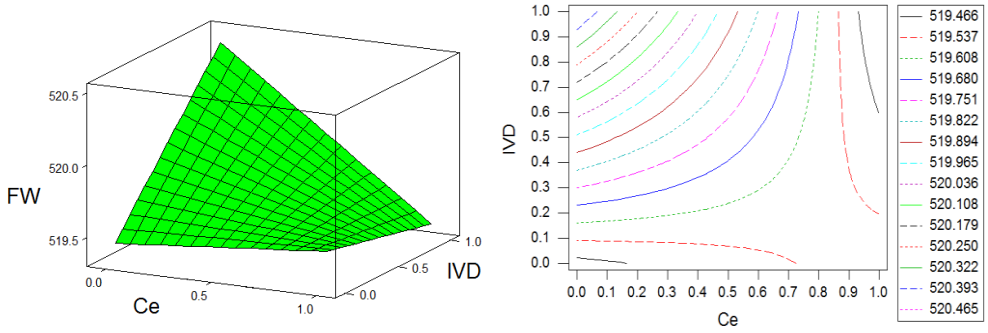

Figure 8-47 RS and RC plots for FW speeds at 2000 rpm rotor spin speed

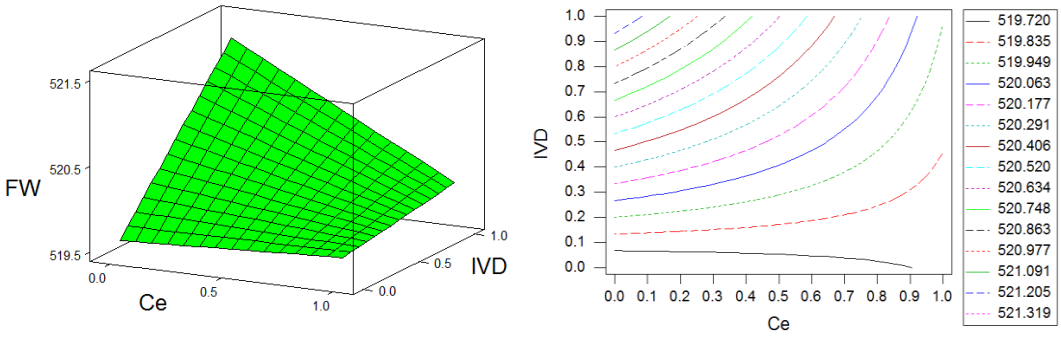

Figure 8-48 RS and RC plots for FW speeds at 4000 rpm rotor spin speed

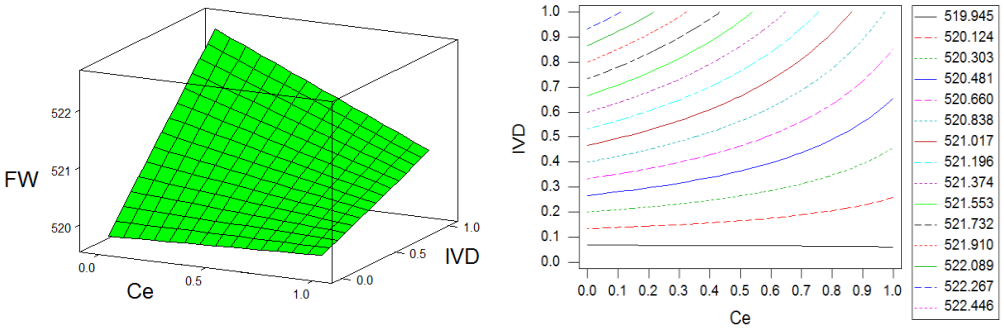

Figure 8-49 RS and RC plots for FW speeds at 6000 rpm rotor spin speed

8.5 PARETO PLOTS

The purpose of the Pareto plot is to highlight the most important among a (typically large) set of factors. It gives the summary of the important factors and its combinations.

8.5.1 PARETO PLOTS FOR BACKWARD WHIRL SPEEDS

8.5.1.1 AT ROTOR SPIN SPEED 2000 RPM

Operating temperature is the most important parameter and external viscous damping least important parameter. Internal hysteretic damping is the next important parameter. The sequence of the importance of all different parameters and its combinations are shown in Figure 8-50.

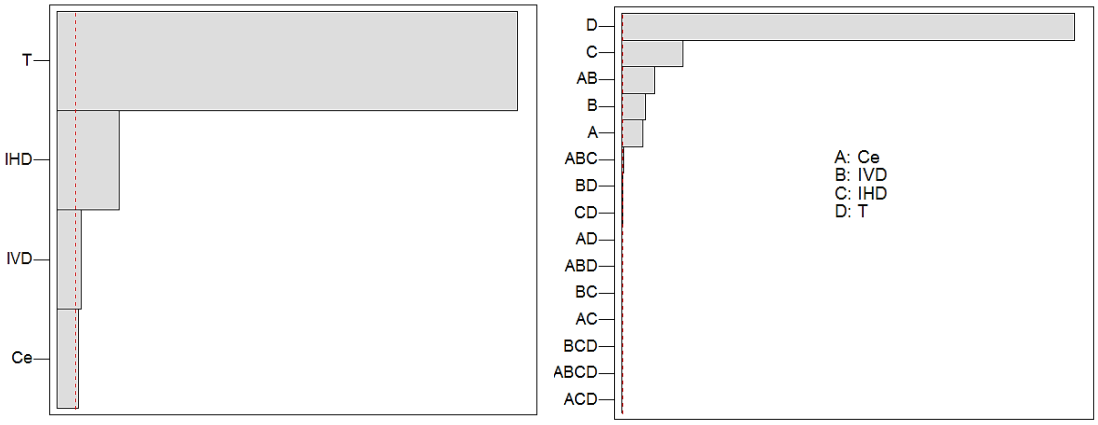

Figure 8-50 Pareto plot for BW speeds at 2000 rpm rotor spin speed

8.5.1.2 AT ROTOR SPIN SPEED 4000 RPM

Operating temperature is the most important parameter and external viscous damping least important parameter. Internal viscous damping is the next important parameter. The sequence of the importance of all different parameters and its combinations are shown in Figure 8-51.

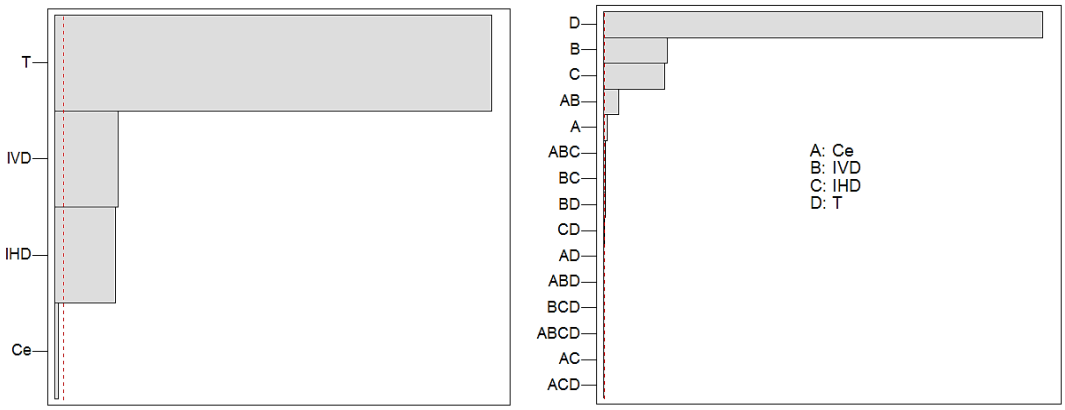

Figure 8-51 Pareto plot for BW speeds at 4000 rpm rotor spin speed

8.5.1.3 AT ROTOR SPIN SPEED 6000 RPM

Operating temperature is the most important parameter and external viscous damping least important parameter. Internal viscous damping is the next important parameter. The sequence of the importance of all different parameters and its combinations are shown in Figure 8-52.

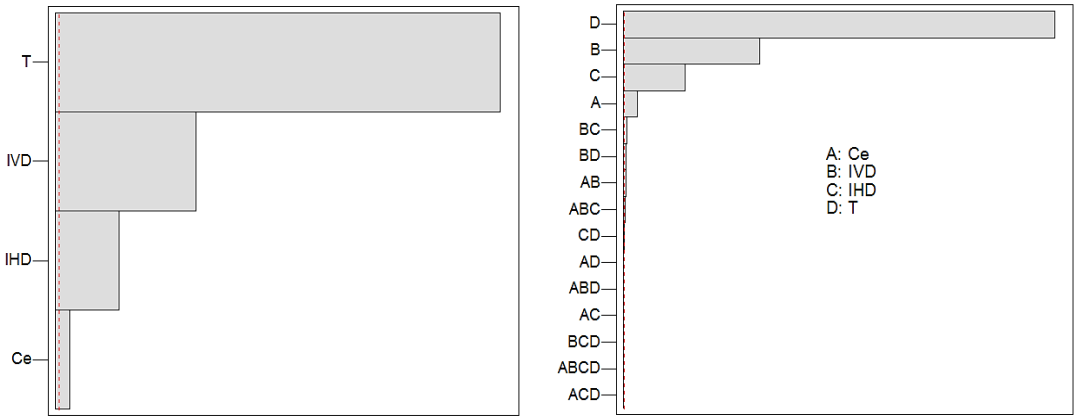

Figure 8-52 Pareto plot for BW speeds at 6000 rpm in rotor spin speed

8.5.2 PARETO SUMMARY OF BACKWARD WHIRL SPEEDS

- Operating temperature is the main parameter at different rotor spin speed.
- Internal viscous damping will become the main critical parameter at high rotor spin speed.
- External viscous damping is the least important parameter.

8.5.3 PARETO PLOTS FOR FORWARD WHIRL SPEEDS

8.5.3.1 AT ROTOR SPIN SPEED 2000 RPM

Operating temperature is the most important parameter and internal viscous damping least important parameter. Internal hysteretic damping is the next important parameter. The sequence of the importance of all different parameters and its combinations are shown in Figure 8-53.

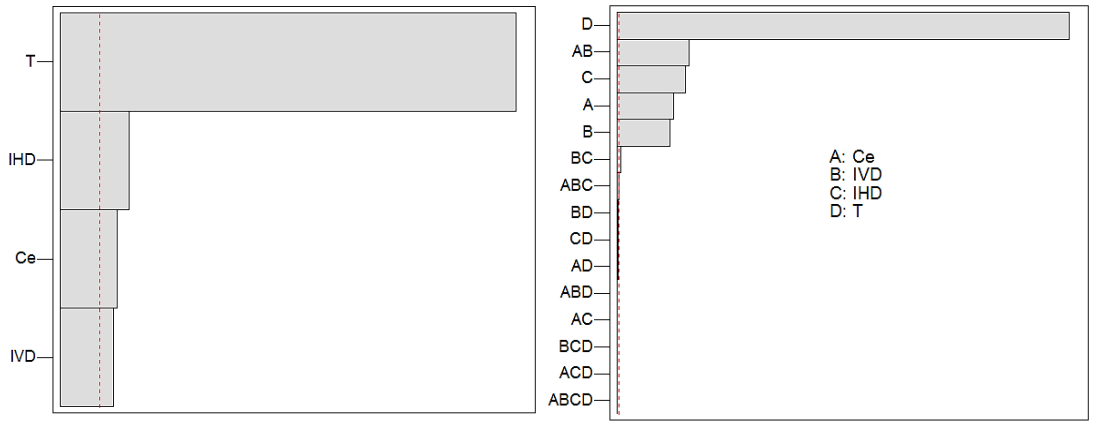

Figure 8-53 Pareto plot for FW speeds at 2000 rpm rotor spin speed

8.5.3.2 AT ROTOR SPIN SPEED 4000 RPM

Operating temperature is the most important parameter and internal hysteretic damping least important parameter. Internal viscous damping is the next important parameter. The sequence of the importance of all different parameters and its combinations are shown in Figure 8-54.

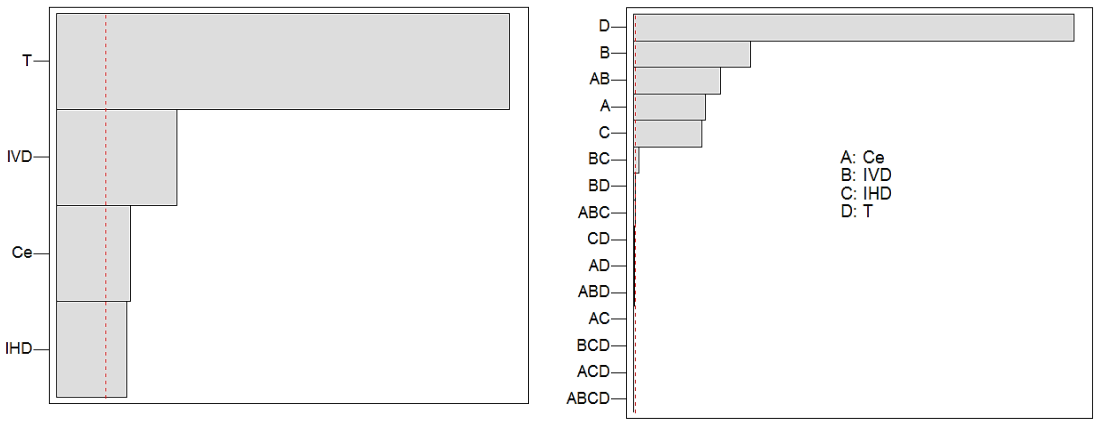

Figure 8-54 Pareto plot for FW speeds at 4000 rpm rotor spin speed

8.5.3.3 AT ROTOR SPIN SPEED 6000 RPM

Operating temperature is the most important parameter and internal hysteretic damping least important parameter. Internal viscous damping is the next important parameter. The sequence of the importance of all different parameters and its combinations are shown in Figure 8-55.

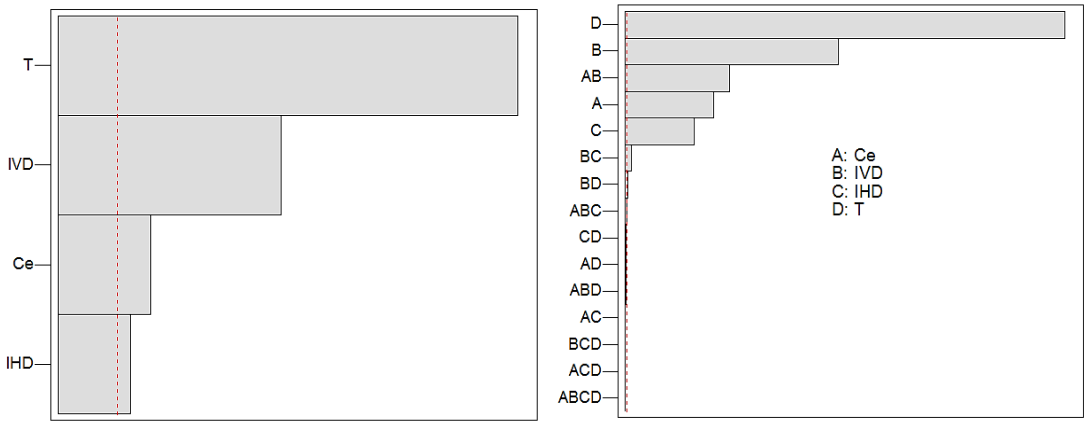

Figure 8-55 Pareto plot for FW speeds at 6000 rpm rotor spin speed

8.5.4 PARETO SUMMARY OF FORWARD WHIRL SPEEDS

- Operating temperature is the main parameter at different rotor spin speed.
- Internal viscous damping will become the main critical parameter at high rotor spin speed.

CHAPTER 9

SUMMARY AND CONCLUSIONS

9.1 SUMMARY

A finite element rotor model is developed to predict the forward whirl speed and backward whirl speed at different rotor spin speeds. It is an assemblage of rigid disks as a point mass, shaft elements of distributed mass and stiffness with discrete bearings as supports. The formulation of Timoshenko beam theory is used to create the finite element model of the rotor which considers rotary inertia and shear deformation. The equations of motion are developed using Lagrange's method.

Different forms of damping viz., internal viscous damping, internal hysteretic damping and external viscous damping and operating temperature models are developed. Updated the equations of motion to include the influence of all the above forms of damping and operating temperature. The equations of motion are developed in a fixed frame or inertial frame of reference and rotating frame or whirl frame of reference.

Simulation studies are carried out to understand the influence of different forms of damping and operating temperature on the whirl speeds and critical speeds. The sixteen possible combinations are listed and studied in detail. Simulation involves the prediction of whirl speeds and critical speeds for different critical parameters like internal viscous damping, internal hysteretic damping, external viscous damping and operating temperature acting either independently or simultaneously.

The non-dimensional term is defined namely ‘change in whirl speed ratio’, to understand the effect of different forms of damping, operating temperature and gyroscopic effect. Six sigma methodologies are employed to analyze the effect of critical parameters on the whirl speeds. It is a systematic approach is proposed to understand the behavior of the critical parameters at high rotor spin speed along with different forms of damping and operating temperature variation. This technique helps to understand the importance of critical parameters, its effect on the output parameters like rotor backward whirl, forward whirl and critical speed.

9.2 CONCLUSIONS AND APPLICATIONS

Based on the present study, the following conclusions are drawn.

9.2.1 CRITICAL PARAMETERS ALONE

i. Baseline or undamped

As expected for the undamped rotor, the spread between forward whirl speed and backward whirl speed increases with increase in rotor spin speed. It also increases at higher modes. This phenomenon is due to gyroscopic effect only.

Application

The undamped rotor is pure theoretical rotor model. This model is a baseline to understand the rotor behavior under the influence of different forms of damping and operating temperature. The simple solid shaft is supported by an anti-friction bearings and neglecting the hysteretic losses and operating temperature effect.

e.g. Lab test rig

ii. Internal viscous damping

The spread between forward whirl speed and backward whirl speed increases with increase in rotor spin speed except for the second mode. This interesting phenomenon is observed only for the second mode. The spread between forward whirl and backward whirl is small for the second mode and it is large for the first, third and fourth mode. This phenomenon is attributed to the nullifying effect of gyroscopic couple for the second mode and contributing effect of gyroscopic couple for other modes. As the internal viscous damping increases, the range of critical speeds also increases with offset at a higher level.

Application

Practical application or situation will be the different parts or components mounted on the shaft with shrink fit and operating temperature is not critical and external viscous damping is not present. The Fan, hub, coupling, balance ring etc are mounted on the shaft with shrink fit and it is supported by anti-friction bearings like ball bearings, roller bearings etc assuming no hysteretic losses in the shaft.

e.g. Lab test rig

iii. Internal hysteretic damping

The spread between forward whirl speed and backward whirl speed increases with increase in the rotor spin speed for all modes. This phenomenon is attributed to the adding effect of gyroscopic couple. The effect of internal hysteretic damping is small compared to that of internal viscous damping. As the internal hysteretic damping increases, the range of critical speeds remains almost same with offset at a higher level.

Application

Practical application or situation will be the simple shaft and operating temperature is not critical and external viscous damping is not present. e.g. shaft is supported with anti-friction bearings like ball bearings, roller bearings etc.

e.g. Lab test rig

iv. External viscous damping

As expected for the external viscous damped rotor, the spread between forward whirl speed and backward whirl speed increases with increase in rotor spin speed for all modes. The spread is large for higher modes. As the external viscous damping increases, the range of critical speeds remains almost same with offset at a higher level.

Application

Practical application or situation will be the simple shaft supported with an external viscous damping. Operating temperature is not critical in this load case. e.g. shaft is supported with sleeve or journal bearings assuming no hysteretic losses in the shaft

e.g. Lab test rig

v. Operating temperature

The spread between forward whirl speed and backward whirl speed increases with increase in rotor spin speed for all modes. This phenomenon is adding to the gyroscopic effect. The effect of operating temperature is considerable on whirl speeds and critical speeds. As the operating temperature increases, the range of critical speeds remains almost same with offset at a lower level.

Application

Practical application or situation will be the simple shaft assuming no hysteretic losses and high-temperature ambient conditions supported with anti-friction bearings like ball bearings, roller bearings etc.

e.g. Lab test rig

9.2.2 CRITICAL PARAMETERS IN COMBINED FORM

i. Internal viscous damping and external viscous damping

The spread between forward whirl speed and backward whirl speed increases with increase in rotor spin speed for all modes. This spread is larger for higher modes and at higher speeds. Critical speed range or spread is also increasing and shifting at higher side with an increase in combined form of internal viscous damping and external viscous damping.

Application

Practical application or situation will be the different parts or components mounted on the shaft with shrink fit and supported by sleeve bearings. The hysteretic losses in the shaft is assumed to be negligible. The operating temperature is not critical. e.g. Fan, hub, coupling, balance ring etc mounted on the shaft with shrink fit and shaft is supported by sleeve bearings.

e.g. Belt conveyor shaft.

ii. Internal hysteretic damping and external viscous damping

The spread between forward whirl speed and backward whirl speed increases with increase in rotor spin speed for all modes. This spread is larger for higher modes and at higher speeds. Critical speed range or spread remains constant and shifting at

higher side with an increase in combined form of internal hysteretic damping and external viscous.

Application

Practical application or situation will be the simple shaft supported on sleeve bearings. The operating temperature is not critical.

e.g. Large drive shaft.

iii. Internal viscous damping and internal hysteretic damping

The spread between forward whirl speed and backward whirl speed increases with increase in rotor spin speed for all modes except for the second mode. This interesting phenomenon is observed only for the second mode. The spread between forward whirl and backward whirl for second is very small and this phenomenon is attributed to the nullifying effect of gyroscopic couple. The spread is large for the first, third and fourth mode. Critical speed range or spread is increasing with the larger magnitude and shifting at higher side with an increase in combined form of internal viscous damping and internal hysteretic viscous damping.

Application

Practical application or situation will be the different parts or components mounted on the shaft with shrink fit and operating temperature is not critical and external viscous damping is not present. e.g. Fan, hub, coupling, balance ring etc mounted on the shaft with shrink fit, the shaft itself is having hysteretic loss and shaft is supported with anti-friction bearings like ball bearings, roller bearings.

e.g. Marine propeller shaft

iv. Operating temperature and internal viscous damping

The spread between forward whirl speed and backward whirl speed increases with increase in rotor spin speed for all modes except for the second mode. This interesting phenomenon is observed only for the second mode. The spread between forward whirl and backward whirl for second is very small and this phenomenon is nullifying to the gyroscopic effect. The spread is large for the first, third and fourth mode. Critical speed range or spread is increasing with the larger magnitude and shifting at the lower side with an increase in combined form of operating temperature and internal viscous damping.

Application

Practical application or situation will be the different parts or components mounted on the shaft with shrink fit and operating temperature is critical. The external viscous damping is not present. e.g. Fan, hub, coupling, balance ring etc mounted on the shaft with shrink fit and shaft is supported with anti-friction bearings like ball bearings, roller bearings. This is operated at high temperature.

e.g. Slow speed gear box.

v. Operating temperature and internal hysteretic damping

The spread between forward whirl speed and backward whirl speed increases with increase in rotor spin speed for all modes. Critical speed range or spread remains same and shifting at the lower side with an increase in combined form of operating temperature and internal hysteretic damping.

Application

The shaft is supported by anti-friction bearings, considering the hysteretic loss in the shaft. Operating at high temperature.

e.g. Exhaust fan shaft.

vi. Operating temperature and external viscous damping

The spread between forward whirl speed and backward whirl speed increases with increase in rotor spin speed for all modes. This spread is larger for higher modes and at higher speeds. Critical speed range or spread remains constant and shifting at the lower side with an increase in combined form of operating temperature and external viscous damping.

Application

Practical application or situation will be the simple shaft and high-temperature ambient conditions supported with sleeve bearings.

e.g. Drive shaft.

vii. Internal viscous damping, internal hysteretic damping and external viscous damping

The spread between forward whirl speed and backward whirl speed increases with increase in rotor spin speed for all modes. This spread is larger for higher modes and at higher speeds. Critical speed range or spread increases and shifting at higher side with an increase in combined form of external viscous damping internal viscous damping and internal hysteretic damping.

Application

Practical application or situation will be the different parts or components mounted on the shaft with shrink fit and supported on sleeve bearings. The operating temperature is not critical. e.g. Fan, hub, coupling, balance ring etc mounted on the shaft with shrink fit and shaft is supported with sleeve bearings.

e.g. Large vertical water pumps.

viii. Operating temperature, internal viscous damping and internal hysteretic damping

The spread between forward whirl speed and backward whirl speed increases with increase in rotor spin speed for all modes except for the second mode. This interesting phenomenon is observed only for the second mode. The spread between forward whirl and backward whirl for second is very small and this phenomenon is nullifying to the gyroscopic effect. The spread is large for the first, third and fourth mode. Critical speed range or spread is increasing with the larger magnitude and shifting at the lower side with an increase in combined form of operating temperature, internal viscous damping and internal hysteretic damping.

Application

Practical application or situation will be the different parts or components mounted on the shaft with shrink fit and operating temperature is critical. The external viscous damping is not present. e.g. Fan, hub, coupling, balance ring etc mounted on the shaft with shrink fit and shaft is supported with anti-friction bearings like ball bearings, roller bearings. This is operated at high temperature.

e.g. Furnace conveyor shaft with different mountings.

ix. Operating temperature, internal viscous damping and external viscous damping

The spread between forward whirl speed and backward whirl speed increases with increase in rotor spin speed for all modes. This spread is larger for higher modes

and at higher speeds. Critical speed range or spread changes slightly and shifting at the lower side with an increase in combined form of operating temperature, external viscous damping and internal viscous damping.

Application

Practical application or situation will be the different parts or components mounted on the shaft with shrink fit and operating temperature is critical. The external viscous damping is also present. e.g. Fan, hub, coupling, balance ring etc mounted on the shaft with shrink fit and shaft is supported with sleeve bearings like ball bearings, roller bearings. This is operated at high temperature.

e.g. Gearbox.

x. Operating temperature, internal hysteretic damping and external viscous damping

The spread between forward whirl speed and backward whirl speed increases with increase in rotor spin speed for all modes. This spread is larger for higher modes and at higher speeds. Critical speed range or spread changes slightly and shifting at the lower side with an increase in combined form of operating temperature, external viscous damping and internal hysteretic damping.

Application

Practical application or situation will be the simple shaft and high-temperature ambient conditions supported with sleeve bearings.

e.g. Drive shafts in power train.

xi. Operating temperature, internal viscous damping, internal hysteretic damping and external viscous damping

The spread between forward whirl speed and backward whirl speed increases with increase in rotor spin speed for all modes. This spread is larger for higher modes and at higher speeds. Critical speed range or spread changes slightly and shifting at the lower side with an increase in combined form of operating temperature, external viscous damping, internal viscous damping and internal hysteretic damping.

Application

Practical application or situation will be the different parts or components mounted on the shaft with shrink fit and supported on sleeve bearings. The operating

temperature is also critical. e.g. Fan, hub, coupling, balance ring etc mounted on the shaft with shrink fit and shaft is supported with sleeve bearings along with high ambient temperature.

e.g. Gas turbines, Steam turbines, Motors, Generators, Compressors etc

Conclusion and application summary:

Consideration of different forms of damping and operating temperature is very critical while designing the high-speed rotors for different applications. Studies on the influence of the critical parameters help in making the robust design. As the trend in the high-speed rotor bearing systems is to operate at higher speeds with greater power requirements, the state of the art is rapidly approaching a point where the effect of external viscous damping, internal viscous damping, internal hysteretic damping and operating temperature of the rotor bearing system cannot be ignored. The present research also gives a general tool for a designer, to choose the appropriate case study based on the applications.

9.3 SCOPE FOR FUTURE WORK

The following future work is proposed:

i. In the present model, studies on different forms of damping and operating temperature were limited to lateral dynamics. The models can be extended for torsional dynamics and axial dynamics.

ii. In the present model, the rotor structure was modelled as lumped mass. The proposed models can be extended to model the rotor geometry with equivalent disks.

iii. The developed finite element model can be extended to complete assembly of powertrain dynamics i.e. turbines connected with a generator, motors connected with pumps or compressors through the couplings.

iv. The scope can be extended for the composite rotor material.

MATRICES FOR THE EQUATIONS OF MOTION

$$\left[M_T^e\right]=\left[M_T\right]_0+\Phi\left[M_T\right]_1+\Phi^2\left[M_T\right]_2$$

$$\left[M_R^e\right]=\left[M_R\right]_0+\Phi\left[M_R\right]_1+\Phi^2\left[M_R\right]_2$$

$$\left[K_B^e\right]=\left[K_B\right]_0+\Phi\left[K_B\right]_1$$

$$\left[G^e\right]=\left[G\right]_0+\Phi\left[G\right]_1+\Phi^2\left[G\right]_2$$

$$\left[\hat{M}_R^e\right]=\frac{1}{2}\left[G^e\right]$$

$$\left[\hat{G}^e\right]=-2\left[M_R^e\right]$$

$$k=\frac{6(1+\nu)\left(1+\left(\frac{d}{D}\right)^2\right)^2}{(7+6\nu)\left(1+\left(\frac{d}{D}\right)^2\right)^2+(20+12\nu)\left(\frac{d}{D}\right)^2}$$

$$[M_T]_0=\frac{\rho AL}{420(1+\Phi)^2}\begin{bmatrix}156 & & & & & & & \\ 0 & 156 & & & Sym & & & \\ 0 & -22L & 4L^2 & & & & & \\ 22L & 0 & 0 & 4L^2 & & & & \\ 54 & 0 & 0 & 13L & 156 & & & \\ 0 & 54 & -13L & 0 & 0 & 156 & & \\ 0 & 13L & -3L^2 & 0 & 0 & 22L & 4L^2 & \\ -13L & 0 & 0 & -3L^2 & -22L & 0 & 0 & 4L^2\end{bmatrix}$$

$$[M_T]_1=\frac{\rho AL}{420(1+\Phi)^2}\begin{bmatrix}294 & & & & & & & \\ 0 & 294 & & & Sym & & & \\ 0 & -38.5L & 7L^2 & & & & & \\ 38.5L & 0 & 0 & 7L^2 & & & & \\ 126 & 0 & 0 & 31.5L & 294 & & & \\ 0 & 126 & -31.5L & 0 & 0 & 294 & & \\ 0 & 31.5L & -7L^2 & 0 & 0 & 38.5L & 7L^2 & \\ -31.5L & 0 & 0 & -7L^2 & -38.5L & 0 & 0 & 7L^2\end{bmatrix}$$

$$[M_T]_2 = \frac{\rho AL}{420(1+\Phi)^2}\begin{bmatrix} 140 & & & & & & & \\ 0 & 140 & & & Sym & & & \\ 0 & -17.5L & 3.5L^2 & & & & & \\ 17.5L & 0 & 0 & 3.5L^2 & & & & \\ 70 & 0 & 0 & 17.5L & 140 & & & \\ 0 & 70 & -17.5L & 0 & 0 & 140 & & \\ 0 & 17.5L & -3.5L^2 & 0 & 0 & 17.5L & 3.5L^2 & \\ -17.5L & 0 & 0 & -3.5L^2 & -17.5L & 0 & 0 & 3.5L^2 \end{bmatrix}$$

$$[M_R]_0 = \frac{\rho L}{(1+\Phi)^2}\begin{bmatrix} \frac{6}{5L} & & & & & & & \\ 0 & \frac{6}{5L} & & & Sym & & & \\ 0 & -\frac{1}{10} & \frac{2L}{15} & & & & & \\ \frac{1}{10} & 0 & 0 & \frac{2L}{15} & & & & \\ -\frac{6}{5L} & 0 & 0 & -\frac{1}{10} & \frac{6}{5L} & & & \\ 0 & -\frac{6}{5L} & \frac{1}{10} & 0 & 0 & \frac{6}{5L} & & \\ 0 & -\frac{1}{10} & -\frac{L}{30} & 0 & 0 & \frac{1}{10} & \frac{2L}{15} & \\ \frac{1}{10} & 0 & 0 & -\frac{L}{30} & -\frac{1}{10} & 0 & 0 & \frac{2L}{15} \end{bmatrix}$$

$$[M_R]_1 = \frac{\rho L}{(1+\Phi)^2}\begin{bmatrix} 0 & & & & & & & \\ 0 & 0 & & & Sym & & & \\ 0 & \frac{1}{2} & \frac{L}{6} & & & & & \\ -\frac{1}{2} & 0 & 0 & \frac{L}{6} & & & & \\ 0 & 0 & 0 & \frac{1}{2} & 0 & & & \\ 0 & 0 & -\frac{1}{2} & 0 & 0 & 0 & & \\ 0 & \frac{1}{2} & -\frac{L}{6} & 0 & 0 & -\frac{1}{2} & \frac{L}{6} & \\ -\frac{1}{2} & 0 & 0 & -\frac{L}{6} & \frac{1}{2} & 0 & 0 & \frac{L}{6} \end{bmatrix}$$

$$[M_R]_2 = \frac{\rho L}{(1+\Phi)^2}\begin{bmatrix} 0 & & & & & & & \\ 0 & 0 & & & Sym & & & \\ 0 & 0 & \frac{L}{3} & & & & & \\ 0 & 0 & 0 & \frac{L}{3} & & & & \\ 0 & 0 & 0 & 0 & 0 & & & \\ 0 & 0 & 0 & 0 & 0 & 0 & & \\ 0 & 0 & \frac{L}{6} & 0 & 0 & 0 & \frac{L}{3} & \\ 0 & 0 & 0 & \frac{L}{6} & 0 & 0 & 0 & \frac{L}{3} \end{bmatrix}$$

$$[K_B]_0 = \frac{EI}{(1+\Phi)L^3}\begin{bmatrix} 12 & & & & & & & \\ 0 & 12 & & & Sym & & & \\ 0 & -6L & 4L^2 & & & & & \\ 6L & 0 & 0 & 4L^2 & & & & \\ -12 & 0 & 0 & -6L & 12 & & & \\ 0 & -12 & 6L & 0 & 0 & 12 & & \\ 0 & -6L & 2L^2 & 0 & 0 & 6L & 4L^2 & \\ 6L & 0 & 0 & 2L^2 & -6L & 0 & 0 & 4L^2 \end{bmatrix}$$

$$[K_B]_1 = \frac{EI}{(1+\Phi)L^3}\begin{bmatrix} 0 & & & & & & & \\ 0 & 0 & & & Sym & & & \\ 0 & 0 & L^2 & & & & & \\ 0 & 0 & 0 & L^2 & & & & \\ 0 & 0 & 0 & 0 & 0 & & & \\ 0 & 0 & 0 & 0 & 0 & 0 & & \\ 0 & 0 & -L^2 & 0 & 0 & 0 & L^2 & \\ 0 & 0 & 0 & -L^2 & 0 & 0 & 0 & L^2 \end{bmatrix}$$

$$[G]_0 = \frac{\rho A r^2}{60(1+\Phi)^2 L}\begin{bmatrix} 0 & & & & & & & \\ 36 & 0 & & & Skew & Sym & & \\ -3L & 0 & 0 & & & & & \\ 0 & -3L & 4L^2 & 0 & & & & \\ 0 & 36 & -3L & 0 & 0 & & & \\ -36 & 0 & 0 & -3L & 36 & 0 & & \\ -3L & 0 & 0 & L^2 & 3L & 0 & 0 & \\ 0 & -3L & -L^2 & 0 & 0 & 3L & 4L^2 & 0 \end{bmatrix}$$

$$[G]_1 = \frac{\rho A r^2}{60(1+\Phi)^2 L}\begin{bmatrix} 0 & & & & & & & \\ 0 & 0 & & & \textit{Skew} & \textit{Sym} & & \\ 15L & 0 & 0 & & & & & \\ 0 & 15L & 5L^2 & 0 & & & & \\ 0 & 0 & 15L & 0 & 0 & & & \\ 0 & 0 & 0 & 15L & 0 & 0 & & \\ 15L & 0 & 0 & 5L^2 & 0 & 0 & 0 & \\ 0 & 15L & -5L^2 & 0 & -15L & 5L^2 & 5L^2 & 0 \end{bmatrix}$$

$$[G]_2 = \frac{\rho A r^2}{60(1+\Phi)^2 L}\begin{bmatrix} 0 & & & & & & & \\ 0 & 0 & & & \textit{Skew} & \textit{Sym} & & \\ 0 & 0 & 0 & & & & & \\ 0 & 0 & 10L^2 & 0 & & & & \\ 0 & 0 & 0 & 0 & 0 & & & \\ 0 & 0 & 0 & 0 & 0 & 0 & & \\ 0 & 0 & 0 & -5L^2 & 0 & 0 & 0 & \\ 0 & 0 & 5L^2 & 0 & 0 & 0 & 10L^2 & 0 \end{bmatrix}$$

$$\left[K_C^e\right] = \frac{EI}{(1+\Phi)L^3}\begin{bmatrix} 0 & & & & & & & \\ -12 & 0 & & & \textit{Skew} & \textit{Sym} & & \\ 6L & 0 & 0 & & & & & \\ 0 & 6L & -4L^2 & 0 & & & & \\ 0 & -12 & 6L & 0 & 0 & & & \\ 12 & 0 & 0 & 6L & -12 & 0 & & \\ 6L & 0 & 0 & 2L^2 & -6L & 0 & 0 & \\ 0 & 6L & -2L^2 & 0 & 0 & -6L & -4L^2 & 0 \end{bmatrix}$$

MATRICES FOR THE EQUATIONS OF MOTION WITH INCORPORATION OF TEMPERATURE

$$\left[M_{Tt}^{e}\right]=\left[M_{Tt}\right]_0+\Phi\left[M_{Tt}\right]_1+\Phi^2\left[M_{Tt}\right]_2$$

$$\left[M_{Rt}^{e}\right]=\left[M_{Rt}\right]_0+\Phi\left[M_{Rt}\right]_1+\Phi^2\left[M_{Rt}\right]_2$$

$$[K_{Bt}^{e}]=[K_{Bt}]_0+\Phi[K_{Bt}]_1$$

$$\left[G_{t}^{e}\right]=\left[G_{t}\right]_0+\Phi\left[G_{t}\right]_1+\Phi^2\left[G_{t}\right]_2$$

$$\left[\hat{M}_{Rt}^{e}\right]=\frac{1}{2}\left[G_{t}^{e}\right]$$

$$\left[\hat{G}_{t}^{e}\right]=-2\left[M_{Rt}^{e}\right]$$

$$\Phi_t=\frac{12E_tI}{\kappa_tAGL^2}$$

$$k_t=\frac{6(1+\nu_t)\left(1+\left(\frac{d}{D}\right)^2\right)^2}{(7+6\nu_t)\left(1+\left(\frac{d}{D}\right)^2\right)^2+(20+12\nu_t)\left(\frac{d}{D}\right)^2}$$

$$[M_{Tt}]_0=\frac{\rho AL}{420(1+\Phi_t)^2}\begin{bmatrix}
156 & & & & & & & \\
0 & 156 & & & Sym & & & \\
0 & -22L & 4L^2 & & & & & \\
22L & 0 & 0 & 4L^2 & & & & \\
54 & 0 & 0 & 13L & 156 & & & \\
0 & 54 & -13L & 0 & 0 & 156 & & \\
0 & 13L & -3L^2 & 0 & 0 & 22L & 4L^2 & \\
-13L & 0 & 0 & -3L^2 & -22L & 0 & 0 & 4L^2
\end{bmatrix}$$

$$[M_{Tt}]_1 = \frac{\rho AL}{420(1+\Phi_t)^2}\begin{bmatrix} 294 & & & & & & & \\ 0 & 294 & & & Sym & & & \\ 0 & -38.5L & 7L^2 & & & & & \\ 38.5L & 0 & 0 & 7L^2 & & & & \\ 126 & 0 & 0 & 31.5L & 294 & & & \\ 0 & 126 & -31.5L & 0 & 0 & 294 & & \\ 0 & 31.5L & -7L^2 & 0 & 0 & 38.5L & 7L^2 & \\ -31.5L & 0 & 0 & -7L^2 & -38.5L & 0 & 0 & 7L^2 \end{bmatrix}$$

$$[M_{Tt}]_2 = \frac{\rho AL}{420(1+\Phi_t)^2}\begin{bmatrix} 140 & & & & & & & \\ 0 & 140 & & & Sym & & & \\ 0 & -17.5L & 3.5L^2 & & & & & \\ 17.5L & 0 & 0 & 3.5L^2 & & & & \\ 70 & 0 & 0 & 17.5L & 140 & & & \\ 0 & 70 & -17.5L & 0 & 0 & 140 & & \\ 0 & 17.5L & -3.5L^2 & 0 & 0 & 17.5L & 3.5L^2 & \\ -17.5L & 0 & 0 & -3.5L^2 & -17.5L & 0 & 0 & 3.5L^2 \end{bmatrix}$$

$$[M_{Rt}]_0 = \frac{\rho L}{(1+\Phi_t)^2}\begin{bmatrix} \frac{6}{5L} & & & & & & & \\ 0 & \frac{6}{5L} & & & Sym & & & \\ 0 & -\frac{1}{10} & \frac{2L}{15} & & & & & \\ \frac{1}{10} & 0 & 0 & \frac{2L}{15} & & & & \\ -\frac{6}{5L} & 0 & 0 & -\frac{1}{10} & \frac{6}{5L} & & & \\ 0 & -\frac{6}{5L} & \frac{1}{10} & 0 & 0 & \frac{6}{5L} & & \\ 0 & -\frac{1}{10} & -\frac{L}{30} & 0 & 0 & \frac{1}{10} & \frac{2L}{15} & \\ \frac{1}{10} & 0 & 0 & -\frac{L}{30} & -\frac{1}{10} & 0 & 0 & \frac{2L}{15} \end{bmatrix}$$

$$[M_{Rt}]_1 = \frac{\rho L}{(1+\Phi_t)^2}\begin{bmatrix} 0 & & & & & & & \\ 0 & 0 & & & Sym & & & \\ 0 & \frac{1}{2} & \frac{L}{6} & & & & & \\ -\frac{1}{2} & 0 & 0 & \frac{L}{6} & & & & \\ 0 & 0 & 0 & \frac{1}{2} & 0 & & & \\ 0 & 0 & -\frac{1}{2} & 0 & 0 & 0 & & \\ 0 & \frac{1}{2} & -\frac{L}{6} & 0 & 0 & -\frac{1}{2} & \frac{L}{6} & \\ -\frac{1}{2} & 0 & 0 & -\frac{L}{6} & \frac{1}{2} & 0 & 0 & \frac{L}{6} \end{bmatrix}$$

$$[M_{Rt}]_2 = \frac{\rho L}{(1+\Phi_t)^2}\begin{bmatrix} 0 & & & & & & & \\ 0 & 0 & & & Sym & & & \\ 0 & 0 & \frac{L}{3} & & & & & \\ 0 & 0 & 0 & \frac{L}{3} & & & & \\ 0 & 0 & 0 & 0 & 0 & & & \\ 0 & 0 & 0 & 0 & 0 & 0 & & \\ 0 & 0 & \frac{L}{6} & 0 & 0 & 0 & \frac{L}{3} & \\ 0 & 0 & 0 & \frac{L}{6} & 0 & 0 & 0 & \frac{L}{3} \end{bmatrix}$$

$$[K_{Bt}]_0 = \frac{E_t I}{(1+\Phi_t)L^3}\begin{bmatrix} 12 & & & & & & & \\ 0 & 12 & & & Sym & & & \\ 0 & -6L & 4L^2 & & & & & \\ 6L & 0 & 0 & 4L^2 & & & & \\ -12 & 0 & 0 & -6L & 12 & & & \\ 0 & -12 & 6L & 0 & 0 & 12 & & \\ 0 & -6L & 2L^2 & 0 & 0 & 6L & 4L^2 & \\ 6L & 0 & 0 & 2L^2 & -6L & 0 & 0 & 4L^2 \end{bmatrix}$$

$$[K_{Bt}]_1 = \frac{E_t I}{(1+\Phi_t)L^3}\begin{bmatrix} 0 & & & & & & & \\ 0 & 0 & & & Sym & & & \\ 0 & 0 & L^2 & & & & & \\ 0 & 0 & 0 & L^2 & & & & \\ 0 & 0 & 0 & 0 & 0 & & & \\ 0 & 0 & 0 & 0 & 0 & 0 & & \\ 0 & 0 & -L^2 & 0 & 0 & 0 & L^2 & \\ 0 & 0 & 0 & -L^2 & 0 & 0 & 0 & L^2 \end{bmatrix}$$

$$[G_t]_0 = \frac{\rho A r^2}{60(1+\Phi_t)^2 L}\begin{bmatrix} 0 & & & & & & & \\ 36 & 0 & & & Skew & Sym & & \\ -3L & 0 & 0 & & & & & \\ 0 & -3L & 4L^2 & 0 & & & & \\ 0 & 36 & -3L & 0 & 0 & & & \\ -36 & 0 & 0 & -3L & 36 & 0 & & \\ -3L & 0 & 0 & L^2 & 3L & 0 & 0 & \\ 0 & -3L & -L^2 & 0 & 0 & 3L & 4L^2 & 0 \end{bmatrix}$$

$$[G_t]_1 = \frac{\rho A r^2}{60(1+\Phi_t)^2 L}\begin{bmatrix} 0 & & & & & & & \\ 0 & 0 & & & \textit{Skew} & \textit{Sym} & & \\ 15L & 0 & 0 & & & & & \\ 0 & 15L & 5L^2 & 0 & & & & \\ 0 & 0 & 15L & 0 & 0 & & & \\ 0 & 0 & 0 & 15L & 0 & 0 & & \\ 15L & 0 & 0 & 5L^2 & 0 & 0 & 0 & \\ 0 & 15L & -5L^2 & 0 & -15L & 5L^2 & 5L^2 & 0 \end{bmatrix}$$

$$[G_t]_2 = \frac{\rho A r^2}{60(1+\Phi_t)^2 L}\begin{bmatrix} 0 & & & & & & & \\ 0 & 0 & & & \textit{Skew} & \textit{Sym} & & \\ 0 & 0 & 0 & & & & & \\ 0 & 0 & 10L^2 & 0 & & & & \\ 0 & 0 & 0 & 0 & 0 & & & \\ 0 & 0 & 0 & 0 & 0 & 0 & & \\ 0 & 0 & 0 & -5L^2 & 0 & 0 & 0 & \\ 0 & 0 & 5L^2 & 0 & 0 & 0 & 10L^2 & 0 \end{bmatrix}$$

$$\left[K_{Ct}^{e}\right] = \frac{E_t I}{(1+\Phi_t)L^3}\begin{bmatrix} 0 & & & & & & & \\ -12 & 0 & & & \textit{Skew} & \textit{Sym} & & \\ 6L & 0 & 0 & & & & & \\ 0 & 6L & -4L^2 & 0 & & & & \\ 0 & -12 & 6L & 0 & 0 & & & \\ 12 & 0 & 0 & 6L & -12 & 0 & & \\ 6L & 0 & 0 & 2L^2 & -6L & 0 & 0 & \\ 0 & 6L & -2L^2 & 0 & 0 & -6L & -4L^2 & 0 \end{bmatrix}$$

REFERENCES

[1] Yukio Ishida and Toshio Yamamoto (2006), Linear and Nonlinear Rotordynamics, 2nd Enlarged and Improved Edition, Published by *Wiley-VCH*, pp. 3.

[2] Downham, E. (1957), Theory of Shaft Whirling. *The Engineer*, pp. 518-522.

[3] Newkirk, B. L. and Taylor, H. D. (1925), Shaft Whipping Due to Oil Action in Journal Bearings, *General Electric Review*, pp. 559-568.

[4] Newkirk, B. L., Taylor, Grobel, L. P., Oil Film Whirl – A Non Whirling Bearing, *Transaction of the ASME, APM* -56-10

[5] Ehrich, F. F. (1964), Shaft Whirl Induced by Rotor Internal Damping, *Journal of Applied Mechanics*, pp. 279-282.

[6] Gunter, E., J., (1966), Dynamic Stability of Rotor – Bearing Systems, *National Aeronautics and Space Administration (NASA)*

[7] Gunter, E. J. (1967), The Influence of Internal Friction on the Stability of High-Speed Rotors, *Journal of Engineering for Society*, pp. 683-688.

[8] Lund, J. W. (1974), Stability and Damped Critical Speeds of a Flexible Rotor in Fluid Film Bearings, *Journal of Engineering for Society*, pp. 509-517.

[9] Nelson, H. D. and McVaugh, J. M. (1976), The Dynamics of Rotor-Bearing Systems Using Finite Elements, *Journal of Engineering for Industry*, pp. 593-600.

[10] Nelson, H. D. (1980), A Finite Rotating Shaft Element Using Timoshenko Beam Theory, *Journal of Mechanical Design*, pp. 793-803.

[11] Zorzi, E.S. and Nelson, H. D. (1977), Finite Element Simulation of Rotor - Bearing Systems with Internal Damping, *Journal of Engineering for Power*, pp. 71-76.

[12] Zorzi, E.S. and Nelson, H. D. (1980), The Dynamics of Rotor - Bearing Systems with Axial Torque - A Finite Element Approach, *Transaction of the ASME*, pp. 158-161.

[13] Glasgow, D. A. and Nelson, H. D. (1980), Stability Analysis of Rotor – Bearing Systems Using Component Mode Synthesis, *Transaction of ASME*, pp. 352-359.

[14] Walton, J., Artilles, A., Lund, J., Zorzi, E. (1991), Internal Rotor Friction Instability, *Mechanical Technology Incorporated Report, 88TR39, 1990*

[15] Artilles, Antonio F. (1991), The Effects of Friction in Axial Splines on Rotor System Stability, *The American Society of Mechanical Engineers*. 91-GT-251.

[16] Lyn M. Greenhill and Guillermo A. Cornejo (1995), Critical speeds resulting from unbalance excitation of backward whirl modes, *Design Engineering Technical Conferences, ASME*.

[17] S. P. Singh and K. Gupta (1996), Dynamic Analysis of Composite Rotors, *International Journal of Rotating Machinery*, pp. 179-186.

[18] Jose Luis Mendoza Zabala (1996), State space formulation for Structural Dynamics, Master of Science Thesis, *Massachusetts Institute of Technology*.

[19] Xiaoqiang Wang (1997), The Influence of a Skewed Disk on a Flexible Rotating Shaft, Master of Science Thesis, *Virginia Polytechnic Institute and State University*.

[20] Forrai, L. (1996), Stability Analysis of Symmetrical Rotor Bearing Systems with Internal Damping using Finite Element Method, *The American Society of Mechanical Engineers*. 96-GT-407.

[21] Forrai, L. (2000), A Finite Element Model for Stability Analysis of Symmetrical Rotor Systems with Internal Damping, *Journal of Computational and Applied Mechanics*, pp. 37-47.

[22] Mayuresh J. Patil (2000), Decoupled Second-Order Equations and Modal Analysis of a General Non-Conservative System, *American Institute of Aeronautics and Astronautics, Dynamics Specialists Conference*, Atlanta.

[23] Sondipon Adhikari (2000), Damping Models for Structural Vibration, PhD Thesis, *Cambridge University Engineering Department*.

[24] Srinivasan, A. (2003) The Influence of Internal Friction on Rotor Dynamic Instability, *MS Thesis, Texas A&M University, College Station, 2003*

[25] Darryl Chauvin (2003), An experimental investigation of whirl instability including effects of lubricant temperature in plain circular journal bearings, PhD Thesis, *Nicholls State University*.

[26] Jean-Jacques Sinou and Fabrice Thouverez (2005), Experimental Study of a Flexible Rotor and Its Dependency on the Rolling-Bearing Temperature, *International Journal of Rotating Machinery*, pp. 1-8.

[27] Jonas Fischer and Jens Strackelijan (2006), FEM-Simulation and stability analyses of high speed rotor systems, *IFToMM – Conference on Rotor Dynamics*, Vienna, Austria

[28] Ana-Diana Ancas and D. Gorbanescu (2006), Theoretical Models in the Study of Temperature effect on Steel Mechanical Properties, *Buletinul Institutului Politehnic DIN IASI, Construct II Arhitectura* pp. 49-54.

[29] Syed M. M. J. (2007), Shrink Fit Effects on Rotor Dynamic Stability: Experimental and Theoretical Study, Ph.D. Thesis, *Texas A&M University, College Station*.

[30] Andras Simon (2009), Adaptive disturbance rejection and stabilization for rotor systems with internal damping, PhD Thesis, *Auburn, Alabama.*

[31] Jhon Malta, M. T. (2009), Investigation of Anisotropic Rotor with Different Shaft Orientation, PhD Thesis, *Darmstadt*.

[32] C. Chattoraj, S. N. Sengupta and M.C. Majumder (2009), Whirling of a Rotor on Isotropic Shaft considering Gyroscopic Effect and Asymmetric Bearing Stiffness, *National Conference on Machines and Mechanisms*, pp. 287-297.

[33] F. E. Boru (2010), Numerical and Experimental Response and Stability Investigations of Anisotropic Rotor-Bearing Systems, PhD Thesis, *Kassel university press GmbH, Kassel*.

[34] H. Roy and J. K. Dutt (2010), Finite Element Modelling of Viscoelastic Rotors: An Operator Based Approach, *Proceedings of ICTACEM 2010*.

[35] V. Rastogi, A. Mukherjee and A. Dasgupta (2011), Dynamic modeling of rotor shaft with internal damping driven through a dissipative coupling, *International Journal of Modeling, Simulation and Scientific Computing*, pp. 105-129

[36] B. Vervisch, K. Stockman and M. Loccufier (2012), Sensitivity of the threshold in linearized rotordynamics, *Proceedings of ISMA 2012*, pp. 1387-1402.

[37] N. Wagner and R. Helfrich (2013), Dynamics of rotors in complex structures, *NAFEMS World Congress*, pp. 1-12.

[38] Dimarogonas, Paipetis and Chondros (2013), Analytical Methods in Rotor Dynamics, 2nd Edition, Chapter 8, *Thermal Effects Due to Vibration of Shafts*, pp. 211-217.

[39] W. M. Miranda and M. T. C. Faria (2014), Finite Element Method Applied to the Eigenvalue Analysis of Flexible Rotors Supported by Journal Bearings, *Engineering*, 6, pp. 127-137.

[40] Inés Pérez-Ullivarri Alabart (2014), Development of a Strategy to Determine the Internal Damping Coefficient in a Rotating Interference Fit to Verify Stability in Rotordynamics, Master Thesis, *Technische Universität Berlin.*

[41] Lili Gu and Fulei Chu (2014), An analytical study of rotor dynamics coupled with thermal effect for a continuous rotor shaft, *Journal of Sound and Vibration*, pp. 31-49

[42] M. Zhuo, L.H. Yang and L. Yu (2014), The steady-state thermal effect on rotordynamics of a rod fastened Rotor-bearing system, *Proceedings of the ASME 2014 International Mechanical Engineering Congress and Exposition.*

[43] M. Tyagi and M. Chouskey (2015), Modal Analysis of Asymmetric Rotor System Using Simple Model, *Universal Journal of Control and Automation*, pp. 10-14.

[44] Mei-Hui Jia and Cheng-Lin Wang (2016), Effect of Temperature on Mechanical Properties and Dynamic Characteristics of the Rotor in High Acceleration, *International Conference on Mechanics Design, Manufacturing and Automation.*

[45] Wen Jeng Chen and Edgar J. Gunter, Introduction to Dynamics of Rotor – Bearing Systems, *Trafford Publishing*, ISBN – 978-1-4120-5190-3.